

**Growth of TiO₂, ZnO Nanostructured Films for
Investigation of Resistive Switching,
Photo-Absorbance Properties, Glucose Sensing
and Structural Phase Transition**

**By
Ashis Kumar Manna
PHYS07201304006**

Institute of Physics, Bhubaneswar

*A thesis submitted to the
Board of Studies in Physical Sciences
In partial fulfillment of requirements
For the Degree of*

**DOCTOR OF PHILOSOPHY
of
HOMI BHABHA NATIONAL INSTITUTE**



July, 2019

Homi Bhabha National Institute

Recommendations of the Viva Voce Committee

As members of the Viva Voce Committee, we certify that we have read the dissertation prepared by Mr. Ashis Kumar Manna entitled "Growth of TiO₂, ZnO nanostructured films for investigation of resistive switching, photo-absorbance properties, glucose sensing and structural phase transition.", and recommend that it may be accepted as fulfilling the dissertation requirement for the Degree of Doctor of Philosophy.

Chairman - Prof. A.M. Jayannavar

A.M. Jayannavar

Date: 26-06-2020

Guide /Convener - Prof. S. Varma

S. Varma

Date: 26/06/2020

Co-guide (if any)

Date:

Examiner - Prof. K.K. Nanda, MRC, IISc Bangalore

K.K. Nanda

Date: 26/06/2020

Member 1 - Prof. T. Som

T. Som

Date:

Member 2 - Prof. P.K. Sahoo (NISER)

P.K. Sahoo

Date: 26/06/2020

Final approval and acceptance of this thesis is contingent upon the candidate's submission of the final copies of the dissertation to HBNI.

I/We hereby certify that I/we have read this thesis prepared under my/our direction and recommend that it may be accepted as fulfilling the thesis requirement.

Date: 26/06/2020

Place: Bhubaneswar

Co-guide (if applicable)

S. Varma

Guide

STATEMENT BY AUTHOR

This dissertation has been submitted in partial fulfillment of requirements for an advanced degree at Homi Bhabha National Institute (HBNI) and is deposited in the Library to be made available to borrowers under rules of the HBNI.

Brief quotations from this dissertation are allowable without special permission, provided that accurate acknowledgement of source is made. Requests for permission for extended quotation from or reproduction of this manuscript in whole or in part may be granted by the Competent Authority of HBNI when in his or her judgment the proposed use of the material is in the interests of scholarship. In all other instances, however, permission must be obtained from the author.

Ashis Kumar Manna
Ashis Kumar Manna

DECLARATION

I, hereby declare that the investigation presented in the thesis has been carried out by me. The work is original and has not been submitted earlier as a whole or in part for a degree/diploma at this or any other Institution/University.

Ashis kumar Manna
Ashis Kumar Manna

List of publications arising from the thesis

Journal

1. The effect of Ti^{+} ion implantation on the Anatase-Rutile phase transformation and resistive switching properties of TiO_2 thin films,
Ashis Manna, A. Barman, Shalik R. Joshi, B. Satpati, P. Dash, Ananya Chattaraj, S.K.Srivastava, P.K.Sahoo, A. Kanjilal, D. Kanjilal, Shikha Varma, Journal Of Applied Physics, **2018**, 124, 155303.
2. Dynamics of surface Evolution of Rutile TiO_2 (110) after ion irradiation,
Ashis Manna, Vanaraj Solanki , D. Kanjilal and Shikha Varma, Radiation Effects and Defects in Solids,**2019**, 174, 3-4.
3. Synthesis and characterization of aligned ZnO nanorods for visible light photocatalysis,
P. Dash, Ashis Manna, N. C. Mishra and Shikha Varma, Physica E: Low-dimensional Systems and Nanostructures,**2019**, 107, 38-46.
4. Non-Enzymetic Glucose Sensing and Bandgap Tailoring of Cu_2O -ZnO Hybrid Nanostructures Prepared by Single Step Coelectrodeposition Technique,
Ashis Manna, Puspendu Guha, S.K Srivastava and Shikha Varma.(Under Review)

Conferences

1. Radiation Effects in Insulators(REI-18), October 2015, Jaipur, Rajasthan, India
Poster– Investigation of patterning of TiO_2 (110) by low energy ions.
2. Radiation Effects in Insulators(REI-18), October 2015, Jaipur, Rajasthan, India
Poster– Size dependent Photo-absorption from Rutile TiO_2 Nanostructures: Grown Via ECR Sputtering.
3. National Conference on Nanotechnology: Materials and Applications, June 2016, Jadavpur University, Kolkata, India
Poster– Optical properties of hydrothermally grown ZnO nanorod arrays.

4. The International Conference on Microscopy and XXXIX Annual Meeting of Electron Microscope Society of India(EMSI-2018) July 2018, Mayfair Convention Centre, Bhubaneswar, India

Poster- Non-Enzymetic Glucose Sensing and Bandgap Tailoring of $\text{Cu}_2\text{O-ZnO}$ Hybrid Nanostructures Prepared by Single Step Coelectrodeposition Technique.

Date: 26/06/2020

Ashis Kumar Manna
Ashis Kumar Manna

To my parents

Acknowledgments

This thesis is the result of a very focused research work that I have carried out at Institute Of Physics, Bhubaneswar for last five years. The active support and necessary guidance of several individuals help me to complete my thesis. I am grateful to many people who have created a joyful and enthusiastic ambiance for me during my stay in IOP. Now it is the perfect time to express my heartiest gratitude to all of them. I apologies if I forget to mention anyone at this moment.

First and foremost, I would like to offer my utmost gratitude to my supervisor Prof. Shikha Varma without whom this thesis would not have been accomplished. I am extremely thankful to her for giving me the opportunity to work in her group. I am indebted to her for her constant support, guidance and encouragement. I learned how to get insight into a physics problems and communicate it in a scientific writing and presentation. She gave me full freedom to lead my academic and social life.

A special acknowledgement goes to Prof. Ajit Mohan Srivastava who always rejuvenates everyone around him with his charming personality. Apart from an excellent physicist, I will remember him as a storyteller and a motivational speaker. The most exiting and enjoyable part of my IOP life was probably the tea time discussion which I am going to miss a lot.

I am also thankful to my lab-mates: Vanaraj Bhaiya, Indrani and Priyadarshini. Priyadarshini didi was like a saviour for me during my initial days at IOP. I must also thank Santosh sir for his help in RAMAN and XPS measurements. His capability of handling instruments is fantastic and without him the smooth operation of all labs is quite impossible.

I would like to acknowledge all my doctoral committee members, Prof. A. M. Jayannavar, Dr. P. K. Sahoo and Prof. T. Som for their valuable suggestions and guideline. I want to express my gratitude to DAE for the financial support. I would like to thank all my collaborators; Prof. A. Kanjilal and his group at shiv nadar university, Dr. Biswarup Satpati and his group at Saha Institute of Nuclear Physics, Dr. D. Kanjilal, Prof. N.C Mishra, Prof. Sanjeev kumar srivastava and Dr. Subrata Majumdar. I take the opportunity to thank Dr. Sachindra Nath Sarangi and Dr. Subrata Majumdar who helped me a lot to strengthen my capability on professional

front.

The persons whom I want to acknowledge next are Dr. Manas Kundu and Dr. Puspendu Guha. These two people helped me both personally and professionally. I also want to thank my IOP friends specially Paramita Maity, Arpan Das and Vijigiri Vikas for their love and support. I also must thank to Prakash jana ,Niladri Jana, Prasanta Char and Kaushik Maity for their constant support during my tough time. I learned many important lessons of life which make me a strong and better person.

Finally, I wish to express my sincere gratitude to my parents, brother and beloved wife Subhadra for their love and affection. It is the blessings of my parents which make my journey joyful and peaceful. They all have believed in me and they never let me give up on my research when there were certain situations. I am indebted them for their continuous support and strong faith in me. I wish to pay my gratitude to Sadguru whose philosophy and wisdom towards life have impacted millions people's lives on the planet. He taught us how to become a blissful human being which is utmost important in the hectic pace of modern life.

Contents

Table of Contents	xiii
Summary	xiv
List of Figures	xv
List of Tables	xxv
1 Introduction	1
1.1 Introduction	1
1.2 Basics of Ion-Solid Interaction:	3
1.3 Ion Beam Sputtering	5
1.3.1 Theory of pattern formation by ion beam sputtering	6
1.3.2 Sigmund Approach and Bradley-Harper Model	7
1.4 Scaling Theory	10
1.5 Structural Phase transformation in TiO ₂ : From Anatase to Rutile . .	11
1.6 Photo-absorption property	13
1.7 Glucose Sensing property	14
1.8 Resistive Switching behaviour	15
2 Experimental Techniques	30
2.1 Techniques for Fabrication of Nanostructures	30
2.1.1 Sputtering deposition	30
2.1.2 Ion Implantation	32
2.1.3 Electrodeposition	34
2.1.4 Chemical synthesis process	36
2.2 Characterization Techniques	37
2.2.1 Electrochemical Techniques	37

2.2.2	Scanning Probe Microscopy (SPM)	39
2.2.3	Electron Microscopy	44
2.2.4	X-Ray Diffraction (XRD)	48
2.2.5	Raman Spectroscopy	49
2.2.6	UV-Vis Spectroscopy	53
2.2.7	Photoluminescence Spectroscopy	57
2.2.8	X-Ray Photoelectron Spectroscopy (XPS)	58
2.3	Structure and properties of the materials	61
2.3.1	Structure of Titania (TiO ₂)	61
2.3.2	Structure of Zinc Oxide (ZnO)	62
2.3.3	Structure of Copper Oxide	63
2.3.4	Structure of Glucose	64
3	Investigating Structural Phase Transformation using Ultraviolet Raman Spectroscopy and Resistive Switching Properties of Ti ion implanted TiO₂ thin films	70
3.1	Introduction	70
3.2	Experimental section	73
3.2.1	Sample Preparation	73
3.2.2	Experimental Techniques	74
3.3	Results and discussion	75
3.4	Conclusions	88
4	Investigating Structural Phase Transformation using Visible Raman Spectroscopy and Photo-absorption Behavior of Ti ion implanted TiO₂ thin films	93
4.1	Introduction	93
4.2	Experimental Section	95
4.3	Results and discussion	96
4.4	Conclusions:	105

5	Surface evolution of TiO₂ thin films after Ti ion implantation	109
5.1	Introduction	109
5.2	Experimental	111
5.3	Results and discussion	112
5.4	Conclusion	120
6	Surface Evolution of TiO₂(110) after Ar⁺ ion irradiation	125
6.1	Introduction	125
6.2	Experimental	129
6.3	Results and discussion	130
6.4	Conclusion	138
7	Resistive Switching Properties and Photoabsorption Behavior of Ti ion implanted ZnO thin films	141
7.1	Introduction	141
7.2	Experimental	143
7.2.1	Sample preparation	143
7.2.2	Experimental details	144
7.3	Result and discussion	144
7.4	Conclusion	151
8	Cu₂O-ZnO nanostructured films grown by Co-electrodeposition: Photoabsorption behavior & Non-Enzymatic Glucose Sensing via Cyclic Voltammetry	158
8.1	Introduction	158
8.2	Experimental	161
8.2.1	Chemical and Reagents	161
8.2.2	Preparation of ZnO-nanostructures using Electrodeposition Method	161
8.2.3	Preparation of Hybrid Cu ₂ O-ZnO nanostructures using single step coelectrodeposition (CED) Method	162
8.2.4	Glucose Sensing Experiments via cyclic voltammetry	163
8.2.5	Characterization techniques	163

8.3	Results and Discussion	164
8.3.1	Structure and Morphology	164
8.3.2	Non-enzymatic Glucose sensing via cyclic voltammetry	168
8.3.3	Photo-absorption response and band gap modification of Cu ₂ O-ZnO hybrid nanostructures	174
8.4	Conclusion	176
9	Cu_xO-ZnO (x=1,2) and CuO-TiO₂ nanostructures: Photo-absorption behavior and Non-Enzymatic Glucose Sensing via Cyclic Voltammetry	181
9.1	Introduction	181
9.2	Experimental	183
9.2.1	Chemical and Reagents	183
9.2.2	Preparation of ZnO and Cu _x O-ZnO nanostructures using Electrodeposition Method	184
9.2.3	Glucose Sensing via Cyclic Voltammetry Experiments using ZnO and Cu _x O-ZnO electrodes	185
9.2.4	Preparation of TiO ₂ and CuO-TiO ₂ nanostructures	185
9.2.5	Glucose Sensing via Cyclic Voltammetry Experiments using TiO ₂ and CuO-TiO ₂ modified GCE electrodes	186
9.2.6	Characterization techniques	186
9.3	Result and discussion	187
9.3.1	Investigations on ZnO & Cu _x O-ZnO nanostructures	187
9.3.2	Photo-absorption response and band gap tailoring in Cu ₂ O-ZnO and Cu _x O-ZnO nanostructures	195
9.3.3	Investigation of CuO-TiO ₂ composite structure	196
9.3.4	Photo-absorption response and band gap modification of CuO-TiO ₂ composite structure	199
9.4	Conclusion	200
10	ZnO nanorods fabricated via Hydrothermal method: Photo-absorbance behavior and Photocatalytic properties	208

10.1 Experimental Details	210
10.2 Results and discussion	212
10.3 Conclusions:	225
11 Conclusion	231

Summary

The present thesis discusses the fabrication of TiO₂ and ZnO nanostructured films by several routes. The films have been investigated for many functional properties like resistive switching (RS), photo-absorbance (PA) response and non-enzymatic glucose sensing via cyclic voltammetry (CV).

In the first part of the thesis, TiO₂ nanostructured films have been explored. RS and PA behaviors have been studied on sputter deposited TiO₂ thin films that were subsequently ion irradiated with 50 keV Ti ions. Techniques such as Atomic Force Microscopy (AFM), X-ray Photoelectron Spectroscopy (XPS), Grazing incidence X-ray diffraction (GIXRD), UV-Raman spectroscopy (with 325 nm laser), visible Raman spectroscopy (with 488 nm laser), Optical absorption (UV-Vis) spectroscopy and High Resolution Transmission Electron Microscopy (HRTEM) have been utilized here. Under the influence of ion beams, interestingly, a phase transformation from anatase (A) to rutile (R), at a critical fluence, has been noticed. Role of oxygen vacancies and dimensions of nano-crystalline anatase zones, in the transformation, have also been explored. Formation of conducting filaments, by these vacancies, is crucial for the development of RS phenomenon. PA response of ion irradiated TiO₂ films depends on the band gap tailoring and shows modulation with fluence.

The surface dynamics of the ion implanted TiO₂ thin films has been investigated here by via scaling formalism. Scaling parameters like roughness exponent (α) and growth exponent (β) have been estimated via height-height correlation and power spectral density calculations. The results show that diffusion dominated processes are leading to the smoothening of the surfaces, at high fluences. Dynamical evolution of Rutile TiO₂(110) single crystal surfaces, after Ar⁺ irradiation, has also been investigated via the scaling studies.

TiO₂ and CuO-TiO₂ composite nanostructured films, synthesized via chemical route, display non-enzymatic glucose sensing via cyclic voltammetry. The detection sensitivity, however, is not as good as that observed for Cu₂O-ZnO nanostructured films, also studied here.

Second part of the thesis investigates the formation the ZnO nanostructured thin

films, prepared by a variety of routes like sputter deposition, electro-deposition and hydrothermal methods. RS and PA response have been studied for sputter deposited ZnO thin films that were subsequently ion implanted with 50 keV Ti ions. XPS as well as Photoluminescence (PL) studies show presence of oxygen vacancies which are important for the formation of conducting filaments (CF). These CF play a significant role in the RS mechanism observed here. Ion implanted ZnO films show a higher PA response.

$\text{Cu}_x\text{O-ZnO}$ ($x=1,2$) nanostructured films have been prepared by co-electrodeposition (CED) method, using different concentrations of Cu^{2+} . Techniques of TEM, FESEM, XRD, XPS, Raman, UV-Vis spectroscopy and cyclic voltammetry have been used here for the investigations. At lower concentrations of Cu^{2+} , nanostructures are of $\text{Cu}_2\text{O-ZnO}$ type, whereas $\text{Cu}_x\text{O-ZnO}$ ($x=1,2$) nanostructures form at high concentrations. These nanostructured films show good sensitivity via cyclic voltammetry for the detection of glucose, with best being for 10% Cu content. These sensor films present good repeatability, long-term stability and reproducibility for glucose detection.

Bandgap modifications and PA properties, in UV-Vis range, have been studied for the CED grown $\text{Cu}_x\text{O-ZnO}$ films. ZnO NR arrays, synthesized by hydrothermal method, exhibit fabrication of 1- dimensional nanorods. These arrays have been investigated via FESEM, XRD, Raman, UV-Vis and PL spectroscopy techniques. Results display an enhanced PA and photo-catalytic behavior. These can be attributed to the decreased recombination of the charge carrier.

Thus, the present thesis explores the formation of TiO_2 and ZnO nanostructured thin films as well as their functional properties in relation to RS, band-gap modification and PA. Glucose sensing nature via CV has also been investigated. Nanostructures have been fabricated by low energy ion irradiation technique on TiO_2 and ZnO thin films. The nanostructures of $\text{Cu}_x\text{O-ZnO}$ and ZnO NR arrays have been prepared by CED and hydrothermal method, respectively. $\text{Cu}_x\text{O-ZnO}$ nanostructures exhibit excellent sensitivity in glucose detection by CV. The observed RS behavior in ion implanted thin films can readily be extended to memory device applications. Moreover, the improved visible light PA, in these films and NR arrays, can be used in photocatalysis application.

List of Figures

1.1	The schematic diagram of basic materials modification processes (a) implantation (b) collision cascade and atomic displacement and (c) surface erosion (from ref [37])	4
1.2	Variation of nuclear energy loss (S_n) and electronic energy loss (S_e) for Ti ion in TiO_2 target. The energy loss curves have been estimated by utilizing SRIM2012 simulation code.	5
1.3	Schematic diagram of Gaussian energy distribution process during ion implantation within the target. θ and γ are global and local angle of incidence, respectively [38].	8
1.4	Schematic of Ion energy deposition profile for two (a) concave and (b) convex surfaces. The energy deposited at 'O' is larger than at O' since $OA < O'A'$ and $OC < O'C'$ [38].	9
1.5	Schematic diagram of different operational state of a RRAM device; (1) initial state (2) forming, (3) reset, and (4) set process [150]. . . .	17
1.6	Schematic diagrams of (a) unipolar switching and (b) bipolar switching in RRAM [153].	17
2.1	The schematic diagram of RF Magnetron sputtering setup.	32
2.2	Negative Ion Implantation facility at IUAC, New Delhi (with permission)	34
2.3	Schematic diagram of electrodeposition set up [5].	35
2.4	Variation of Excitation potential during CV experiment.	38
2.5	A typical illustration of cyclic voltammogram for a reversible electrochemical system [10]).	38

2.6	(a)PGSTAT 302N Autolab electrochemical workstation with a chemical cell set up and (b) Schematic diagram of the electrode arrangement within the chemical cell.	39
2.7	AFM set up at IOP	41
2.8	The schematic representation of the AFM operation	41
2.9	Force (F) versus Distance (r)	42
2.10	Schematic representation of experimental setup of FESEM	45
2.11	The schematic diagram displaying (a) the Bragg's diffraction in single crystal and (b) X-ray diffractometer setup.	48
2.12	Schematic diagram of vibrational energy level demonstrating three types of scattering phenomena; Raleigh and Raman (Stokes and Anti-Stokes) scattering	50
2.13	Raman set-up at IOP.	52
2.14	Molecular energy level diagram and all possible transition.	53
2.15	UV-Vis absorption spectra (a) and Tauc plot (b) of the ZnO nanoparticles.	55
2.16	Schematic of UV-vis spectroscopy set up.	56
2.17	UV-Visible set-up at IOP.	57
2.18	Schematic representation of X-ray photoelectron emission process	59
2.19	(a) Schematic representation of XPS instrument and (b) energy band diagram to calculate the Binding energy of the photoelectron	59
2.20	VG microteck XPS system at Institute Of Physics	61
2.21	Crystal structure of TiO ₂ :(a) anatase, (b) rutile, (c) brookite [48]	61
2.22	Crystal structures of ZnO:(a) cubic rocksalt (b) cubic zinc blende and (c) hexagonal wurtzite. [55]	63
2.23	Crystallographic structures of the cubic Cu ₂ O lattice (a) and the monoclinic CuO lattice [63]	63
2.24	(a) Structure and (b) chemical formula of the D-glucose.	64

3.1	(a) XRD from as-deposited TiO ₂ thin films and after ion implantation at various fluences (ions/cm ²). (b) Area under R (A _R) and A (A _A) as a function of ion fluence, (c) Crystallite size L of anatase as a function of ion fluence, and (d) Phase content of rutile W _R and ratio A _R /A _A as a function of ion fluence.	76
3.2	UV-Raman spectra from as-deposited TiO ₂ thin films and after ion implantation with various fluences (ions/cm ²).	77
3.3	(a) UV-Raman normalized spectra in the low-frequency region from as-deposited TiO ₂ thin films and after ion implantation with various fluences (ions/cm ²), along with fitting components for R, A and A _n (b) Ratios A _R /A _A and A _R /A _{A_n} as a function of ion fluence (c) A _n Raman mode of TiO ₂ fitted with PCM (○) as described by Eq. 3.2, L is size of anatase nanoparticles as determined by the PCM fit to the data. . . .	79
3.4	(a) UV- Raman normalized spectra in the high-frequency region from as-deposited TiO ₂ thin films and after ion implantation with various fluences (ions/cm ²) along with fitting components for R and A (b) Ratio A _R /A _A as a function of ion fluence.	82
3.5	(a) Bright-field XTEM image of the as-deposited TiO ₂ film. High resolution XTEM image of (b) as-deposited TiO ₂ thin film and after ion implantation with (c) 1×10 ¹⁴ and (d) 1×10 ¹⁵ ions/cm ² . Black and white contours respectively mark the rutile and anatase regions. Lattice fringes and FFT of (e) Anatase and (f) Rutile regions, from corresponding squares marked in (b).	83
3.6	Ti(2p) XPS spectra from as-deposited TiO ₂ thin films and after ion implantation with various fluences (ions/cm ²). Peak fitted components for Ti ⁴⁺ and Ti ³⁺ states are shown. Ratio of oxygen vacancy (Ti ³⁺) w.r.t. Ti ⁴⁺ is shown in inset.	84

3.7	For a sample implanted with 1×10^{15} ions/cm ² (a) AFM image ($500 \times 500 \text{ nm}^2$) showing surface topography (b) c-AFM image ($500 \times 500 \text{ nm}^2$) showing current map with +2V bias applied at the Au back electrode (c) Line profile of surface topography and current profile (d) Local I-V characteristics acquired by sweeping the applied potential across the AFM tip and the Au back electrode from -4 V to +4V and back to -4 V and compliance current (I_c) 10 nA. Schematic diagram of c-AFM experiments on TiO ₂ /Au/Ni/SiO ₂ /Si with Pt/Ir tip acting as movable top electrode for c-AFM is also shown.	86
4.1	Raman spectra from as-deposited TiO ₂ thin films and after ion implantation with various fluences (ions/cm ²).	96
4.2	(a) Raman spectra in the high-frequency region from as-deposited TiO ₂ thin films and after ion implantation with various fluences (ions/cm ²) along with fitting components for R, A and A _n (b) Ratio A_R/A_A as a function of ion fluence.	97
4.3	(a) Raman spectra in the low-frequency region from as-deposited TiO ₂ thin films and after ion implantation with various fluences (ions/cm ²), along with fitting components for A and A _n (b) Ratio A_R/A_A as a function of ion fluence (see text). (c) Raman profiles as obtained using PCM for L = 5.7, 8.0, 10.0 and 28 nm. Profile for bulk is also shown. PCM is described by Eq. 3.2 where L is size of anatase nanoparticles (d) Raman mode A _n has been fitted using PCM (o-o) and L is size of anatase nanoparticles as determined by the PCM fit to the data. . . .	99
4.4	(a) GIXRD from as-deposited TiO ₂ thin films and after ion implantation at various fluences. (b) GIXRD (range 47.5 to 62.5°) from as-deposited TiO ₂ thin films and after ion implantation at 1×10^{12} and 1×10^{15} ions/cm ² . (c) $A_R/A_{A(105)}$ as a function of ion fluence.	101

4.5	(a) O(1s) XPS spectra from as-deposited TiO ₂ thin films and after ion implantation with various fluences. Peaks have been fitted with two components related to bulk lattice oxygen (O _{lattice}) and oxygen vacancies (O _v). (b) The area under O _v is shown as a function of ion fluence.	103
4.6	(a) Photo-absorbance response for as-deposited TiO ₂ thin films and after ion implantation with various fluences (ions/cm ²) (b) Tauc plots at various fluences (α is absorption coefficient and E is photon energy) (c) Bandgap as a function of ion fluence.	104
5.1	2D AFM images (500×500 nm ²) of (a) as-deposited TiO ₂ thin film and after ion irradiation with fluences of (b) 1×10 ¹⁰ (c) 1×10 ¹² (d) 1×10 ¹³ (e) 1×10 ¹⁴ and (f)1×10 ¹⁵ ions/cm ²	112
5.2	3D AFM images (500×500 nm ²) of (a) as-deposited TiO ₂ thin film and after ion irradiation with fluences of (b) 1×10 ¹⁰ (c) 1×10 ¹² (d) 1×10 ¹³ (e) 1×10 ¹⁴ and (f)1×10 ¹⁵ ions/cm ²	113
5.3	Size distribution (diameter) of nanostructures for (a) as-deposited TiO ₂ thin film and after ion irradiation with fluences of (b) 1×10 ¹⁰ (c) 1×10 ¹² (d) 1×10 ¹³ (e) 1×10 ¹⁴ and (f)1×10 ¹⁵ ions/cm ²	114
5.4	Variation of rms roughness (σ) as a function of irradiation time (t) for three different scan lengths. Top scale shows ion fluence.	115
5.5	HHC function for as-deposited and ion irradiated TiO ₂ thin films. . .	117
5.6	PSD as a function of spatial frequency k for as-deposited and ion irradiated TiO ₂ thin films.	119
6.1	SPM images (a) for pristine TiO ₂ and after ion irradiation of TiO ₂ at fluences of (b) 1× 10 ¹⁶ , (c) 1× 10 ¹⁷ , (d) 5× 10 ¹⁷ , (e) 5× 10 ¹⁸ , and (f) 1× 10 ¹⁹ ions/cm ² . Images of (a) and (b) are 1×1 μ m ² in size whereas images from (c) to (f) are 2×2 μ m ² in size. Ion beam projection direction (arrow on top) was always along [001] direction. Crystallographic axes of the surface are shown.	130

6.2	Log-log plot of rms roughness, σ , as a function of irradiation time (t) and fluence.	132
6.3	Ti-2p core-level XPS spectra from pristine TiO ₂ surface and after irradiation at various fluences (ions/cm ²).	134
6.4	HHC for pristine TiO ₂ as well as after ion irradiation.	135
6.5	PSD as a function of spatial frequency k for pristine TiO ₂ as well as after irradiation.	136
6.6	Exponent γ as a function of irradiation time (t) and fluence.	137
7.1	(a) GIXRD from as-deposited ZnO thin films and after ion implantation at various fluences (ions/cm ²), (b) Variation of lattice parameter, c , and crystallite size, d , with ion fluence.	145
7.2	UV-Raman spectra from as-deposited ZnO thin films and after ion implantation with various fluences (ions/cm ²).	146
7.3	(a)Room temperature PL spectra of the as-deposited and ion implanted ZnO films (b) Corresponding magnified PL spectra in visible region.	147
7.4	(a)Zn(2p) XPS spectra from as-deposited ZnO thin films and after ion implantation with various fluences (ions/cm ²). (b) O(1s) XPS spectra at various fluences. Peaks have been fitted with three components related to bulk lattice oxygen (O_L), oxygen vacancies (O_V) and chemisorbed oxygen (O_C). (c) Ratio of the intensity of O_V w.r.t O_L , as a function of ion fluence.	148
7.5	(a)Photoabsorbance response for as-deposited ZnO thin films and after ion implantation with various fluences (ions/cm ²) (b) Tauc plots at various fluences (α is absorption coefficient and E is photon energy)	149

7.6	For ZnO thin films implanted with 1×10^{15} ions/cm ² (a) AFM image (500×500 nm ²) showing surface topography, (b) c-AFM image (500×500 nm ²) showing a current map with +10V bias applied at Au back electrode, (c) schematic diagram of c-AFM experiments on ZnO/Au/Ni/SiO ₂ /Si with Pt/Ir tip acting as the movable top electrode for c-AFM, (d) local I-V characteristics acquired by sweeping the applied potential across the AFM tip and Au back electrode from -10 V to +10 V and back to -10 V, compliance current (I_c) was 1 nA.	150
8.1	Schematic illustration of the CED process and growth of Cu ₂ O-ZnO: (a) Growth cell (b) simultaneous presence of both Cu ²⁺ and Zn ²⁺ ions in the solution (c) CED growth of hybrid Cu ₂ O-ZnO nanostructures upon application of cathodic voltage.	163
8.2	(a) SEM image of electrodeposited ZnO nanostructures. SEM images from Hybrid Cu ₂ O-ZnO nanostructures (b) C ₁ and (c) C ₁₀ . EDX elemental mapping images of Zn, O, and Cu in the C ₁₀ sample, taken from the box of (c).	165
8.3	XRD of ZnO nanostructures as well as of Cu ₂ O-ZnO nanostructures C ₁ and C ₁₀	165
8.4	(a) Low magnification TEM micrograph of Cu ₂ O-ZnO C ₁₀ sample (b) high resolution TEM image of marked region in (a); (c), (d) and (e) high resolution (filtered) images from blue, green and magenta regions respectively and inset shows their corresponding FFT patterns.	166
8.5	(a) Raman spectrum of ZnO nanostructures as well as of Cu ₂ O-ZnO nanostructures C ₁ and C ₁₀ . (b) Zn(2p) core level XPS spectrum of ZnO nanostructures as well as of Cu ₂ O-ZnO nanostructures C ₁ and C ₁₀ . (c) Cu(2p) core level XPS spectra from Cu ₂ O-ZnO nanostructures C ₁ and C ₁₀ . (d) O(1s) XPS spectrum of ZnO nanostructures as well as of Cu ₂ O-ZnO nanostructures C ₁ and C ₁₀	167

8.6	(a) Blank CV curves for ITO, ZnO nanostructures and for Cu ₂ O-ZnO nanostructures C ₁ and C ₁₀ . (b) CV curves with 1 mM glucose for ITO, ZnO nanostructures and for Cu ₂ O-ZnO nanostructures C ₁ and C ₁₀ . The scan rate is 10 mV/sec. Inset shows the schematic illustration of the Electron transfer process for enzymeless Glucose electro-oxidation on hybrid Cu ₂ O-ZnO nanostructure electrode.	169
8.7	(a) CV curves of Cu ₂ O-ZnO sample C ₁₀ upon addition of different concentrations of Glucose (b) Amperometric response of Cu ₂ O-ZnO sample C ₁₀ upon successive addition of Glucose with marked concentrations to 0.1 M NaOH solution at an applied potential of 0.4 V. Inset (top) shows the corresponding calibration curve of the current vs. concentration of glucose. Inset (bottom) shows a partial magnification of the current response towards a low concentration of glucose solution. (c) Amperometric response of Cu ₂ O-ZnO sample C ₁₀ to 0.2 mM glucose and successive injection of interfering species (0.02 mM UA, 0.02 mM AA, and 0.02 mM DA) in 0.1 M NaOH with stirring.	170
8.8	(a) The stability of the Cu ₂ O-ZnO sample C ₁₀ in 0.1 M NaOH solution containing 1 mM glucose at different temperatures from 20° - 62° C. Inset shows CV of Cu ₂ O-ZnO C ₁₀ sample at different temperatures. (b) CV of the Cu ₂ O-ZnO C ₁₀ sample in 0.1 M NaOH solution at a scan rate 10 mV/s containing 1 mM Glucose at different cycles. Inset shows the variation of the maximum response current density for the Cu ₂ O-ZnO C ₁₀ sample in 0.1 M NaOH containing 1 mM glucose up to 90 cycles. (c) Stability of the Cu ₂ O-ZnO C ₁₀ sample over 34 day period using 0.1 M NaOH with 1 mM glucose at +0.4 V.	173
8.9	Photo response UV-Vis spectra of ZnO nanostructures and from C ₁ and C ₁₀ . Inset shows the Tauc plots and the associated bandgaps (α is absorption coefficient and E is photon energy).	175
9.1	(a) Raman spectra of CED grown ZnO, C ₂ and C ₅₀ . (b) XPS of Zn(2p) and (c) XPS of Cu(2p)	188

9.2	XRD of ZnO, C ₂ and C ₅₀	189
9.3	FESEM image of (a) electrodeposited ZnO, (b) C ₂ and (c) C ₅₀ . EDX (in bottom) is shown for C ₅₀ with elemental mapping images of Zn, O, and Cu taken from the box of (c).	190
9.4	Top: Two-dimensional (1.5 μ m x 1.5 μ m) AFM images of (a) electrodeposited ZnO, (b) C ₂ and (c) C ₅₀ . Bottom shows the corresponding three-dimensional AFM images.	191
9.5	CV curves for ITO, ZnO, C ₂ and C ₅₀ electrodes in (a) absence of glucose and (b) presence of 0.6 mM glucose. The scan rate is 10 mV/sec. . .	192
9.6	(a) CV curves of C ₅₀ upon addition of different concentrations of Glucose. (b) Amperometric response of C ₅₀ upon successive addition of glucose with marked concentrations to 0.1 M NaOH solution at an applied potential of 0.4 V. Inset (top) shows corresponding calibration curve. (c) Amperometric response of C ₅₀ to 0.2 mM glucose and successive injection of interfering species (0.02 mM UA, 0.02 mM AA, and 0.02 mM DA) in 0.1 M NaOH with stirring.	193
9.7	CV profile of the C ₅₀ electrode in 0.1 M NaOH containing 0.6 mM glucose at different days. Inset shows corresponding stability curve of peak oxidation current as a function of days.	195
9.8	UV-Vis Photo response of ZnO, C ₂ and C ₅₀ . Inset shows Tauc plots and the associated band gap (α is absorption coefficient and E is photon energy).	196
9.9	SEM image of (a) as-deposited TiO ₂ and (b) T ₁₀ composites. (c) EDX of T ₁₀	197
9.10	XRD patterns of (a) as-deposited TiO ₂ and (b) T ₁₀ composites. . . .	197
9.11	Raman spectrum of as-deposited TiO ₂ and CuO-TiO ₂ (T ₁₀) composites.	198
9.12	(a) CV curves of T/GCE (i) and CT/GCE (iii) in the presence of 4.0 mM glucose. CV of CT/GCE in absence of glucose (ii). (b) CV curves of CT/GCE upon addition of different concentrations of glucose in 0.10 M NaOH solution. Glucose concentrations ranged from 2 to 10 nM. Scan rate was 30 mV.s ⁻¹	199

9.13	UV-visible absorption spectra of (a) as-deposited TiO ₂ and (b) T ₁₀ composites. Inset shows Tauc plot and the associated band gaps (α is the absorption coefficient and E is the energy).	200
9.14	UV-Vis Photo response of ZnO, C ₁ , C ₂ , C ₁₀ and C ₅₀	202
10.1	Schematic of the layer structures of samples A to D ((a) to (d) respectively) used in this work.	212
10.2	(a) SEM images of ZnO seed layer (sample A) and its (b) GIXRD spectrum.	212
10.3	For sample B, top view (a) and side view (b) SEM images. (c) EDS spectrum and (d) GIXRD Spectrum.	213
10.4	Top view SEM images of ZnO nanorods (a) Sample C and (b) Sample D, GIXRD Spectra of (c) Sample C and (d) Sample D.	214
10.5	(a) top view (b) magnified view SEM images of ZnO NRs grown without seed layer.	216
10.6	Raman spectra of ZnO single crystal and ZnO NRs.	216
10.7	Magnified Raman spectra of ZnO single crystal and ZnO NRs.	218
10.8	UV-visible absorbance spectra of ZnO NRs and single crystal (inset).	219
10.9	Tauc plots (α is absorption coefficient and E is energy of photons) of ZnO NRs. Inset shows Tauc plot of single crystal.	219
10.10	Room temperature PL spectra of ZnO seed layer (Sample A) and nanorods (Sample B, C, D).	221
10.11	Time-dependent UV-Vis absorbance spectra of the MB solution using ZnO seed layer and NRs as photocatalysts.	222
10.12	Variation of degradation rate of the MB dye with irradiation time for ZnO seed layer (sample A) and NRs (samples B,C,D)	223

List of Tables

5.1	Scaling Exponents from height-height correlation (HHC) function. . .	117
6.1	Scaling Exponents from height-height correlation (HHC) function. . .	134
7.1	Structural parameters of as-deposited and Ti ion implanted ZnO thin films	146
8.1	Comparison of the non-enzymetic glucose sensing properties of the hybrid Cu ₂ O-ZnO sample C ₁₀ with some other glucose sensors based on Cu ₂ O.	172
9.1	Comparison of Non-enzymatic Glucose sensitivity via cyclic voltammetry. Photo-absorption Band gaps as measured by UV-Vis spectroscopy are also mentioned.	201
10.1	Structural parameters of ZnO NRs.	215
10.2	Wave number and symmetries of the modes found in Raman spectrum of ZnO single crystal, nanorods and their assignments.	217

Chapter 1

Introduction

1.1 Introduction

Fields of nanoscience and nanotechnology have led to amazing advances and exciting developments in numerous technologically important functional properties of materials. Encompassing roles of synthesis routes, characterization, manipulation and applications of low-dimensional materials, having at least one dimension in nano-scale ($\leq 100\text{nm}$) regime, nano-science presents exceptional promise in many interdisciplinary and diverse areas like biotechnology, medicine, water, energy, space science, information technology, memory devices, communication etc. [1–7]. Characterized by large surface area and a plethora of associated attributes, low dimensional nanoscale materials can demonstrate many unique and fascinating properties, not expressed by their bulk counterparts [8, 9]. Some such realizations are related to higher coercivity [10], enhanced photo-absorbance [11, 12], giant magneto-resistance [13], higher thermal stability and super plasticity [14, 15], enhanced sensing performance [16, 17], fast resistive switching mechanism [18, 19] etc.. Accomplishments in many such areas including photo-catalysis, solar cells, optoelectronics, sensors, nano-photonics, nano-devices and nano-electronics [8, 21] have prompted focused road maps for achieving many important goals [20]. Explorations of large number of such characteristic advantages, associated with nano-scale materials, depend crucially on their synthesis routes and successful growth of controlled size and shape morphologies. There are thus numerous challenges in realizing many exciting targets. Still, the immense promise reflected by the possibility of achieving many potentially path breaking, magnificent

and exciting goals have contributed to enormous synergetic interdisciplinary efforts and phenomenal research in this field.

For fabrication of nano-scale materials with desired properties, synthesis routes play an important role and these can be broadly characterized under two approaches: Bottom Up and Top Down. With each of these techniques presenting many specific advantages and challenges, determination and realization of the appropriate process constitute as important steps in achieving materials with preferred morphologies and selective behavior [22, 23]. In the case of bottom-up technique, the structures are assembled using smaller units such as atoms, molecules or clusters. On the other hand, the top-down approach involves the down-scaling of bulk material to achieve nano-sized structures. A few examples of the methods that employ bottom-up approach are vapor deposition, sol-gel, pulse laser deposition, atomic layer deposition, spray pyrolysis, electrodeposition etc.. Lithography and ion irradiation are a few of the widely used top down techniques.

The present thesis discusses the synthesis of TiO_2 and ZnO nanostructured films, prepared by several methods, and some associated functional properties like resistive switching (RS) characteristics, photo-absorbance (PA) behavior and non enzymetic glucose sensing nature. Thin TiO_2 and ZnO films, fabricated via sputtering method, have been utilized in the investigations of RS and PA behavior. These properties have also been studied after the films were irradiated with Ti ions. Oxygen vacancies, that get created during this process, crucially influence the observed properties. A structural phase transformation is also noticed in TiO_2 films, after they are irradiated beyond a critical fluence. Scaling concepts have been utilized for understanding the surface evolution after ion irradiation of TiO_2 films. CuO-TiO_2 and $\text{Cu}_x\text{O-ZnO}$ thin films, prepared respectively by chemical route and co-electrodeposition technique, present a non-enzymetic glucose sensing behavior as well as show PA response in UV-Visible regime. Hydrothermally grown ZnO thin films have also been investigated for their photocatalytic and PA response.

This chapter is organized in the following manner. Section 1.2 discusses the basics of ion-solid interaction. The ion beam sputtering process and the theory of pattern formation have been discussed in section 1.3. Section 1.4 discusses the details of

scaling theory. Structural phase transition in TiO_2 has been discussed in section 1.5. Details of properties like photo-absorption, glucose sensing and resistive switching behavior are presented in sections 1.6, 1.7 and 1.8, respectively.

1.2 Basics of Ion-Solid Interaction:

Interactions of an energetic ion with matter are controlled by non-equilibrium processes. During such interactions, the ion loses its energy within the material through electronic loss (S_e) and nuclear loss (S_n) processes. The relative strength of these losses are governed by the material aspects and the ion beam parameters, with ion energy being a predominant factor. These losses can often induce significant modifications in the physical and chemical properties of the material [34]. Contributed by these losses, the incident ions can produce displacements of lattice atoms during their passage through the material and with displaced atoms further colliding, with other atoms, collision cascades or displacement cascades develop within the regions surrounding the ion trajectory. The incident ions may eventually lose their energy and may get implanted, creating concentration dependent profile within the material. Such a scenario, governed by many ion beam and material aspects, induces alterations in the structure as well as the composition of the material. Other prominent effect of ion beam -matter interaction may include (a) emission of particles and radiation from the surface (b) rearrangement of surface atoms. Electronic interactions are responsible for the emission of characteristic X-rays, optical photons, and Auger or secondary electrons whereas sputtered atoms and elastically recoiled target atoms arise from the nuclear interaction. Figure 1.1 shows the schematic diagram illustrating various processes which cause material modification during ion beam irradiation. Figure 1.1(b) displays the displacement of target atoms from the regular lattice position due to the head-on-collision between the incident ion and the target atoms. The head-on collisions can cause considerable structural damage within the host matrix. Additionally, processes like sputtering may also occur as shown in Figure 1.1(c). Such phenomenon can often induce self-assembled surface patterning.

All the processes depicted in Fig. 1.1 are strongly controlled by the energy of the

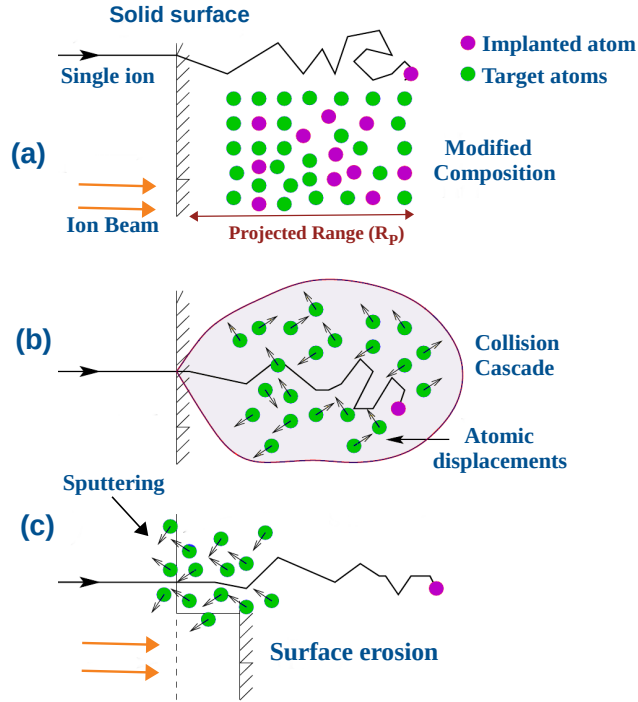


Figure 1.1: The schematic diagram of basic materials modification processes (a) implantation (b) collision cascade and atomic displacement and (c) surface erosion (from ref [37])

incident projectile ion. For low energy (keV) ions, sputtering is a dominant phenomenon whereas material modification and deep layer implantation become important at higher (MeV) energies. The projectile ions continuously lose their energy while passing through the material via two uncorrelated processes viz. S_n and S_e . During such losses, ion projectiles can induce vacancies and interstitial atoms along its path causing introduction of variety of defects in the material. The extent of this damage will be governed by several factors, including the energy and flux of the incident ion, substrate temperature, ion fluence, implanted species etc.. The energy deposition can be assessed by the stopping power ($\frac{dE}{dx}$) which measures the ion-energy (E) transferred per unit length (x) along the trajectory [35]. S_n corresponds to the elastic collision with the target nuclei whereas S_e [35] relates to the inelastic excitations. The total transferred energy is the sum of both the energy loss processes. The ion and electron interact via pure coulomb potential whereas the ion-nucleus interaction is mediated by a screened coulomb potential. At lower ion energies (keV), S_n is the dominant

phenomenon. In this energy regime, ion velocity is less than the Bohr velocity of the electron and therefore ion-nucleus interactions prevail. At higher energies (MeV), the Bohr velocity of the electron becomes comparable to the projectile velocity and S_e usually becomes more significant in slowing down the projectile ions. The transfer of energy in nuclear collisions is discrete and significant angular deflections of the ions may occur causing displacements of the atoms in the host material. With sufficient energy, such atoms may be able to produce a cascade of displacements, thus producing disordered regions along the ion track. A large concentration of such displaced atoms can sometimes induce amorphization in the host material.

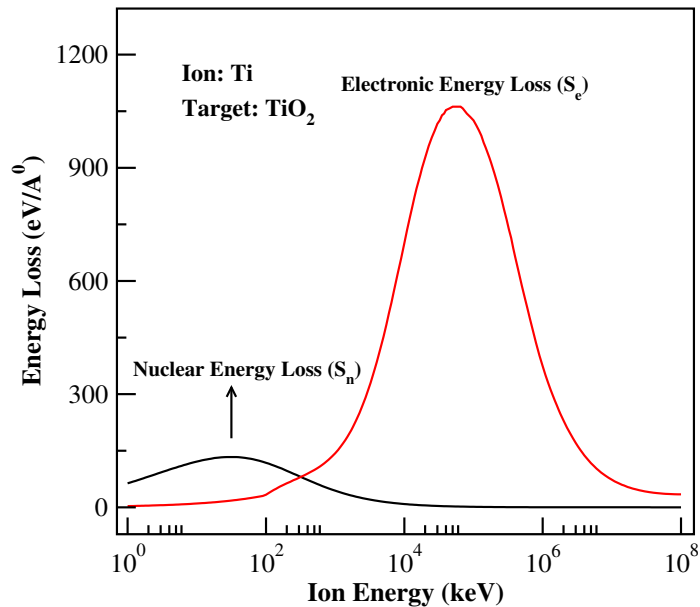


Figure 1.2: Variation of nuclear energy loss (S_n) and electronic energy loss (S_e) for Ti ion in TiO_2 target. The energy loss curves have been estimated by utilizing SRIM2012 simulation code.

Figure 1.2 shows the dominant regions of S_n and S_e , as a function of ion energy, for Ti ion in Titanium oxide (TiO_2). The energy loss has been estimated using the SRIM2012 simulation code [36].

1.3 Ion Beam Sputtering

In the sputtering process, the surface atoms of the material are ejected when energetic ions hit the surface [38]. This process occurs if the imparted energy is large enough to

break the atomic bonds. Momentum is exchanged between projectile and the atoms during the collisions [38]. The sputtering yield (S) is defined as the mean number of escaped target atoms per incident ion:

$$S = \alpha N S_n(E) / E_B \quad (1.1)$$

Here, α is a parameter which is dependent on the geometry of the material, N is the atomic density of the target and E_B is the binding energy of the surface atoms. From this expression, it is clear that the number of ejected atoms are directly proportional to the number of incoming particles, given that all other factors in the expression remain constant. Thus, sputtering yield depends on many parameters such as binding energy of target atoms, kinetic energy of the projectile and stoichiometry of the material [39]. In the case of crystalline materials, it also depends on the crystallographic orientation, lattice structure etc. [40, 41]. The sputtering yield is not same for all the elemental constituents of a multi-component target. This can become responsible for the preferential sputtering of lighter mass atoms, compared to the heavier ones. Such phenomenon may result in a surface, where ion beam impinges, as well as near-surface layers acquiring different stoichiometry than the bulk material [40, 41].

1.3.1 Theory of pattern formation by ion beam sputtering

The ejection of near-surface atoms, during ion beam sputtering, can often lead to the development of self-organized patterns on the surface. These patterns reflect the evolution of the surface via non-equilibrium processes. Several examples of these phenomena also exist in nature. The most common being the formation of ripples, by wind, on the sand beds in desert. The creation of ripple pattern by ion bombardment was first reported on a glass substrate by Navez et al. in 1956 [42]. After that, several experimental and theoretical investigations have been performed to understand the development of such self-organized structures on a variety of surfaces such as insulators, metals, semiconductors, polymers etc. [45–57]. These structures arise due to the competition between the erosive and diffusive processes. The diffusive processes are responsible for the relaxation or smoothening of a surface. The shape, size and orientation of the patterns can be controlled by various ion beam parameters,

like incidence angle, ion energy, fluence, current density etc.. Anisotropic surface diffusion and Ehrlich-Schwoebel barrier can also play a major role in this pattern formation [43, 44, 51]. The morphological evolution of a surfaces has been discussed in the framework of Bradley and Harper (BH) theory [49] as well as through the curvature dependent sputtering formalism presented by Sigmund [58]. Various physical processes like viscous flow, re-deposition, anisotropic diffusion, step edge barrier, nonlinear effect etc. [59–61] can also be crucial in controlling the dynamics of an evolving surface. These theories reflect the dynamic nature of the surface and introduce parameters important for understanding its evolution.

1.3.2 Sigmund Approach and Bradley-Harper Model

The process of ion induced sputtering has been discussed by Sigmund [58] using a model that demonstrates the development of an instability on a planar surface due to the erosion processes. A schematic diagram of this model describing the erosion process is shown in Fig. 1.3. An infinite amorphous target is assumed and the probability of removal of an atom from the target is proportional to the energy received by the atom from a nearby collision processes. Let us consider a projectile ion which hits the surface at point ‘O’ and penetrates up to a distance ‘a’ (fig. 1.3) within the target material before coming to rest. A fraction of the total energy released at point ‘O’ can reach to the point ‘P’ on the surface. The surface atoms located at ‘P’ use this energy in breaking their bonds and escaping from the surface or diffusing into the bulk.

The solid surface is described by a height function $h(x, y)$. γ and θ are the local and global incidence angles (fig. 1.3). In this frame, x and y axes are parallel to the flat surface. According to the Sigmund model, in the low energy (keV) regime, the spatial distribution of the average deposited energy by an ion at point ‘O’ is approximated by a Gaussian distribution. The energy deposited at ‘O’ due to an incident ion striking at P' with kinetic energy ϵ is given as:

$$E(r) = \frac{\epsilon}{(2\pi)^{3/2}\sigma\mu^2} \exp\left[-\frac{x'^2 + y'^2}{2\mu^2} - \frac{(z' + a)^2}{2\sigma^2}\right] \quad (1.2)$$

The origin of the coordinate system $r' = (x', y', z')$, set up at P' and z' is along

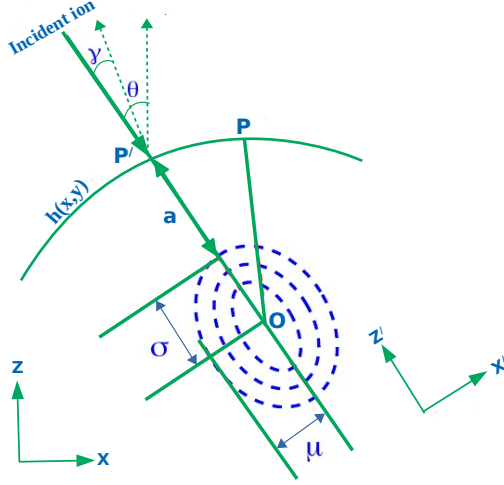


Figure 1.3: Schematic diagram of Gaussian energy distribution process during ion implantation within the target. θ and γ are global and local angle of incidence, respectively [38].

the ion beam direction. The longitudinal and transverse straggling widths of the gaussian distribution are represented by σ and μ . Several ions penetrate the material at different positions. The erosion velocity, v , at point 'P' depends on the total energy deposited by all ions within the region R and is described as:

$$v = A \int_R \phi(r') E(r') dr' \quad (1.3)$$

Here $\phi(r')$ is the corrected ion flux due to variation in the local slope. Constant A is dependent on the surface binding energy and scattering cross-section. Figure 1.4 shows the curvature dependent erosion process at the surface. Let us consider that a homogeneous flow of ions are striking at two different regions of surface: a trough (concave) and a crest (convex). The geometry of the interface at the two position is such that $OA < O'A'$ and $OC < O'C'$. Therefore, the smaller penetration depth of ions at A and C induce large energy deposition at O for the trough region than the crest region.

The rate of erosion is proportional to the total deposited energy (equation 1.3). Erosion is faster at O than at O'. This implies that the valleys or trough are eroded faster than the crests which cause difference in height between the two structures. The surface instability caused by the difference in erosion rate is balanced by the

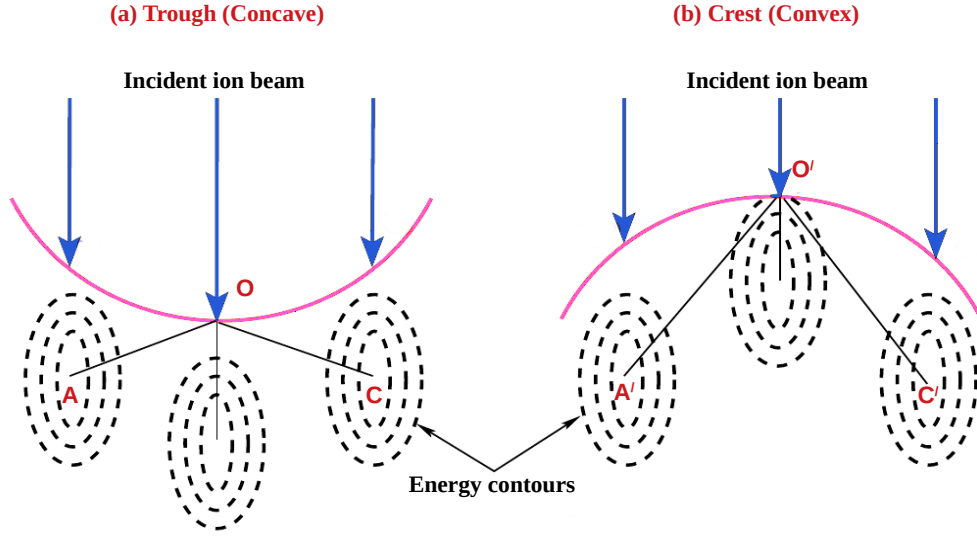


Figure 1.4: Schematic of Ion energy deposition profile for two (a) concave and (b) convex surfaces. The energy deposited at ‘O’ is larger than at O’ since $OA < O'A'$ and $OC < O'C'$ [38].

alternative smoothing processes. The surface finally stabilizes with the formation of self-organized structures such as ripples, dots, etc.. The BH model, based on Sigmund theory, proposes a differential equation for the evolution of a slowly varying surface. The variation in height modulation $h(x, y, t)$ of such a surface at time, t , is described as [49]:

$$\frac{\partial h}{\partial t} = -v_o + \nu \nabla^2 h - D \nabla^4 h \quad (1.4)$$

Here v_o is the constant erosion velocity, ν and D are the effective negative surface tension and surface diffusion coefficient, respectively. The solution of this equation represents an exponential growth of the surface height with the fluence. The characteristic wavelength of a pattern on the surface can be estimated from this equation and is found to be independent of the ion fluence. There are several cases, however, where by varying the sputtering conditions, variety of surface morphologies have been generated. This cannot be explained by the BH model. To overcome this, Cuerno and Barabasi (CB) [62] together developed a model where they have shown that ion irradiated surface morphology can be described at early time scale by the BH model. However, nonlinear terms have been introduced by Kuramoto-Tsuzuki [63] to de-

scribe the surface dynamics at later time scales. Incorporating the nonlinear effects, the modified equation for slowly varying surface is given as:

$$\frac{\partial h}{\partial t} = -v_o + \nu \nabla^2 h - D \nabla^4 h + \frac{\lambda}{2} (D \nabla h)^2 + \eta \quad (1.5)$$

Here the term η represents an uncorrelated noise with zero mean. The term $\frac{\lambda}{2} (D \nabla h)^2$ demonstrates the slope dependent erosive component which helps to stabilize the surface by saturating the surface roughness with time. The sign of the the nonlinear term determines the surface evolution which may show kinetic roughening [64–66].

1.4 Scaling Theory

The dynamic evolution of any surface may be controlled by several competitive roughening and smoothening processes [67]. Knowledge of scaling theories is effective in assessing the predominant factors responsible for controlling the morphological evolution of any surface [68]. Such studies provide important scaling exponents which can facilitate the description of an evolving surface under the framework of certain universality classes [69–71]. This is an exceptionally fundamental and powerful technique that emphasizes the role of exponents in deriving essential ingredients assisting the evolution of a surface. Such an evolution, for any given surface with height function $h(x,y)$ at any given point (x,y) , can be described by an interface width which relates to its rms roughness or fluctuations in the height. The rms roughness (σ) is an important descriptor of any surface and is defined as :

$$\sigma(r, t) = \langle [h(x, y, t) - \langle h(x, y, t) \rangle]^2 \rangle^{1/2} \quad (1.6)$$

σ is calculated by taking ensemble average of all x,y points on the surface. In general, σ depends on both time, t , and length scale of observation, L . The Family Vicsek scaling function describes the variation of σ w.r.t t and L , and is given as [72]:

$$\sigma(L, t) = L^\alpha f(t/L^{\alpha/\beta}) \quad (1.7)$$

Using this function, two important relations have been presented by Family and Vicsek which reflect the dynamics of surface evolution in different time regimes, separated

by a crossover time, t_c . In the small time regimes when $t \ll t_c$, σ varies as a power law:

$$\sigma(L, t) \propto t^\beta \quad (1.8)$$

At larger time ($t \gg t_c$), the rms width saturates to σ_{sat} . This saturated value shows a functional dependence of L as:

$$\sigma_{sat}(L) \propto L^\alpha \quad (1.9)$$

α and β are the roughness and growth exponents, respectively, that describe many crucial characteristics of any surface. These exponents are very important for understanding the underlying universality class to which the growing surfaces may belong [71, 72]. In the present thesis, the scaling studies have been utilized to investigate the self organized structures on ion irradiated TiO_2 single crystals and thin films.

1.5 Structural Phase transformation in TiO_2 : From Anatase to Rutile

TiO_2 occurs in three polymorphs: rutile, anatase and brookite. Out of these, rutile and anatase are the most important polymorphs which show many interesting properties. Rutile is the most stable phase among these polymorphs. Anatase is the low temperature phase which transforms irreversibly to rutile at elevated temperatures. Though pure bulk anatase usually transforms into rutile in air at $\sim 600^\circ\text{C}$, a wide range of transition temperatures (250°C - 1200°C) have been reported corresponding to different processing methods, heat flow conditions, raw materials, volume of the material taken, presence of impurities, particle size and shape etc. [73–80]. Considerable interest has been drawn towards understanding these conditions in controlling the kinetics of the phase transformation. In applications like gas sensors, porous gas separation membranes etc. [81–83], where high-temperature processes are involved, the performance of the devices may alter due to phase transformations. Therefore, a deep understanding about the stability of different TiO_2 polymorphs and their size

dependant phase transformation kinetics are crucial for determining the long-term consistency of these devices.

To understand the underlying mechanism behind the phase transformation in TiO_2 , many studies have been carried out. Shannon et al. showed that the nucleation of rutile phase begins at the surface which then spreads into the internal anatase phase [77]. Lee et al. have reported that anatase particles were initially absorbed into rutile which grew at the expense of the anatase particles [94]. A more comprehensive investigation of phase transformation has been done by Zhang et al. [122]. They suggested that the interface nucleation initiates at a lower temperature whereas the surface and bulk nucleation may occur at intermediate and very high temperatures. The interfaces of the neighbouring anatase particles are the most active zones where nucleation of the rutile phase can take place.

Bulk rutile is thermodynamically stable in comparison to the anatase due to its lower Gibbs free energy [85]. However, anatase has lower surface energy than rutile [86]. It has been reported that extremely small crystallite (~ 10 nm) of anatase is more stable [74, 86, 87]. In this case, surface thermodynamics prevails and total energy (bulk and surface) becomes lower in anatase than rutile. Despite this, smaller anatase grains transform into rutile more easily than larger grains. This is probably due to the fact that bigger grains have fewer interfaces and a smaller surface area. Therefore, the growth of anatase phase and its transition to rutile are considered as competitive processes [88].

The presence of impurities and dopants can severely affect the kinetics of the phase transition [89]. The cationic or anionic doping can dramatically influence the kinetics and the temperature of the transformation. The role of cationic dopants has been extensively investigated over the years. It is well known that cationic doping and oxygen vacancy can accelerate the transition [74, 86]. Presence of oxygen vacancy can reduce the structural rigidity of the oxygen sub-lattice. This helps the reconstructive process of the transition from anatase to rutile phase [77]. The cations having small radii and a low valence (<4) are expected to promote the anatase to rutile transformation by increasing the amount of oxygen vacancy [75, 77, 90].

1.6 Photo-absorption property

Photo-absorption property is a significant characteristic of any semiconducting material, controlling and dominating its role in optoelectronic devices. The performance and functioning of such devices as well as research in solar cell, photo-catalysis, photovoltaic etc. demand a sound knowledge of the photo-absorption behavior. Here, creation of electron-hole pair is the most crucial step. The electrons get excited from the valance to the conduction band, by absorbing photons of a suitable energy from the incident radiation. For this to occur, the energy of the photons must be equal to, or higher than, the band gap of the semiconductor. In this process, positively charged holes get created in the valance band. These photo generated species, however, tend to recombine and dissipate energy as heat or radiation, contributing to poor photo-catalysis as well as photo-absorbance characteristics. Such recombination processes can be mitigated through the charge separation of electron and hole pair. Defects like, vacancy and interstitials, have been shown to be effective in controlling these aspects [91]

Metal oxides demonstrate many potential applications in photo-voltaics and photo-catalysis due to their efficient light trapping characteristics as well as high carrier collection abilities. However, often their activity is limited by their bandgap, restricting their operational wavelength range. For example, many functionally attractive oxide materials have wide band gaps, hindering their applications in visible wavelength regions. Enhancing this absorbance is considered of crucial and immediate importance due to its predominant role in a variety of applications in visible-wavelength regime. In this regard, bandgap engineering via several research routes like fabrication of nanostructured materials having modified band gaps, incorporation of dopants within material, dye sensitization etc. have gained enormous significance. In this direction, a variety of dopants such as Cu, N, S, Au, Ag, Co etc. have been used in order to facilitate enhanced visible light photo-absorbance for metal oxides [92–100].

1.7 Glucose Sensing property

A recent survey of WHO (World Health Organization) has revealed that over 200 million people around the world have been affected by diabetes which is expected to double in the next 20 years [101]. This has led to an immense research in the field for the development of fast, reliable and accurate glucose sensors [102]. Still, these developments face many challenges and require numerous innovations [103].

The working principle of a glucose sensor is most often based on the electrochemistry. A typical reversible electrochemical reaction is given as,



where O and R are the oxidized and reduced species, respectively. Number of electrons, involved in the reaction is denoted by n. The forward reaction is called the reduction reaction whereas the reverse one is the oxidation reaction. Both O and R form a redox couple. The potential at which the redox reaction occurs is called the redox potential (E_0).

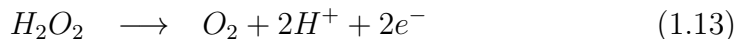
To trace any particular redox reaction, an electrochemical cell is set up with three-electrodes (arrangement details given in the experimental section) that are dipped in an electrolyte solution containing the analyte that undergoes the redox reaction. The potential of the working electrode (where the redox reaction takes place) is varied from a minimum to a maximum preset value. The redox reaction occurs at a particular potential and the current signal (i) generated, due to the reaction, can be expressed via the Randles-Sevcik equation as [105]:

$$i = 2.69 \times 10^5 n^{3/2} A C D^{1/2} v^{1/2}. \quad (1.11)$$

Here A, C, D and v are the electrode area, concentration of the analyte, diffusion coefficient and the potential scan rate, respectively. The concentration, n, of the analyte can be easily determined if the other parameters are known.

A glucose sensor, based on the principle of electrochemistry, can be broadly classified into two areas on the basis of its functioning: enzymatic and non-enzymatic. Historically, sensors were designed based on the principle where an enzyme, glucose

oxidase (GOx), was necessary for the detection of glucose via the following reactions:



The electrode for such an enzymatic glucose sensor is prepared by immobilizing GOx on a bio-compatible materials. A nafion layer is necessary for binding GOx to the electrode. Nafion layer also protects GOx from diffusing into the electrolyte solution. Though enzymetic sensors display good selectivity and low detection limit [106,107], they face some major drawbacks due to the thermal and chemical instability of the enzyme [108, 120]. In this respect, immobilization of enzyme produces numerous challenges. Environmental conditions such as humidity, temperature, pH, presence of ionic detergents and enzyme-poisoning molecules pose additional difficulties for obtaining error-free and reproducible measurements [110]. To overcome these limitations, enormous reserach efforts have been undertaken to design and develop enzyme-free glucose sensors. Research activities have exhibited the role of some metal and transition metal oxides in this direction [111–125]. Large research efforts are also focused on the development of sensors based on the hybrid materials which display many advanced and exceptional sensing properties [126–128]. Such properties are governed by the hybrid template as well as the morphology, composition and the phase of the materials [129]. Surfaces with nano-dimensional structures are becoming increasingly significant in many glucose-sensing applications as they present functionally attractive framework, and large exposed surface area, that can facilitate fast electron response behavior [131]. In the present thesis, $\text{Cu}_x\text{O-ZnO}$ ($x=1,2$) and CuO-TiO_2 nanostructured composites have been prepared and studied for their non-enzymetic glucose sensing applications.

1.8 Resistive Switching behaviour

Memory devices in the form of hard disks, tapes and flash memory devices are ubiquitous in the present day scenario [132, 133]. However, they suffer from many drawbacks like poor writing speed, scalability issues, low endurance, requiring high voltage

for writing operations, etc.. To overcome these difficulties, immense research work is ongoing for developing new types of nonvolatile memory devices like magnetic random access memory (MRAM), phase-change random access memory (PRAM), ferroelectric random access memory (FRAM) and resistive random access memory (RRAM) [134–144].

RRAM is becoming an excellent candidate for the next generation nonvolatile device due to its many advanced properties related to the scalability, fast switching speeds (<10 ns), simple design and excellent compatibility with the complementary metal-oxide-semiconductor (CMOS) technology [145–149]. It can function both as working memory and main memory. As a working memory, RRAM exhibits a low voltage operation with a fast write and erase speeds. At the same time, the enormous storage capacity of non volatile nature enables RRAM to function as a main memory. The first RRAM device was reported by Beck et al. [151] in 2000. Its discovery soon triggered a huge interest in the research community [152]. Several oxides, polymers, organic molecules, perovskites etc. demonstrate resistive switching (RS) properties [152–162]. Controlling conduction filament formation under biasing, understanding the associated conduction mechanism and estimating the current percolation properties, however, are still challenging issues. Additional bias voltage, sometimes necessary for *forming process* in memory devices [163] is a limitation requiring higher voltages for switching on the device. A *forming-free* device is more suitable in memory integration. Achieving low reset currents is also important for the low power consuming electronic devices.

A typical RRAM consists of an active layer (I) material sandwiched between two conducting metal electrodes (M). The Metal-Insulator-Metal (MIM) like structure of RRAM is shown in Fig 1.5. The working principle of RRAM lies in the fact that the conductivity of the insulator layer depends on the external applied electric field [164, 165] that induces the formation of conducting filament by applying the *forming* bias. The device can be triggered from a high resistive state (HRS) to a low resistive state (LRS) and vice versa. The former is called an OFF state whereas the later is an ON state. When RRAM is switched from HRS to LRS, the process is called the Set process and the reverse is the Reset process. RRAM is categorized as

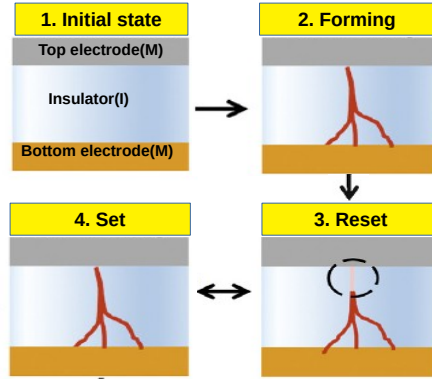


Figure 1.5: Schematic diagram of different operational state of a RRAM device; (1) initial state (2) forming, (3) reset, and (4) set process [150].

bipolar or unipolar depending on the polarity of the operating voltage. The operation of the two types of RRAM is schematically displayed in fig 1.6.

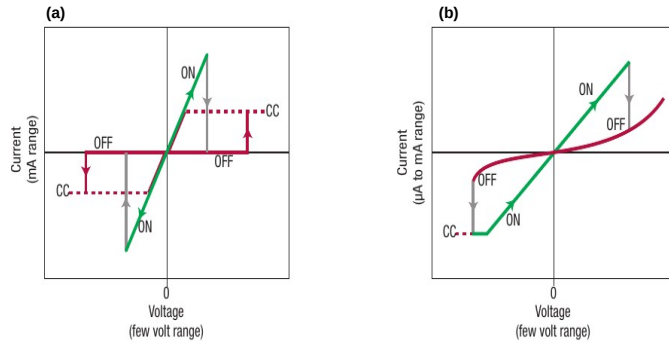


Figure 1.6: Schematic diagrams of (a) unipolar switching and (b) bipolar switching in RRAM [153].

In a unipolar device, the set and the reset processes occur at potentials of the same polarity but different magnitudes whereas potentials of different polarities are needed for the bipolar operations (fig 1.6). The mechanism for a unipolar switching is usually governed by Joule heating effect and thus, does not depend on the polarity of the applied potential. However, the bipolar action is usually mediated by a redox reaction which depends on the polarity of the potential. The RS mechanism can be explained by the conducting filament (CF) model [166,167]. In this model, a CF is formed between two electrodes by the migration of multiple charged species like oxygen vacancy, oxygen ions, metal ions etc.. Figure 1.5 displays the basic mechanism

for RS action. The formation of CF starts when a high voltage is applied to the electrodes and RRAM is switched into LRS. When the reset voltage is applied, CF ruptures and RRAM is switched from LRS to HRS. Thus, the state can be altered back and forth by applying set and reset voltages. Ion implantation can sometimes induce oxygen vacancies via preferential sputtering of metal oxides. Hence, these oxides present an important basis for fabricating active layer in RS devices [152–162].

This thesis has been organized in the following fashion. Chapter 2 discusses the experimental aspects and the experimental systems utilized for the synthesis and characterization of TiO_2 and ZnO nanostructured films. In the first part of the thesis, in chapters 3 to 6, nanostructured TiO_2 films and their properties have been discussed. Chapters 3 and 4 investigate the Ti ion irradiated TiO_2 nanostructured films and some of their advanced properties like resistive switching behavior and photo-absorbance behavior. These ion irradiated TiO_2 thin films also exhibit a phase transformation, at a critical ion fluence. Such structural phase transitions, from anatase to rutile, have also been investigated here, in chapters 3 and 4. The morphological evolution of the Ti ion irradiated TiO_2 surfaces has been investigated by applying the theoretical concepts, of scaling formalism, in chapter 5. Such scaling concepts have also been applied to investigate Ar^+ ion irradiated TiO_2 surfaces in chapter 6. In the second part of this thesis, in chapters 7 to 10, thin ZnO nanostructured films have been discussed. Chapter 7 investigates the Ti ion irradiated ZnO nanostructured films along with some advanced properties like resistive switching behavior and photo-absorbance behavior. Thin $\text{Cu}_x\text{O-ZnO}$ and $\text{Cu}_2\text{O-ZnO}$ nanostructured films have been synthesized here by electrochemical route. These nanostructures display non-enzymatic glucose sensing response. This sensing behavior as well as their photo-response has been investigated in chapters 8 and 9. Formation of CuO-TiO_2 composites structures have also discussed in chapter 9. These chemically synthesized structures have been investigated for glucose sensing and photo-absorbance properties. The photo-response and the photo-catalytic behavior of hydrothermally grown ZnO nano-rods has been investigated in chapter 10. The conclusion is presented in chapter 11.

Bibliography

- [1] M. S. Gudiksen, L. J. Lauhon, J. Wang, D. C. Smith and C. M. Lieber, *Nature*, 415, 617 (2002)
- [2] L. J. Lauhon, M. S. Gudikson, D. Wang and C. M. Lieber, *Nature*, 420, 57 (2002)
- [3] U. Srinivasan, M. A. Helmbrecht, R. S. Muller and R. T. Howe, *Optics Photonics News*, 13, 20 (2002)
- [4] K. F. Bohringer, *J. Micromech. Microeng.*, 13, S10 (2003)
- [5] C. N. R. Rao, P. J. Thomas and G. U. Kulkarni, *Nanocrystals: Synthesis, Properties and Applications* (Springer, 2007).
- [6] S. Link and M. A. El-Sayed, *J. Phys. Chem. B*, 103, 8410 (1999)
- [7] W. P. Halperin, *Rev. Mod. Phys.*, 58, 583 (1986)
- [8] A. D. Maynard, R. J. Aitken, T. Butz, V. Colvin, K. Donaldson, G. Oberdorster, M. A. Philbert, J. Ryan, A. Seaton, V. Stone, S. S. Tinkle, L. Tran, N. J. Walker, and D. Warheit, *Nature*, 444, 267 (2006)
- [9] D. Caruntu, G. Caruntu, and C. J. OConnor, *J. Phys. D: Appl. Phys.*, 40, 5801 (2007)
- [10] S. Nafis, Z. X. Tang and B. Dale, *J. Appl. Phys.*, 64, 5835 (1988)
- [11] S. Majumder, D. Paramanik, V. Solanki, B. P. Bag, and S. Varma, *Appl. Phys. Lett.*, 98, 053105 (2011).
- [12] V. Solanki, S. Majumder, I. Mishra, P. Dash, C. Singh, D. Kanjilal, and S. Varma, *J. Appl. Phys.*, 115, 124306 (2014).

- [13] A. E. Berkowitz, J. R. Mitchell and M. J. Carey, *Phys. Rev. Lett.*, 68, 3745 (1992).
- [14] H. Gleiter, *Acta Material*, 48, 1 (2000)
- [15] A. S. Eldenstein, J. S. Murday and B. B. Rath, *Progress in Materials science*, 42, 5 (1997)
- [16] Nguyen Duc Khoang, Do Dang Trung, Nguyen Van Duy, Nguyen Duc Hoa, Nguyen Van Hieu, *Sensors and Actuators B*, 174, 594 (2012)
- [17] Narendar Gogurla, Arun Kumar Sinha, Sumita Santra, Santanu Manna and Samit Kumar Ray, *Scientific Reports*, 4, 6483 (2014)
- [18] Masayuki Fujimotoa and Hiroshi Koyama, *Appl. Phys. Lett.*, 89, 223509 (2006)
- [19] Jivika Sullaphen, Kashinath Bogle, Xuan Cheng, John M. Gregg, and Nagarajan Valanoor, *Appl. Phys. Lett.*, 100, 203115 (2012)
- [20] Z.l. wang, *Appl. Phys. A*, 88, 7 (2007)
- [21] George M. Whitesides and Bartosz Grzybowski, *Science*, 295, 2418 (2002)
- [22] G. M. Whitesides, and B. Grzybowski, *Science*, 295, 2418 (2002)
- [23] K. K. Nanda, and S. N. Sahu, *Appl. Phys. Lett.*, 79, 2743 (2001)
- [24] Jing Li, Hongbo Li , Yan Xue, Hailin Fang, Wei Wang, *Sensors and Actuators B*, 191,(2014)
- [25] J. Zhu, Z. Gui, Y. Ding, Z. Wang, Y. Hu, and M. Zou, *J. Phys. Chem. C*, 111, 5622 (2007)
- [26] N. Serpone, and E. Pelizzetti, *Photocatalysis - Fundamentals and Applications*, (John Wiley Sons, New York (1989)
- [27] N D Hoa, N van Quy,H Jung, D Kim, H Kim and S K Hong, *Sensors Actuators B*,146, 266 (2010).

- [28] P Raksa, A Gardchareon, T Chairuangstri, P Mangkorntong, N Mangkorntong and S Choopun, *Ceram. Int.*, **35**, 649 (2009).
- [29] D Li, J Hu, R Wu and J.G Lu, *Nanotechnology*, **21**, 485502 (2010)
- [30] Chen Z et. al., *J. Mater. Res.*, **25**, 3 (2010)
- [31] S Gubbala, J Thangala and M K Sunkara, *Sol. Energy Mater. Sol. Cells.*, **91**, 813 (2007).
- [32] C.T. Hsieh, J.M. Chen, H.H. Lin, H.C. Shih, *Applied Physics Letters*, **83**, 3383 (2003)
- [33] P. Podhjeck, Z. Zbransk, P. Novk, Z. Dobiov, R. ern, V. Valvoda, *Electrochimica Acta*, **35**, 245 (1990)
- [34] L.C. Feldman, J.W. Mayer and S.T. Picraux In: *Material Analysis By Ion Channeling*, Academic Press, New York (1982)
- [35] U. Littmark, J. F. Ziegler, *Handbook of Range Distributions for Energetic Ions in All Elements*, Vol. 6, Pergamon Press, New York (1980); J. F. Ziegler, *Handbook of Stopping Cross Sections for Energetic Ions in All Elements*, Pergamon Press, 1980; and J. F. Ziegler, J. P. Biersack, U. Littmark, *Proceedings of the US-Japan Seminar on Charged Particle Penetration Phenomena*, ORNL report CONF 820131 (1982)
- [36] L. G. Haggmark, *Nucl Instrum. Meth*, **174**, 257 (1980),
- [37] M. A. Makeev, R. Cuerno, and A. L. Barabsi, *Nucl. Instr. Meth. Phys. Res. B*, **197**, 185 (2002).
- [38] P. Sigmund, *Nucl. Instr. Meth. Phys. Res. B*, **27**, 1 (1987).
- [39] P. Sigmund, *Ion Sputtering by Particle Bombardment*, I, R. Behrisch, ed. (Springer- Verlag: Berlin (1981)).
- [40] Z.L. Liau, J.W. Mayer, W.L. Brown, and J.M. Poate, *J. Appl. Phys.*, **49**, 5295 (1978).

- [41] H. H. Andersen, and H. L. Bay, *J. Appl. Phys.*, 46, 2416 (1975).
- [42] M. Navez, C. Sella, and D. Chaperot, *C. R. Acad. Sci. Paris*, 254, 240 (1962).
- [43] H. B. Huntington, and G. A. Sullivan, *Phys. Rev. Lett.*, 14, 177 (1965).
- [44] M. Kolmer, A. A. Zebari, M. Goryl, F. B. de Mongeot, F. Zasada, W. Piskorz, P. Pietrzyk, Z. Sojka, F. Krok, and M. Szymonski, *Phys. Rev. B*, 88, 195427 (2013).
- [45] A. Keller, S. Rossbach, S. Facsko, and W. Mller, *Nanotechnology* ,19, 135303 (2008).
- [46] F. Frost, and R. Rauschenbach, *Appl. Phys.*, A 77, 1 (2003).
- [47] R. Gago, L. Vzquez, R. Cuerno, M. Varela, C. Ballesteros, and J. Albella, *Nanotechnology*, 13, 304 (2002).
- [48] T. Basu, J. R. Mohanty, and T. Som, *Appl. Surf. Sci.*, 258, 9944 (2012).
- [49] R. M. Bradley, and J. M. E. Harper, *J. Vac. Sci. Technol. A*, 6, 2390 (1988).
- [50] A. R. Cubero, R. Gago, F. Palomares, A. Mucklich, M. Vinnichenko, and L. Vazquez, *Phys. Rev. B*, 86, 085436 (2012).
- [51] U. Valbusa, C. Boragno, and F. B.de Mongeot, *J. Phys.: Cond. Matt.*, 14, 8153 (2002).
- [52] S. Rusponi, G. Constantini, C. Boragno, and U. Valbusa, *Phys. Rev. Lett.*81,, 4184 (1998).
- [53] S. Habenicht, W. Bolse, K. P. Lieb, K. Reimann, and U. Geyer, *Phys. Rev. B*, 60, 2200 (1999).
- [54] G.W. Lewis, M.J. Nobes, G. Carter, and J.L. Whitton, *Nucl. Instr. Meth.*, 179, 363 (1980).
- [55] M. Navez, D. Chaperot and C. Sella C, *C R Hebdomadaires Seances Acad Sci*, 254, 240 (1962).

- [56] J.D. Erlebacher and M.J. Aziz, Mater Res. Soc. Symp. Proc., 440, 461 (1997).
- [57] S.Habenicht, Phys Rev B, 63, 125419 (2001).
- [58] P. Sigmund, J. Mat. Sci., 8, 1545 (1973).
- [59] A. D. Brown, J. Erlebacher, W. L. Chan, and E. Chason, Phys. Rev. Lett., 95, 056101 (2005).
- [60] D. A. Pearson, and R. M. Bradley, J. Phys. Cond. Matt., 27, 015010 (2015).
- [61] Q. Wei, J. Lian, L. Boatner, L. Wang, and R. Ewing, Phys. Rev. B, 80, 085413 (2009).
- [62] R. Cuerno and A.L. Barabasi, Phys. Rev. Lett., 74, 4746 (1995).
- [63] Y. Kuramoto and T. Tsuzuki, Prog. Theor. Phys., 55, 356 (1976).
- [64] Rodolfo Cuerno, Hernan A. Makse, Silvina Tomassone, Stephen T. Harrington, and H. Eugene Stanley, Phys. Rev. Lett., 75, 4464 (1995)
- [65] Martin Rost and Joachim Krug, Phys. Rev. Lett., 75, 3894 (1995).
- [66] S. Park, B. Kahng, H. Jeong, and A.-L. Barabas, Phys. Rev. Lett., 83, 3486 (1999).
- [67] E.A. Eklund, E.J. Snyder, and R.S. Williams, Surf. Sci., 285, 157 (1993).
- [68] Z.J. Liu, N. Jiang, Y. G. Shen, Y.W. Mai, J. Appl. Phys., 92, 3559 (2002); A.E. Litand John, E. Sanchez, J. Appl. Phys., 85, 876 (1999).
- [69] A.L. Barabasi, H.E. Stanley, Fractal Concepts in Surface Growth, Cambridge University Press, Cambridge, 1995.
- [70] F. Family, T. Vicsek (Eds.), Dynamics of Fractal Surfaces, World Scientific, Singapore, 1991.
- [71] P. Meakin, Phys. Rep. 235 (1993) 189; T. Halpin-Healey, Y.C. Zhang, Phys. Rep., 254, 215 (1995).

- [72] F. Family and T. Vicsek, *J. Phys. A*, 18, L15 (1985).
- [73] Qiang Gao, Xiaomei Wu, Yueming Fan, *Dyes and Pigments*, 95, 96 (2012).
- [74] Dorian A. H. Hanaor, Charles C. Sorrell, *J Mater Sci.*, 46, 855 (2011).
- [75] KJD Mackenzie, *Trans. J. Br Ceram. Soc.*, 74,77 (1975)
- [76] J Kim , KC Song, S. Foncillas, S. Pratsinis, *J. Eur. Ceram. Soc.*, 21, 2863 (2001)
- [77] RD Shannon, JA Pask, *J. Am. Ceram. Soc.*, 48, 391 (1965)
- [78] H Zhang, JF Banfield, *J. Mater. Res.*, 15, 437 (2000)
- [79] PI Gouma, MJ Mills, *J. Am. Ceram. Soc.*, 84, 619 (2001)
- [80] Z. Jing, X Qian, F. Zhaochi, L. Meijun, L. Can, *Angew Chem. Int. Ed.*, 47, 1766 (2008)
- [81] KNP Kumar, K. Keizer, AJ Burggraaf, *J. Mater. Sci. Lett.*, 13, 59 (1994)
- [82] RL Penn, JF Banfield, *Am. Miner.*, 84, 871 (1999)
- [83] A Rothschild, A Levakov, Y Shapira, N Ashkenasy, Y Komem, *Surf. Sci.*, 532, 456 (2003)
- [84] GH Lee, HM Zuo, *J. Am. Chem Soc.*, 87,473 (2004)
- [85] TB Ghosh, S Dhabal, AK Datta, *J. Appl. Phys.*, 94, 4577 (2003)
- [86] H Zhang, JF Banfield, *J. Mater. Chem.*, 8, 2073 (1998)
- [87] A. A. Gribb and J. F. Banfield, *Am. Mineral.*, 82, 717 (1997).
- [88] Ding X, Li X, *J. Mater. Res.*, 13, 2556 (1998)
- [89] DJ Reidy, JD Holmes, MA Morris, *J. Eur. Ceram. Soc.*, 26, 1527 (2006)
- [90] KJD MacKenzie, *Trans J. Br. Ceram. Soc.*, 74, 29 (1975)
- [91] P. Dash, Ashis Manna, N. C. Mishra and Shikha Varma, *Physica E: Low-dimensional Systems and Nanostructures*, 107, 38 (2019).

- [92] R. Asahi, T. Morikawa, T. Ohwaki, K. Aoki, and Y. Taga, *Science*, 293, 269271 (2001).
- [93] S. Kim, S. J. Hwang, W. Choi, *J. Phys. Chem. B*, 109, 24260 (2005).
- [94] M. S. Lee, S. S. Hong, M. Moheseni, *J. Mol. Catal A*, 242, 135 (2005).
- [95] R. Yu, Q. Lin, S. F. Leung, and Z. Fan, *Nano Energy*, 1, 57 (2012).
- [96] Niya Mary Jacob, Giridhar Madras, Nagaraju Kottam, and Tiju Thomas, *Ind. Eng. Chem. Res.*, 53, 5895, (2014)
- [97] Muhammad Ahsan Shafique, Saqlain A Shah, Muhammad Nafees, Khalid Rasheed, Riaz Ahmad, *International Nano Letters*, 31 (2012)
- [98] Hongchun Qin, Weiyang Li, Yujing Xia, and Tao He, *ACS Appl. Mater. Interfaces*, 3, 3152 (2011)
- [99] Dojalisa Sahu, N.R.Panda, B.S.Acharya, A.K.Panda, *Optical Materials*, 36, 1402 (2014)
- [100] Ronghua Wang, John Haozhong Xina, Yang Yangb, Hongfang Liuc, Liming Xuc, Junhui Hud, *Applied Surface Science*, 227, 312 (2014)
- [101] WHO, Fact sheet No. 312 in World health Organization (2009).
- [102] T. Raj kumar, K. Justice Babu, Dong Jin Yoo, Ae Rhan Kim and G. Gnana kumar, *RSC Adv.*, 5, 41457, (2015)
- [103] Joseph Wang, *Electroanalysis*, 13, 983 (2001)
- [104] Lowe, C. R. *Biosensors. Trends in Biotechnology*, 2(3),59 (1984).
- [105] Crouch, Stanley R and Skoog, Douglas A: "Principles of instrumental analysis" Cengage Learning 2006, ISBN 0-49501-201-7
- [106] L.C. Jiang, W.D. Zhang, *Biosens. Bioelectron.*, 25, 1402 (2010)
- [107] S. Luo, F. Su, C. Liu, J. Li, R. Liu, Y. Xiao, Y. Li, X. Liu, Q. Cai, *Talanta*, 86, 157 (2011).

- [108] I. Katakis, E. Dominguez, *Trends Anal. Chem.*, 14, 310 (1995)
- [109] F. Cao, J. Gong, *Anal. Chim. Acta*, 723, 39 (2012)
- [110] R. Wilson, A.P.F. Turner, *Biosens. Bioelectron.*, 7, 165 (1992)
- [111] R. O'Neill, S. Chang, J. Lowry, C. McNeil, *Biosensors and Bioelectronics*, 19, 1521 (2004)
- [112] A. Guts, C. Carraro, R. Maboudian, *Electrochimica Acta*, 56, 5855 (2011)
- [113] S. Mahshid, A. Dolati, M. Ghorban, L. Yang, S. Luo, Q. Cai, *Journal of Alloys and Compounds*, 554, 169 (2013)
- [114] Y. Ding, Y. Liu, L. Zhang, Y. Wang, M. Bellagamba, J. Parisi, C. Li, Y. Lei, *Electrochimica Acta*, 58, 209 (2011)
- [115] X. Niu, M. Lan, C. Chen, H. Zhao, *Talanta*, 99, 1062 (2012)
- [116] X. Bo, J. Bai, L. Yang, L. Guo, *Sensors and Actuators B*, 157, 662 (2011)
- [117] B. Zheng, S. Xie, L. Qian, H. Yuan, D. Xiao, M. Choi, *Sensors and Actuators B*, 152, 49 (2011)
- [118] S. Cherevko, C. Chung, *Sensors and Actuators B*, 142, 216 (2009)
- [119] D. Liu, Q. Luo, F. Zhou, *Synthetic Metals*, 160, 1745 (2010)
- [120] F. Cao, J. Gong, *Anal. Chim. Acta* 723, 39 (2012)
- [121] X. Wang, C.G. Hu, H. Liu, G.J. Du, X.S. He, Y. Xi, *Sens. Actuators B*, 144, 220 (2010)
- [122] X.J. Zhang, A.X. Gu, G.F. Wang, Y. Wei, W. Wang, H.Q. Wu, B. Fang, *Cryst. Eng. Comm.*, 12, 1120 (2010)
- [123] E. Reitz, W.Z. Jia, M. Gentile, Y. Wang, Y. Lei, *Electroanalysis*, 20, 2482 (2008)
- [124] S. Cherevko, C.H. Chung, *Talanta*, 80, 1371 (2010)

- [125] K. Singh, A. Umar, A. Kumar, G.R. Chaudhary, S. Singh, S.K. Mehta, *Sci. Adv. Mater.*, 4 , 994 (2012)
- [126] Y.D. Yin, R.M. Rioux, C.K. Erdonmez, S. Hughes, G.A. Somorjai, A.P. Alivisatos, *Science*, 304, 711 (2004)
- [127] A.P. Alivisatos, *Science*, 271 , 933 (1996)
- [128] C. Burda, X.B. Chen, R. Narayanan, M.A. El-Sayed, *Chem. Rev.*, 105 , 1025 (2005)
- [129] P. Liu, Y. Wang, H.M. Zhang, T.C. An, H.G. Yang, Z.Y. Tang, W.P. Cai, H.J. Zhao, *Small*, 8, 3664 (2012)
- [130] Shin SoYoon, Ananthakumar Ramadoss, Balasubramaniam Saravanakumar, Sang Jae Kim, *Journal of Electroanalytical Chemistry*, 90, 717 (2014)
- [131] Chunyang Zhou, Lin Xu, Jian Song, Ruiqing Xing, Sai Xu, Dali Liu Hongwei Song, *Scientific Reports*, 4,7382 (2014)
- [132] D. Kahng, S. M. Sze, *Bell Syst. Tech. J.*, 46, 1288 (1967)
- [133] S.M. Sze, *Semiconductor Devices Physics and Technology*, Wiley, Hoboken, NJ,USA, 2002.
- [134] Inchan Hwang, Yong-Jun Cho, Myoung-Jae Lee, and Moon-Ho Jo, *App. Phys. Lett.*, 106 , 193106 (2015)
- [135] A. Gyanathan and Yee-Chia Yeo, *J. Appl. Phys.*, 112,104504 (2012)
- [136] S. Raoux, Anja K. Knig, HuaiYu Cheng, Daniele Garbin, Roger W. Cheek, Jean L. JordanSweet, Matthias Wuttig, *Phys. Status Solidi B*, 249, 1999 (2012)
- [137] D. Loke, T. H. Lee, W. J. Wang, L. P. Shi, R. Zhao, Y. C. Yeo, T. C. Chong, S. R. Elliott, *Science*, 336, 1566 (2012)
- [138] T. Kojima, Tomohiro Sakai, Takayuki Watanabe, and Hiroshi Funakubo, *Appl. Phys. Lett.*, 80, 2746 (2002) .

- [139] Roberto Bez, Agostino Pirovano, *Mater. Sci. Semicond. Process* 7, 349 (2004)
- [140] H. Ishiwara, *Curr. Appl. Phys.*, 12 (3), 603 (2012)
- [141] Jian-Gang Zhu and Youfeng Zheng, *J. Appl. Phys.*, 87, 6668 (2000)
- [142] Naoki Nishimura, Tadahiko Hirai, Akio Koganei, Takashi Ikeda, Kazuhisa Okano, Yoshinobu Sekiguchi, and Yoshiyuki Osada, *J. Appl. Phys.*, 91, 5246 (2002)
- [143] A. Ney, C. Pampuch, R. Koch and K. H. Ploog, *Nature*, 425, 485 (2003)
- [144] Ting-Chang Chang, Fu-Yen Jian, Shih-Cheng Chen and Yu-Ting Tsai, *Mater. Today*, 14, 608 (2011)
- [145] W W Zhuang, W Pan, B D Ulrich, *IEDM Tech Dig*, 193 (2002)
- [146] Chih-Yi Liu, Pei-Hsun Wu, A. Wang, Wen-Yueh Jang, Jien-Chen Young, Kuang-Yi Chiu, Tseung-Yuen Tsen, *IEEE Electron Device Lett*, 26, 351 (2005)
- [147] C C Lin, B C Tu, C C Lin, *IEEE Electron Device Lett*, 27,725 (2006)
- [148] T. Fujii, M. Kawasaki, A. Sawa, H. Akoh, Y. Kawazoe and Y. Tokura, *Appl Phys Lett*, 86, 012107 (2004)
- [149] B.O. Cho, T. Yasue, H. Yoon, M.S. Lee, I.S. Yeo, U.I. Chung, J.T. Moon, B.I. Ryu, *IEDM Tech Dig*, 1 (2006)
- [150] A. Sawa, *Mater. Today*, 11, 28 (2008)
- [151] KM Kim, DS Jeong, CS Hwang, *Nanotechnology*, 22, 254002, (2011)
- [152] A Beck, JG Bednorz, C Gerber, C Rossel, D Widmer, *Appl Phys Lett.*, 77, 139 (2000).
- [153] Rainer Waser and Masakazu Aono, *Nature materials*, 6 (2007).
- [154] BJ Choi, DS Jeong, SK Kim, C Rohde, S Choi, JH Oh, *J Appl Phys.*, 98, 033715 (2005)

- [155] CB Lee, BS Kang, A Benayad, MJ Lee, SE Ahn, KH Kim, *Appl. Phys Lett.*, 93, 042115 (2008)
- [156] KC Liu, WH Tzeng, KM Chang, YC Chan, CC Kuo, CW Cheng, *Microelectron Reliab*, 50, 670 (2010)
- [157] KM Chang, WH Tzeng, KC Liu, YC Chan, CC Kuo, *Microelectron Reliab.*, 50, 1931 (2010)
- [158] A Mehonic , S Cuff , M Wojdak , S Hudziak , O Jambois , C Labbe , *J Appl Phys.*, 11, 074507 (2012)
- [159] C Dou, K Kakushima, P Ahmet, K Tsutsui, A Nishiyama, N Sugii, *Microelectron Reliab.*,52, 688(2012)
- [160] WL Kwan, B Lei, Y Shao, Y Yang, *Curr Appl Phys.*, 10, 50 (2010)
- [161] B Cho, KH Nam, S Song, Y Ji, GY Jung, T Le, *Curr Appl Phys.*, 12, 940 (2012)
- [162] A Sawa, T Fujii, M Kawasaki, Y Tokura, *Appl Phys Lett.*, 85, 4073 (2004)
- [163] Muhammad Younas, Chi Xu, Muhammad Arshad, Lok Ping Ho, Shengqiang Zhou, Fahad Azad, Muhammad Javed Akhtar, Shichen Su, Waqar Azeem and Francis C. C. Ling, *ACS Omega*, 2, 8810 (2017)
- [164] JJ Yang, MD Pickett, X Li, DAA Ohlberg, DR Stewart, RS Williams, *Nat Nanotechnol.*, 3, 429 (2008)
- [165] R Bruchhaus, R Muenstermann, T Menke, C Hermes, F Lentz, R Weng, *Curr Appl Phys.*, 11, 75 (2011)
- [166] D Li, M Li, F Zahid, J Wang, Guo, J. *Appl. Phys.*, 112, 073512 (2012)
- [167] MG Sunga, SJ Kim, MS Joo, JS Roh, C Ryu, S Hong, *Solid-State Electronics*, 63, 115 (2011)

Chapter 2

Experimental Techniques

This chapter discusses various experimental aspects related to the fabrication and characterization of TiO_2 and ZnO nanostructured films. They have been prepared by utilizing various synthesis methods such as sputter deposition, ion implantation, electrodeposition, hydrothermal growth and chemical route. Several techniques like Atomic Force Microscopy (AFM), Field Emission Scanning Electron Microscopy (FE-SEM), Transmission Electron Microscopy (TEM), X-ray Photoelectron Spectroscopy (XPS), X-ray Diffraction (XRD), Raman Spectroscopy, UV-Vis Spectroscopy (UV-Vis), Photoluminescence Spectroscopy (PL) and Cyclic Voltammetry (CV) have been employed for investigating these nanostructures and some functional properties.

This chapter is organized in the following order. Section 2.1 discusses several synthesis processes. The characterization techniques are presented in section 2.2. Structures of TiO_2 , ZnO , CuO , Cu_2O and glucose are briefly discussed in section 2.3.

2.1 Techniques for Fabrication of Nanostructures

2.1.1 Sputtering deposition

The continuous development of film deposition techniques has enabled path-breaking innovations in the field of optical coatings, magnetic recording media, electronic semiconductor devices, Light Emitting Diodes (LED), solar cells and batteries. To grow good quality films, various vapor deposition methods have been developed over the years. They are broadly categorized as: physical vapor deposition (PVD) and chemical vapor deposition (CVD). Sputter deposition is a widely used PVD technique

for growing thin films of variety of materials on a substrate. The thickness of the grown films can vary from nanometers to micrometers. In this technique, a plasma of positively charged ions are created and then accelerated towards a negatively biased target material. The surface atoms from the target material are ejected out by making collisions with incoming energetic ions. The ejected target atoms, then get deposited on the substrate [1]. A mixture of argon and oxygen gas is used as the sputtering gas for creating plasma inside the main chamber. The rate of deposition is governed by factors such as target material composition, type of the incident ion, binding energy of the target material, experimental geometry, applied sputter power etc.. The growth parameters like deposition rate, background gas pressure, substrate material and temperature govern the properties of the deposited film. Two types of sputter deposition techniques have been developed depending on the nature of the used power supply: direct current (DC) and radio frequency (RF). Sputtering system with DC power source is commonly used for growing metal films. In this method, when the ions strike the target, a localized positive space charge region is created near the target which opposes further bombardment. The RF sputtering technique is developed to overcome these difficulties. Here, the target is bombarded by electrons and positive ions simultaneously by applying RF potential. The accumulated space charge near the target is removed with each cycle of RF potential. This technique is suitable for growing films of insulator materials. In an advanced RF sputter deposition systems, a closed magnetic field is used near the cathode to trap electrons in order to enhance the sputter yield [2]. In the present thesis, TiO_2 and ZnO nanostructured thin films have been grown via RF magnetron sputter deposition technique.

A schematic diagram of the deposition system is shown in fig. 2.1. Different parts of the instrument are highlighted with colour. The main deposition chamber is equipped with four sputtering guns and is connected to a load lock. The deposition is carried out in high vacuum conditions which is achieved by simultaneous operation of a rotary and turbo molecular pump. Uniform deposition is attained by rotating the substrate. Usually films are deposited at normal incidence angle w.r.t target. However, deposition can also be performed at an oblique angle with the help of a manipulator.

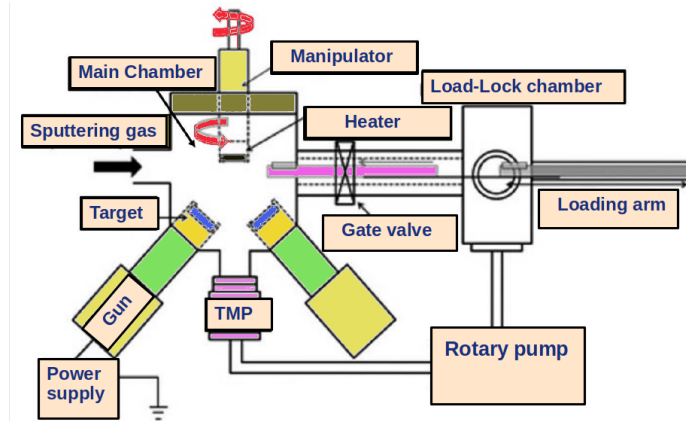


Figure 2.1: The schematic diagram of RF Magnetron sputtering setup.

TiO₂ and ZnO thin films have been deposited on Au/Ni/SiO₂/Si substrate at room temperature by using 100 W RF sputtering (Excel Instruments) system. The substrate is rotated with a speed of 9 rpm to get uniform deposition. High purity Ar (purity 99.99%) and oxygen (99.99%) gases have been purged into the main chamber at a flow rate of 30 sccm and 12 sccm, respectively, for controlling the stoichiometry of the deposited films.

2.1.2 Ion Implantation

Ion implantation is a single step procedure for introducing foreign atoms into a solid target. Here, an energetic ion beam is created and focused on a target material. The ion-matter interaction crucially depends on parameters like ion species, ion current, ion energy etc.. The incident ions can penetrate into the materials upto few microns depending on its energy. Lattice atoms get displaced when ions traverse through the material. These displaced atoms further collide with nearby atoms and that will produce collision cascade in the region around the ion path. This will lead to the generation of interstitial atoms, vacancies and other type of lattice disorder which affect the structural, optical and electrical properties of the material. The ion implantation technique can also be used in synthesis of nanostructured materials, ion-beam mixing and ion induced phase transformation. Modern VLSI (Very-large-scale integration) technology has also embraced this method for doping and fabricating devices. Several ion accelerator systems have been developed worldwide to achieve steady, well-focused

and contamination free ion beams for research work. Each of them consists of components such as ion source, magnetic analyser, target chamber, vacuum pumps, high voltage accelerating set up, electric or magnetic quadrupole lenses, electrostatic scanning arrangement, etc.. Here, we briefly discuss the ion accelerator systems which have been used for the implantation work in this thesis.

(a) Negative Ion Implanter:

In the present thesis, ZnO and TiO₂ thin films have been implanted with 50 keV Ti ions using Negative Ion Implanter at Inter University Accelerator Center (IUAC), New Delhi. The typical ion energies, delivered by this implanter are in the range of 30-200 keV. This facility is equipped with a new modified MC-SNICS (multi cathode source of negative ion by Cesium sputtering) source which can accommodate 40 samples at a time. The source is installed inside a high voltage deck. Extracted ions from the source are accelerated by applying high accelerating potential (~ 300 eV). The beam is passed through several electromagnetic lenses (e.g. electrostatic quadrupole triplets) and finally focused on a target. The electrostatic steerers are used for accurate and low power electrostatic steering of the charged particle beams. To measure the ion current, Faraday cups are used at different places on the beam line. Different controllers like Beam Line Valve (BLV) controllers, Faraday cup controllers etc. are utilized to produce a collimated beam. Turbo molecular pumps are utilized to maintain the high vacuum (5×10^{-8} torr) in the beam line. The whole control system for this negative ion implanter is indigenously developed and named as Indigenous Measurement And Control System (IMACS). The negative implanter facility at IUAC, shown in fig. 2.2, was used for implanting 50 keV Ti ions in ZnO and TiO₂ thin films with fluences ranging from 1×10^{10} to 1×10^{15} ions/cm².

(b) Low Energy Ion Beam Facility (LEIBF):

In this thesis, TiO₂ single crystals have been irradiated by low energy Ar⁺ ion using Electron Cyclotron Resonance (ECR) based Low Energy Ion Beam Facility (LEIBF) at Inter University Accelerator Centre (IUAC), New Delhi. This facility is capable of producing singly charged ions of energy in the range of 15-400 keV and



Figure 2.2: Negative Ion Implantation facility at IUAC, New Delhi (with permission)

ion currents in the range of $0.05\text{-}20\ \mu\text{A}$. The ECR ion source with all its electronic control devices, power supplies and vacuum pumps are placed on a 400 kV high voltage deck. The whole beam line (from source to target chamber) is kept under high vacuum condition for maintaining a stable and contamination free ion beam. Rotary as well as turbo molecular pumps are also used for this purpose. Different electric and magnetic quadrupole lenses [3] are used to focus the beam on the target with required spot size. The ECR facility has been utilized for 60 keV Ar^+ ion irradiation of $\text{TiO}_2(110)$ single crystals. Several fluences between 1×10^{15} and 1×10^{19} ions/cm² have been used for irradiation.

2.1.3 Electrodeposition

Electrodeposition is an electrochemical process where a material gets deposited on the surface of a conductive substrate. This is a low cost, high throughput and scalable technique [5] which has been practiced for a century to grow thin films for achieving corrosion protection of many metal and metallic alloy surfaces. Electrodeposition technique was first developed by an Italian scientist, Luigi V. Brugnatelli in 1805 [4]. He successfully electrodeposited gold on a conducting surface from a dissolved gold solution. Later on, this technique has been improved many-folds and is now widely used in metal plating, decorative coatings etc..

Working Principle

Fig. 2.3 displays the electrodeposition process. The electrolyte solution is taken in an electrochemical cell. Three electrodes assembly, submerged in the solution, are used for deposition. These are the Working Electrode (WE), the Reference Electrode (RE) and the Counter Electrode (CE). The growth of the desired material takes place at WE. The potential at the WE is controlled by RE. To complete the current path inside the solution, a third electrode, CE is required. The charge carrier migrates between CE and WE. The motion stops at the surface of the electrode where the charged species deliver their charges via redox reactions. The electrolyte solution may contain many charge species. Out of them, the desired ion will reach WE and will get deposited after charge transfer. This can only be possible at a particular potential, applied to WE. The rate of the deposition primarily depends on factors like concentration of charge carriers, separation between WE and CE and rotation speed of the stirrer. The electrodeposition can be carried out via two modes: Galvanostatic or Potentiostatic. In galvanostatic mode, current between the WE and CE is maintained at a constant value. On the other hand, the potential at WE is kept fixed for potentiostatic mode.

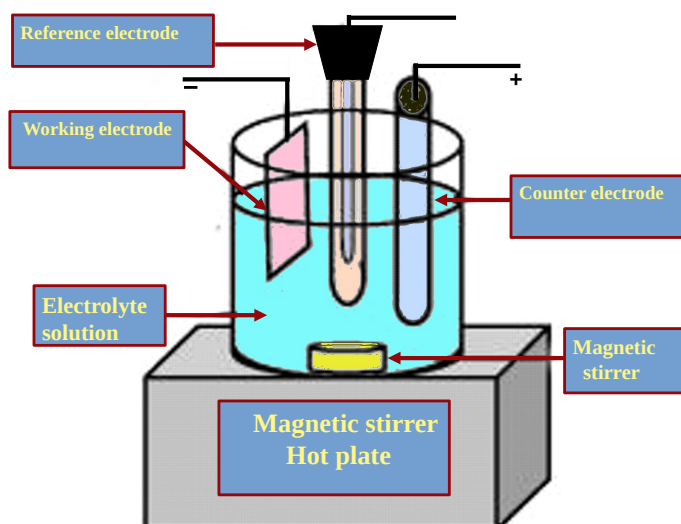


Figure 2.3: Schematic diagram of electrodeposition set up [5].

In the present thesis, ZnO and hybrid $\text{Cu}_x\text{O-ZnO}$ nanostructures have been grown

on transparent conducting indium tin oxide (ITO) by using potentiostatic mode. A three electrode electrochemical configuration has been assembled with a Pt sheet as CE, Ag/AgCl as the RE and ITO as WE. The electrolyte solution is of aqueous nature. It is prepared with the required precursor ions in distilled water. The Autolab PGSTAT 302N system was utilized for electrodeposition.

2.1.4 Chemical synthesis process

The Chemical synthesis processes provide usually simple routes to achieve a variety of materials with interesting properties. Such processes involve chemical reactions of the reactants. These methods can also be tuned to provide nanostructured materials for many fundamental and applied research work. The chemical reactions can occur in two modes. There are reactions which start spontaneously when the reactants come in contact whereas for non-spontaneous case, energy in the form of heat, pressure etc. is required to start the reaction. Chemical synthesis process is usually performed in an aqueous or alcoholic solution containing the reactants. The end product is the precipitate which is filtered out to get the required material. In the present thesis, CuO-TiO₂ composite structures have been synthesized using this method.

Hydrothermal method is a type of chemical synthesis process which occurs under a given temperature and pressure. This is a well known process for fabricating metal oxide nanostructures. A typical hydrothermal process is carried out in a sealed reactor. This reactor is filled with a precursor solution, prepared in distilled water. The solution contains the metallic cations, whose oxide phase is to be grown. The temperature is set to below 100°C. Pressure within the sealed vessel is developed automatically and rises with reaction temperature. The self-developed pressure also depends on the concentration of dissolved salts and percentage fill of the vessel [6, 7]. In the present thesis, ZnO nanorod arrays have been grown on ITO and Si substrate using this method.

2.2 Characterization Techniques

2.2.1 Electrochemical Techniques

Electrochemistry is a branch of analytical chemistry where the electron transfer mechanism between an electrodes and the reactant molecules is studied. Different electroanalytical techniques such as potentiometry, coulometry, voltammetry and amperometry have been developed for analyzing the electrochemical reactions. Among them, voltammetry and amperometry are two widely used techniques in the field of electrochemical sensors, energy storage devices and electrocatalysts. These are actually family of techniques among which Cyclic voltammetry and Chronoamperometry method have been utilized in the present thesis work. Here, we briefly discuss about them.

(i) Cyclic voltammetry (CV)

The term ‘Voltammetry’ was first introduced by I. M. Kolthoff and H. A. Laitinen in 1940. Cyclic voltammetry (CV) is a versatile and inexpensive voltammetry technique which offers valuable information about the kinetics and thermodynamics of a redox process [8]. This technique was discovered by Randles and Sevsick in 1938 [9]. In CV technique, the potential (E) at the WE is varied w.r.t time and the corresponding current response is measured. A cyclic voltammogram is plotted as current vs. potential. Figure 2.5 shows a typical cyclic voltammogram of a reversible redox system. The potential at the WE is ramped linearly with time from a preset value. After reaching a desired end potential value, the ramp is inverted and the potential of WE goes back to the initial value. The excitation signal forms a triangular (E-t wave) curve as shown in Fig. 2.4. The duration of a complete cycle is usually chosen between 1 ms to 100 s. The cycle may be repeated many times if needed. As displayed in Figure 2.5, the oxidation and reduction reactions occur in forward and reverse scans, respectively. The oxidation reaction is represented by the anodic peak current (I_{pa}) and the peak potential (E_{pa}). Similarly, the cathodic peak current (I_{pc}) and the peak potential (E_{pc}) indicate the reduction reaction.

All the voltammetric studies are conducted within an electrochemical cell consist-

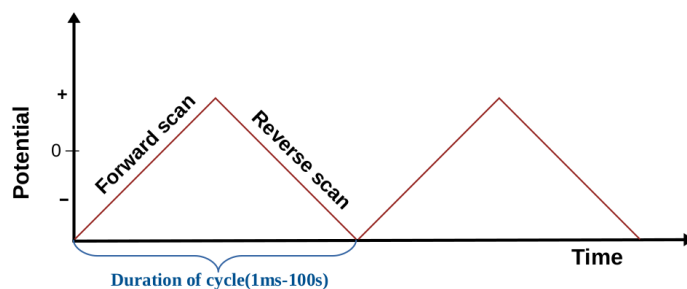


Figure 2.4: Variation of Excitation potential during CV experiment.

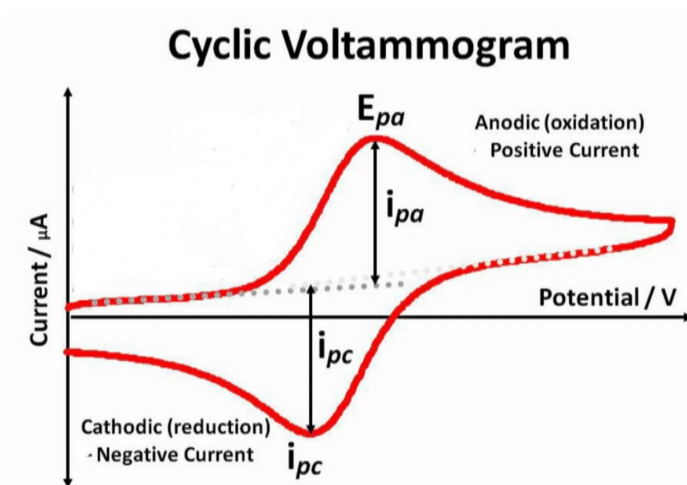


Figure 2.5: A typical illustration of cyclic voltammogram for a reversible electrochemical system [10]).

ing of a three electrode assembly (fig. 2.6(b)). The redox process occurs at the WE. In the present thesis, the glucose sensing experiments using ZnO and TiO₂ nanostructures, have been performed utilizing CV technique in Autolab PGSTAT 302N electrochemical workstation. The system is shown in Fig. 2.6(a) with a chemical cell set up (Fig. 2.6(b)). The glucose sensing measurements were carried out at room temperature within a potential window of -0.3-0.8V. CV were recorded at scan rate of 10 mV/s in an unstirred 20 ml of 0.1 M NaOH solution.

(ii) Chronoamperometry (CA)

In Chronoamperometry (CA) technique, the current response of the WE is measured with time at a fixed applied potential. The plot of current vs. time is called the chronoamperogram. In the present thesis, the chronoamperometric technique has



Figure 2.6: (a) PGSTAT 302N Autolab electrochemical workstation with a chemical cell set up and (b) Schematic diagram of the electrode arrangement within the chemical cell.

been used in glucose sensing experiments. The potential was fixed at ~ 0.4 V and the chronoamperogram was recorded in a stirred 20 ml of 0.1 M NaOH solution.

2.2.2 Scanning Probe Microscopy (SPM)

Scanning probe microscopy (SPM) [11] is a family of techniques which are able to produce high resolution images of surface topography. The imaging can be done by mechanically scanning the probe back and forth over the surface and recording the probe surface interactions. Since the working principle of SPMs are based on the probe surface interaction, it is altogether a different technique in comparison to the optical microscopy. It is a well known fact that the resolution of the conventional optical microscope is diffraction limited which cannot probe features of a surface down to a few nanometers. This is the reason why SPM techniques have become much relevant today. A variety of SPM techniques have been developed over a period of time depending on the probe surface interactions. Here, we make a list of all the SPM techniques and corresponding probe surface interactions.

Techniques

1. Scanning Tunneling Microscopy (STM)
2. Atomic Force Microscopy (AFM)

Interaction involved

- Tunneling current
- van der Waals force

3. Magnetic Force Microscopy(MFM)	Magnetic force
4. Electrostatic Force Microscopy(EFM)	Electrostatic force
5. Conducting Atomic Force Microscopy(CAFM)	Tunneling current
6. Piezoresponse Force Microscopy (PFM)	Electromechanical coupling

The first member of SPM family is Scanning Tunneling Microscopy (STM) which was invented by H. Rohrer and G. Binnig in 1981 at IBM Zurich [12]. The importance of their discoveries was acknowledged soon and they were awarded Nobel Prize in 1986. This remarkable invention was followed by the development of many other related techniques such as AFM, MFM etc..

Atomic Force Microscopy(AFM)

After the invention of STM, Binnig and his colleagues developed the second member of the SPM family viz. the Atomic Force Microscopy (AFM) in 1986 [13]. It is the most versatile and useful extension of the SPM family. In AFM technique, a sharp tip (fig. 2.8) is used to probe the surface topography. The tip is usually made of silicon or silicon nitride and attached to one end of a elastic cantilever. The length of the cantilever is usually 100-200 μm . The radius of curvature of the tip is usually between 10-30 nm.

AFM set up is shown in fig. 2.7 and fig. 2.8. The main parts of AFM are head, scanner and base. The head consists of a tip-holder arrangement along with a fitted laser. The sample is mounted on a piezoelectric scanner made of Lead Zirconium Titanate which can move in x and y directions. The base contains the electronics for operating the scanner in all the possible directions. During scanning, the tip is brought close enough (few nm) to the surface so that it can feel the interactive forces which cause deflection in the cantilever. This deflection can be recorded via position sensitive photo detector. A constant deflection in the cantilever is maintained by the feedback loop, programmed in the electronics of AFM instrument. When the feedback loop is switched on, it tries to maintain the tip-sample force to a pre-determined value. This is the constant force mode where a topographical image of a surface can be

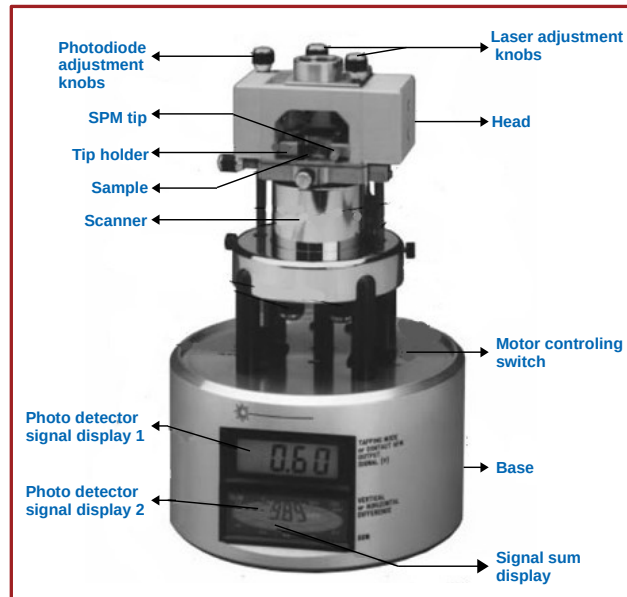


Figure 2.7: AFM set up at IOP

generated. There is another mode of operation, called constant height or deflection mode where feedback is not needed. This mode is helpful for imaging nearly flat surfaces.

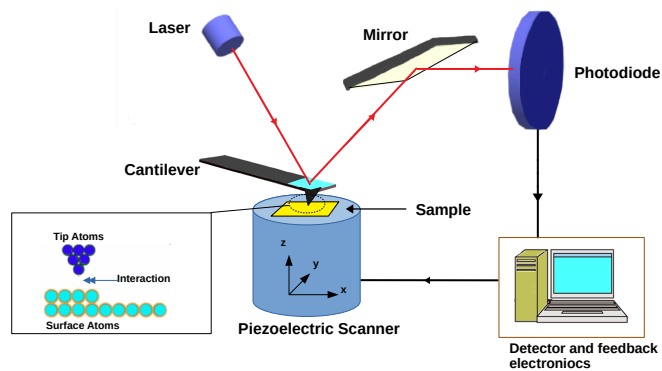


Figure 2.8: The schematic representation of the AFM operation

The deflection of the cantilever depends on the strength of tip-surface interaction. This can be qualitatively explained by considering a short range repulsive and long range van der Waals attractive interactions. Fig. 2.9 exhibits the force-distance curve for two atoms interacting via Lennard-Jones potential which takes into account both these interactions. The Lennard-Jones potential can be expressed as:

$$F(r) = -\frac{A}{r^7} + \frac{B}{r^{13}} \quad (2.1)$$

Here, A and B are constants. r is the tip-sample separation.

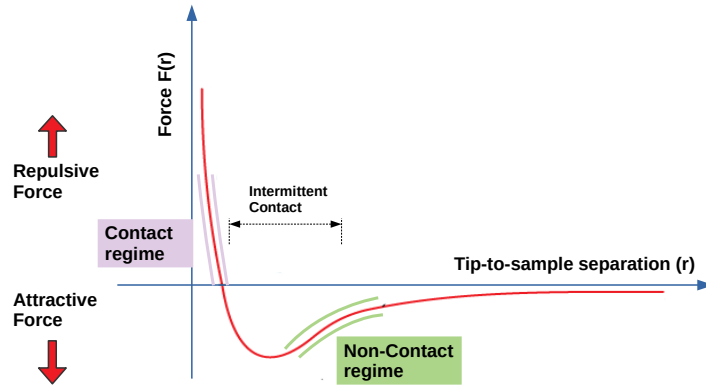


Figure 2.9: Force (F) versus Distance (r)

The first term of the expression represents the long-range attraction caused by a dipole-dipole interaction whereas the second term demonstrates the short range repulsion obeying the Pauli's exclusion principle. The nature of the force in different distance regimes is shown in the Fig. 2.9. Depending on the tip-surface distance, the AFM can be operated in three different modes. These are briefly discussed below.

(i) Contact Mode

In contact mode, the probe physically touches the sample [14]. The tip, made of silicon nitride (low spring constant) is used for scanning hard surfaces. However, this mode is not suitable for soft surfaces [14] (e.g. biological samples) where the repulsive force is strong enough to cause deformation. This mode is capable of recording images in liquid environment and works well in high speed measurements.

(ii) Non-contact or attractive mode

In non-contact mode, the sample surface is scanned by a vibrating cantilever. The AFM tip operates in the attractive force regime (fig. 2.9). It is far away from the repulsive force regime which makes the non-contact mode a truly non-invasive technique.

Hence, this mode is suitable for making measurements on soft surfaces. However, the image resolution is poor in comparison to the contact mode. The cantilever used in this mode is made of silicon having a high spring constant. In non-contact regime, the attractive force is very weak in comparison to repulsive force in contact regime. The weak attractive force can easily influence the oscillation of a cantilever. Therefore, the tip is subjected to a small oscillation to detect the weak attractive forces by measuring changes in the oscillating parameter.

(iii) Tapping mode or intermittent contact mode

In case of tapping mode operation, the tip is brought close enough (a few nanometer) to the surface so that it can barely hit or tap the surface. As seen in fig. 2.9, the tip operates in between the repulsive and the attractive force regime. This is the reason for naming it also as intermittent-contact mode [14]. The soft samples which may either be damaged in the contact mode or difficult to obtain good resolution in the non-contact mode, can easily be scanned in the tapping mode with high resolution. The cantilever is subjected to an oscillation (frequency: 50-500 kHz) using a piezoelectric crystal. When the probe approaches the surface, state of the oscillation changes due to the strong tip-surface interaction. In tapping mode operation, the change in amplitude is monitored to probe the surface topography. The amplitude of the oscillation is in the range of 100-200 nm which is automatically set and maintained by a feedback loop. During scanning, if the tip passes over a bump, its amplitude of oscillation decreases. Reverse phenomenon occurs when the tip goes over a depression. The change in amplitude is detected and the digital feedback loop is activated which maintains the tip-sample separation. The vertical movement of the piezo scanner is recorded which will provide the morphological images. The present mode is inherently capable of overcoming the tip-sample adhesion force.

In the present thesis, multimode AFM (Nanoscope V, Bruker) was used for acquiring 2D and 3D topographic images in the tapping mode. These images have been analyzed using Nanoscope 1.6 software.

Conductive atomic force microscopy (c-AFM)

Conductive atomic force microscopy (c-AFM) is a popular, widely used extension of the AFM which measure the localized current with a high resolution. The topography and the current distribution of a surface can simultaneously be measured by a nanometer-scale conductive probe. The conducting probe is usually made of silicon material with a thin conducting coating of Platinum-Iridium. The c-AFM can measure current in the range of picoamps (pA) to nanoamps (nA). The working principle of c-AFM is similar to Scanning Tunneling Microscopy (STM). In both cases, the tunnelling current is measured by applying a potential between the probe and sample surface. With the help of the c-AFM technique, the variation in conductivity across the grain boundaries can also be identified. Moreover, this technique is useful in tracking conducting paths and micro shunts in a sample.

In the present thesis, the c-AFM measurements were carried out using PARK XE-7 system. A Pt/Ir tip with radius of curvature of 40 nm was used to measure the conductivity profile of the surface. The bias voltage at the tip was swept back and forth from a low to a high potential value. The corresponding I-V data was recorded which provided the conductivity map of the surface.

2.2.3 Electron Microscopy

Electron microscopy techniques provide powerful avenues for investigating morphology and microstructural nature of any material [15, 16]. As optical microscopy is limited in assessing the dimensions shorter than the wavelength of visible light, electron microscopy through the usage of high energetic electronic beam was as immensely significant development for probing nano and sub-nano dimensions. Two important members of the electron microscopy family are Field Emission Scanning Electron Microscopy (FESEM) and Transmission Electron Microscopy (TEM) which are discussed below.

Field Emission Scanning Electron Microscopy (FESEM)

Field Emission Scanning Electron Microscope (FESEM) is a versatile, non-destructive electron microscopy technique which is used for surface topography and elemental analysis. The first instrument was developed in 1937 by Manfred Von Ardenne [17].

Since then, extensive developments have been undertaken to enhance the efficiency and ease of operation with automated controls.

In FESEM, a finely focused electron beam (energy ~ 30 keV) scans the sample surface. The system is operated in high vacuum condition (10^{-6} torr) and can produce 1,00,000 times magnified image of the probed surface. The resolution of the system can reach upto a fraction of a nm. When an energetic electron beam strikes a sample surface, it undergoes a series of elastic and inelastic collisions. Secondary electrons, emitted from these interactions are used in FESEM for imaging sample surface.

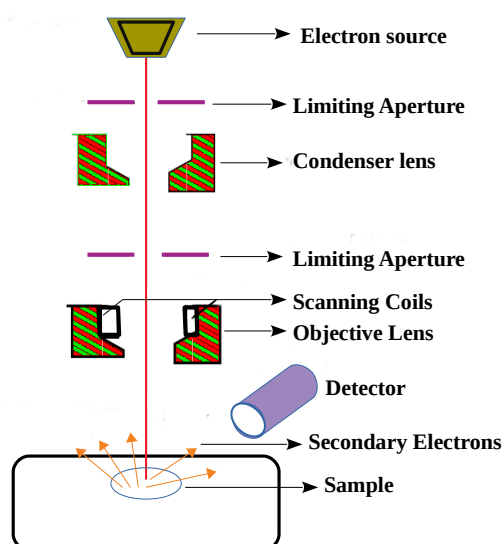


Figure 2.10: Schematic representation of experimental setup of FESEM

The schematic diagram of the set up is shown in fig. 2.10. The main components of the microscope are electron gun, electromagnetic aperture, magnetic lens, scanning coils, electrostatic lens, sample stage, detectors, display and data acquisition devices. The electron gun consists of a thin wire of lanthanum hexaboride (LaB_6) having tip radius of 10 nm. A high electrical potential gradient pulls the electron from the emitter and the beam is nearly 1000 times narrower than produced from conventional thermionic guns. The electron beam generated from the source is guided and simultaneously accelerated towards the sample by a combination of electromagnetic lens and apertures. The thin and focused electron beam is then deflected by the scan coils

and objective lens so that the beam can scan the surface.

Energy-dispersive X-ray spectrometry (EDX) is an analytical technique which is utilized for elemental mapping or chemical characterization of a sample. Characteristic X-rays are emitted when an energetic electron interacts with the material. An energy dispersive spectrometer fitted in FESEM system can measure the number and the energy of the X-ray photons. As the emitted X-rays are the characteristic feature of a particular electronic transition in an atom, they reveal elemental information of the specimen.

In the present thesis, two different instruments have been used. They are Carl Zeiss-make FESEM and FEI-ESEM (Environmental Scanning Electron Microscope) Quanta 200. The Carl Zeiss FESEM has schottky thermal field emitter electron source which works with an acceleration voltage of 0.02-30 kV. The FEI ESEM has a tungsten emitter which also works in the similar accelerating voltage range.

Transmission Electron Microscopy (TEM)

Transmission electron microscopy (TEM) [18, 19] is an important member of the electron microscopy family which is widely used for studying structure, orientation, microstructure and composition of a material [20,21]. Like other electron microscopes, it also uses energetic electron beams. At an energy of 200 keV, a typical energy used in TEM, the electron beams will have a de Broglie wavelength of 0.025 \AA . However, due to the aberrations in the electromagnetic lenses, the resolution is limited to 1-2 \AA . The first TEM was developed by two German scientists, M. Knoll and E. Ruska, in 1932 [22].

A typical TEM set up has three sections: illumination system, objective lens and imaging system. The illumination section consists of the electron source, the acceleration column and the condenser lenses. In TEM, the field emission gun (FEG) with LaB_6 crystal filament is used for the electron emission. The main job of the illumination system is to produce a focused electron beam which has to pass through a thin sample. The specimen should be thin enough ($<100 \text{ nm}$) such that a large number of incident electrons can easily pass through the sample. With the help of the intermedi-

ate lenses and the projector lenses, a magnified image can be formed on the phosphor screen, kept below the sample stage. The final image or the diffraction pattern is recorded by a photographic film or a charge coupled device (CCD) which is coupled to the system computer for further analysis. A high vacuum condition (10^{-8} mbar) is maintained during TEM operation. Two types of data can be extracted from TEM instrument: the morphological images and the electron diffraction patterns. In TEM images, the darker areas imply a denser region whereas lighter regions of the image represent a thinner or less dense zone of the sample. The diffraction mode of TEM is used to study the crystalline nature of the specimen. This technique is analogous to X-ray diffraction. Electron diffraction from a single crystal will produce spot patterns whereas a larger grain poly-crystal will generate a ring pattern. A high-resolution TEM (HRTEM) imaging technique is another important tool which is widely used to measure the lattice spacing. This technique is also helpful in investigating defect structures in a lattice.

Sample preparation for TEM

TEM analysis can be performed on powdered and film samples. Two separate procedures have to be followed to prepare the samples for characterization. For investigating a film specimen, its thickness should be less than 100 nm and even smaller (<50 nm) for HRTEM analysis. These thin film samples can be characterized by either Cross-sectional TEM (XTEM) or planar TEM techniques. The XTEM technique can examine the interfaces as well whereas planar TEM is used to probe the surface morphology. For doing XTEM analysis, the specimen is thinned by employing methods like disc cutting, mechanical polishing, dimple grinding and ion-beam etching. To analyse a powder sample, it is dispersed in acetone and put onto a Cu grid. The grid is then placed directly into the chamber for performing TEM experiment.

In the present thesis, two different TEM systems have been used. They are from JEOL and FEI Tecnai. The JEOL TEM is equipped with a LaB₆ electron gun and a charge coupled-device (CCD) based detector (Model 832, Gatan Inc.). The point-to-point resolution of this system is 0.19 nm, and lattice resolution is 0.14 nm at 200 keV electron energy. The FEI TEM is operated at 300 kV and is equipped with a

Gatan Orius CCD camera and Fischione 3000 high angle annular dark field (HAADF) detector. The system has a 0.20 nm point-to-point resolution.

2.2.4 X-Ray Diffraction (XRD)

X-Ray Diffraction (XRD) is a widely used technique for investigating the structure, unit cell dimensions, phase identification and crystalline nature of a material. Monochromatic X-rays with photon energies in the range of 10-100 keV can penetrate well below the surface of a material to provide information about the crystalline structure of the material. When a beam of energetic X-rays strikes a material target, the incident beam is scattered by the electron clouds of the atoms. Depending on the geometry of the atomic arrangement, constructive or destructive interference occurs. Constructive interference obeys the Bragg's diffraction criterion [23];

$$2d\sin\theta = n\lambda \quad (2.2)$$

Here d , θ and λ are the inter-planar spacing, angle of incidence and wavelength of the incident X-ray photon, respectively. n is an integer representing the order of diffraction

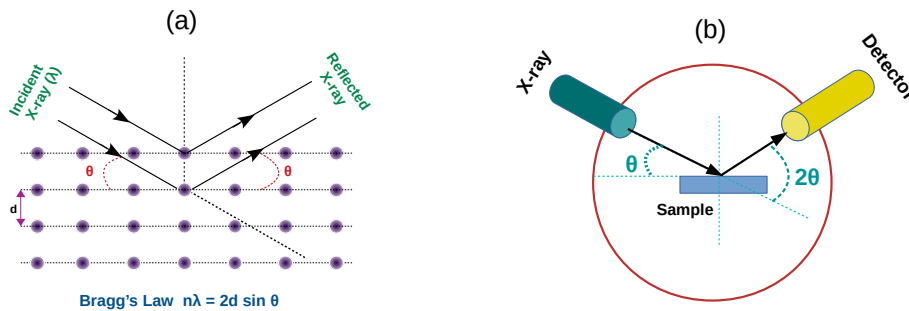


Figure 2.11: The schematic diagram displaying (a) the Bragg's diffraction in single crystal and (b) X-ray diffractometer setup.

As shown in Fig. 2.11(a), a path difference of $2d\sin\theta$ is created between the incident and the reflected X-rays. All specularly reflected rays will combine constructively in phase if the path difference is a multiple of the wavelength of the incident X-ray. The use of the glancing angle θ is conventional in X-ray crystallography rather than

the angle of incidence. Each peak in the diffraction pattern can be assigned to a set of planes which is labeled by Miller indices. The schematic diagram of XRD process is illustrated in Fig . 2.11(b). XRD instrument primarily consists of a goniometer, X-ray source and a detector. The X-ray source and the detector are rotated in the θ and 2θ planes, respectively, to collect the interfered beam from all the possible directions. The width of a diffraction peak provides an estimation of the average crystallite size which can be calculated by Scherrers formula [24],

$$D = \frac{k\lambda}{\beta \cos \theta} \quad (2.3)$$

Here D and λ are the crystallite size and wavelength of the X-ray, respectively. Full width at half maximum (FWHM) of the diffraction peak is denoted by β . k is a dimensionless shape factor.

In the present thesis, XRD data was recorded on a Bruker D8 Discover system. The X-ray source of this system produces Cu-K α ($\lambda=0.154059$ nm) radiation and a scintillation counter is used as the detector. The operating voltage of the X-ray source is 40 kV. The geometry of the X-ray diffractometer is structured in such a way that the θ - 2θ angular relationship between the source and the detector (see fig. 2.11(b)) is always maintained. The system can operate in a wide-ranging step sizes and has a continuous scan capability.

2.2.5 Raman Spectroscopy

Raman spectroscopy is associated with the phenomenon of inelastic scattering of light with matter. This is one of the most versatile and non-destructive spectroscopic technique which has some distinct advantages such as simple operation, easy sample preparation and possibility to carry out experiments at normal ambient conditions. Raman spectroscopy is an important technique that is used to investigate the vibrational modes of molecules. Being highly sensitive to the physical and chemical properties of matter, this technique can be utilized in determining the composition, the phase and the crystallinity of the semiconductor materials. Raman effect was first discovered by Prof. C. V. Raman in 1930.

As seen in Fig. 2.12, a molecule can be excited from its ground electronic state to

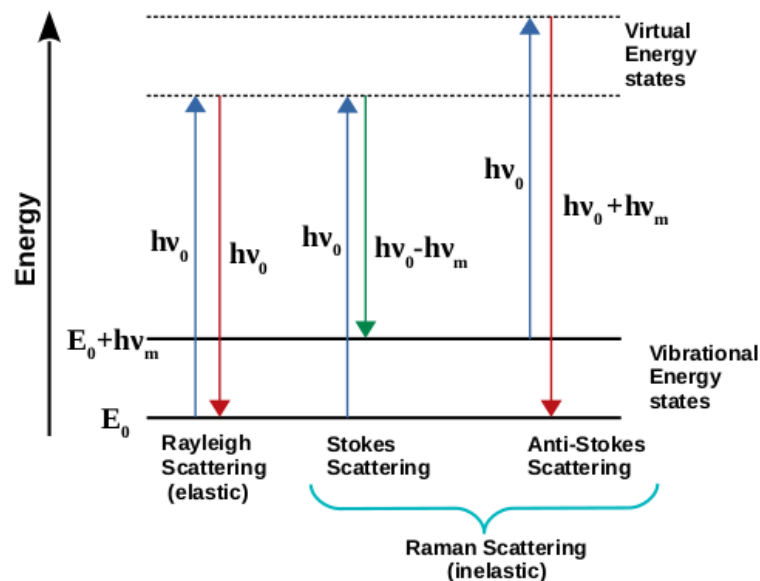


Figure 2.12: Schematic diagram of vibrational energy level demonstrating three types of scattering phenomena; Raleigh and Raman (Stokes and Anti-Stokes) scattering

a virtual state by absorbing photons. Much of the time, the molecule relaxes back to its ground state leading to elastically scattered photon having same frequency as the incident photon. This is known as Rayleigh scattering. For an inelastic scattering process, the molecule relaxes back into a vibrational level different than from where it had originated. Thus, there is a frequency difference between the incident and scattered photons, which is known as Raman shift. Since the shift is an inherent property of a particular molecule under study, it does not depend on the excitation frequency. The number of Raman scattered photons is very small in comparison to the number of incident photons (approximately 1 in 10^7). This results in a weak intensity of Raman line compared to the Rayleigh line. For a transition to a higher vibrational state, the scattered photons are shifted to the longer wavelengths whereas for a transition to a lower state, the shift is towards the shorter wavelength side. The former is known as the Stokes scattering while the latter as the anti-Stokes scattering. Figure 2.12 shows the schematic diagram representing the three scattering processes: Rayleigh scattering, Stokes and anti-Stokes Raman scattering.

The origin of Raman scattering process can be explained with the help of a classical theory of scattering. Let us consider a monochromatic light of frequency, ν ,

propagating in a particular direction. The amplitude of oscillating electric field, E , at any time, t , can be expressed as [25]:

$$E = E_0 \cos 2\pi\nu t \quad (2.4)$$

Here, E_0 is the maximum amplitude of the electric field. Let us consider a diatomic molecule for representing a material. If the molecule has a natural frequency of vibration, ν_0 , the nuclear displacement (q) can be written as,

$$q = q_0 \cos 2\pi\nu_0 t \quad (2.5)$$

Here, q_0 is the amplitude of the vibration. When the electromagnetic field of the incident photon interacts with this molecule, a dipole moment, P , is induced which is given by,

$$P = \alpha E = \alpha E_0 \cos 2\pi\nu t \quad (2.6)$$

Here, α is polarizability. For small vibrations, α can be written using Taylor's series expansion as:

$$\alpha = \alpha_0 + \left(\frac{\partial \alpha}{\partial q} \right)_0 q + .. \quad (2.7)$$

α_0 demonstrates the polarizability at the equilibrium position and $\frac{\partial \alpha}{\partial q}_0$ is the rate of change of α w.r.t q , calculated at the equilibrium position. Due to the small vibrations, α can be considered as a linear function of q and the series can be terminated by keeping only linear terms.

Combining all the previous equations, we have

$$P = \alpha E_0 \cos 2\pi\nu t \quad (2.8)$$

$$= \alpha E_0 \cos 2\pi\nu t + \left(\frac{\partial \alpha}{\partial q} \right)_0 E_0 q_0 \cos 2\pi\nu t \cos 2\pi\nu_0 t \quad (2.9)$$

$$= \alpha E_0 \cos 2\pi\nu t + \frac{1}{2} \left(\frac{\partial \alpha}{\partial q} \right)_0 E_0 q_0 [\cos 2\pi(\nu - \nu_0)t + \cos 2\pi(\nu + \nu_0)t] \quad (2.10)$$

The first term in the expression represents Rayleigh scattering of frequency ν . The second and third terms correspond to Stoke (frequency = $\nu - \nu_0$) and anti-Stoke (frequency = $\nu + \nu_0$) Raman scattering, respectively. Notably, if the polarizability

becomes independent of the displacement, q , the second term in the equation 2.9 vanishes and the particular vibration will be Raman inactive.

In the case of Rayleigh scattering, the frequency as well as the energy of the radiation remain unchanged after scattering. If the collision is inelastic, the scattered photons may either gain or lose energy. The difference in energy corresponds to the energy of the molecular vibration. The intensity of Rayleigh scattering however, is much higher than that of Raman scattering. Therefore, in order to observe Raman lines, the Rayleigh peak should be cut off from the spectrum. In a typical experiment, Raman spectrum is recorded as the scattered light intensity vs. Raman shift. Raman shift is measured as the wave number difference of the scattered photon and the incident photon.

In the present thesis work, Raman investigations were carried out using T64000 Horiba Jobin Yvon triple monochromator system having a liquid nitrogen cooled Charged Coupled Device (CCD) detector as shown in fig. 2.13. The measurements were performed at room temperature using a back-scattering geometry. Two lasers are attached with the Raman system for excitation: Argon (Ar) ion laser and helium cadmium (He-Cd) laser. The laser lines of 488 nm and 514.5 nm from Argon laser and 325 nm from He-Cd laser were used for acquiring Raman data.

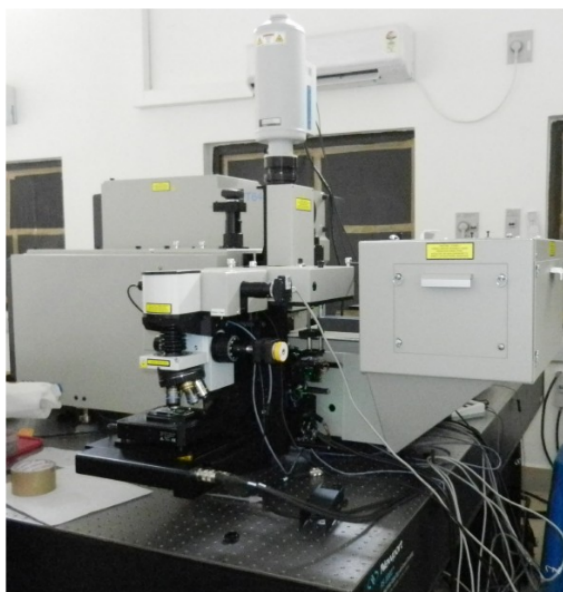


Figure 2.13: Raman set-up at IOP.

2.2.6 UV-Vis Spectroscopy

UV-Vis spectroscopy is an important characterization technique which is widely used for investigating the optical properties of materials. This technique measures the attenuation of radiation when it passes through a sample. The absorption of radiation will be governed by the electronic transitions occurring between different molecular levels of the material. In a molecule, overlapping of atomic orbitals create different molecular orbital levels. The lower energy levels are the bonding orbitals while the higher energy orbitals are the anti-bonding orbitals. Three different types of bonding orbitals can be formed: σ , π and n . The two anti-bonding orbitals are σ^* and π^* orbitals. Different types of allowed transitions among these orbitals are displayed in the schematic diagram (fig. 2.14).

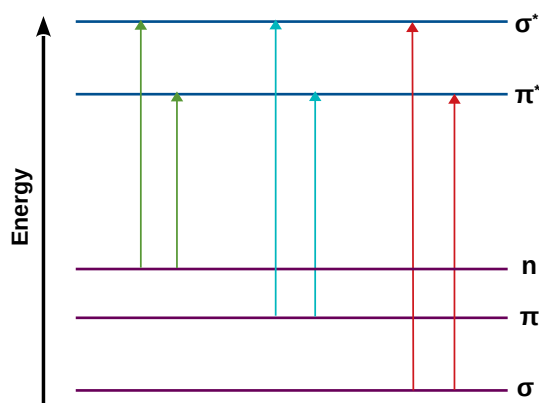


Figure 2.14: Molecular energy level diagram and all possible transition.

The wavelength at the maximum absorption and the extent of absorption can provide valuable information about the structure of the molecule and the amount of a particular absorbing species, respectively. The proposition of the absorption is based on two laws as follows:

(a) Beer's Law : According to Beer's law, the rate of decrease of the intensity of a radiation with the concentration of the absorbing medium is directly proportional to the intensity of the incident light.

(b) Lambert's law : According to Lamberts law, the rate of decrease of the inten-

sity of a radiation with the thickness of the medium is proportional to the intensity of the incident light.

These two laws are combined together to formulate a new expression which can provide quantitative measurement of the absorbing species within a substance. This form is known as the 'Beer-Lambert Law' [26] which is given as:

$$A = \epsilon_{\lambda}lc = \alpha l \quad (2.11)$$

Here, A is the absorbance or extinction coefficient, ϵ_{λ} is the molar absorptivity constant at a wavelength λ , l is the path length of the substance, c is the concentration of the analyte and α is the absorption coefficient of the material. Let I_0 be the incident radiation intensity and I be the intensity of the radiation after it passes the substance. Then, the amount of absorbed radiation within the material can be measured by estimating the transmittance (T) as follows:

$$T = \frac{I_0}{I} \quad (2.12)$$

$$\%T = 100T \quad (2.13)$$

$$A = \log T \quad (2.14)$$

$$A = 2 - \log \%T \quad (2.15)$$

Here, both the quantities T and A are unit less. There are a few restrictions on using the Beer-Lambert law. Firstly, the sample must be homogeneous and does not interact with the incident irradiation. Secondly, the incident radiation must be monochromatic in nature. In case of analytes in a matrix (e.g. solution, glass etc.), the absorption may be governed by the strong interactions between the absorbing species and the incident radiation. For this reason, the absorber concentration must be kept very low to avoid possible interactions.

Electronic Bandgap measurement

In a semiconducting material, the conduction band is separated from the valence band by an energy gap which is known as the band gap. The electrons from the

valance band can make transition to the conduction band by absorbing radiation of energy equal to or larger than the band gap energy (E_g). The band gap E_g is usually evaluated using Tauc plot method [27]. In this technique, the relation between the band gap and the absorptivity of a substance can be expressed as:

$$\alpha h\nu = A(h\nu - E)^n \quad (2.16)$$

Here, the constants α and A are related to the absorbance of the material. The nature of transition is determined by the exponent n which takes the following values [28]:

- $n= 1/2$ for direct allowed transitions
- $n= 3/2$ for direct forbidden transitions
- $n= 2$ for indirect allowed transitions
- $n= 3$ for indirect forbidden transitions

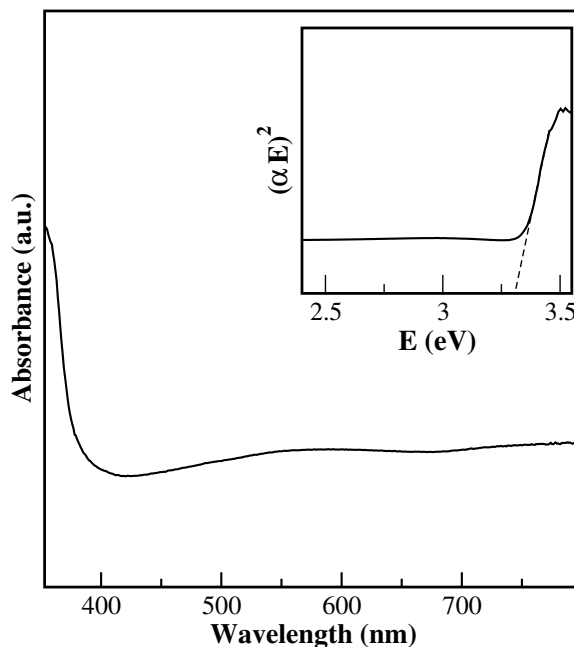


Figure 2.15: UV-Vis absorption spectra (a) and Tauc plot (b) of the ZnO nanoparticles.

To calculate the band gap, the quantity $\alpha h\nu^{1/n}$ is plotted on the ordinate with $h\nu$ on abscissa (Fig. 2.15(b)). E_g is then estimated by extrapolating the linear region in

the plot to the abscissa. A typical example of the absorbance spectra of ZnO nanoparticles is displayed in fig. 2.15(a). Tauc plot method has been utilized to calculate the band gap of ZnO nanoparticles which is observed to be 3.32 eV (fig. 2.15(b)).

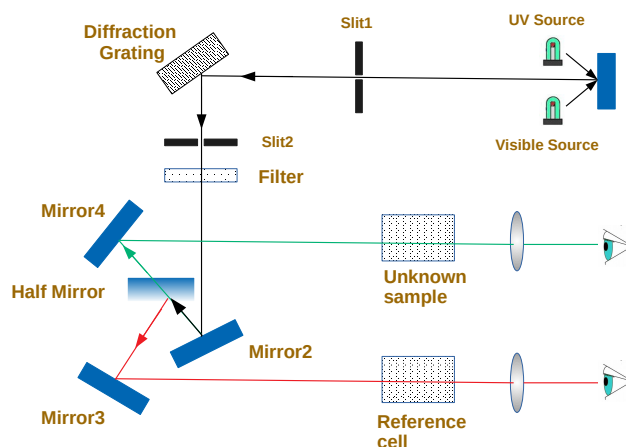


Figure 2.16: Schematic of UV-vis spectroscopy set up.

The photo-absorption spectrum is measured by utilizing a UV-Visible spectrophotometer set-up. Here, the absorption properties of a material can be measured as a function of wavelength. The schematic diagram of the system is displayed in Fig. 2.16. The instrument consists of two light sources. A deuterium arc discharge lamp and tungsten lamp are used for taking measurements in the UV and visible region, respectively. The instrument is capable of operating smoothly by swapping lamps automatically from visible to the UV. The design of the spectrometer and all its optical components are optimized so as to reject the stray light efficiently. The double beam splitter splits the incoming light from the monochromator into two separate beams. One of them passes through the sample while the other one transmits through the reference cell (Fig. 2.16). The detector detects the difference in the signal at all the wavelengths which provide the absorbance spectrum. In the present thesis, Cary 5000 spectrophotometer was utilized for UV-Visible (UV-Vis) measurements. The resolution offered by the system is 0.05 nm. Figure 2.17 shows the UV-Vis spectrometer setup at IOP.



Figure 2.17: UV-Visible set-up at IOP.

2.2.7 Photoluminescence Spectroscopy

Photoluminescence (PL) is a powerful and non-destructive spectroscopic technique which is routinely used to investigate the optical properties of a semiconductor material. This technique is also used to monitor the impurity or defect levels within a material. PL refers to the light emission from a material which is photo-excited by energetic radiation. For a typical PL investigation, a monochromatic laser (photon energy $h\nu > E_g$) is used for excitation. The electrons get excited to the conduction band by absorbing the photon energy and creates a hole in the valence band. These electron-hole pairs are then rapidly thermalized and set up a quasi equilibrium distribution. Finally, they recombine and the emitted photon is detected as photoluminescence. Time period of the whole process varies from femtosecond to a millisecond. The photoluminescence spectrum is displayed as an intensity vs. wavelength plot. From PL peak position, the band gap energy can be estimated whereas the peak intensity provides the information about the relative rates of the radiative and the non-radiative recombination processes. PL is very sensitive to the impurities and native defects.

The PL instrument consists of an excitation source (usually laser), a spectrometer and a detector. In this thesis work, a 50 mW He-Cd laser (wavelength: 325 nm) was used as an excitation source. PL measurements were carried out using T64000 Horiba Jobin Yvon triple monochromator system having a liquid nitrogen cooled UV sensitive CCD detector. PL spectra were acquired at room temperature with a

spectral resolution of 0.1 nm.

2.2.8 X-Ray Photoelectron Spectroscopy (XPS)

X-ray photoelectron spectroscopy (XPS) technique has shown tremendous applicability in studying solid surfaces. The working principle of XPS is based on the well-known photoelectric effect which was discovered by Heinrich Rudolf Hertz in 1887. In 1905, Albert Einstein [29] successfully explained the theoretical framework of the photoelectric effect using the concept of quantum mechanical interaction of light with matter. After several major improvements, Kai Siegbahn and his group in 1954 measured the first XPS spectrum of the sodium chloride (NaCl) [31]. Siegbahn was awarded the Nobel Prize in 1981 for his pioneer work [30]. XPS technique is widely used for [32–35]:

1. Compositional analysis of a surface (upto few nm)
2. Chemical state and charge state of elements in the surface
3. Quantitative analysis
4. Contamination on the surface
5. Elemental mapping and depth profiling

When an X-ray beam is incident on the surface, the energy can be absorbed by the electrons and a core electron may get ejected out. The ejection of the photoelectron will depend on the energy of the incident photon. Figure 2.18 shows the schematic of an X-ray photoelectron emission process. The binding energy (E_B) of the emitted electrons can be calculated as:

$$K_E = h\nu - E_B - \phi_s \quad (2.17)$$

Here, h is the Planck's constant. ν is the frequency of the incident radiation. K_E is the kinetic energy of the emitted photo-electron. ϕ_s is the spectrometer work function. A typical XPS system (fig. 2.19(a)) consists of X-ray source, usually Mg- $K\alpha$ and Al- $K\alpha$,

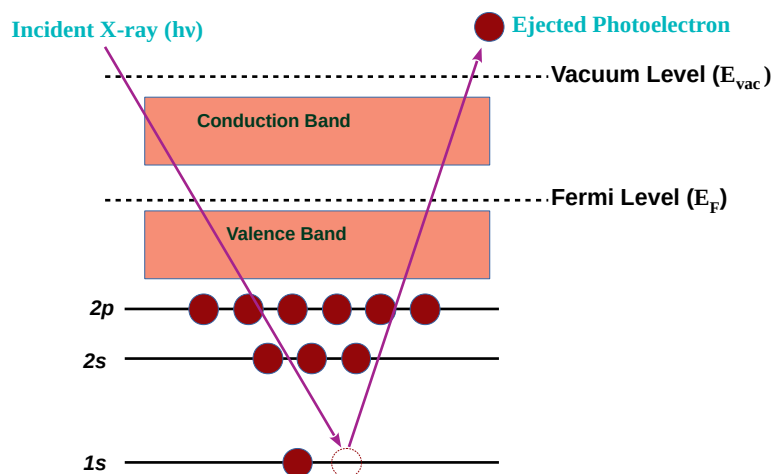


Figure 2.18: Schematic representation of X-ray photoelectron emission process

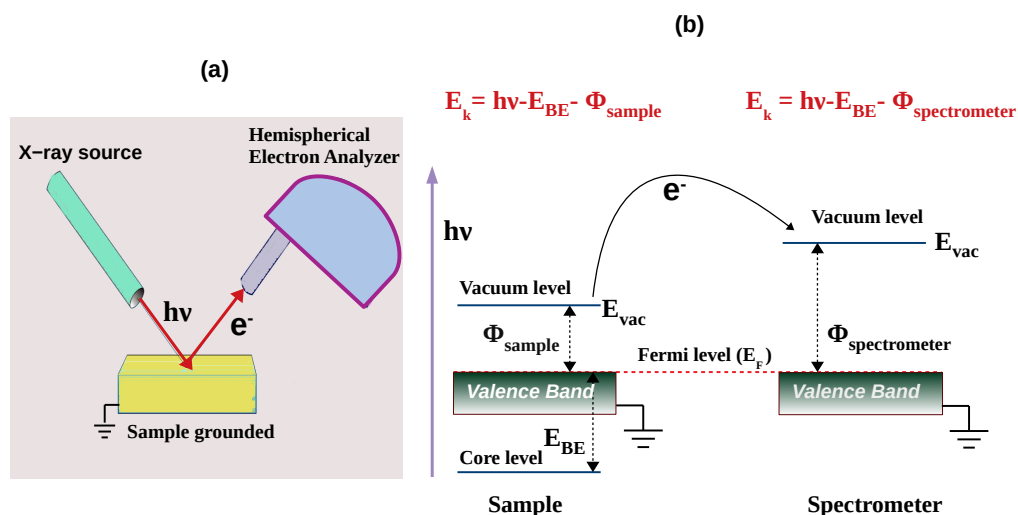


Figure 2.19: (a) Schematic representation of XPS instrument and (b) energy band diagram to calculate the Binding energy of the photoelectron

a hemispherical analyser, a manipulator for appropriate positioning of the sample and related electronics. The main system is under Ultra high vacuum conditions.

XPS is a very surface sensitive technique. Though the penetration depth of the X-ray photons is very large (few micrometer), the photoelectrons are only able to escape from the topmost surface (few nm) due to small inelastic mean free path (IMFP) of the electrons. The elastically scattered electrons produce sharp XPS peaks

corresponding to a specific electronic levels of an element whereas the inelastically scattered electrons form the background of the XPS spectrum. The appearance of XPS peak at a specified binding energy position confirms the presence of a particular element within a sample. The intensity of the peak is strongly dependent on the concentration of the element present. For a given element E in a material, the XPS photoelectron intensity (I_E) depends on its concentration (N_E) via [36]

$$I_E(\theta, x) = FS_E N_E(x) \exp\left(\frac{-x}{\lambda \cos \theta}\right) \quad (2.18)$$

Here, F, S_E and λ are the transmission function, relative sensitivity factor and IMFP of electrons, respectively. The photo-electrons are emitted from a depth x below the sample surface and at an angle θ to the surface normal.

This technique has some limitation. XPS analysis is applicable to all the elements except Hydrogen ($Z = 1$) and Helium ($Z = 2$) [34]. Further, the high-volatile samples and the materials which get easily disintegrated upon X-ray irradiation, should be avoided.

In this thesis work, two different XPS systems have been used. They are from ULVAC-PHI, INC and VG microteck. The PHI 5000 Versa ProbeII XPS instrument is equipped with a microfocused (100 μm , 25W, 15KV) monochromatic Al- $K\alpha$ source (1486.6 eV). The system operates under UHV with a base pressure of 10^{-10} torr in the analysis chamber. Initially, survey scan is done in the range of 1-1000 eV which is followed by high resolution scans for detailed analysis. The resolution of the instrument is 0.6 eV. The background correction to XPS spectra is corrected out using Shirley or linear background profile. Charge correction is performed using C(1s) reference peak. The VG microteck system is equipped with dual anode gun, Mg- $K\alpha$ (1253.6 eV) and Al- $K\alpha$ (1486.6 eV), a hemispherical analyzer, and a channeltron unit. The main chamber is maintained at a base pressure of 10^{-11} mbar. The resolution of this instrument is 0.9 eV. The system is shown in fig. 2.20.

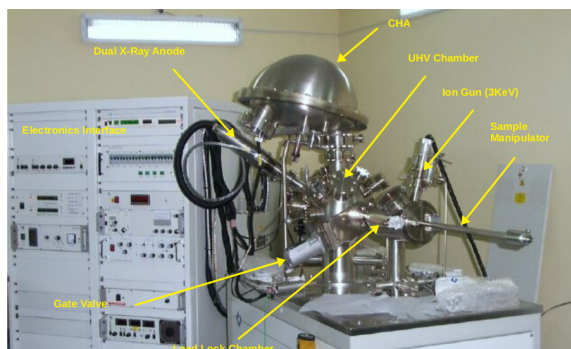


Figure 2.20: VG microteck XPS system at Institute Of Physics

2.3 Structure and properties of the materials

2.3.1 Structure of Titania (TiO_2)

TiO_2 is a wide band gap semiconductor material which has received immense attention in the field of science and technology. It was first discovered in 1791 by chemist William Gregor who found it in the form of a mineral, called ilmenite. In 1795, a German scientist, M. H. Klaproth also independently discovered this material. Titanium is found in the earth crust in the form of silicates and oxide minerals in a very small percentage. TiO_2 exhibits excellent properties in photo catalysis [37], bio-compatible implants [38, 39], photovoltaic solar cells [37, 40], waste water treatment [41], gas sensor [42, 43], memory switching devices and optical coating [44].

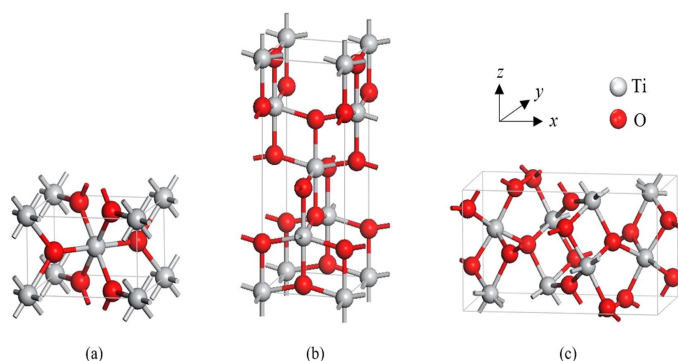


Figure 2.21: Crystal structure of TiO_2 :(a) anatase, (b) rutile, (c) brookite [48]

Titanium dioxide is a highly stable transition metal oxide which has a melting point of 1855°C . It exists in three different forms: anatase($a=b=3.782 \text{ \AA}$, $c=9.502 \text{ \AA}$),

rutile($a=b=4.584 \text{ \AA}$, $c=2.953 \text{ \AA}$) and brookite($a=5.436 \text{ \AA}$, $b=9.166 \text{ \AA}$, $c=5.135 \text{ \AA}$). The rutile and anatase have tetragonal structures while brookite has orthorhombic structure. Figure 2.21 shows the crystal structures of all the three polymorphs of TiO_2 . Each of them is made up of one Ti^{4+} and six O^{2-} atoms arranged together to form a TiO_6 octahedron [45]. The octahedron state is distorted orthorhombically for anatase and rutile. The anatase is more distorted than the rutile. The stability order for all the three phases is as follows: rutile > brookite > anatase [46]. The reported band gap values of all three phases are 3.2 eV (anatase), 3.0 eV (rutile) and 3.3 eV (brookite), respectively [47].

2.3.2 Structure of Zinc Oxide (ZnO)

Zinc Oxide (ZnO) has received enormous attention in the scientific community due to its many exciting properties such as high electron mobility, large exciton binding energy, wide band gap, excellent luminescence etc.. It is a wide direct band gap (3.4 eV) n-type semiconductor [49]. ZnO has displayed numerous interesting properties in transparent conductive oxide (TCO), piezo-electric and opto-electronic devices, solar cell and sensors [50–52]. Moreover, with exciting properties like nice bio-compatibility, strong absorption ability, high isoelectric point, non-toxicity, high catalytic efficiency and chemical stability, ZnO becomes an excellent functional material for bio-sensing applications [53, 54]. A variety of ZnO nanostructures have been fabricated in the form of nanobelts, nanowires, nanorods, nanoflowers etc.. ZnO is found in nature in the form of the mineral zincite. It has three different crystal structures: hexagonal wurtzite (WZ), cubic zincblende (ZB) and rocksalt (RS). Out of the three, the WZ structure is the most stable form at the ambient condition. ZB form is less stable and can be achieved by growing ZnO on substrates having a cubic lattice structure. In both the structures, zinc and oxygen ions are tetrahedrally arranged within the crystal. Both these structures convert to RS at high pressure (10 GPa) [49]. The three different crystal structures of ZnO are shown in fig. 2.22.

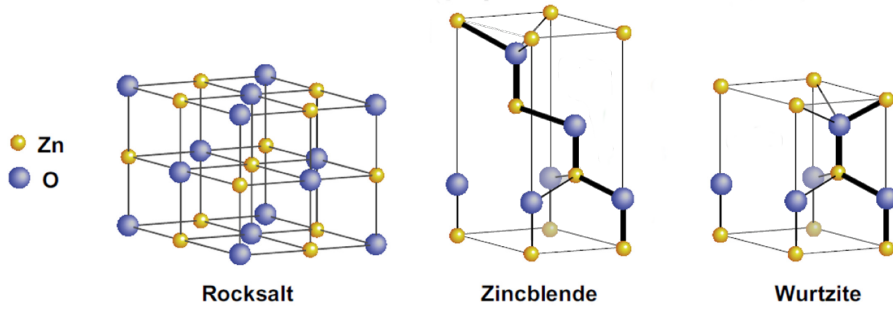


Figure 2.22: Crystal structures of ZnO:(a) cubic rocksalt (b) cubic zinc blende and (c) hexagonal wurtzite. [55]

2.3.3 Structure of Copper Oxide

Two stable oxides of copper are found in nature: Cuprous oxide (Cu_2O) and cupric oxide (CuO). They both are p-type semiconductors having a band gap of 2.0 eV and 1.2 eV, respectively. These metal oxides exhibit excellent properties in photocatalysis, photovoltaic devices, sensors [56–58], optoelectronic devices etc. [59, 62]. In addition, their non-toxic nature, low cost, appropriate redox potential, high electrocatalytic activity, high stability etc. make them promising candidates for glucose sensing application [60]. CuO and Cu_2O are found in the form of minerals cuprite and tenorite, respectively. The crystal structure of CuO is monoclinic whereas Cu_2O is cubic (fig. 2.23). In monoclinic structure, the copper atom is coordinated by four oxygen atoms in square planar configuration [61]. In cubic structure, the arrangement of Cu and O atoms are arranged in fcc and bcc sub-lattice, respectively, which are separated by a quarter along the body diagonal. The crystal structures of the Cuprous oxide (Cu_2O) and the cupric oxide (CuO) are displayed in fig. 2.23.

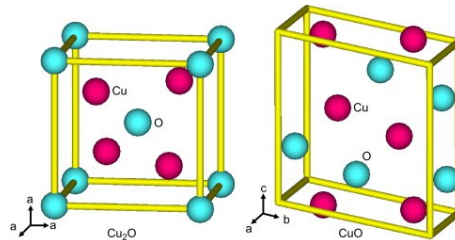


Figure 2.23: Crystallographic structures of the cubic Cu_2O lattice (a) and the monoclinic CuO lattice [63]

2.3.4 Structure of Glucose

Glucose is one of the simplest carbohydrates which is an important source of energy in all the organisms. Plants produce it via the photosynthesis process. The chemical formula of glucose is $C_6H_{12}O_6$ (fig. 2.24(b)). A glucose molecule can be categorized as: D-glucose or L-glucose. The first one is a naturally occurring glucose whereas the latter is produced synthetically. The aromatic structure of a D-glucose molecule is shown in fig. 2.24(a).

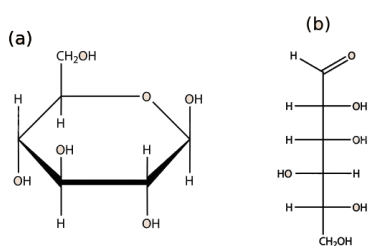


Figure 2.24: (a) Structure and (b) chemical formula of the D-glucose.

Bibliography

- [1] R.V. Stuart, 'Vacuum technology, thin film and sputtering' (Academic Press, Inc.) 1985
- [2] A. Anders, Thin solid Films, 502 , 22 (2006)
- [3] A. Mandal, D. Kanjilal, S. Kumar, and G.O. Rodrigues, Proceedings of IPAC 2011, San Sebastin, Spain
- [4] https://wikipedia.org/wiki/Louis_Valentino_Brugnatelli
- [5] I. M. Dharmadasaz and J. Haigh, Journal of The Electrochemical Society, 153, 47 (2006)
- [6] K. Byrappa, and M. Yoshimura, Handbook of Hydrothermal Technology (Norwich, New York: Noyes Publications, 2001), Chapter 2: History of Hydrothermal Technology.
- [7] R. A. Laudise, Chem. Eng. News, 65, 30 (1987).
- [8] M. Noel, K.I Vasu, Cyclic voltammetry and the frontiers of electrochemistry, 1st ed., Oxford and IBH publishing Co. Pvt. Ltd., 1990.
- [9] J. E. B. Randles, Trans. Faraday Soc., 44, 327 (1948).
- [10] <http://urrjaa.blogspot.com/2013/08/cyclic-voltammetry-urrjaa-p0110-2013.html>
- [11] R. Wiesendanger, 'Scanning Probe Microscopy and Spectroscopy: Methods and Applications', (Cambridge University Press, 1998); D. Bonnell, 'Scanning Probe Microscopy and Spectroscopy: Theory, Techniques, and Applications', 2nd ed.,

- (Wiley-VCH, New York, 2001); C.J. Chen, 'Introduction to Scanning Tunneling Microscopy', (Oxford University Press, 1993)
- [12] G. Binnig, H. Rohrer, Ch. Gerber and E. Weibel, Phys. Rev. Lett., 50, 120 (1983).
- [13] G. Binnig, C. F. Quate and Ch. Gerber, Phys. Rev. Lett., 56, 930 (1986).
- [14] Y. Sugawara, 'Atomic Force Microscopy in Roadmap of Scanning Probe Microscopy'(Springer, Berlin- Heidelberg), 2007
- [15] B. G. Yacobi, D. B. Holt, and L. L. Kazmerski, 'Scanning Electron Microscopy, in Microanalysis of solids', (Plenum Press, New York), 1994
- [16] P. S. Turner, C. E. Nockolds, and S. Bulcock, 'Electron Microscope Techniques for Surface Characterization, in Surface Analysis Methods in Materials Science', (Springer, Berlin Heidelberg),2003.
- [17] M. Von Ardenne, Improvements in electron microscopes. GB 511204, convention date (Germany) (1937).
- [18] A.J. G. Reed, 'Transmission Electron Microscopy, in Microanalysis of Solid', edited by B. G. Yacobi, D. B. Holt, and L. L. Kazmerski.(Plenum Press, New York), 1994
- [19] D. B. Williams and C. Barry Carter, 'Transmission Electron Microscopy, Vol. I-IV ', (Plenum Press, New York), 1996.
- [20] John C. H. Spence, 'High-resolution Electron Microscopy', (Oxford Science Publications), 2013.
- [21] B. Fultz and J. Howe, 'Transmission Electron Microscopy and Diffractometry of Materials', (Springer, 2nd Ed.), 2005,
- [22] M. Knoll and E. Ruska, Z. Physik., 78, 318 (1932).
- [23] W. L. Bragg, Nature, 90, 410 (1912)

- [24] A. L. Patterson, *Phys. Rev.*, 56 , 978 (1939)
- [25] John R. Ferraro, Kazuo Nakamoto, 'Introductory Raman Spectroscopy', (Academic Press), 2012.
- [26] J. D. J. Ingle and S. R. Crouch, 'Spectrochemical Analysis', (Prentice Hall, New Jersey), 1988.
- [27] J. Tauc, *Materials Research Bulletin*, 3, 37 (1968).
- [28] E. A. Davis and N. F. Mott, *Philosophical Magazine* ,A 22, 903 (1970)
- [29] A. Einstein, *Ann. Phys.*, 31, 132 (1905).
- [30] K. Siegbahn, *Rev. Mod. Phys.*, 54, 709 (1982).
- [31] K. Siegbahn, and K. Edvarson, *Nuclear Physics*, 1, 137 (1956).
- [32] C. D. Wagner, W. M. Rigs, L. E. Davis, J. F. Moulder and G. E. Muilenberg, 'Handbook of X-ray photoelectron spectroscopy', (Perkin-Elmer, Eden Prairie, MN), 1978.
- [33] V. I. Nefedov, 'X-ray Photoelectron Spectroscopy of Solid Surfaces', (Brill-VSP Publishers),1988; Andrew Zangwill, 'Physics at surfaces'(Cambridge University Press), 1988
- [34] D. Briggs and M. P. Seah, 'Practical Surface Analysis-Auger and X-ray Photoelectron Spectroscopy', (Wiley Interscience), 1990; John F. Watts, John Wolstenholme, 'An introduction to surface analysis by XPS and AES', (Wiley Interscience), 2003
- [35] T. A. Carlson, 'X-ray Photoelectron Spectroscopy', (Academic Press), 1978
- [36] G. Binning, and H. Rohrer, *Helv. Phys. Acta*, 55, 726 (1982).
- [37] M. Gratzel, *Nature*, 414, 338 (2001).
- [38] B. Kasemo, and J. Gold, *Adv. Dent. Res.*, 13, 8 (1999).

- [39] S. Majumder, I. Mishra, U. Subudhi, and S. Varma, *Appl. Phys. Lett.*, 103, 063103 (2013).
- [40] A. Fujishima, T. N. Rao, and A. D. Tryk, *J. Photochem. Photobiol. C: Photochem. Rev.*, 1, 1 (2000).
- [41] N. Serpone, and E. Pelizzetti, 'Photocatalysis-Fundamentals and Applications', (John Wiley Sons, New York), 1989.
- [42] W. Gopel, G. Rocker and R. Feierabend, *Phys. Rev. B*, 28, 3427 (1983).
- [43] V. E. Henrich and P. A. Cox, 'The surface science of metal oxides', (Cambridge University Press), 1996.
- [44] H. K. Pulker, G. Paesold, and E. Ritter, *Appl. Opt.*, 15, 2986 (1976).
- [45] O Carp, C L Huisman and A Reller, *Prog. Solid State Chem.*, 32, 33 (2004).
- [46] A. Navrotsky, *Chem. Phys. Chem.*, 12, 2207 (2011).
- [47] M. Pelaez, N. T. Nolan, S. C. Pillai, M. K. Seery, P. Falaras, A. G. Kontos, P. S. M. Dunlop, J. W. J. Hamilton, J. A. Byrne, K. OShea, M. H. Entezari, D. D. Dionysiou, *Appl. Catal. B Environ.*, 125, 331 (2012).
- [48] M.H.Samat, A.M.M.Ali, M.F.M.Taib, O.H.Hassan, M.Z.A.Yahya, *Results in Physics.*, 6, 891 (2016)
- [49] U. Ozgur, Y. I. Alivov, C. Liu, A. Teke, M. A. Reshchikov, S. Dogan, V. Avrutin, S. J. Cho, and H. Morkoc, *J. Appl. Phys.*, 98, 041301 (2005).
- [50] A. Bakin, A. ElShaer, A. C. Mofor, M. AlSuleiman, E. Schlenker, A. Waag, *Physica Status Solidi C.*, 4, 158 (2007)
- [51] H. T. Wang, B.S Kang, F. Ren, L.C. Tien, P.W. Sadik, D.P. Norton, S.J. Pearton, Jenshan. Lin, *Applied Physics Letters.*, 86, 243503 (2005) .
- [52] Zhong Lin Wang, Jinhui Song, *Science*, 312, 242 (2006)

- [53] L. Chow, O. Lupan , G. Chai , H. Khallaf , L.K. Ono , B. Roldan Cuenya , I.M. Tiginyanu ,V.V. Ursaki, V. Sontea, *Sensors and Actuators A*, 189, 399 (2013)
- [54] M. Li, G. Meng, Q. Huang, and S. Zhang, *Sci.Rep.*, 4, 4284 (2014)
- [55] Chin Boon Ong, Law Yong Ng, Abdul Wahab Mohammad, *Renewable and Sustainable Energy Reviews.*, 81, 536 (2018).
- [56] N D Hoa, Quy N van, H Jung, D Kim, H Kim and S K Hong, *Sensors Actuators B.*, 146, 266 (2010)
- [57] P Raksa, A Gardchareon, T Chairuangstri, P Mangkorntong, N Mangkorntong and S Choopun, *Ceram. Int.*, 35, 649 (2009)
- [58] D Li, J Hu, R Wu and J G. Lu, *Nanotechnology*, 21, 485 (2010)
- [59] Zhebo Chen, Thomas F. Jaramillo, Todd G. Deutsch, Alan Kleiman-Shwarscstein, Arnold J. Forman, Nicolas Gaillard, Roxanne Garland, Kazuhiro Takanabe, Clemens Heske, Mahendra Sunkara, Eric W. McFarland, Kazunari Domen, Eric L. Miller, John A. Turner and Huyen N. Dinh , *J. Mater. Res.*, 25, 3 (2010)
- [60] L. Wang, J. Fu. H. Hou, Y. Song, *Int.J. Electrochem. Sci.*, 7 , 12587 (2012)
- [61] J.B. Forsyth, S. Hull , *J. Phys.: Condens. Matter*, 3, 5257 (1991)
- [62] S Gubbala, J Thangala and M K Sunkara, *Sol. Energy Mater. Sol. Cells.*, 91, 813 (2007)
- [63] Takeo Oku, Ryosuke Motoyoshi, Kazuya Fujimoto, Tsuyoshi Akiyama, Balachandran Jeyadevan, John Cuya, *Journal of Physics and Chemistry of Solids*, 72 , 1206 (2011)

Chapter 3

Investigating Structural Phase Transformation using Ultraviolet Raman Spectroscopy and Resistive Switching Properties of Ti ion implanted TiO₂ thin films

3.1 Introduction

TiO₂ has received immense attention in recent years as it exhibits several advanced properties which show applications in areas like sensors, photocatalysis, photovoltaic cells, renewable and clean energy sources etc. [1, 2], along with other metal oxide films [3–5]. TiO₂ has two important polymorphs: rutile is stable whereas anatase is metastable. Both of them have tetragonal crystal structure, consisting of TiO₆ octahedra, with four shared edges in anatase and two in rutile [7]. The anatase to rutile (A-R) transition occurs via breaking and reforming of bonds and creates 8% reduction in the overall volume along with a contraction along c-axis, resulting in a higher density for rutile. Though the A-R transition for TiO₂ is expected to occur irreversibly and exothermally in air at 600°C, much lower temperatures of 200 - 320° have been reported depending on the processing methods [6–8]. Other than hydrothermal synthesis methods, rutile is usually obtained through annealing processes [7]. For thin layers and nano powders, the rutile phase in TiO₂ can be generated at lower temperatures [9]. It is well known that cationic doping and oxygen vacancies (O_V)

can dramatically reduce the transition temperature and enhance the kinetics [7, 10]. Amount of O_V , on the oxygen sub-lattice (TiO_{2-x}), is considered to be the most important factor that influences the phase transition [7, 11]. Presence of O_V facilitates the A-R transformation by reducing the structural rigidity of the oxygen sub-lattice. Nucleation of rutile can also be accelerated by substitutional incorporation of some cations, depending on their valency [7, 10]. Interfacial boundaries between anatase particles are the active regions where nucleation and growth of rutile takes place [7]. Though bulk rutile is thermodynamically more stable due to its lower free energy, anatase has lower surface energy and for very small crystallites (~ 10 nm), anatase is the more stable phase [7, 10, 12]. Controlled by surface thermodynamics, smaller anatase crystallites transform more easily into rutile. This is usually also expected as bigger anatase grains will have relatively smaller surface area, which will hinder the interface mediated growth of rutile. Consequently two processes, growth of anatase crystallite and its transition to rutile, compete with each other.

Ion beams have the potential to modify the material via non-equilibrium and far from-equilibrium processes. Consequently, such materials sometimes display many novel structures and properties which are not attainable by other techniques [13–16]. When an ion interacts with matter, its kinetic energy gets transferred to the primary knock-on atoms (PKA) which get displaced from their lattice positions. The PKA induce further cascades of atomic displacements as well as sub-cascades, thus losing their energy in the process. The kinetic energy of the recoil atoms gets thermalised within a small localized zone in the crystal lattice by producing a *temperature spike*. Such thermal spikes are short lived and when located in the vicinity of metastable phase can induce phase transformation, by thermally activating the region. Nature of cascade and sub cascade structure is expected to depend on the ion-target specifications. Thermal spike model has received immense attention in the realm of swift heavy ion (SHI) induced modifications [17]. Role of thermal spikes that form near the surfaces of solids when bombarded by ions of low and medium energy (1-150 keV) has received much less attention [18] and the studies in this area are very limited. Irradiation with 150 keV Ar^+ , for example, induces a trigonal to rock-salt structural transition in thin $Ge_2Sb_2Te_5$ films [19]. Even a 1 keV Ar^+ ion impact on Ti/Pt

multilayers, in MD simulations, introduces an interface mixing after thermal spike process [20]. $\text{Fe}_{69}\text{Ni}_{31}$ films implanted by 20 keV Ar ions undergo a *bcc* to *fcc* structural transition with transformations taking place in the metastable media through thermal spike and related collision cascades [21]. Localized temperature spike after 500 keV Ar^+ impact are responsible also for grain boundary growth in nanocrystalline Au metal foils [22]. Temperature spikes during cascade collisions can consequently produce variety of structural modifications at low and medium energies.

Oxygen vacancies play a very significant role in the functioning of TiO_2 based resistive random access memory (RRAM) devices. RRAM devices demonstrate reversible switching (RS) behavior, between a high resistance (HRS) and a low resistance (LRS) state [23, 24]. The fundamental working principle of RRAM relies on the formation and disruption of conducting filaments (CF) in the metal-oxide layer of the device upon application of an electric field [25]. RS behavior in Ar^+ implanted TiO_x films is via migration of O_V through self-assembled nanochannels [26]. Excess oxygen vacancies can promote nucleation of local CF along grain boundaries.

This chapter explores the ion beam induced structural phase transition and electrical resistive switching properties in TiO_2 films. Here the goal was to understand the role of a heavy ion like Ti on the structural modifications and RS properties in TiO_2 films. Considering 80 nm film thickness, the energy of the impinging ions has been extracted initially by SRIM calculations [27]. 50 keV Ti ions with projected range of 32 nm (± 13 nm) in TiO_2 were chosen for implantation. TiO_2 films were implanted at several fluences, 1×10^{10} , 1×10^{12} , 1×10^{13} , 1×10^{14} and 1×10^{15} ions/cm². All the samples, prior to and post implantation, were investigated with UV-Raman, grazing incidence x-ray diffraction (GIXRD), Transmission electron microscopy (TEM), x-ray photo electron spectroscopy (XPS) and conducting atomic force microscopy (c-AFM) techniques. The as-deposited and ion implanted films display presence of mixed A and R phases. At a critical fluence, surprisingly, a phase transformation of some A to R is noticed. Such influence of ion beam on structural transformation in TiO_2 films can be significant in the study of ion induced processes as well as TiO_2 based devices. Additionally, although cations are known to enhance A-R transition, yet the role of Ti ion in TiO_2 has not received much attention [7]. The critical fluence is found to be

slightly lower via GIXRD (1×10^{13} ions/cm²), than UV-Raman (1×10^{14} ions/cm²) which is a surface sensitive probe. This may reflect beginning of phase transformation first in bulk. O_V play an important role in the A-R transition and their number, studied here using XPS, increases with fluence. The A-R transition may be proceeding via the aggregation of anatase nano-crystallites present in the TiO₂ films. Oxygen vacancies and thermal spike created after Ti ion implantation are also crucial in the transformation of phases observed here. Various features of these processes can be of significant importance for practical and theoretical understanding. The resistive switching properties of ion implanted TiO₂ films have also been explored. Here also, O_V are necessary for the formation of CF which control the transition from HRS to LRS. This is highlighted by the fact that films exposed to the highest fluence alone exhibited the RS behavior with bipolar reversible character.

3.2 Experimental section

3.2.1 Sample Preparation

Prior to the growth of TiO₂ film, a gold film was deposited on Ni/SiO₂/Si substrate by e-beam evaporation method. On p-SiO₂/Si(100) a 12nm thin Ni layer was grown, by e-beam technique, in order to achieve a smooth gold deposition. The Ni layer also acts as a good adhesive for the gold film, since Au sticks poorly on SiO₂/Si(100). A gold film, necessary for electrical conducting measurements, was then deposited on Ni/SiO₂/Si. This deposition was performed using Knudsen cell with 99.995 % pure gold at a base pressure of 2×10^{-7} mbar. The deposition rate and the sample rotation speed were maintained at 0.1 \AA s^{-1} and 20 rpm, respectively. The gold film was 50 nm in thickness.

The TiO₂ films of thickness 80 ± 5 nm were deposited on Au/Ni/SiO₂/Si substrates using radio frequency magnetron sputtering technique at room temperature (RT). The parameters for TiO₂ film deposition were same as in previous work [26]. The working pressure was 8 mTorr and a purging of Ar and O₂ gases, at a ratio of 30:12 sccm, was done during sputtering. The purity of Ar and oxygen gases was 99.999% and 99.99%, respectively.

The implantation of TiO₂ films was carried out at RT with 50 keV Ti ions at normal incidence. Chamber pressure was maintained at 5×10^{-6} Torr. Implantation was performed at the fluences of 1×10^{10} , 1×10^{12} , 1×10^{13} , 1×10^{14} and 1×10^{15} ions/cm². For the lowest three fluences, flux was 3×10^9 ions/cm².sec and for other fluences flux used was 1.7×10^{11} ions/cm².sec. The projected range and the longitudinal straggling of Ti ions in TiO₂ lattice have been estimated using SRIM code to be 32 and 13 nm, respectively [27]. Thus, the implanted Ti ions were fully confined within the TiO₂ film.

It may be noted that the ion current was maintained below 70 nA for all the samples. Sample holder was a thick copper block which behaves like a heat sink and so the given ion flux was much lower for any rise in temperature of the sample surface. The ion beam was scanned over the sample, in order to achieve uniform implantation.

3.2.2 Experimental Techniques

GIXRD patterns were recorded on a Bruker-D8 Discover x-ray diffractometer system by scanning 2θ range of 20-35°. The XRD measurements were taken in the grazing configuration with incident angle of 0.5°. The operating voltage was 40 kV and the step size for the measurement was 0.02 degree. The accuracy of the system is 0.005 degree.

Micro UV-Raman scattering studies have been performed using UV(325 nm) Laser in backscattering geometry on a T64000 triple monochromator Horiba Jobin Yvon system with a liquid nitrogen cooled CCD detector. Measurements were carefully acquired with a laser power of below 1 mW and a laser spot diameter of about 4 μ m. The spectral window was less than 150 cm⁻¹, and the resolution is 0.2 cm⁻¹.

XPS investigations were performed on a PHI 5000 VersaProbeII (ULVAC PHI, Inc.) with a micro-focussed (100 μ m, 25 W, 15 KV) monochromatic Al -K _{α} source (1486.6 eV), where the emitted photoelectrons were analyzed with the help of a hemispherical analyzer coupled with a multichannel detector.

TEM was utilized to determine the microstructure, grain size and different crystallinity of the samples. Cross-sectional TEM (XTEM) specimens were prepared using the standard method of mechanical thinning and dimpling with final thinning

using a precision-ion-polishing system (PIPS, Gatan, Pleasanton, CA). The ion polish was carried out at 3.0 keV energy without liquid nitrogen cooling and followed by a 1.2 keV cleaning process.

For TEM study, specimens were aligned on [110] zone axes of Si. TEM investigation was carried out using FEI, Tecnai G2 F30, ST microscope operating at 300 kV equipped with a Gatan Orius SC1000B CCD camera. The compositional analysis was performed by energy dispersive X-ray spectroscopy (EDS, EDAX Inc) attachment on the Tecnai G2 F30.

Conducting AFM (c-AFM) measurements were performed using a Park XE-7 system using conducting Pt/Ir tip with radius of curvature 40 nm and current compliance of 10 nA. For c-AFM measurements, voltage (V) between the AFM tip and the bottom Au electrode is swept, under sample bias conditions. The corresponding current (I) is measured. The voltages were swept from -5 to +5 V in the positive direction and from 5 to -5 V in the reverse direction. c-AFM measurements have been performed on various regions of the sample.

3.3 Results and discussion

Fig. 3.1 shows GIXRD data from the as-grown and ion implanted films. As-deposited films show presence of mixed anatase and rutile phases and the peaks associated with anatase(101) and rutile(110) are observed at 25.34° and 27.57° , respectively [10]. Such mixed phases are also observed after films were implanted with Ti ions. The integrated XRD intensities of rutile (A_R) and anatase (A_A) features were measured and are shown (fig. 3.1(b)). Though A_R and A_A increase mildly up to 1×10^{12} ions/cm², but subsequently A_R rises drastically. Simultaneously beyond 1×10^{13} ions/cm², A_A declines. The reduction in A_A and corresponding enhancement in A_R indicates towards the initiation of ion induced A-R structural transition, contributed by the transformation of some A into R. Ratio A_R/A_A versus ion fluence shows a particularly interesting behavior(fig. 3.1(d)). Though there is nearly no change up to 1×10^{12} ions/cm², the ratio suddenly rises rapidly for higher fluences. Consequently, 1×10^{13} ions/cm² reflects a critical fluence where R content in the film drastically in-

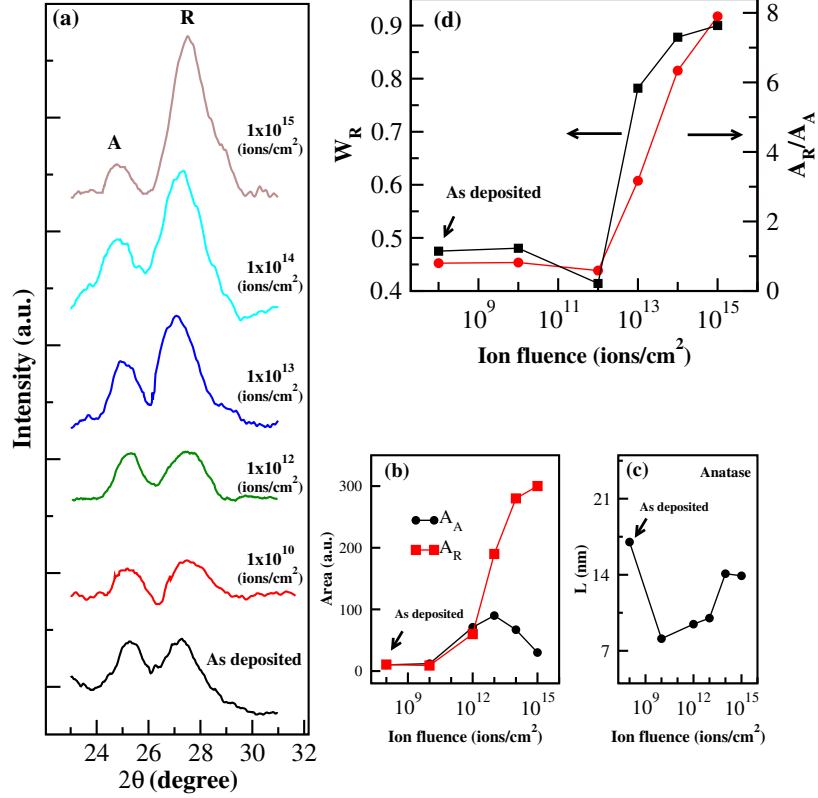


Figure 3.1: (a) XRD from as-deposited TiO₂ thin films and after ion implantation at various fluences (ions/cm²). (b) Area under R (A_R) and A (A_A) as a function of ion fluence, (c) Crystallite size L of anatase as a function of ion fluence, and (d) Phase content of rutile W_R and ratio A_R/A_A as a function of ion fluence.

creases at the expense of A content. At this juncture then, the A-R transition seems to get first introduced in the films. It then increases with further ion fluence. The weight fraction of R content (W_R) in the films can be estimated by utilizing A_R and A_A and is given by [12]

$$W_R = \frac{A_R}{0.884A_A + A_R} \quad (3.1)$$

Fig. 3.1(d) exhibits the change in W_R as a function of fluence. It is nearly 0.5 in the as-deposited films and shows little variation up to 1×10^{12} ions/cm². Beyond this, however, it increases in an accelerated fashion with fluence, becoming nearly 0.9 at the highest fluence. Thus after 1×10^{13} ions/cm², R content increases whereas A content reduces reflecting towards conversion of some A into R phase. These results are corroborated by the Raman and TEM results discussed below.

Anatase XRD features indicate an asymmetry towards lower 2θ values suggesting presence of some nano-crystallites as well. Average anatase grain size, L , has been calculated using Scherrer formula (fig. 3.1(c)). In the as-deposited films, some small (20 nm) anatase nanoparticles are present whereas after implantation, smaller nano-particles (8 - 13 nm) are also noticed. We note that similar sizes of anatase nanoparticles have been observed earlier by Alhomoudi et al. in the as-grown TiO_2 films [28]. At low fluences (1×10^{10} and 1×10^{12} ions/cm²), XRD peaks of A appear little broader than the pristine. Development of smaller sized anatase nanostructures (see fig. 3.1(c)) can cause this. Some ion induced defects will also be present. At higher fluences, increase in the nanostructure size can create slightly smaller peak widths. Rutile XRD peaks also display some broadening reflecting presence of nanoparticles. Small stress may also be involved in the as-deposited films as reported by other authors as well [28]. GIXRD results present predominantly bulk characteristics of TiO_2 film.

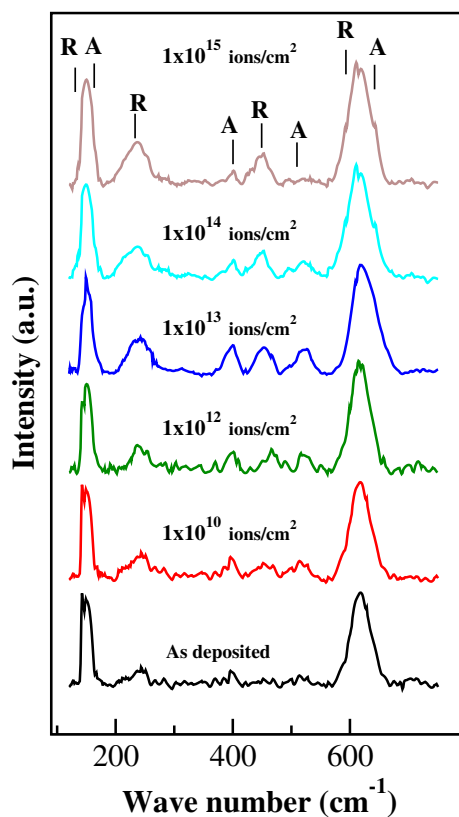


Figure 3.2: UV-Raman spectra from as-deposited TiO_2 thin films and after ion implantation with various fluences (ions/cm²).

UV-Raman, performed with UV laser creates resonance Raman conditions making it a powerful surface sensitive technique for assessing the structural phase transition in materials. Rutile TiO_2 has a point group D_{4h}^{14} symmetry whereas anatase belongs to the symmetry space group D_{4h}^{19} [29]. The primary Raman bands of anatase are at 144, 196, 399, 515/519 (combined) and 639 cm^{-1} and these can be assigned to E_g , E_g , B_{1g} , A_{1g}/B_{1g} and E_g , respectively. Major rutile related Raman modes are at 143, 235, 447 and 612 cm^{-1} . These are related to B_{1g} , two phonon scattering, E_g and A_{1g} , respectively. The UV-Raman spectra from the as-deposited and ion implanted TiO_2 films are shown in fig. 3.2. The Raman spectrum of the as-prepared TiO_2 film indicates presence of anatase as well as rutile phases. After ion implantation also, films show presence of mixed A and R phases. In order to understand the structural transformations taking place in the TiO_2 films, two prominent regimes of Raman spectra have been considered: the low frequency ($140\text{-}170 \text{ cm}^{-1}$) and the high frequency ($550\text{-}720 \text{ cm}^{-1}$) regions, as the strongest A and R modes are at 144 cm^{-1} and 612 cm^{-1} , respectively.

Low frequency ($140\text{-}170 \text{ cm}^{-1}$) Raman spectra are shown in fig. 3.3(a). Under Raman resonance conditions, along with anatase (E_g) mode, Rutile (B_{1g}) mode is also observed in this region [10]. For the as-deposited film, R mode appears at 144.2 cm^{-1} displaying a small shift of 1.2 cm^{-1} towards higher wavenumbers. The A mode, observed at 151.2 cm^{-1} , also shows a 7.2 cm^{-1} blue shift. Such shifts towards higher wavenumbers can be attributed to phonon confined nano-particles as well as compressive stress and earlier studies on as-deposited TiO_2 films have reported similar scenario [28,30]. Studies on Si, InP and TiO_2 [31–33] have also exhibited shifts and asymmetric broadening in Raman signal reflecting phonon- confinement effects. XRD results (in fig. 3.1) also delineated role of nanoparticles in TiO_2 films. Along with A mode, another feature A_n is also noticed at 157.5 cm^{-1} (fig. 3.3(a)). This corresponds to the anatase (E_g) mode affected predominantly by oxygen deficiency [34]. Some contribution of nano-phase is also possible [30,34]. The as-deposited and ion implanted TiO_2 films contain oxygen vacancies, Ti^{3+} , as discussed later. Presence of such sites in anatase phase produce the A_n peak [34].

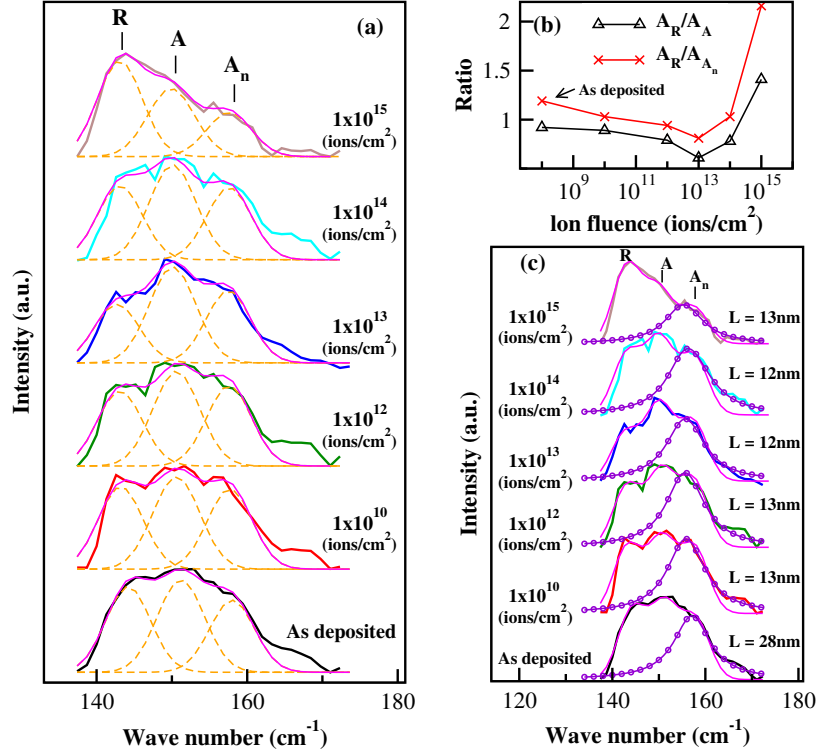


Figure 3.3: (a) UV-Raman normalized spectra in the low-frequency region from as-deposited TiO₂ thin films and after ion implantation with various fluences (ions/cm²), along with fitting components for R, A and A_n (b) Ratios A_R/A_A and A_R/A_{A_n} as a function of ion fluence (c) A_n Raman mode of TiO₂ fitted with PCM (○) as described by Eq. 3.2, L is size of anatase nanoparticles as determined by the PCM fit to the data.

Spectra of fig. 3.3(a) have been fitted with three gaussian functions related to R, A and A_n. With A_R , A_A and A_{A_n} being their respective integrated intensities, the ratios of these intensities viz. A_R/A_A and A_R/A_{A_n} are shown in fig. 3.3(b). Interestingly, A_R/A_A and A_R/A_{A_n} present similar trends. Importantly, one notices that up to the fluence of 1×10^{13} ions/cm², A_R/A_A (and A_R/A_{A_n}) decreases but shows an increase at 1×10^{14} ions/cm² and beyond. Further, along with a drastic increase a much higher A_R/A_A (and A_R/A_{A_n}) is seen at the highest fluence. Confirming the GIXRD observations, these results also suggest existence of a critical fluence (1×10^{14} ions/cm²) beyond which an A-R transition in the films takes place. The critical fluence here however is 1×10^{14} ions/cm², slightly higher than that observed in GIXRD. This may be attributed to transformation first initiating in bulk as noticed in GIXRD, rather in UV-Raman which happens to be a surface sensitive technique.

At this stage the A content begins to reduce and R becomes larger (fig. 3.3(a)). Once phase transition is initiated, more anatase transforms to rutile causing the increase in A_R/A_A (and A_R/A_{A_n}) at higher fluences (fig. 3.3(b)). Some anatase is present even at the highest fluence, but A_R/A_{A_n} is much larger than A_R/A_A proposing that A_n may have transformed more than A into R (as also seen in fig. 3.3(a)).

The phonon confinement model (PCM), proposed by Richter et al. [35], has also been applied here to estimate the size (L) of the Anatase nanocrystals in TiO₂ films. With confinement of phonons in a nanocrystal, the $k = 0$ selection rule gets relaxed [31,32] which induces asymmetric broadening of the Raman modes. In TiO₂, phonon confinement produces an asymmetric broadening towards higher wavenumbers for the E_g mode in anatase [36], as also observed here for the case of A_n (E_g) mode (in fig. 3.3(a)). By applying PCM, the intensity of the A_n mode can be given as [35]:

$$I(\omega) = \int_0^{2\pi/a_0} \frac{|C(q)|^2 4\pi q^2 dq}{(\omega - \omega(q))^2 + (\Gamma_0/2)^2} \quad (3.2)$$

where a_0 is the lattice constant (0.3768 nm) and Γ_0 is the Raman intrinsic line width at room temperature ($\Gamma_0 = 7 \text{ cm}^{-1}$) for bulk anatase. The weight factor $C(q)$ for the scattering with wave vector q is given by:

$$|C(q)|^2 = \exp\left(\frac{-q^2 L^2}{16\pi^2}\right) \quad (3.3)$$

and the phonon dispersion relation $\omega(q)$ for the E_g Raman mode in the anatase phase is taken as [36]:

$$\omega(q) = \Delta \times (1 - \cos(qa_0)) + \omega_0 \quad (3.4)$$

where $\Delta = 20 \text{ cm}^{-1}$ and ω_0 is the wave number of anatase A_n (E_g) Raman band (157.5 cm^{-1}). By fitting the experimental Raman spectra with PCM analysis, the size (L) of the anatase nano-particles have been determined in TiO₂ thin films and the results are shown in Fig. 3.3(c). The results indicate that the as-deposited films have anatase nanoparticles of about 28 nm size. The size of the nanoparticles, however, reduces after ion implantation and is found to be nearly 12-13 nm. Thus, the as-deposited films contain larger ($\sim 28 \text{ nm}$) anatase grains, which get reduced ($\sim 12-$

13 nm) after ion implantation. These observations are consistent with the results obtained via GIXRD (fig. 3.1(c)) which presented nanoparticle-dimensions similar to those estimated here. Additionally, GIXRD results also demonstrated that the bigger nano particles (~ 20 nm), of the as-deposited films, become smaller in size ($\sim 10-13$ nm) after ion implantation. GIXRD, however, shows nanoparticle size to increase slightly at the two highest fluences (fig. 3.1(c)) whereas Raman PCM results do not demonstrate this. This difference may be caused by the fact that UV- Raman is a surface sensitive technique and GIXRD reflects information from bulk.

High frequency region ($550-720\text{ cm}^{-1}$) of Raman spectra are shown in fig. 3.4(a). Strong R feature (A_{1g} mode) at 612 cm^{-1} and a weaker A feature (E_g mode) at 638 cm^{-1} are observed. These spectra have been fitted with two gaussian functions related to R and A and the corresponding integrated intensities A_R and A_A were measured. The peak widths of both the components do not change with fluence. However, some assymetry in R feature is noticed at the highest fluence which can be due to the presence of some nano-crystallites. In agreement with the low-frequency UV-Raman (fig. 3.4), an A-R transition occurs when films are implanted with 1×10^{14} ions/cm². Correspondingly a large increase in A_R/A_A (fig. 3.4(b)) is observed. Although R and A features in high frequency (fig. 3.4) and low frequency Raman (fig. 3.3) are associated with different phonon modes, yet characteristic peaks in both the regions reflect similar behavior in A_R/A_A confirming the process of phase transition at the critical fluence of 1×10^{14} ions/cm².

The as-deposited TiO₂ films can be characterized as having big grains of both R and A phases, as well as some large sized ($\sim 20-28$ nm) anatase nanoparticles. Post-implantation, as exhibited by XRD and UV-Raman, films contain small sized ($\sim 10-13$ nm) anatase- nanoparticles as well. The presence of such nanoparticles is supported by thermodynamic studies which show that though under ambient conditions rutile is a more stable phase than anatase, however, this stability is size dependent and for nanoparticles smaller than 10-14 nm, anatase is a more stable phase [10]. Using UV-Raman scattering, from low frequency and high frequency regions, as well as XRD, it is demonstrated that ratio A_R/A_A does not display much change up to the critical fluence but accelerates after that. A phase transition thus occurs at the critical fluence,

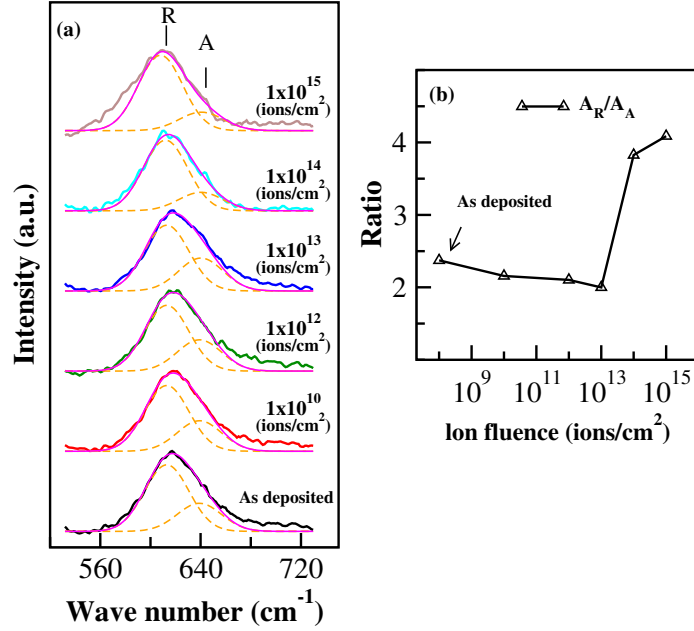


Figure 3.4: (a) UV- Raman normalized spectra in the high-frequency region from as-deposited TiO₂ thin films and after ion implantation with various fluences (ions/cm²) along with fitting components for R and A (b) Ratio A_R/A_A as a function of ion fluence.

where some anatase content transforms to rutile. This transformation possibly occurs by the coarsening and aggregation of anatase crystallites and nanoparticles [10]. During this process, the initial rutile phase nucleates at the interfaces of the anatase particles which are in contact, i.e. via agglomeration of anatase TiO₂ particles [10]. As the anatase particles grow in size they transform to rutile, that being the more stable phase. At the highest fluence only a very small content of anatase remains. Some rutile nanoparticles are also expected at all fluences.

Cross-sectional TEM (XTEM) investigations were undertaken for microstructural studies. The bright-field image of the as-deposited TiO₂ film is shown in fig. 3.5(a). A typical high resolution XTEM image (fig. 3.5(b)) from the as deposited film shows the presence of anatase (A) and rutile (R) crystallites, in agreement with our XRD and the UV-Raman analysis. The A and R regions are marked by white and black lines, respectively, with corresponding lattice fringes and fast Fourier transform (FFT) patterns shown in fig. 3.5(e,f). After Ti ion implantation with the fluence of 1×10^{14} ions/cm², XTEM image displays (fig. 3.5(c)) some irregular shaped nano crystallites

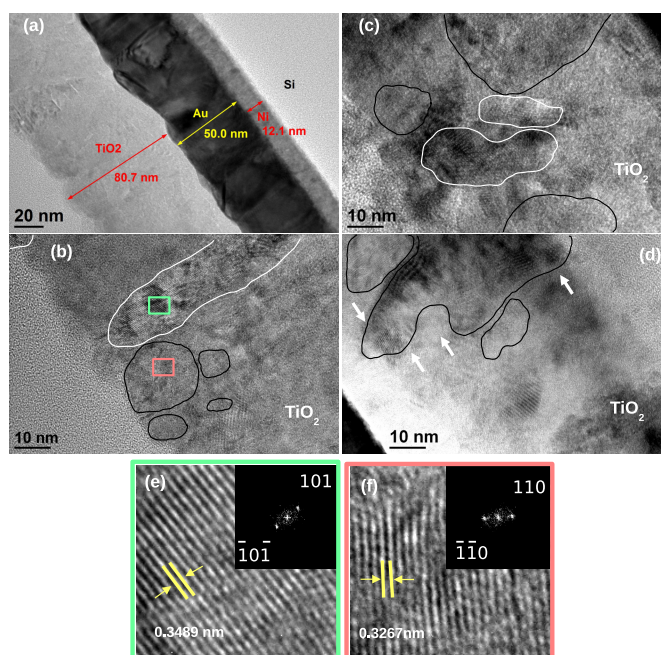


Figure 3.5: (a) Bright-field XTEM image of the as-deposited TiO_2 film. High resolution XTEM image of (b) as-deposited TiO_2 thin film and after ion implantation with (c) 1×10^{14} and (d) 1×10^{15} ions/ cm^2 . Black and white contours respectively mark the rutile and anatase regions. Lattice fringes and FFT of (e) Anatase and (f) Rutile regions, from corresponding squares marked in (b).

of A. Very few bigger crystallites of A (not shown here) have also been observed. For R, most content is in form of big grains. Few nano crystallites of R have also been seen (fig. 3.5(c)). These observations are in agreement with the UV-Raman and XRD results which reflected the presence of anatase nanocrystallites. Also overall, the content of A has decreased at this stage and the content of R increases. After the implantation at 1×10^{15} ions/ cm^2 , a typical XTEM image shows only R content (fig. 3.5(d)). In some images, very few small crystallites of A (not shown) are also observed. TEM results corroborate XRD and UV-Raman observations by showing that most of the anatase content has transformed into rutile at this fluence. Interestingly, we also observe some big R zones (one shown here marked by arrows) extending all

the way from the top of the film to the bottom.

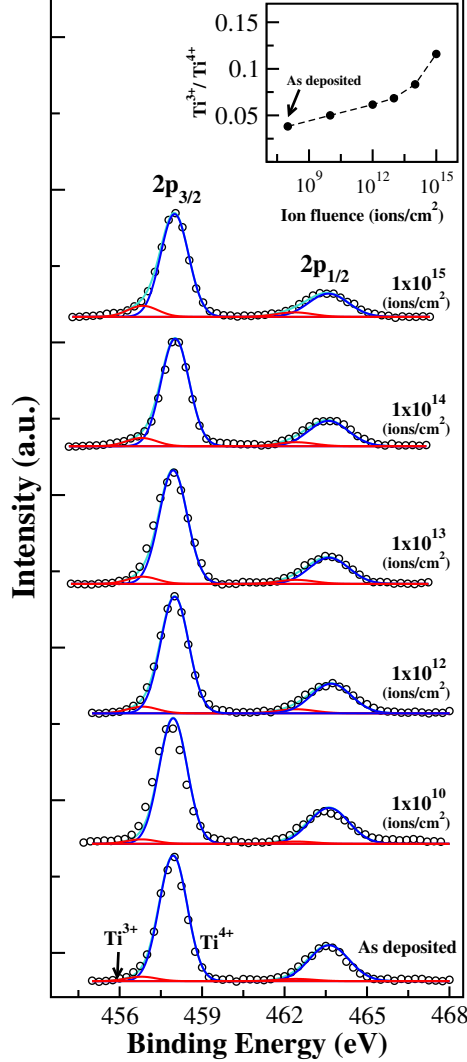


Figure 3.6: Ti(2p) XPS spectra from as-deposited TiO₂ thin films and after ion implantation with various fluences (ions/cm²). Peak fitted components for Ti⁴⁺ and Ti³⁺ states are shown. Ratio of oxygen vacancy (Ti³⁺) w.r.t. Ti⁴⁺ is shown in inset.

Next, we have explored the modification in oxygen vacancies in these films, as they are expected to play an important role in facilitating A-R transition. The core level XPS spectra from Ti(2p) region are shown in fig. 3.6. For the as-deposited film two main features, 2p_{3/2} and 2p_{1/2}, at 457.9 and 463.6 eV correspond to Ti⁴⁺ states of TiO₂ [37, 38]. Very small amount of inherent oxygen vacancy (O_V) states, Ti³⁺, are also noticed at 456.8 and 462.4 eV [37, 38]. After Ti ion implantation with 1x10¹⁰ ions/cm², the main features 2p_{3/2} and 2p_{1/2} are observed at the same position

as pristine. These spectra also delineate presence of small Ti^{3+} states. However, though the intensity of Ti^{4+} features does not change much after implantation, the intensity of the Ti^{3+} has increased slightly, indicating an enhancement in the ratio $\text{Ti}^{3+}/\text{Ti}^{4+}$. Ion implantation of metallic oxides, like TiO_2 , can produce preferential sputtering [37,38] wherein the lower mass oxygen atoms are sputtered out producing O_V (Ti^{3+}) states, by reducing Ti^{4+} sites on the surface. The reduction process occurs as the 2p-electrons from oxygen get transferred to the empty 3d orbitals of the Ti atoms on the surface [39]. With increasing fluence the O_V states (Ti^{3+}) are also observed to increase. Inset of fig. 3.6 shows the ratio $\text{Ti}^{3+}/\text{Ti}^{4+}$ and it can be observed that this ratio increases with fluence. These results show that the TiO_2 films get reduced after implantation. In this process, some Ti rich centers may also form on the surface [33,37]. Implantation thus generates O_V as well as Ti interstitials in the host lattice. This influences the lattice dynamics as reflected by the modification in the Raman spectra with ion implantation.

Implantation of 50 keV Ti ions in TiO_2 films here, will create PKA and associated cascades and sub cascades. Such collisional cascades, triggered by PKA, can induce thermal spike in localized regions [18–22]. The thermal spike striking a metastable anatase zone can deposit the energy necessary for A-R transition. With ion bombardment, the number of generated O_V (Ti^{3+}) states also increase (fig. 3.6). This in turn further accelerates intense energy dissipation, affecting the dynamics of the atoms in the material [40]. A-R phase transformation occurs via breaking of Ti-O bonds and cooperative movement of the Ti and O atoms [41]. Such changes in atomic arrangements require space which can be provided by the oxygen vacancies and earlier results have shown that presence of O_V appreciably promote A-R transitions [40]. O_V also facilitate mass transport which assist anatase particle in acquiring a critical size crucial for the initiation of A-R transition [40].

Simulations in this directions, with the inclusion of ion flux, number of thermal spikes induced by ions, oxygen vacancies and dopants, will be necessary for further understanding and will be taken up in a future study. The transition from anatase to rutile, has a strong dependence of thermodynamic stability on particle size. This is due to the fact that growth rates of various polymorphs differ and consequently their

relative stability during phase transition will also differ. Phase transformation will, in general, also be governed by several other factors like number of anatase- crystallites and nanoparticles, their packing, surface energies, coarsening rates, oxygen vacancies etc..

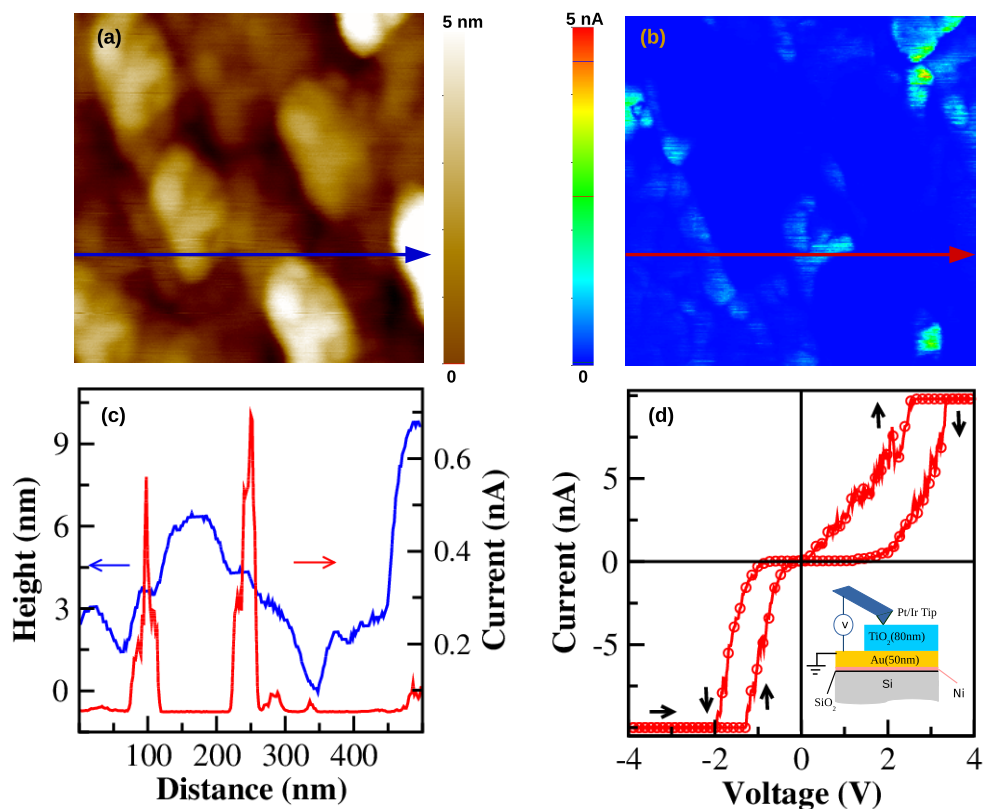


Figure 3.7: For a sample implanted with 1×10^{15} ions/cm² (a) AFM image ($500 \times 500 \text{ nm}^2$) showing surface topography (b) *c*-AFM image ($500 \times 500 \text{ nm}^2$) showing current map with +2V bias applied at the Au back electrode (c) Line profile of surface topography and current profile (d) Local I-V characteristics acquired by sweeping the applied potential across the AFM tip and the Au back electrode from -4 V to +4V and back to -4 V and compliance current (I_c) 10 nA. Schematic diagram of *c*-AFM experiments on TiO₂/Au/Ni/SiO₂/Si with Pt/Ir tip acting as movable top electrode for *c*-AFM is also shown.

Ion implantation and O_V can also influence the electrical properties of TiO₂ films, and here Current-Voltage (I-V) characteristics of these films have been studied using *c*-AFM. For the as-deposited TiO₂ films or for films implanted at low fluences, no current could be detected. However, films implanted at the highest fluence

(1×10^{15} ions/cm²) demonstrate resistive switching behavior. AFM image (fig. 3.7(a)) shows the surface topography of the sample implanted at 1×10^{15} ions/cm². The corresponding c-AFM image (fig. 3.7(b)) displays several distinct locations of the increasing surface current density. A line profile of the topography and the corresponding current profile are also displayed (fig. 3.7(c)). Variation in the current density as a function of changing bias voltage gives clear signature of the RS behavior (fig. 3.7(d)). A percolation threshold is observed near -1 V with a sharp rise in current, demonstrating a transition from a high resistance state (HRS) to a low resistance state (LRS). Hence, an electrical conduction across the TiO₂ film is observed after implantation at the highest ion fluence. This scenario reflects a transition of the insulating-to-conducting type in TiO₂ layers. Presence of the largest number of O_V at this fluence (see fig. 3.6) appears to be responsible for this transition. O_V act as donor species, and their introduction improves the electrical conductivity. These O_V can fill the nano-channels, passing through the film, transporting the carriers during conduction [26].

Formation of nano-channels or conducting filament (CF) is necessary for the observation of RS characteristics and migration of oxygen vacancies contribute in the formation of CF [26]. When a sufficiently negative bias is applied, oxygen vacancies become mobile and start to diffuse towards the cathode. Oxygen ions, on the other hand migrate towards the anode. CF can get formed when O_V extend from anode to cathode, making the device to switch to *on* state by going from HRS to LRS state. Once switching from HRS to LRS state is achieved, V is reduced and swept in the opposite direction and LRS to HRS transition is observed. During this process the CF rupture and subsequently degrade. The transitions from HRS to LRS at V_{set} , and LRS to HRS at V_{reset} suggest existence of two stable, HRS and LRS, states for ion implanted TiO₂ films. Moreover, this behavior is reversible indicating presence of *bi-stable reversible switching* behavior. This switching is also of bipolar nature with both, V_{set} and V_{reset} , being of different polarity. Hence under an applied electric field, resistive memory device here gets SET to low resistance state (LRS) at one polarity while gets RESET to high resistance state (HRS) upon reversing the applied electric field polarity. Back and forth migration of mobile oxygen vacancies, under the influence of electric field, is considered to be the factor responsible for activating this

process [42]. Low resistance state is called the R_{on} state, and High resistance state is called the R_{off} state [43]. In the present study SET occurs at negative polarity (V_{set}) while RESET takes place at positive polarity (V_{reset}).

As RS behavior critically depends on the formation of CF, due to the migration of O_V , a sufficient number of vacancies will be required. Presence of large number of vacancies at the highest fluence may present the optimum O_V threshold necessary for RS, and may be the reason for not observing this phenomenon at lower fluences.

3.4 Conclusions

This chapter investigates the role of 50 keV Ti ion implantation towards the structural phase transition and electrical resistive switching properties in TiO_2 thin films. A phase transition from anatase to rutile has been observed which gets initiated at a critical fluence and then accelerates further with increasing fluence. Such ion induced phase transition in TiO_2 films can have significant role in exploring ion induced processes and device development. The transformation is a consequence of the introduction of O_V and the formation of thermal spikes in films during Ti ion implantation. With the presence of thermodynamically stable small ($\sim 10-13$ nm) anatase nanoparticles also in the films, phase transformation may proceed via their aggregation. GIXRD presenting a slightly smaller value of critical fluence (1×10^{13} ions/cm²) than UV-Raman (1×10^{14} ions/cm²) may correspond to the initiation of the transition first in bulk. Oxygen vacancies play a significant role in modifying electrical properties also and the films implanted at the highest fluence display resistive switching behavior. Presence of O_V in conducting filaments can facilitate this switching process.

Bibliography

- [1] H. Li, Y. Zhang, S. Wang, Q. Wu, and C. Liu, *J. Hazard. Mater.* **169**, 1045 (2009).
- [2] U. Diebold, *Surf. Sci. Rep.* **48**, 53 (2003).
- [3] E. Manikandan, G. Kavitha, J. Kennedy, *Ceramics International.* **40**, 16065 (2014)
- [4] B. Sathyaseelan , E. Manikandan , V. Lakshmanan , I. Baskaran , K. Sivakumar , Rasiah Ladchumananandasivam , J. Kennedy , M. Maaza , *J. Alloy Compd.* **671**, 486 (2016).
- [5] E. Manikandan, M. K. Moodley, S. Sinha Ray, B. K. Panigrahi, R. Krishnan, N. Padhy, K. G. M. Nair, and A. K. Tyagi , *J. Nanoscience and nanotechnology* **10**, 5602 (2010).
- [6] Qiang Gao, Xiaomei Wu, Yueming Fan, *Dyes and Pigments* **95**, 96 (2012).
- [7] Dorian A. H. Hanaor, Charles C. Sorrell, *J Mater Sci.***46**, 855 (2011).
- [8] K. J. D. Mackenzie, *Trans. J. Br. Ceram. Soc.* **74**, 29 (1975).
- [9] G.B. Song, J.K. Liang, F.S. Liu, T.J. Peng, G.H. Rao, *Thin Sol. Films* **491**, 110 (2005)
- [10] H. Zhang, J. F. J. Banfield, *Mater. Chem.* **8**, 2073 (1998).
- [11] S. Vargas, R. Arroyo, E. Haro, R. Rodriguez, *J Mater Res.***14**, 3932 (1999).
- [12] A. A. Gribb, J. F. Banfield, *Am. Mineral.* **82**, 717 (1997).

- [13] J. Kennedy , P.P. Murmu , E. Manikandan , S.Y. Lee , J. Alloy Compd. **616**, 614 (2014)
- [14] K. Thanigaiaru , J. Ramana Ramya , S.C. Vanithakumari, P. Magudapathy ,U. Kamachi Mudali , K.G.M. Nair , S. Narayana Kalkura, Mater. Lett. **153**, 182 (2015)
- [15] K. Thanigaiaru, K. Elayaraja, P. Magudapathy, U. Kamachi Mudali, K.G.M. Nair, M. Sudarshan, J.B.M. Krishna, A. Chakraborty, S. Narayana Kalkura, Ceramics International. **39**, 3027 (2013)
- [16] F.T. Thema , P. Beukes , B.D. Ngom , E. Manikandan , M. Maaza, J. Alloy Compd. **648**, 326 (2015)
- [17] Udai B. Singh, Compesh Pannu, Dinesh C. Agarwal, Sunil Ojha, Saif A. Khan, Santanu Ghosh, and Devesh K. Avasthi, J. Appl. Phys. **121**, 095308 (2017).
- [18] M. Nastasi and J. Mayer, Ion Implantation and Synthesis of Materials (Springer Series in Materials Science) 2006.
- [19] S. M. S. Privitera, A. M. Mio, E. Smecca, A. Alberti, W. Zhang, R. Mazzarello, J. Benke, C. Persch, F. La Via, and E. Rimini, Phys. Rev. B **94**, 094103 (2016).
- [20] P. Sule, M. Menyhard, K.Nordlund, Nucl. Instru. and Meth. in Phys. Res. B **211**, 524 (2003).
- [21] V. V. Ovchinnikov (1994) Self-propagating phases transformations in metastable media induced by ion bombardment Proc. XVI International Symposium on Discharges and Electrical Insulation in Vacuum 2259ed. Mesyats GA(Moscow-St.Petersburg.SPIE)605-608
- [22] D. Kaoumi, A. T. Motta, and R. C. Birtcher, J. Appl. Phys. **104**, 073525 (2008).
- [23] W. R. Hiatt and T. W. Hickmott, Appl. Phys. Lett. **6**, 106 (1965).
- [24] I. G. Baek, M. S. Lee, S. Seo, M. J. Lee, D. H. Seo, D. S. Suh, J. C. Park, S. O. Park, H. S. Kim, I. K. Yoo, U. I. Chung, and J. T. Moon, Tech. Dig. Int. Electron Devices Meet. 587, (2004).

- [25] D. S. Jeong, R. Thomas, R. S. Katiyar, J. F. Scott, H. Kohlstedt, A. Petraru, and C. S. Hwang, *Rep. Prog. Phys.* **75**, 076502 (2012).
- [26] A. Barman, C. P. Saini, P. Sarkar, B. Satpati, S. R. Bhattacharyya, D. Kabiraj, D. Kanjilal, S. Dhar, and A. Kanjilal, *Jour. Appl. Phys.* **118**, 224903 (2015).
- [27] J. F. Ziegler, J. P. Biersack and M. D. Ziegler, *SRIM - The Stopping and Range of Ions in Matter* (SRIM Co., Chester, MD,USA, 2008).
- [28] Ibrahim A. Alhomoudi, G. Newaz, *Thin Solid Films.* **517**, 4372 (2009).
- [29] S. P. S. Porto, P. A. Fleury, and T. C. Damen, *Phys. Rev.* **154**, 522 (1967).
- [30] W. F. Zhang, Y. L. He, M. S. Zhang, Z. Yin and Q. Chen, *J. Phys. D: Appl. Phys.* **33**, 912 (2000).
- [31] Soma Dey, C. Roy, A. Pradhan, Shikha Varma, *J. App. Phys.* **87**, 1110 (2000).
- [32] D. Paramanik, Shikha Varma, *J. App. Phys.* **101**, 023528 (2007).
- [33] Subrata Majumder, D. Paramanik, V. Solanki, I. Mishra, D. K. Avasthi, D. Kanjilal and Shikha Varma, *Appl. Surf. Sci.* **258**, 4122 (2012).
- [34] J. C. Parker and R.W. Siegel, *J. Mater. Res.* **5**, 1246 (1990).
- [35] H.Richter, Z.P.Wang and L.Ley, *Solid State Commun.* **39**, 625 (1981).
- [36] D. Bersani, P.P. Lottici and X.Z. Ding, *Appl. Phys. Lett.* **72**, 73 (1998).
- [37] V. Solanki, S. Majumder, I. Mishra, P. Dash, C. Singh, D. Kanjilal and S. Varma, *J. Appl. Phys.* **115**, 124306 (2014).
- [38] Shalik Ram Joshi, B. Padmanabhan, Anupama Chanda, V. K. Malik, N. C. Mishra, D. Kanjilal, Shikha Varma, *Appl. Phys. A* **122**, 713 (2016).
- [39] Z. Zhao, X. Zhang, G. Zhang, Z. Liu, D. Qu, X. Miao, P. Feng, and Z. Sun, *Nano Research.* **8**, 4061 (2015).
- [40] Y. Hu, H. L. Tsai, C. L. Huang, *Materials Science and Engineering: A.* **344**, 209 (2003).

- [41] P. I. Gouma, M. J. Mills, *Journal of the American Ceramic Society*. **84** **619**, (2001).
- [42] Dmitri B. Strukov, Gregory S. Snider, Duncan R. Stewart, and R. Stanley Williams, *Nature* **453**, 80 (2008).
- [43] H.-S. Philip Wong, Heng-Yuan Lee, Shimeng Yu, Yu-Sheng Chen, Yi Wu, Pang-Shiu Chen, Byoungil Lee, Frederick T. Chen, and Ming-Jinn Tsai, *Proceedings of the IEEE*, **100**, 1951 (2012).

Chapter 4

Investigating Structural Phase Transformation using Visible Raman Spectroscopy and Photo-absorption Behavior of Ti ion implanted TiO₂ thin films

4.1 Introduction

TiO₂ nanocrystals, appearing mostly in two dominant polymorphs of anatase and rutile, display an array of applications in the fields of biomedical sciences, solar cells, photocatalysis, photovoltaic cells, resistive switching memory devices, renewable and clean energy sources etc. [1,2]. With most of the fabrication routes producing mixed phases, their detection and transformation under non-equilibrium conditions present numerous challenges for establishing link with application platforms. Though rutile is the thermodynamically stable form, considerations of surface energy, along with free energy, determine the nanocrystal behavior [3]. Under this framework, at lower dimensions (~ 10 nm) when surface energy is high, anatase form of TiO₂ displays higher stability. Once coarsened, the free energy of the crystallite becomes dominant and rutile form is supported [3–5]. Such competing forces can be significantly effected by the presence of dopant and defects. Oxygen vacancies also play a very crucial role in stimulating these transformations by inherently modifying the structural rigidity [4,6]. Determining the structural form and its relative concentration is necessary for

understanding the fundamental framework controlling the behavior of any material and the associated novel properties.

Ion-beams can create a rich variety of structural modifications in a material via several non-equilibrium and far from equilibrium processes which can introduce metastable phases of amorphous or simple crystalline structures [7]. When energetic ions impinge on a solid they move through the medium and lose their energy primarily via two processes, nuclear energy loss (S_n) and electronic energy loss (S_e). At lower (keV) energies, S_n dominates the loss processes. Here, the energy is lost via elastic collisions of ions with the target nuclei. Such interactions can disturb the nuclei and can displace them from equilibrium positions. At higher (MeV) energies, S_e becomes relatively more important. As ions move inside the material, they predominantly excite the electrons through the inelastic collisions. The total amount of energy lost will be crucially governed by the energy of the impinging ion and is responsible for several modifications in the structure and associated properties. The dopant delivery, generated defect concentration and localized thermal spike related processes lead to many exceptional phenomenon even during low and medium energy ion irradiation, e.g. localized melting, structural phase transformations, grain boundary growth, interface mixing etc. [8–12]. Swift heavy ions involve even higher S_e dominated processes [13].

Investigations on phase transformation in TiO_2 are of significant importance due to their fundamental significance as well as their role in effecting many inherent properties. Although A-R transition with temperature has been explored in TiO_2 films and nanostructures prepared by variety of routes, influence of ion beams towards phase transformation has not been explored in literature in detail. In chapter 3, we focused on ion beam induced transformations in TiO_2 films after irradiation with 50 keV Ti ions. The results display a transition of anatase (A) nanocrystallites into rutile (R) beyond a critical fluence. An evolution of R zones, at the expense of A crystallites, established a framework where a competition between thermodynamics and surface energy seems to be regulating the process. These Raman investigations were performed under resonance conditions with UV probing laser. Resonance Raman is a surface sensitive probe, compared to the measurements with visible laser. For understanding the relative nature of R, A, and their associated phase transformation in

the deeper layers, in this chapter we have undertaken Raman measurements with the visible laser probe. Here also, R form increases at the expense of A beyond a critical fluence. The nanocrystalline characteristics and dimensional estimates of A form, during the phase transformation, have also been presented. The photo-absorption properties (PA) in the ultraviolet-visible (UV-Vis) range and the modulations in the bandgap behavior of TiO₂ thin films, upon ion irradiation, have also been investigated here. The results indicate that PA properties are getting modified and are governed by the structural transformations taking place in the films.

4.2 Experimental Section

80 ± 5 nm thick TiO₂ films were deposited, at room temperature, on Au/Ni/SiO₂/Si substrates using radio frequency magnetron sputtering technique. The gold film, on Ni/SiO₂/Si substrate, was deposited by e-beam evaporation method. The detailed parameters for the growth of gold and TiO₂ films are the same as given in chapter 3.

The TiO₂ films were implanted at the room temperature with 50 keV Ti ions. All the implantation parameters are the same [14] as used in chapter 3. The ion implantation was carried out at normal incidence in a chamber that was maintained at a pressure of 5 × 10⁻⁶ Torr. Several fluences of 1 × 10¹⁰, 1 × 10¹², 1 × 10¹³, 1 × 10¹⁴ and 1 × 10¹⁵ ions/cm² were used during implantation. SRIM code has been utilized to calculate the projected range and the longitudinal straggling of Ti ions in TiO₂ lattice [15]. These are respectively found to be 32 and 13 nm. Accordingly, the range of Ti ions is overall within the TiO₂ film.

X-ray photo-electron spectroscopy (XPS) measurements have been undertaken using a PHI 5000 VersaProbeII (ULVAC PHI, Inc.) system. It is equipped with a micro-focused (100 μm, 25 W, 15 KV) monochromatic Al -K_α source (1486.6 eV). It also consists of an hemispherical analyzer and a multichannel detector.

Raman scattering studies were carried out in backscattering geometry on a T64000 triple monochromator Horiba Jobin Yvon system with a liquid nitrogen cooled CCD detector. A visible (488 nm) laser was used. Other parameter were same as used in chapter 3. UV-Vis absorption spectra were recorded using Cary 5000 spectropho-

tometer with an integrating sphere using BaSO₄ as a standard.

X-ray diffraction (XRD) measurements were undertaken on a Bruker-D8 Discover system in θ - 2θ geometry. The scanning 2θ range was 22-72°. The XRD spectra were acquired in the grazing configuration with the incident angle of 0.5°.

4.3 Results and discussion

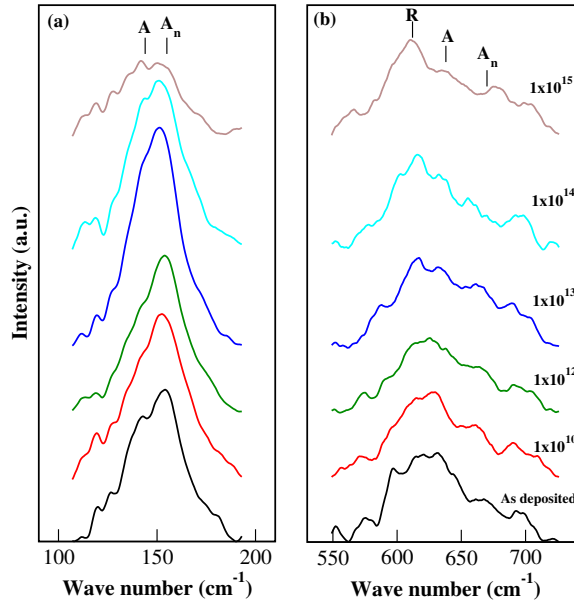


Figure 4.1: Raman spectra from as-deposited TiO₂ thin films and after ion implantation with various fluences (ions/cm²).

Raman is a powerful techniques for understanding structural phases and defects in any material. Rutile TiO₂ is tetragonal having a point group D_{4h}^{14} symmetry with two TiO₂ molecules per unit cell. The strongest anatase and rutile Raman modes, with visible (488 nm) probing laser, appear respectively at 144 cm⁻¹ (E_g) and 612 cm⁻¹ (A_{1g}) [16]. The rutile A_{1g} is a polar mode attributed to the out of phase vibration of apical and equatorial oxygen ions along the unit dipole vector. Fig. 4.1 shows the presence of both rutile (R) and anatase (A) Raman modes in the as-deposited TiO₂ films. The films are thus of mixed type containing both R and A. The low frequency region (110-190 cm⁻¹) consists of A (E_g) mode which appears very broad as well as displays another feature (A_n) shifted towards larger wavenumbers. E_g modes are very sensitive to oxygen defects, and the appearance of A_n feature is attributed to

the presence of oxygen vacancies in nanophase anatase TiO_2 [14, 17–20]. The high frequency ($550\text{--}725\text{ cm}^{-1}$) Raman spectrum from the as-deposited TiO_2 film shows presence of both R and A phases with R(A_{1g}) at 612 cm^{-1} and A(E_g) at 639 cm^{-1} (fig. 4.1(b)). Similar to the lower wavenumbers (fig. 4.1(a)), here also A displays broadening and shift towards larger wavenumbers. Feature A_n , ascribed to oxygen vacancies and nanosized anatase TiO_2 , is also observed [18].

Raman Spectra from TiO_2 films after their implantation with Ti ions, at various fluences, are also shown in Fig. 4.1. These films also illustrate presence of both R and A phases. In order to understand the behavior of these modes with increasing ion fluence, the detailed studies of the low and high frequency Raman regimes have been undertaken.

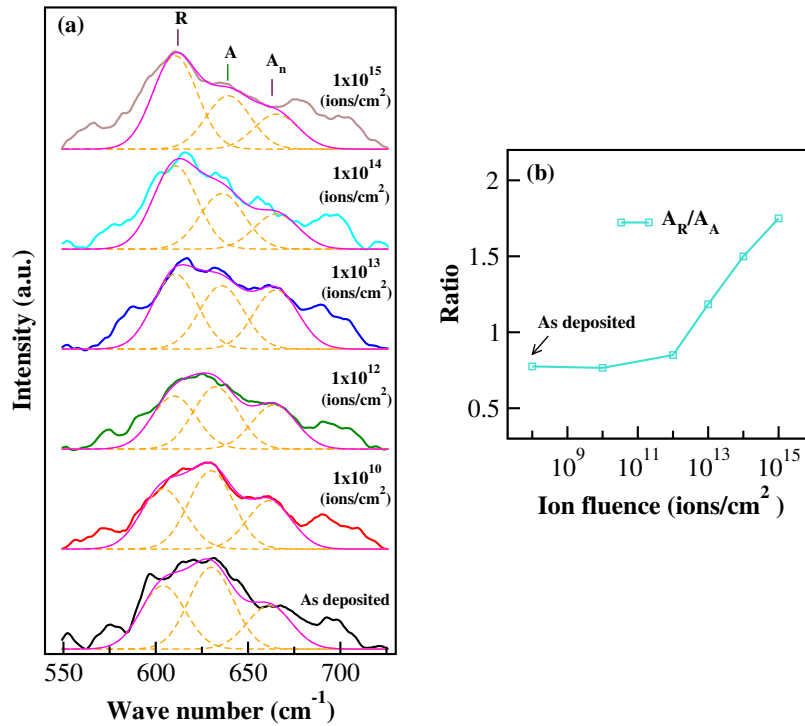


Figure 4.2: (a) Raman spectra in the high-frequency region from as-deposited TiO_2 thin films and after ion implantation with various fluences (ions/cm^2) along with fitting components for R, A and A_n (b) Ratio A_R/A_A as a function of ion fluence.

Fig. 4.2(a) exhibits the expanded view of Raman spectra in the high frequency ($550\text{--}725\text{ cm}^{-1}$) region. For as-deposited films, along with a strong rutile R mode, anatase feature A and A_n are also observed. Oxygen vacancies and nanosized anatase

contribute to A_n feature in TiO_2 [18]. Some modes can also be observed at wave numbers higher than A_n . Smaller anatase nanophased zones with richer oxygen vacancies may cause this [18]. Rutile mode is of A_{1g} type whereas anatase modes have E_g character. Earlier studies have shown that R mode undergoes downward dispersion in the presence of rutile nanoparticles [19]. In fig. 4.2(a), this mode indeed shows an asymmetric broadening towards the lower wave numbers. This asymmetry is largest at the highest fluence (1×10^{15} ions/cm²) indicative of the presence of nano-sized particles. These spectra get severely modified as the ion fluence is increased. The rutile mode (612 cm^{-1}), for example, develops into a more prominent feature with increasing fluence. Spectra in fig. 4.2(a) have been fitted with three gaussian components due to R, A and A_n and their respective areas A_R , A_A and A_{A_n} have been estimated. The ratio of intensities of rutile w.r.t. anatase i.e A_R/A_A is shown in fig. 4.2(b) as a function of ion fluence. Although A_R/A_A does not change much up to the fluence of 1×10^{12} ions/cm², it increases rapidly at higher fluences. This suggests that some structural phase transformation, from anatase to rutile, is occurring at 1×10^{13} ions/cm². At this critical fluence, the rutile content in the film, compared to anatase, drastically increases. The critical fluence observed here is slightly smaller than that observed in chapter 3 under resonance Raman conditions. With UV laser (in Resonance Raman experiments) penetrating only the top 12- 25 nm surface region in TiO_2 film [21], but visible laser used in the present chapter, penetrating and probing the full (80 nm) film, a little lower fluence observed here may reflect towards a critical fluence that is depth dependent.

The low frequency (110-190 cm^{-1}) Raman spectra are shown in fig. 4.3(a). A strong $A(E_g)$ (144 cm^{-1}) is observed in the as-deposited as well as all ion implanted films. Here also, many significant changes can be observed post-implantation. The intensity of A mode, for example, increases up to 1×10^{13} ions/cm² but then reduces and becomes very small at the highest fluence (1×10^{15} ions/cm²). Oxygen vacancies can substantially influence the properties of TiO_2 films. The large shifts in the $A(E_g)$ mode, due to oxygen vacancies, contribute to A_n feature [17,18] which is also observed in all, as-deposited as well as ion implanted films. These spectra (fig. 4.3(a)) have been fitted with two gaussian functions due to A and A_n and their respective areas

A_A and A_{A_n} have been calculated. Ratio of A_A with respect to A_R (of rutile mode at 612 cm^{-1} in fig. 4.2(a)) are shown in fig. 4.3(b). Here too, A_R/A_A displays a rapid enhancement after $1 \times 10^{13}\text{ ions/cm}^2$. Peaks due to A in the low and high frequency Raman regimes are related to different characteristic phonon modes, yet both the regions display similar trends after the critical fluence where R content appears to grow at the expense of A.

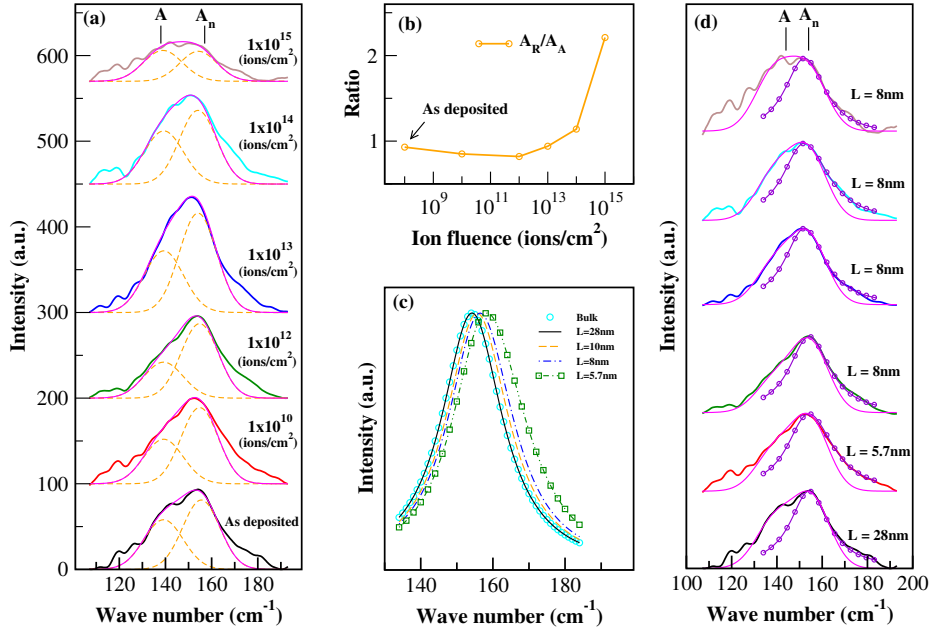


Figure 4.3: (a) Raman spectra in the low-frequency region from as-deposited TiO_2 thin films and after ion implantation with various fluences (ions/cm^2), along with fitting components for A and A_n (b) Ratio A_R/A_A as a function of ion fluence (see text). (c) Raman profiles as obtained using PCM for $L = 5.7, 8.0, 10.0$ and 28 nm . Profile for bulk is also shown. PCM is described by Eq. 3.2 where L is size of anatase nanoparticles (d) Raman mode A_n has been fitted using PCM ($\circ\text{-}\circ$) and L is size of anatase nanoparticles as determined by the PCM fit to the data.

Ion implantation can induce nucleation of nanoparticles [22] and it can also generate defects which may support nucleation of such nanozones. As discussed, A_n reflects the presence of nano-dimensional anatase with oxygen vacancies. This mode also exhibits an asymmetric peak broadening towards high wavenumbers. Earlier studies on Si, InP and TiO_2 [22–25] have also exhibited asymmetric broadening in Raman signal reflecting phonon- confinement effects. Such studies show that implantation in thin films can lead to the development of nano- crystalline zones, with dimensions smaller

than phonon coherence length [22–24]. Asymmetry in Raman spectrum reflects the confinement of such phonons by the small crystalline zones created during irradiation [22–24]. Asymmetry in A_n mode can provide knowledge of phonon confined nanograin sizes that will be important for understanding the evolution of structural and absorption properties in TiO_2 thin films.

With confinement of phonons, the phonon coherence length is reduced and the $k = 0$ selection rule gets relaxed [22]. This induces shifts and asymmetric broadening of the Raman modes. With the break down of lattice translational symmetry, the phonon confinement model (PCM) proposed by Richter et al. [26], and discussed in chapter 3, can be applied to estimate the phonon confinement length or the size of the nanocrystals (L) in thin films. For estimating the anatase nanocrystal sizes in the TiO_2 films, the PCM has been applied to the anatase-nano (A_n) mode and its intensity is given by equations 3.2 to 3.4.

Figure 4.3(c) displays the theoretical Raman intensity profiles calculated using Eq.3.2 for various nanocrystal size diameters (L) 28, 10, 8, 5.7 nm. As the nanostructure-sizes reduce, the asymmetry of the mode as well as its width increases. In this situation, phonons away from the zone center are involved in the confinement. These results represent a picture of Raman mode variation in the presence of nanocrystallites [19].

By fitting the experimental Raman spectra A_n (of fig. 4.3(a)) with PCM, the size (L) of the anatase nanocrystallites have been determined in the ion irradiated TiO_2 thin films and the results ($\circ-\circ$) are shown in Fig. 4.3(d). The asymmetry of the Raman band shape is excellently reproduced by the PCM results in the high wave numbers. Interestingly, the results indicate that the as-deposited films have anatase nanocrystallites of about 28 nm size. We note that similar sizes of anatase nanocrystals have been earlier reported in the as-grown TiO_2 films [27]. The size of the nanocrystallites, however gets reduced after ion implantation and is found to be nearly 5.7 nm after 1×10^{10} ions/cm² and about 8 nm at other fluences (fig. 4.3(d)). Thus, though as-deposited films show the presence of bigger TiO_2 anatase nanoparticle, implanted films also contain nanosizes of 6-8 nm dimensions. In agreement with these estimations, phonon confinement results acquired under Resonance Ra-

man conditions in chapter 3 showed that though the as-deposited films contained larger (~ 28 nm) anatase nanoparticles, reduced (~ 12 - 13 nm) nano sizes are also present after implantation. In chapter 3, Scherrer relation was also applied to GIXRD A(101) feature to determine the anatase nanoparticles sizes. These were also found to be about 20 nm in the as-deposited films and nearly 6-8 nm in the ion implanted films. Surface thermodynamics of anatase nanoparticles is an important determining factor for A - R transformation. Although rutile is the more stable form, for very small crystallites (~ 10 nm) anatase is the more stable phase [3–5]. The interfaces of anatase nanocrystals are the active centers of nucleation of rutile phase. Rutile content in the ion implanted TiO_2 films has also been investigated, in chapter 3, by utilizing Rutile(110) GIXRD feature. In the following, we explore the GIXRD results for higher 2θ values.

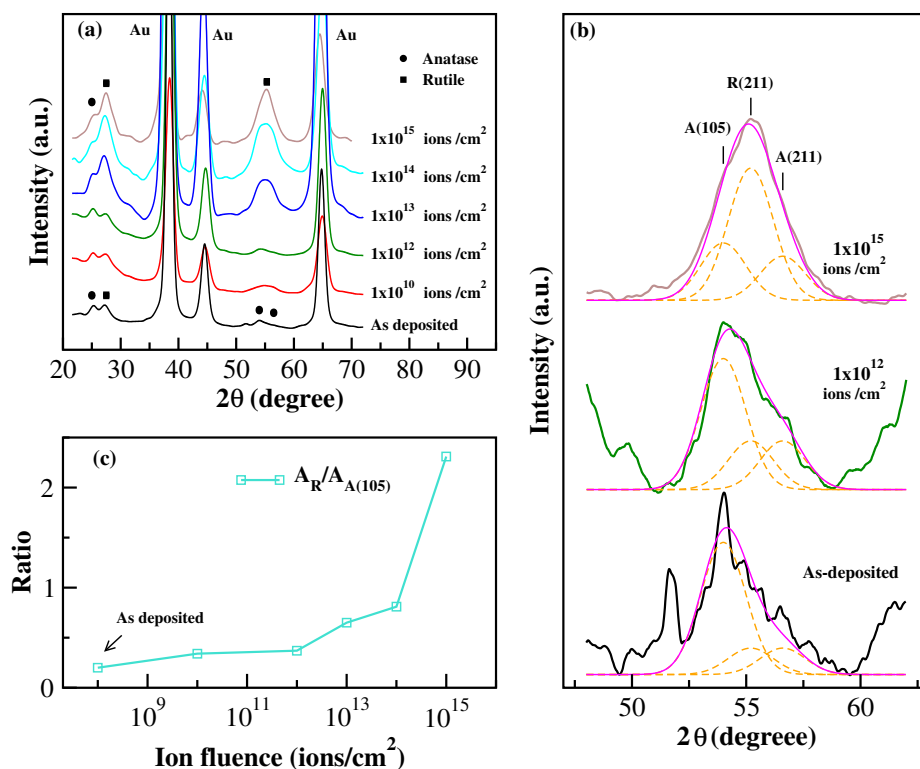


Figure 4.4: (a) GIXRD from as-deposited TiO_2 thin films and after ion implantation at various fluences. (b) GIXRD (range 47.5 to 62.5°) from as-deposited TiO_2 thin films and after ion implantation at 1×10^{12} and 1×10^{15} ions/cm². (c) $A_R/A_{A(105)}$ as a function of ion fluence.

Figure 4.4 illustrates the XRD patterns of the pristine and ion implanted TiO_2

films. The as-deposited as well as ion implanted films contain a mixture of Rutile and Anatase phase. The as deposited films show some weak and broad peaks at 2θ of 25.34, 53.86, and 56.15° representing the (101), (105) and (211) planes of anatase [3,28,29]. Features at 27.57, and 55.13° correspond to indices of (110) and (211) planes of rutile phase [28–30].

Some expanded XRD patterns in the range of 47.5-62.5° reveal (see fig. 4.4(b)) presence of an intense A(105) feature in the as-deposited films, as also after implantation at 1×10^{12} ions/cm². In both the cases, Rutile R(211) feature is weaker. However, after implantation at the highest fluence (1×10^{15} ions/cm²), the intensity of A(105) decreases while that of R(211) increases. This is demonstrated by $A_R/A_{A(105)}$ (fig. 4.4(c)), where A_R and $A_{A(105)}$ are the integrated intensities of R(211) and A(105), respectively. These results also reflect a critical fluence of 1×10^{13} ions/cm², where a significant increase in the ratio is noticed. A similar effect was also seen, in chapter 3, at low 2θ values where though R(110) and A(101) had nearly similar intensities in the as-deposited film and after implantation at low fluences, their areal ratio (A_R/A_A) increased rapidly after 1×10^{13} ions/cm². In the present chapter GIXRD as well as Raman spectroscopic measurements display presence of both A and R phases in the ion implanted TiO₂ films that undergo A to R transformation at the critical fluence. Moreover, all these studies suggest a similar critical fluence of 1×10^{13} ions/cm². As the resonance Raman studies, with UV laser probing only top (12- 25 nm) surface region [21] in chapter 3, suggested a critical fluence of 1×10^{14} ions/cm², it is possible that surface regions may require a little higher fluence for undergoing such A-R transformations.

The core level XPS spectra from O(1s) region are shown in fig. 4.5(a) for the as-deposited as well as ion implanted films. For the as-deposited film two main features, at 529.3 and 531.0 eV are observed. These are respectively related to the lattice oxygen from TiO₂ and the oxygen vacancy states (O_v) [31]. XPS spectra have been fitted with two components and an increase in the oxygen vacancy content, with Ti ion fluence, is noticed (fig. 4.5(b)). Implantation of TiO₂ with metallic ions induces preferential sputtering of oxygen atom causing the development of oxygen vacancy states on the surface [32–35]. Within this process, electrons from oxygen sites transfer

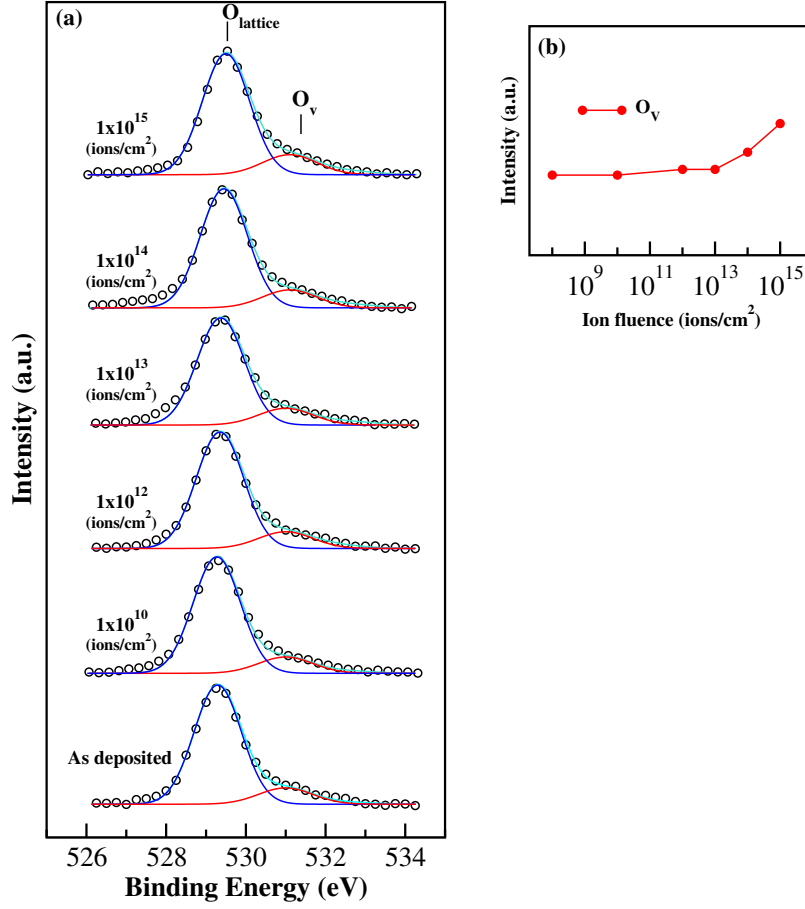


Figure 4.5: (a) O(1s) XPS spectra from as-deposited TiO₂ thin films and after ion implantation with various fluences. Peaks have been fitted with two components related to bulk lattice oxygen ($O_{lattice}$) and oxygen vacancies (O_v). (b) The area under O_v is shown as a function of ion fluence.

to the empty 3d orbitals of the Ti atoms on the surface [36]. This process enhances with fluence causing an increased oxygen vacancy states on the surface. Creation of oxygen vacancy also leads to the development of Ti interstitial centers on the surface [25, 32]. The two in conjunction play important role in guiding the lattice dynamics of TiO₂ surface which displays many modifications in Raman behavior after implantation.

UV-Vis absorption behavior reflects the characteristics of inherent phases as well as implantation induced dopants and defects. The diffuse reflectance UV-Vis spectra from TiO₂ films are presented in fig. 4.6. Films after high fluence implantation, delineate relatively larger absorbance compared to the as-deposited in the 400 - 700 nm

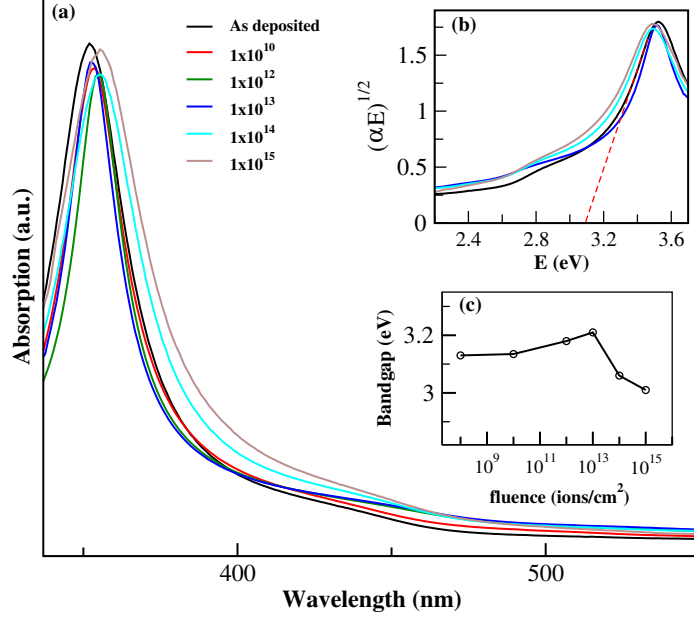


Figure 4.6: (a) Photo-absorbance response for as-deposited TiO₂ thin films and after ion implantation with various fluences (ions/cm²) (b) Tauc plots at various fluences (α is absorption coefficient and E is photon energy) (c) Bandgap as a function of ion fluence.

range (data up to 550 nm is shown in fig. 4.6). A weak blue shift towards lower wavelengths in the band edge has been noticed, compared to the as-deposited, for low fluences of 1×10^{10} to 1×10^{13} ions/cm². Interestingly for higher fluences, the band edge becomes red shifted. Both Raman Spectroscopy and GIXRD measurements have suggested a critical fluence of 1×10^{13} ions/cm² where a rapid enhancement of R content compared to A occurs. Such structural transformation in thin TiO₂ films may be crucially responsible for the band edge changes observed here. Growth and development of nanodimensional zones and defects will also play a role. Tauc plots provide important information about the band gap energy (E_g). The absorption coefficient (α) is given by the following relation:

$$\alpha \propto (E - E_g)^{m/2}. \quad (4.1)$$

Here, E is the photon energy and for TiO₂, that allows only indirect transitions, $m=1$ [37]. The plots of $(\alpha E)^{1/2}$ as a function of E (in fig. 4.6(b)) have been utilized to extract E_g . Rutile and anatase phases, respectively, display an indirect band gap of

3.0 and 3.2 eV [38–40]. The as-deposited films show an indirect band gap of 3.13 eV (in fig. 4.6(c)). This will be expected since TiO₂ films here contain a mixture of both R and A. The band gaps are shown in fig. 4.6(c) as a function of ion fluence. Although not much modification in bandgap has been observed at low ion fluences, a drastic decrease occurs beyond the fluence of 1×10^{13} ions/cm². This effect can be ascribed to the phase transformation from A to R at the critical fluence. At the highest fluence, the band gap of 2.98 eV presents a scenario where most of the content in the films may be in R form. These results concur with the Raman and GIXRD measurements presented here.

4.4 Conclusions:

Visible Raman spectroscopy has been utilized here to understand the structural phase transformations occurring in thin TiO₂ films after their implantation with 50 keV Ti ions. R and A modes, from both the low and high frequency regions, have been investigated by Raman spectroscopy. These results, as well as GIXRD measurements, suggest a critical fluence of 1×10^{13} ions/cm² where the R content in the films increases whereas A content decreases. This transformation occurs via the aggregation of anatase crystallites and their thermodynamic stability, controlled via their sizes, play an important role in regulating this phenomenon. Phonon confinement description, used to estimate the nanodimensional sizes of anatase during phase transformation, demonstrates that though the nanoparticles are bigger (~ 28 nm) in the as-deposited film, reduced (~ 6 -8 nm) crystallite sizes are also present in the ion implanted films. These results are in agreement with Resonance Raman measurements presented in chapter 3. Photo- absorption measurements display a shift of band edge as a function of ion fluence. Compared to the as-deposited films, a weak blue shift is observed at the fluences lower than the critical fluence, whereas a red shift occurs at higher fluences. Along with the contribution of nanodimensional crystallites and defects, this suggests an important influence of A-R transformation.

Bibliography

- [1] H. Li, Y. Zhang, S. Wang, Q. Wu, and C. Liu, *J. Hazard. Mater.* **169**, 1045 (2009).
- [2] U. Diebold, *Surf. Sci. Rep.* **48**, 53 (2003).
- [3] H. Zhang, J.F.J. Banfield, *Mater. Chem.*, **8**, (1998) 2073.
- [4] Dorian A. H. Hanaor, Charles C. Sorrell, *J Mater Sci*, **46**, 855 (2011)
- [5] A.A. Gribb, J.F. Banfield, *Am. Mineral*, **82**, 717 (1997)
- [6] K.J.D. Mackenzie, *Trans. J. Br. Ceram. Soc.*, **74**, 29 (1975)
- [7] B.X. Liu, W.L. Johnson, M.A. Nicolet, S.S. Lau: *Appl. Phys. Lett.*, **42**, 45 (1983)
- [8] M. Nastasi and J. Mayer, *Ion Implantation and Synthesis of Materials* (Springer Series in Materials Science) 2006.
- [9] S. M. S. Privitera, A. M. Mio, E. Smecca, A. Alberti, W. Zhang, R. Mazzarello, J. Benke, C. Persch, F. La Via, and E. Rimini, *Phys. Rev. B*, **94**, 094103 (2016).
- [10] P. Sule, M. Menyhard, K.Nordlund, *Nucl. Instru. and Meth. in Phys. Res. B*, **211**, 524 (2003).
- [11] V. V. Ovchinnikov (1994) Self-propagating phases transformations in metastable media induced by ion bombardment *Proc. XVI International Symposium on Discharges and Electrical Insulation in Vacuum 2259* ed. Mesyats G A (Moscow-St.Petersburg. SPIE) p 605-608
- [12] D. Kaoumi, A. T. Motta, and R. C. Birtcher, *J. Appl. Phys.*, **104**, 073525 (2008).

- [13] Udai B. Singh, Compesh Pannu, Dinesh C. Agarwal, Sunil Ojha, Saif A. Khan, Santanu Ghosh, and Devesh K. Avasthi, *J. Appl. Phys.*, **121**, 095308 (2017).
- [14] Ashis Manna, A. Barman, Shalik R. Joshi, B. Satpati, P. Dash, Ananya Chattaraj, S. K. Srivastava, P. K. Sahoo, A. Kanjilal, D. Kanjilal, Shikha Varma, *J. Appl. Phys.*, **124**, 155303 (2018).
- [15] J. F. Ziegler, J. P. Biersack and M. D. Ziegler, *SRIM -The Stopping and Range of Ions in Matter* (SRIM Co., Chester, MD,USA, 2008).
- [16] S. P. S. Porto, P. A. Fleury, and T. C. Damen, *Phys. Rev.*, **154**, 522 (1967).
- [17] W. F. Zhang, Y. L. He, M. S. Zhang, Z. Yin and Q. Chen, *J. Phys. D: Appl. Phys.*, **33**, 912 (2000)
- [18] J. C. Parker and R.W. Siegel, *J. Mater. Res.*, **5**, 1246 (1990).
- [19] D. Bersani and P. P. Lottici, and Xing-Zhao Ding, *Appl. Phys. Lett.*, **72**, 73 (1998)
- [20] S. Music, M. Gotić, M. Ivanda, S. Popović, A. Turković, R. Trojko, A. Sekulić, K. Furic, *Materials Science and Engineering B*, **47**, 33 (1997)
- [21] Ana Stevanović, Michael Buttner, Zhen Zhang, and John T. Yates, Jr., *J. Am. Chem.Soc.*, **134**, 324 (2012)
- [22] Soma Dey, C. Roy, A. Pradhan, Shikha Varma, *Jour. Appl. Phys.*, **87**, 1110 (2000)
- [23] D. Paramanik, Shikha Varma, *J. App. Phys.*, **101**, 023528 (2007)
- [24] D. Paramanik, Asima Pradhan, Shikha Varma, *Jour. App. Phys.*, **99**, 014304 (2006)
- [25] Subrata Majumder, D. Paramanik, V. Solanki, I. Mishra, D.K. Avasthi, D. Kanjilal, and Shikha Varma, *Appl. Phys. Lett*, **258**, 4122 (2012)
- [26] H.Richter, Z.P.Wang and L.Ley, *Solid State Commun.*, **39**, 625 (1981).

- [27] Ibrahim A. Alhomoudi, G. Newaz, Thin Solid Films, **517**, 4372 (2009)
- [28] Jing Zhang, Meijun Li, Zhaochi Feng, Jun Chen, and Can Li, J. Phys. Chem. B, **110**, 927 (2006)
- [29] T. Sreethawong, Y. Suzuki, S. Yoshikawa S, J Solid State Chem, **178**, 329 (2005)
- [30] J. Dhanalakshmi, S. Iyyapushpam, S. T. Nishanthi, M. Malligavathy and D. Pathinettam Padiyan, Adv. Nat. Sci.: Nanosci. Nanotechnol., **8**, 015015 (2017)
- [31] Sang-Joon Park, Jeong-Pyo Lee, Jong Shik Jang, Hyun Rhu, Hyunung Yu, Byung Youn You, Chang Soo Kim, Kyung Joong Kim, Yong Jai Cho, Sunggi Baik and Woo Lee, Nanotechnology, **24**, 295202 (2013)
- [32] V. Solanki, S. Majumder, I. Mishra, P. Dash, C. Singh, D. Kanjilal and S. Varma, J. Appl. Phys., **115**, 124306 (2014).
- [33] Subrata Majumder, D. Paramanik, V. Solanki, B.P. Bag and Shikha Varma, Appl. Phys. Lett., **98**, 53105 (2011)
- [34] Shalik Ram Joshi, B. Padmanabhan, Anupama Chanda, V. K. Malik, N. C. Mishra, D. Kanjilal, Shikha Varma, Appl.Sur. Sci., **387**, 938 (2016)
- [35] S. R. Joshi, T. Bagarti, S. Varma, Surf. Sci., **641**, 170 (2015).
- [36] Z. Zhao, X. Zhang, G. Zhang, Z. Liu, D. Qu, X. Miao, P. Feng, and Z. Sun, Nano Research, **8**, 4061 (2015)
- [37] A. E. Jimenez Gonzalez and S. Gelover Santiago, Semiconductor Science and Technology, **22**, 709 (2007)
- [38] D Reyes-Coronado, G Rodriguez-Gattorno, M E Espinosa-Pesqueira , C Cab, R de Coss and G Oskam, Nanotechnology, **19**, 145605 (2008)
- [39] H. Tang, K. Prasad, R. Sanjines, P.E. Schmid, F. Levy, J. Appl. Phys., **75**, 2042 (1994)
- [40] N. Daude, C. Gout, C. Jouanin, Phys. Rev. B, **15**, 3229 (1977)

Chapter 5

Surface evolution of TiO₂ thin films after Ti ion implantation

5.1 Introduction

Recently, nanostructures of oxide semiconductors have attracted considerable attention for fundamental as well as application oriented research. These nanostructures exhibit various interesting and exceptional properties in variety of research fields such as sensors, opto-electronic devices, multi-ferroics, spintronics, self-cleaning surfaces, photocatalyst, environmental remediation etc. [1–7]. Among oxides, TiO₂ displays many unique and interesting properties [7, 9]. It is a wide band gap semiconductor with two prominent phases: anatase (bandgap 3.2 eV) and rutile (bandgap 3.0 eV). Varying TiO₂ surface morphologies induce several exciting and advanced properties with multitudes of applications in the field of solar cells, photocatalysis, magnetic storage media, bio-implants, waste water management, environmental remediation etc. [7–12]. These properties get further influenced by the development of nanostructures and generation of defects on the surfaces [7, 9]. Therefore, crucial importance is imparted for synthesizing surfaces of specific morphologies which in turn can induce some desired properties [13–15]. For this goal, ion beam irradiation has attracted immense attention. It is of vast importance in semiconductor industry. It provides a technologically simple and single-step methodology for fabricating nanostructured surfaces [7, 16, 17]. Being a top-down synthesis technique, it is capable of producing rich variety of nanostructures and self-assembled patterns on the surfaces [7, 16–19]. Control of ion beam parameters and energy scales have led to fascinating surface

morphologies. This approach of generation of self assembled nanostructures provides a simple and unique technique for achieving surfaces with interesting, advanced and tunable properties [5, 7, 16–24].

During ion irradiation as the ion traverses the material, it loses energy due to energy loss processes. Two main energy loss processes are: nuclear energy loss (S_n) and electronic energy loss (S_e). The energy loss processes strongly depend on the energy of the incoming ion [25]. S_n is an elastic process and is significant at higher (MeV) energies whereas S_e is an inelastic process and plays a more crucial role at lower (keV) energies. The surface morphology, after ion irradiation, is primarily controlled by two competing processes like erosion and diffusion [24]. Erosive processes, that induce instability in the surface, and curvature dependent sputtering, that becomes important for structure formation, together control the surface morphology. S_n loss processes are responsible for the displacement of atoms from their respective positions, producing damage within the material. This can sometimes induce track-like defects along the path of the traveling ion [26]. However, energy loss also leads to diffusive processes causing the self-annealing [27] of the damage and smoothing of the surfaces [28–30]. For multi-atom oxide surfaces, preferential sputtering of low mass ions provides another avenue for developing metal rich nano-zones. These zones play an important role in the development of nanostructures on many single-crystal semiconductor oxide surfaces [7, 17].

Based on above scenario, many theoretical models have been proposed for understanding the mechanisms which control the formation of self-assembled nanopatterned surfaces. The importance of the curvature dependent sputtering has been introduced by Bradley and Harper (BH) in their theory for the evolution of amorphous surfaces [24, 31]. The step-edge Ehrlich-Schwoebel barrier is also important in the case of metal and oxides surfaces [32]. Furthermore, several processes such as anisotropic diffusion, non-linear effects, re-deposition, solid mass flow, etc. [33, 34] also play significant role in surface evolution. All these processes cannot be incorporated in a single model and hence dynamic scaling studies become essential. The necessary processes, involved in the generation of the self-assembled nano-structures, can be extracted by applying proper scaling theories. The scaling studies are useful in understanding the

parameters and phenomenon essential for surface morphologies and their evolution. Within the dynamic scaling hypothesis, introduced by Family-Vicsek, the interface width or rms roughness ($\sigma(L, t)$) of such surfaces show scaling behavior in spatial and temporal regimes [35, 36]. The exponents extracted from these scaling studies provide important information on the universality class to which the surface evolution belongs [35]. They also present a framework for understanding the surface evolution under varying processing conditions. Several such studies have been reported on the formation of nano-patterned and self-assembled surfaces after ion irradiation. On TiO₂ and ZnO single crystal surfaces [7, 37–39] scaling studies depict the role of preferential sputtering. There are however no studies of TiO₂ thin films. Modified energy dissipation, damage in the thin film and varying sputtering rates at the film interface can contribute to results different from bulk single crystal.

The present chapter describes the surface evolution of the TiO₂ thin films after 50 keV Ti ion irradiation. The scaling properties have been studied by height-height correlation (HHC) and power spectral density (PSD) analysis. The roughness exponent (α) estimated here, indicates that the surfaces are self-affine with their rms roughness (σ) decreasing with fluence. The negative value of the growth exponent (β) suggests a diffusion dominated smoothing process that is controlling the surface morphology. The HHC investigations reveal a decrease in the correlation length with fluence, implying a reduction in the nano-structural dimensions.

5.2 Experimental

Thin films of TiO₂ (thickness 80 ± 5 nm) were irradiated with 50 keV Ti ions at normal incidence using ECR based LEIBF facility at IUAC, New Delhi. The TiO₂ thin films were deposited on Au/Ni/SiO₂/Si substrate by radio frequency magnetron sputtering technique. Details of the thin film deposition and ion irradiation have been reported in chapter 3 and 4. Irradiation with Ti ions was carried out with fluences of 1×10^{10} , 1×10^{12} , 1×10^{13} , 1×10^{14} and 1×10^{15} ions/cm². The flux for lowest three fluences was 3×10^9 ions/cm².sec whereas the flux was 1.7×10^{11} ions/cm².sec for other fluences. The irradiation was performed at room temperature in a target chamber with a base

vacuum of 5×10^{-6} Torr. The penetration depth and the longitudinal straggling of Ti ions, in TiO_2 films, have been estimated to be 32 and 13 nm, respectively, using SRIM code [40].

The evolution of the surface morphology has been investigated by Atomic Force Microscope (AFM) from Bruker (Nanoscope V) in tapping mode. Nearly 100 AFM images were acquired at several regions of the TiO_2 thin films in ambient condition. Images were taken for several scan sizes varying from 500 nm to 10 μm . Power spectral density (PSD) and height-height correlation (HHC) analysis have been carried out by utilizing the AFM data.

5.3 Results and discussion

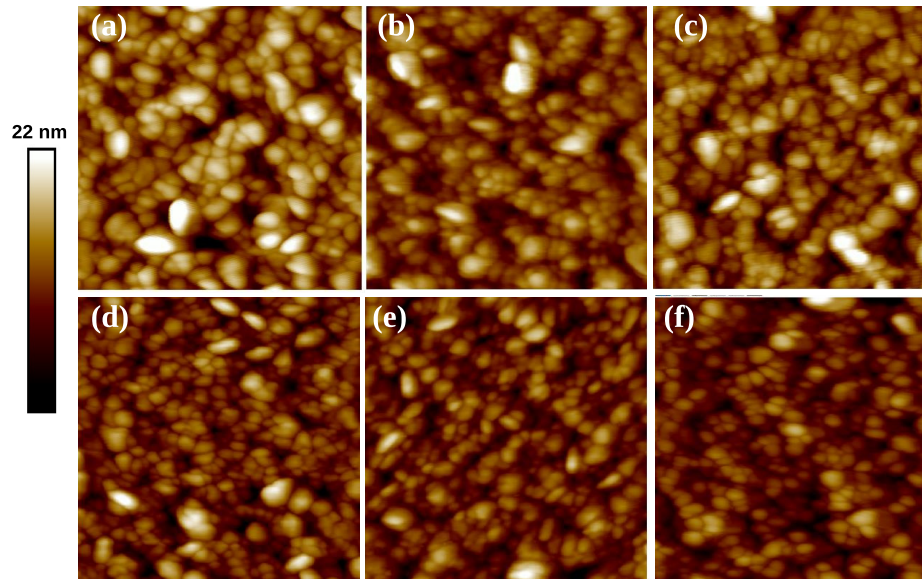


Figure 5.1: 2D AFM images ($500 \times 500 \text{ nm}^2$) of (a) as-deposited TiO_2 thin film and after ion irradiation with fluences of (b) 1×10^{10} (c) 1×10^{12} (d) 1×10^{13} (e) 1×10^{14} and (f) $1 \times 10^{15} \text{ ions/cm}^2$.

Figure 5.1 shows the morphological evolution of the as-deposited and various ion irradiated TiO_2 thin films. The corresponding high resolution 3D images are shown

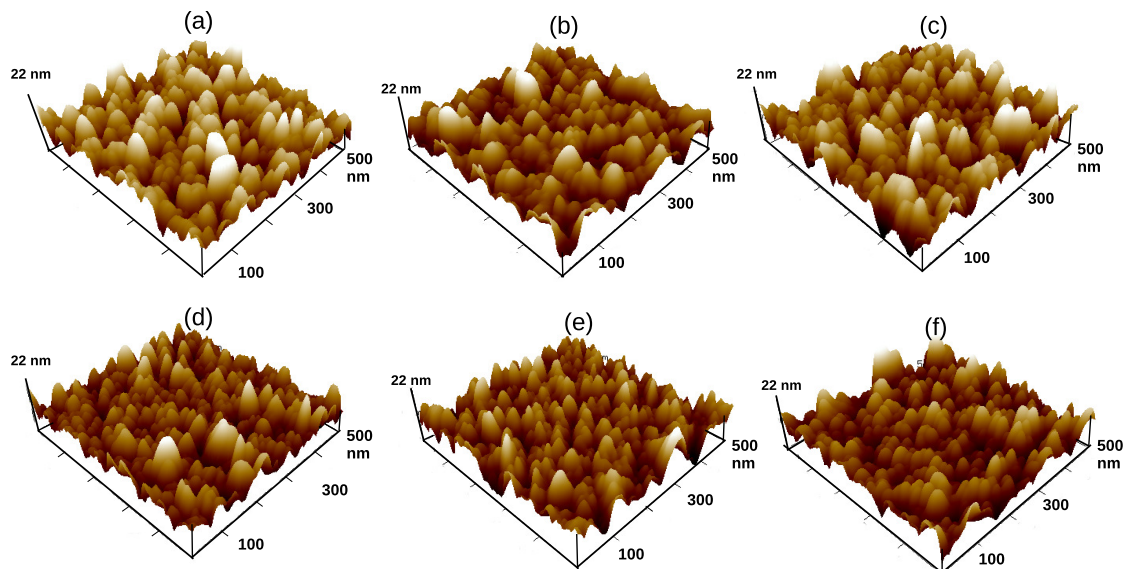


Figure 5.2: 3D AFM images ($500 \times 500 \text{ nm}^2$) of (a) as-deposited TiO_2 thin film and after ion irradiation with fluences of (b) 1×10^{10} (c) 1×10^{12} (d) 1×10^{13} (e) 1×10^{14} and (f) $1 \times 10^{15} \text{ ions/cm}^2$.

in Fig. 5.2. The as-deposited film displays presence of nanostructures (NS) of sizes ranging from 15 to 50 nm (fig 5.3). The average size of the nanostructures is observed to decrease with fluence, varying from 27 nm for the as-deposited sample to nearly 21 nm for the samples irradiated at the highest fluence of ($1 \times 10^{15} \text{ ions/cm}^2$). The average height of the nanostructures also reduces after ion irradiation. This average NS-height is about 13 nm in the as-deposited films and decreases to about 8 to 10 nm for ion irradiated films (Fig. 5.1,5.2). Such inverse ripening of nanostructures have been reported earlier [28–30]. Here, using AFM it is not possible to assess the phases of the nanostructures. In addition to the reduction in the average size of the nanostructures with fluence, a decrease in surface rms roughness is also noticed. For the as-deposited sample the rms roughness is nearly 3.22 nm but after the irradiation at the highest fluence ($1 \times 10^{15} \text{ ions/cm}^2$) it is only 2.25 nm. Fig. 5.1 also shows the presence of some void (dark) regions in as-deposited films. The formation of

such nano void regions have also been reported for irradiated TiO_2 thin films [42,43]. Here, these voids appear to become smaller with irradiation. Hence reduction in NS diameter and height, conjugated with filling of voids seems to introduce smoothing of the irradiated surfaces (fig. 5.1). In thin films, nanostructured grain boundaries and voids can become the sink for defects which can facilitate surface smoothing [41].

The dynamics of the surface evolution during ion irradiation is controlled by many competing processes. The curvature dependent sputtering induces erosion and instabilities on the surface. The ion bombardment also creates vacancy clusters [44]. In contrast, the adatom diffusion assists in restoring the equilibrium on the surface [44]. The smoothing of the surface can be explained via diffusion of adatoms [16, 18], created during ion bombardment. Inverse ripening and fragmentation of nanostructures along with a mass flow has also been shown, by Paramanik et al. [28–30], to be responsible for smoothing of $\text{InP}(111)$ surfaces after keV Ar^+ irradiation.

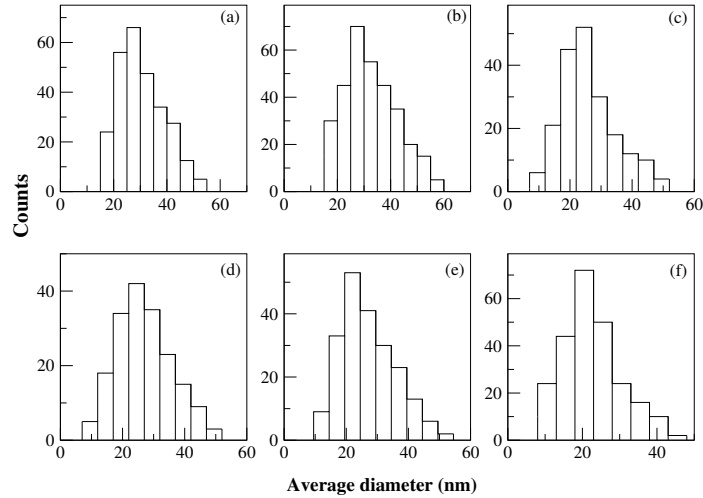


Figure 5.3: Size distribution (diameter) of nanostructures for (a) as-deposited TiO_2 thin film and after ion irradiation with fluences of (b) 1×10^{10} (c) 1×10^{12} (d) 1×10^{13} (e) 1×10^{14} and (f) 1×10^{15} ions/cm^2 .

The evolution of a surfaces or an interface during ion irradiation occurs via non-equilibrium processes. A dynamic scaling theory can be applied to describe the growth of such surfaces. The rms roughness (σ), or interface width, of any surface can be described as [35, 36]:

$$\sigma = \langle [h(x,y) - \langle h(x,y) \rangle]^2 \rangle^{1/2} \quad (5.1)$$

Here, height at position (x,y) on the surface is represented as h(x,y). The growth via non-equilibrium processes often exhibit self-affine surfaces. A self-affine surface remains statistically invariant under an anisotropic dilatation. This is in contrast to a self-similar surface which is invariant only under isotropic dilatation. The rms roughness (σ) of a self-affine surface scales w.r.t. time, t , and the length, L , according to Family-Vicsek dynamic scaling theory [35, 45]:

$$\sigma(L,t) = L^\alpha f(t/L^{\alpha/\beta}) \quad (5.2)$$

Two asymptotic limit can be obtained as:

$$\sigma(L,t) \propto \begin{cases} L^\alpha & \text{if } t/L^{\alpha/\beta} \rightarrow \infty \\ t^\beta & \text{if } t/L^{\alpha/\beta} \rightarrow 0 \end{cases} \quad (5.3)$$

Here, α and β are the roughness and growth exponents, respectively, which can be estimated by utilizing the above equations. The roughness of the interface and its time dependent dynamics can be described by these exponents. α and β [35, 36] are the two important exponents which characterize any specific growth process.

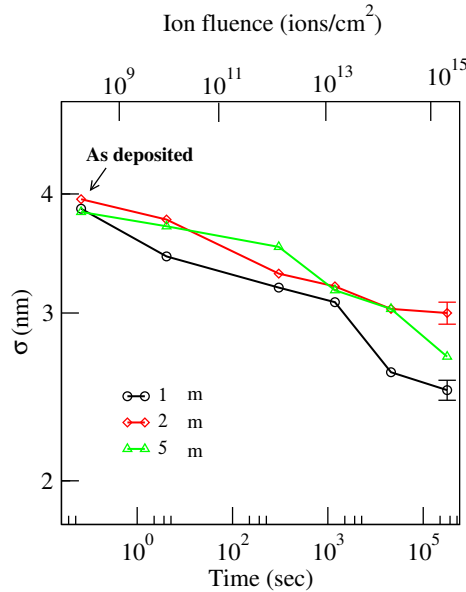


Figure 5.4: Variation of rms roughness (σ) as a function of irradiation time (t) for three different scan lengths. Top scale shows ion fluence.

In order to understand the surface evolution, we have investigated the rms roughness, σ , as a function of ion fluence. Fig. 5.4 shows the variation of rms roughness w.r.t ion fluence and irradiation time. These have been plotted for three different (L) scan sizes (1 μm , 2 μm and 5 μm). All the plots display nearly similar trends with σ consistently decreasing with fluence. For the as-deposited sample, an rms surface roughness of $\sim 4\text{nm}$ has been observed which decreases with irradiation time. The growth exponent, β , has been estimated here to be ~ -0.03 . Existence of a negative β implies that some smoothing of the surface is taking place through ion irradiation. AFM images (fig. 5.1,5.2) also reflected that the smoothing of the surface is occurring via the fragmentation of the nanostructures where the NS as well as the void-like zones become smaller in size. Negative values of β have also been observed earlier [46–48]. In these studies also inverse ripening of nanostructures is causing the surface smoothing.

The dynamics of evolution of irradiated surfaces can be understood by studying the scaling properties of the surface fluctuations. The behavior of these surface fluctuations can be analysed by employing techniques of height-height correlation (HHC) and power spectral density (PSD) functions. The topographical properties of a surface in a real space is characterized by HHC function. The equal time height-height correlation (HHC) function $G(\mathbf{r},t)$ is described as [35,36]:

$$G(\mathbf{r}, t) = \frac{1}{L} \sum_{\mathbf{r}'} \langle [h(\mathbf{r} + \mathbf{r}', t) - h(\mathbf{r}', t)]^2 \rangle. \quad (5.4)$$

Here r is the translational length between adjacent height features. The height profile of a rough surface at position, \mathbf{r} , and time, t , is denoted by $h(\mathbf{r},t)$ where $\langle \rangle$ is the ensemble average. According to the dynamic scaling hypothesis, the HHC function for self affine surfaces is formulated as [35]

$$G(\mathbf{r}) \sim \begin{cases} r^{2\alpha} & \text{if } \mathbf{r} \ll \xi \\ 2\sigma^2 & \text{if } \mathbf{r} \gg \xi \end{cases} \quad (5.5)$$

where ξ is the lateral correlation length. The degree of irregularity of the surface is reflected in the roughness exponent α ($0 < \alpha < 1$). High value of α represents a locally smooth surface [43] whereas low values correspond to jagged surfaces. ξ indicates a

length scale where HHC function saturates to σ and beyond which the power law $G(r) \propto r^{2\alpha}$ does not hold. Surface correlation only exists for length scale less than ξ .

The HHC function for the as-deposited and ion implanted surfaces are presented in Fig. 5.5. It behaves as a straight line for short length scales but saturates to σ at higher lengths. The roughness exponent α can be evaluated from the slope of the straight line. Here σ , α and ξ have been estimated by utilizing HHC function and the results are presented in Table 5.1.

Fluence ($ions/cm^2$)	σ (nm)	α	ξ (nm)
As-deposited	4.12	0.50	19
1×10^{10}	3.8	0.52	17
1×10^{12}	3.53	0.57	16.5
1×10^{13}	3.24	0.65	15.4
1×10^{14}	3.04	0.72	14.8
1×10^{15}	2.82	0.81	14

Table 5.1: Scaling Exponents from height-height correlation (HHC) function.

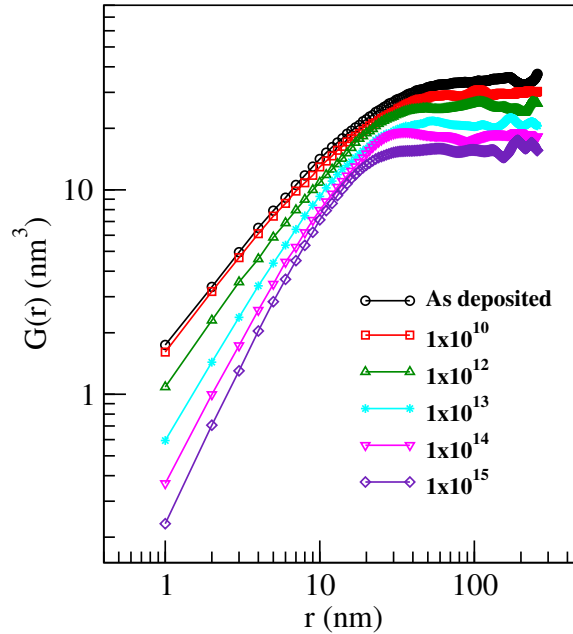


Figure 5.5: HHC function for as-deposited and ion irradiated TiO_2 thin films.

The estimated values of σ , from HHC function, are in accordance with those obtained from AFM results. These results also indicate a decrease in σ with fluence.

Surface smoothening, as discussed earlier, seems to be responsible for this. The exponent α is found to be between 0.5 and 0.8 (Table 5.1) depicting these surfaces to be self affine ($0.5 < \alpha < 1$) [35, 43]. The dynamics of the self affine surfaces is significantly controlled by the diffusion processes [35, 43]. The as-deposited surface displays a low value of α (0.5) suggesting the surface to be rough. After the fluence of 1×10^{10} ions/cm², α increases slightly. For higher fluences, a systematic increase in α is observed. At the highest fluence (1×10^{15} ions/cm²) α of 0.81 is observed which suggests a locally smoother surface. The as-deposited surface displays a high value for ξ which reflects the presence of long range correlations. These correlations become smaller with irradiation due to the reduction in NS sizes as discussed earlier.

The knowledge of rms roughness (σ) is not sufficient to provide the complete information about the processes involved in surface evolution. Power Spectral Density (PSD) is a Fourier Transformation technique which can be used to extract valuable information for surface modifications. It utilizes the fourier space or reciprocal space via spatial frequency (k) mapping of surface topography. For better understanding of the self-affine surfaces, PSD function becomes an effective tool by providing quantitative information about the spatial distributions and periodic characteristics of the surface across multiple length scales [49, 50]. PSD is also independent of the scan size and is defined as the square of Fourier transformation of a surface profile $h(r)$ at position $r=(x,y)$ [28, 51]:

$$PSD = \frac{1}{Area} \left| \int \int \frac{d^2r}{2\pi} e^{-ik \cdot r} \langle h(r) \rangle_t \right|^2, \quad r = (x, y), \quad (5.6)$$

Using the above equation, 1D PSD plots were extracted from the AFM images (Fig. 5.1) for the as-deposited and ion irradiated thin films. These are shown in Fig. 5.6 as a function of spatial wave vector (k). Two distinct regions are observed in the PSD curves. The constant PSD in the low frequency region refers to the uncorrelated white noise while a power law decaying behaviour at high frequencies indicates spatial correlations in the system. The Correlation length ($1/k$) of a surface is an important parameter which delineates the lateral extent of fluctuations. For a length scale greater than correlation length, the PSD function is independent of k [51]

indicating an uncorrelated white noise. However, PSD becomes k dependent for the lengths smaller than correlation length.

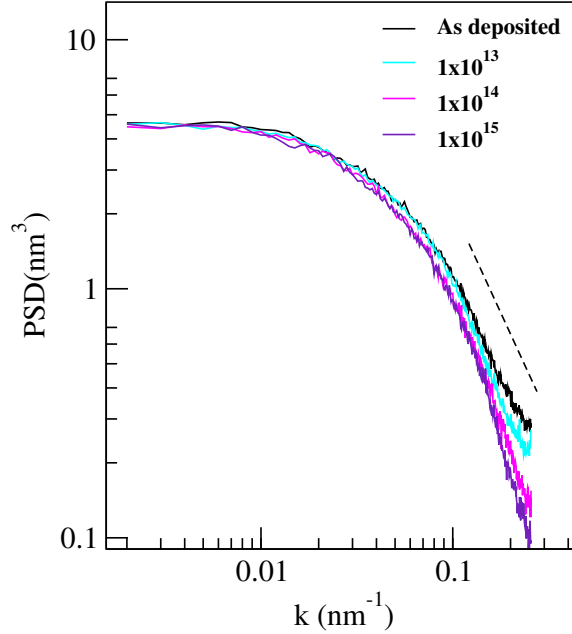


Figure 5.6: PSD as a function of spatial frequency k for as-deposited and ion irradiated TiO_2 thin films.

The PSD function at high frequencies, displays a power law behaviour with the following scaling form [28]:

$$PSD \sim k^{-\gamma} \quad (5.7)$$

γ is an exponent which displays different evolutionary processes taking place on the surface. The value of γ has been estimated here by fitting the high frequency region of PSD with a straight line (Fig. 5.6). γ is found to be ~ 2 for low fluences (up to 1×10^{13} ions/cm²). However, it increases slightly at higher fluences and is found to be ~ 2.5 at the highest fluence. Although knock off phenomenon is most significant in controlling the surface evolution at $\gamma=2$, bulk diffusion becomes important at $\gamma=3$ [52]. Therefore, the obtained γ values (between 2 and 3) as observed here, indicate that both sputter induced erosion and diffusive processes are involved in the morphological evolution of the TiO_2 thin films after ion irradiation. The diffusive processes are becoming dominant at the higher fluences which lead to the smoothening

of the surfaces.

5.4 Conclusion

In this chapter, we have studied the surface evolution of the sputter deposited TiO₂ thin films after 50 keV Ti ion irradiation. AFM studies showed that the size of the nanostructures becomes smaller and surface becomes smoother after ion irradiation. To understand the dynamics of the surface evolution, appropriate scaling theories have also been introduced. The scaling exponents (α , β and γ), estimated from HHCF and PSD investigation, reveal that the surface evolution becomes diffusion dominated at high fluences. Decrease in correlation length ξ for higher fluences implies an inverse coarsening and fragmentation of the nanostructures. Therefore, diffusion dominated smoothing process is significant in controlling the dynamics of the ion irradiated TiO₂ thin films.

Bibliography

- [1] A. Fujishima, K. Honda, *Nature*, 238, 37 (1972).
- [2] K. Hashimoto, H. Irie, A. Fujishima, *Jpn. J. Appl. Phys.*, 44, 8269 (2005).
- [3] B. O'Regan, M. Gratzel, *Nature*, 353, 737 (1991).
- [4] V. Solanki, S.B. Krupanidhi, K.K. Nanda, *Appl. Phys. Lett.*, 110, 263506 (2017).
- [5] V. Solanki, I. Mishra, S.R. Joshi, P. Mishra, P. Dash, C. Singh, D. Kanjilal, Shikha Varma, *Nucl. Instrum. Methods Phys. Res. B*, 365, 82 (2015)
- [6] V. Solanki, S. B. Krupanidhi, K. K. Nanda, *ACS Appl. Mater. Interfaces*, 9, 41428 (2017)
- [7] S. Majumder, D. Paramanik, V. Solanki, B.P. Bag, S. Varma, *Appl. Phys. Lett.*, 98, 053105 (2011)
- [8] X. Chen, S.S Mao, *Chem. Rev.*, 107, 2891 (2007).
- [9] S. Majumder, I. Mishra, U. Subudhi, S Varma, *Appl. Phys. Lett.*, 103, 063103 (2013).
- [10] M. Qamar, and M. Muneer, *Desalination*, 249 535 (2009) .
- [11] K. S. Ahn, Y. Yan, S. Shet, K. Jones, T. Deutsch, J. Turner, and M. Al-Jassim, *Appl. Phys. Lett.*, 93, 163117 (2008).
- [12] Q. Yu, and C. Cao, *J. Nanosci. Nanotech.*, 12, 3984 (2012).
- [13] Y. Cui, Q. Wei, H. K. Park, C. M. Lieber, *Science*, 293, 1289 (2001).

- [14] U. Diebold, Surf. Sci. Rep., 48, 53 (2003).
- [15] Yan Wang, Yiming He, Qinghua Lai, Maohong Fan, J. Environmental Sci., 26, 2139 (2014).
- [16] F. Frost, A. Schindler, F. Bigl, Phys. Rev. Lett., 85 4116 (2000)
- [17] V. Solanki, S. Majumder, I. Mishra, P. Dash, C. Singh, D. Kanjilal, S. Varma, J. Appl. Phys., 115, 124306 (2014).
- [18] S. Facsko, T. Dekorsy, C. Koerdt, C. Trappe, H. Kurz, A. Vogt, and H. L. Hartnagel, Science, 285, 1551 (1999).
- [19] A. Keller, S. Rossbach, S. Facsko, and W. Miller, Nanotechnology, 19, 135303 (2008).
- [20] Z.L. Wang, J. Phys.: Condens. Matter, 16, R829 (2004).
- [21] A.B. Djurisic, A.M.C. Ng, X.Y. Chen, Prog. Quantum Electron., 34, 191 (2010)
- [22] Z.L. Wang, J. Song, Science, 312, 242 (2006)
- [23] V. Solanki, S.R. Joshi, I. Mishra, D. Kabiraj, N.C. Mishra, D.K. Avasthi, Shikha Varma, J. Appl. Phys., 120, 054303 (2016)
- [24] R.M. Bradley, J.M.E. Harper, J. Vac. Sci. Technol. A, 6, 2390 (1988)
- [25] U.B Singh, C Pannu, D Agarwal, S Ojha, S Khan, S Ghosh, D. K Avasthi, J. Appl. Phys., 121, 095308 (2017)
- [26] Soma Dey, Shikha Varma, Nuclear Instruments and Methods in Physics Research B, 212, 228 (2003)
- [27] Soma Dey, Shikha Varma, Nuclear Instruments and Methods in Physics Research B, 212, 146 (2003)
- [28] D. Paramanik, S. Majumdar, S. R. Sahoo, S. N. Sahu, and S. Varma, J. Nanoscience and Nanotechnology, 8, 4227(2008)

- [29] Dipak Paramanik, Shikha Varma, Nuclear Instruments and Methods in Physics Research B, 266, 1257 (2008)
- [30] Dipak Paramanik, S N Sahu and Shikha Varma, J. Phys. D: Appl. Phys., 41, 125308,(2008)
- [31] P. J. Sigmund, Mater. Sci., 8, 1545 (1973)
- [32] P. Politi, and J. Villain, Phys. Rev. B, 54, 5114 (1996)
- [33] E. Chason, W.L Chan, J. Phys.: Condens. Matter, 21, 224016 (2009)
- [34] R Cuerno, H.A Makse, S. Tomassone, S.T Harrington, H. E Stanley, Phys. Rev. Lett., 75, 4464 (1995)
- [35] F Family, T Vicsek, Dynamics of Fractal Surface; World Scientific: Singapore, 1991.
- [36] A.L Barabasi, H.E Stanley, Fractal Concepts in Surface Growth (Cambridge University Press:Cambridge), 1995.
- [37] Vanaraj Solanki, D. Kabiraj , D.K. Avasthi , Shikha Varma, Nuclear Inst, and Methods in Physics Research B, 434, 56 (2018)
- [38] I. Mishra, S.R. Joshi, S. Majumder, A.K Manna, S. Varma, S. Radiat. Eff. Def. Solids, 171, 594 (2016)
- [39] V. Solanki, S. R. Joshi, I. Mishra, D. Kanjilal, S Varma, Metall. Mater. Trans. A, 49, 3117 (2018)
- [40] J. F. Ziegler, J. P. Biersack and M. D. Ziegler, SRIM - The Stopping and Range of Ions in Matter (SRIM Co., Chester, MD,USA, 2008).
- [41] B.P.Uberuaga, Xian-Ming, J. Phys.: Condens. Matter, 23, 435004 (2011).
- [42] P Romero-Gomez, A Palmero, T Ben, J. G. Lozano, S.I Molina, A. R. Gonzalez-Elipse, Phys. Rev. B, 82, 115420 (2010)

- [43] A Barman, C P Saini, P Sarkar, B Satpati, S R Bhattacharyya, D Kabiraj, D Kanjilal, S Dhar, A Kanjilal, *J. Appl. Phys.*, 118, 224903 (2015)
- [44] U. Valbusa, C. Borangno, and F. R. de Mongeot, *J. Phys. Condens. Matter*, 14, 8153 (2002).
- [45] F. Family and T. Vicsek, *J. Phys. A*, 18, L75 (1985).
- [46] Dipak Paramanik, 'Nano-structures formation on InP(111) semiconductor surfaces by ion beam irradiation', thesis (Homi Bhabha National Institute)
- [47] S Dey, D Paramanik, V Ganeshan and S Varma, *Appl.Surf. Sci.*, 253, 1116 (2006)
- [48] R Edrei, E N Shauly and A Hoffman, *J. Vac. Sci. Technol.A*, 20, 344 (2002)
- [49] F Biscarini, P Samori, O Greco, R Zamboni, *Phys. Rev. Lett.*, 78, 2389 (1997)
- [50] J. Bennett, L. Mattsson, *Introduction to Surface Roughness and Scattering*; Optical Society of America: Washington DC, 1999.
- [51] R. Petri, P. Brault, O. Vatel, D. Henry, E. Andre, P. Dumas, F. Salvan, *J. Appl. Phys.*, 75, 7498 (1994)
- [52] M.W.Tong, R.S. Williams, *Annu. Rev. Phys. Chem.*, 45, 401 (1994)

Chapter 6

Surface Evolution of $\text{TiO}_2(110)$ after Ar^+ ion irradiation

6.1 Introduction

Nanostructures of oxide semiconductors show many exceptional properties in the field of photovoltaics, spintronics, multi-ferroics, photocatalyst, sensors etc. [1, 2]. These properties are, however, strongly controlled by the shapes and sizes of nanoparticles and in last few decades a large number of studies are devoted to synthesizing structures of various morphologies and nano-dimensions [3]. Nanostructures can be produced usually by two routes, bottom up and top down. In the bottom up approach smaller units join together to develop bigger structures whereas for top down approach larger structures are reduced into smaller dimensional units. Ion beam modification of the material, through top down synthesis technique is a technologically simple method where self assembled fabrication of nanostructures take place. Being a self assembled method, it provides distinct advantage as it does not require multi-step processing techniques and can be used in same fashion on any crystalline or amorphous materials [2, 4, 5]. Ion bombardment can induce roughening and patterning on the surface. Such patternings can create nanostructures or ripples on the surface.

An ion while passing through the material loses its energy via energy loss processes. Though low energy ions (1 keV) will remain near surface, higher energy ions (100 keV) can get implanted. Energy loss processes can produce material modifications as well as some defects. The range of ions and energy loss processes will depend on the type of ion and its energy. Energetic ions, bombarded on a solid, move through the

medium and lose their energy primarily via two processes, nuclear energy loss (S_n) and electronic energy loss (S_e). During (S_n) dominant processes, the energy is lost via elastic collision of ions with target nuclei. Such interactions disturb the nuclei and can displace them from equilibrium positions. Ions also interact in-elastically with the electrons and the energy lost by ions (S_e) causes the electrons in its path to get excited. The amount of energy lost by these two processes depends on the energy of the impinging ion [6]. At low energies, energy is predominantly lost by S_n whereas at high energies S_e is more important. At very high energies as in swift heavy ion (SHI) irradiation, ions can induce localized melting creating tracks in the material [6]. At lower keV energies also some defects can be produced during the passage of ion or at the end of range [2, 5]. Still, system modification with ion beams is attractive due to the fact that this technique can produce self-assembled nanostructures exhibiting wide variety of applications [2, 4, 5]. Material modification with ion beams is an active research area as it can generate many nano-dimensional surface structures, metastable phases, advanced hetero-structures and self organized systems [2, 4, 5]. Instabilities develop on surface during sputtering processes that create competition between erosion and surface diffusion [7]. This can result in the production of a variety of nanodimensional structures like hills, valleys, ripple, hemispherical dots etc. on the surfaces [8]. Spontaneous formation of nanoscale structures by ion irradiation has been described by Bradley Harper (BH) model [7]. Here, competition between various smoothening and roughening mechanisms control the surface evolution.

TiO₂ is a wide band gap semiconductor (3.2 eV for anatase and 3.0 eV for rutile) and shows many advanced properties in the field of photo-catalyst, photovoltaics, magnetic storage media, waste water management, bio-implants, etc. [9]. Nano-dimensional structures of TiO₂ demonstrate many enhanced behavior [2]. These are however limited by the preparation methods. Achieving nano-dimension structures by a single step ion irradiation process is attractive as it does not involve many preparation steps. Evolution of such surfaces occurs *spontaneously* by the process of kinetic roughening [4, 7, 10, 11].

The morphology of nano-patterns and many of their characteristic properties (like long range distribution, correlations, power spectral density etc.) evolve during irra-

diation process, and are guided only by the nature of surface and ion beam parameters [4, 7, 8, 12, 13]. Systematic study of such surfaces and their distributions are useful in providing information on the processes that are important for surface evolution.

Several theoretical growth models have been proposed for understanding the self assembled morphology generated after ion beam irradiation. Based on Sigmund model, Bradley and Harper (BH) had shown the role of curvature dependent sputtering on the evolution of many amorphous surfaces [7, 12]. For metals and their oxides, a step-edge Ehrlich-Schwoebel barrier also becomes important [11]. Additionally, many surface processes like non-linear effect, solid mass flow, re-deposition, anisotropic diffusion, competition between roughening and smoothening processes etc. regulate the ultimate surface morphology [14, 15]. Including all such processes in single model approach is difficult and hence dynamic scaling studies that provide exponents for various types of growth studies have become very successful. Investigations of these exponents can help us to understand the processes involved in a surface evolution.

In general, the evolution of an ion irradiated surface can be described by a Langevin equation in continuum limit as [11, 14, 15]

$$\partial_t h(x, t) = \nu \nabla^2 h + \lambda \nabla^2 (\nabla h)^2 - D \nabla^4 h - F_0 + \eta(x, t). \quad (6.1)$$

Here height at position x and time t is given by $h(\mathbf{x}, t)$. D and ν are, respectively, diffusion and surface tension coefficients. ν also controls Schwoebel Barrier effects. The first term on the right hand side corresponds to the erosion caused by curvature effects whereas the third term is related to smoothening via diffusion mechanism. The erosion processes create a negative surface tension such that the surface becomes rough [16, 17]. Random diffusion of surface atoms and vacancies induce smoothening. Random fluctuations are incorporated in η while effect of factors like flux, angle of incidence, energy of incoming ions etc. are accounted in F_0 . The non linear behavior incorporated through $\lambda \nabla^2 (\nabla h)^2$ is responsible for the lateral growth like ripple patterns, and λ is a tuning parameter [13, 15]. Thus, the surface evolution occurs via a competition between the roughening and smoothening mechanisms [14–17]. For low energy ion beams although erosive phenomenon are important, yet diffusion currents can become dominant effects as observed for the case of TiO_2 [18]. Large anisotropic

diffusion of surface species cause generation of ripple patterns [18]. Understanding surface evolution by such Langevin equations is possible in the continuum limit [16,17]. Dynamics of such surfaces can be studied using scaling formalism [16,17]. The scaling results and associated exponents reflect the evolution process.

Surfaces modified by ion irradiation present characteristics that are shown by many other widely different non-equilibrium growth processes like atom-deposition, growth of tumors, bacterial colonies, etc. [16,17]. The description of such surfaces can be explained under the framework of *kinetic roughening*. Here, a flat surface evolves and roughens, with time, under non-equilibrium process. Within the *dynamic scaling hypothesis* the rms roughness, $\sigma(L, t)$, of such surfaces can be described by scaling behavior in spatial and temporal regimes [16,17] and the exponents provide the information on the processes controlling the surface growth. Ion bombarded surfaces present complex surface morphology and scaling studies can give knowledge about the parameters crucial for the surface-evolution [2,16,17,19]. Scaling studies can be useful in providing the characteristic parameters of surface evolution, e.g roughness (α) and growth (β) exponents as well as the correlation length due to surface fluctuations.

In chapter 5, we have discussed the morphological evolution of the Ti ion implanted TiO₂ thin films as well as the surface dynamics of these films by applying scaling formalism. These films are nearly 80 nm thick and contain mixed nanostructures, of anatase (A) and rutile (R) forms of TiO₂, as discussed in chapters 3 and 4. These ion irradiated films have also been investigated for several functional properties. A to R structural transformation, beyond a critical fluence, was explored by applying techniques like Raman spectroscopy, X-ray Diffraction, Transmission Microscopy etc.. The role of anatase crystallite nano-dimensions, in the transformation, was also presented. Existence of nanostructured grains on the as-deposited TiO₂ films and their evolution with ion fluence was observed via Atomic Force Microscopy (AFM) in chapter 5. The surfaces also delineate existence of some voids. A reduction in the average nanostructure size as well as the decrease in the surface roughness (σ) with fluence, reflects presence of some smoothing process. The scaling formalism, height-height correlation function (HHCF) and power spectral density (PSD) were utilized to extract various scaling parameters, including roughness exponent (α), growth exponent

(β) and correlation length (ξ). Scaling results demonstrate that diffusive processes are inducing the surface- smoothening at high fluences. Boundaries of the nanostructures and voids, in thin films, can act as sink for defects and can contribute to volume adjustments, facilitating the surface smoothening.

The present chapter investigates the evolution of single crystal rutile $\text{TiO}_2(110)$ surfaces after ion irradiation. $\text{TiO}_2(110)$ surfaces, ion irradiated with Ar^+ ions, displayed a fluence dependent evolution of nanostructures such that ripple like channels appear at high fluence. Preferential sputtering, during ion irradiation, creates oxygen vacancy states which are active and mobile species. These vacancies diffuse anisotropically on the crystalline $\text{TiO}_2(110)$ surface, promoting the formation of rippling structures. Dynamics of these surfaces, evolving under irradiation, has been determined by utilizing scaling formalism based on HHCF and PSD. Here, diffusion dominated dynamics is observed at lower fluences. However, sputter induced erosion controls the surface dynamics at high fluences.

6.2 Experimental

$\text{TiO}_2(110)$ single crystals, commercially purchased from Mateck, Germany, have been irradiated at room temperature. Ar^+ ions of 60 keV from electron cyclotron resonance (ECR) source, were bombarded on TiO_2 at an incident angle of 60° with respect to surface normal. The Ar^+ ion beam was incident along the [001] direction of $\text{TiO}_2(110)$ single crystals. Several fluences between 5×10^{15} to 1×10^{19} ions/ cm^2 , with an average ion flux of 1.8×10^{14} ions/ $\text{cm}^2\cdot\text{sec}$ were used for irradiation. During irradiation, the residual pressure in the chamber was kept at 2×10^{-6} mbar. Ar^+ ions have an average penetration depth of 42 nm in TiO_2 at 60 keV [20]. The corresponding longitudinal and lateral straggling are 16 and 11 nm, respectively.

Surface morphology has been investigated by Atomic Force Microscope (AFM) from Bruker (Nanoscope V) in tapping mode. Nearly 100 AFM images were acquired for several scan sizes, varying from 500 nm to 10 μm . Power spectral density (PSD) and height-height correlation (HHC) studies have also been undertaken by utilizing

these AFM images. Core level studies were undertaken on a VG X-ray Photoelectron Spectroscopy (XPS) system under ultra-high vacuum conditions. System is equipped with two X-ray sources (Mg- K_{α} and Al- K_{α}) and a hemispherical analyzer. XPS measurements were carried out with Mg- K_{α} source (1253.6 eV) at 20 eV pass energy with a take-off angle of 30° w.r.t. surface normal.

6.3 Results and discussion

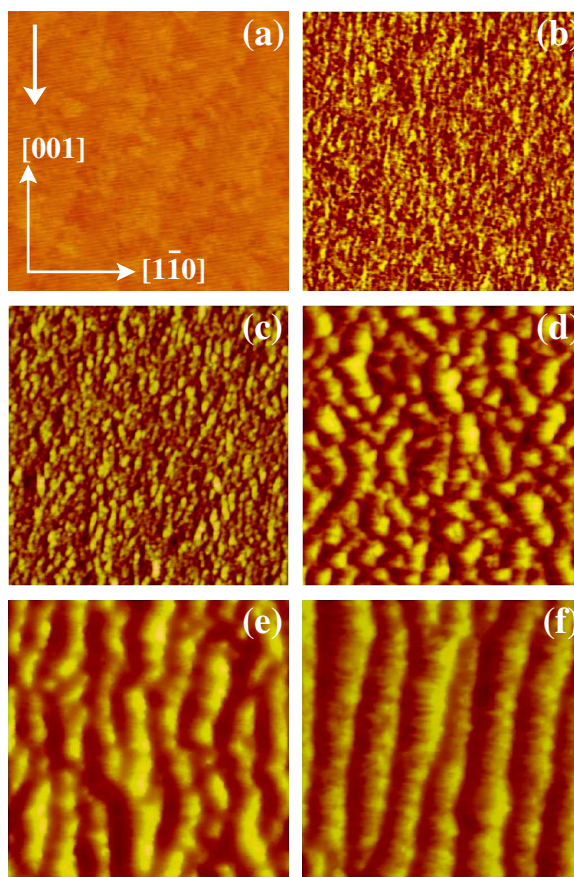


Figure 6.1: SPM images (a) for pristine TiO_2 and after ion irradiation of TiO_2 at fluences of (b) 1×10^{16} , (c) 1×10^{17} , (d) 5×10^{17} , (e) 5×10^{18} , and (f) 1×10^{19} ions/ cm^2 . Images of (a) and (b) are $1 \times 1 \mu\text{m}^2$ in size whereas images from (c) to (f) are $2 \times 2 \mu\text{m}^2$ in size. Ion beam projection direction (arrow on top) was always along [001] direction. Crystallographic axes of the surface are shown.

AFM images from the clean and ion irradiated TiO_2 surfaces are shown (Fig. 6.1). Initially at low ion fluences (1×10^{16} ions/ cm^2), nearly 10 nm sized nanostructures are observed. These, however, evolve into ripples at higher fluences. Anisotropic

nature of the ripples has been investigated earlier [5, 18]. Here we investigate the surface dynamics and the scaling behavior of these single crystal TiO₂ surfaces as they evolve under ion irradiation.

When an ion bombards a single crystal surface it creates adatoms and vacancies. At the same time, sputtering processes induce erosion and instabilities on the surface. The smoothing of the surface occurs via diffusion of adatoms [4, 8]. Ion while passing through the material loses its energy and produces many collision cascades. These cascades can transfer some energy to the surface atoms causing their ejection and surface erosion. An interplay of erosion of surface atoms and diffusion of active defect species on the surface produce the nano-patterns observed here. According to BH model, the erosion depends on the local curvature of the surface [7]. Consequently, valleys on the surface undergo more erosion than the hills. In the process surface evolves, its roughness changes and nano-dimensional structures coarsen. Formation of such self assembled nanostructures, fabricated by irradiation techniques, show many interesting behavior [2, 5].

Ion irradiated surfaces evolve via non equilibrium processes and their growth can be explained by dynamic scaling formalism. Such surfaces show rms surface roughness (σ) or interface width described as [16, 17]

$$\sigma = \langle [h(x, y) - \langle h(x, y) \rangle]^2 \rangle^{1/2} \quad (6.2)$$

Here $h(x, y)$ represents the height at (x, y) position on the surface. Such surfaces show rms roughness that exhibits scaling w.r.t. time t and the length L [16]:

$$\sigma(L, t) = L^\alpha f(t/L^{\alpha/\beta}) \quad (6.3)$$

and

$$\sigma(L, t) \propto \begin{cases} L^\alpha & \text{if } t/L^{\alpha/\beta} \rightarrow \infty \\ t^\beta & \text{if } t/L^{\alpha/\beta} \rightarrow 0 \end{cases} \quad (6.4)$$

These equations can be utilized to obtain exponents α and β which are respectively the roughness and growth exponents [16, 17].

The root mean square roughness (σ) has been plotted, in fig. 6.2, as a function of irradiation time (t) and fluence. For the pristine surface, a very small (~ 0.04 nm) rms roughness is observed which increases with irradiation time and saturates at late time.

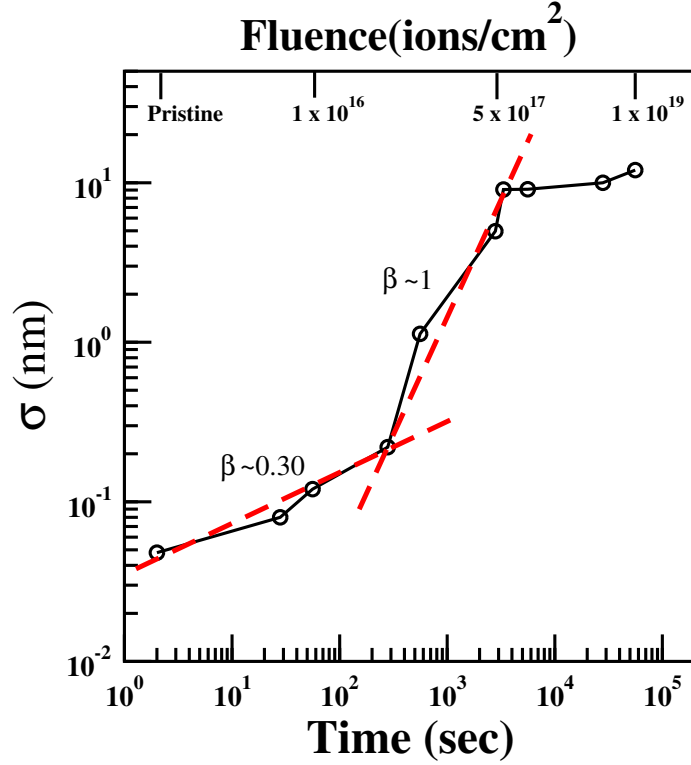


Figure 6.2: Log-log plot of rms roughness, σ , as a function of irradiation time (t) and fluence.

σ displays power law scaling relation w.r.t. t and shows two slopes. By utilizing eq. 6.4 ($\sigma \propto t^\beta$), values of β have been obtained. For low fluences, ($\leq 5 \times 10^{16}$ ions/cm²) β of 0.3 ± 0.01 is observed. This, as suggested by numerical simulations can be described by noisy Kuramoto and Tsuzuki equation [21]. Non-linear effects, here, smoothen the surface through diffusion. For fluences between 5×10^{16} and 5×10^{17} ions/cm², $\beta = 1$ is observed. Destabilizing growth, non-local effects and shadowing instability can contribute to this behaviour [22–24]. Anisotropic ripple-like nanostructures can produce shadow effects and textures upon irradiation. Finally, rms surface roughness saturates at higher fluences.

Sputtering of oxide surfaces can cause preferential sputtering of oxygen atoms due to its lower mass. Consequently the electrons from the outgoing oxygen atom are transferred to two Ti lattice atoms resulting in the formation of oxygen vacancy Ti³⁺ states [2, 5]. Fig. 6.3 displays the Ti(2p) core level XPS for the pristine and some ion irradiated TiO₂ surfaces. Ti 2p_{3/2} and Ti 2p_{1/2} states, respectively, at 458.4 and

464.1 eV can be attributed to the Ti^{4+} states on the pristine surface. Two very small peaks are also observed at the lower binding energies of both these features. These are associated with the existence of tiny Ti^{3+} states on the pristine surface. With ion irradiation, the intensities of Ti^{3+} , or oxygen vacancy states, on the surfaces become much higher. This occurs due to the preferential sputtering of oxygen ions during irradiation. In addition to Ti^{3+} , presence of Ti^{2+} states is also noticed. Irradiation at the highest fluence (1×10^{19} ions/cm²) also produces some Ti^0 states. Formation of species like Ti^{3+} , Ti^{2+} and Ti^0 reflect reduction of Ti^{4+} states and development of Ti_2O_3 , TiO and Ti on the surface [2, 5]. Creation of such vacancy states also causes formation of Ti rich centers which become the nucleation zones where the nanostructures first form. These vacancy states and related Ti rich centers crucially control the nanostructure formation as well as govern the dynamics of the surface evolution.

The equal time height-height correlation (HHC) function $G(\mathbf{r}, t)$, for a translational length \mathbf{r} along lateral direction, can be described as:

$$G(\mathbf{r}, t) = \frac{1}{L} \sum_{\mathbf{r}'} \langle [h(\mathbf{r} + \mathbf{r}', t) - h(\mathbf{r}', t)]^2 \rangle. \quad (6.5)$$

Here, $\langle \rangle$ is the ensemble average. For non-equilibrium conditions, surface morphology is guided by noise induced roughening and HHC is expected to scale as [16]:

$$G(\mathbf{r}) \sim \begin{cases} \mathbf{r}^{2\alpha} & \text{if } \mathbf{r} \ll \xi \\ 2\sigma^2 & \text{if } \mathbf{r} \gg \xi \end{cases} \quad (6.6)$$

where σ is the rms surface roughness or the interface width. α is the roughness exponent which is low for a locally jagged surface but high for locally smooth surface [17]. ξ is the correlation length, where HHC saturates to σ . It also indicates a length-scale above which $\sigma \propto L^\alpha$ scaling does not hold.

The HHC function for pristine and ion implanted surfaces are shown in fig. 6.4. For short lengths r , the HHC function displays a linear behavior whose slope can provide α . At higher r , HHC saturates to σ . ξ is the cross-over length beyond which saturation occurs. This also reflects the typical wavelength of fluctuations present on the surface [11]. The values of α and ξ have been estimated here, using eq. 6.6, and

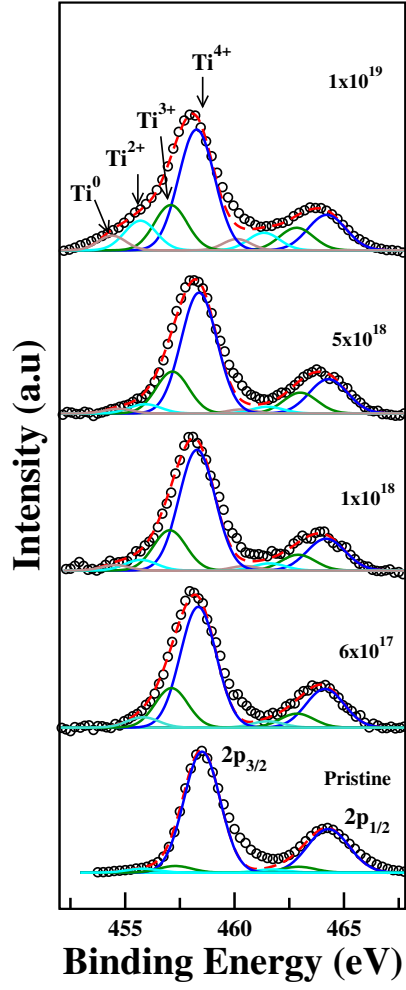


Figure 6.3: Ti-2p core-level XPS spectra from pristine TiO_2 surface and after irradiation at various fluences (ions/cm^2).

are presented in table 6.1.

Fluence (ions/cm^2)	α (± 0.02)	ξ (nm) (± 2)
Pristine	0.90	6
5×10^{15}	0.72	12
1×10^{16}	0.74	12
5×10^{16}	0.74	14
1×10^{17}	0.85	14
5×10^{17}	0.85	28
1×10^{18}	0.85	50
5×10^{18}	0.85	65
1×10^{19}	0.90	80

Table 6.1: Scaling Exponents from height-height correlation (HHC) function.

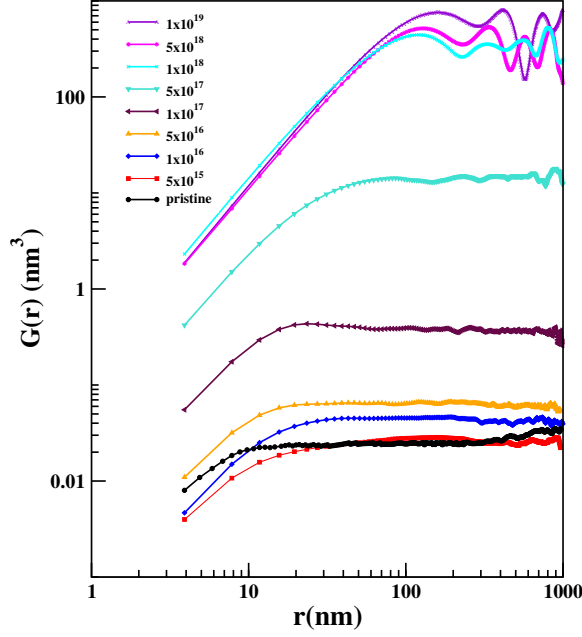


Figure 6.4: HHC for pristine TiO_2 as well as after ion irradiation.

For the pristine surface α has a value of 0.9, indicating surface to be locally smooth. After an irradiation at 5×10^{15} ions/cm², α reduces to 0.72. Ion bombardment of the surface causes sputtering of the atoms, thus leading to surface roughening and lowering of α . Up to 5×10^{16} ions/cm², α is 0.74 but increases to 0.85 for higher fluences. At the highest fluence (1×10^{19} ions/cm²) α is 0.9, delineating a locally smooth surface. Ion irradiation thus plays an important role in modifying the morphology of the surface. Since the values of α found here are in the range of 0.7 to 0.9, these ion irradiated surfaces can be characterized as self affine ($0.5 < \alpha < 1$) and their growth will be significantly dominated through diffusion processes [16, 17].

Pristine surface displays a small value for ξ (in fig. 6.4) as expected for a flat surface. An increase in ξ occurs after ion irradiation (table 6.1). ξ contains knowledge of lateral dimensions of nanostructures present on the surface as well as surface fluctuations and their wavelengths [11]. It also indicates the diffusion length on the surface [25]. For high fluences ($\geq 1 \times 10^{18}$ ions/cm²) some periodic modulations at large r (fig. 6.4) are indicative of the ripples on the surface. Such behavior is noticed in fig. 6.1 also.

The rms roughness of the surface delineates the knowledge from the vertical di-

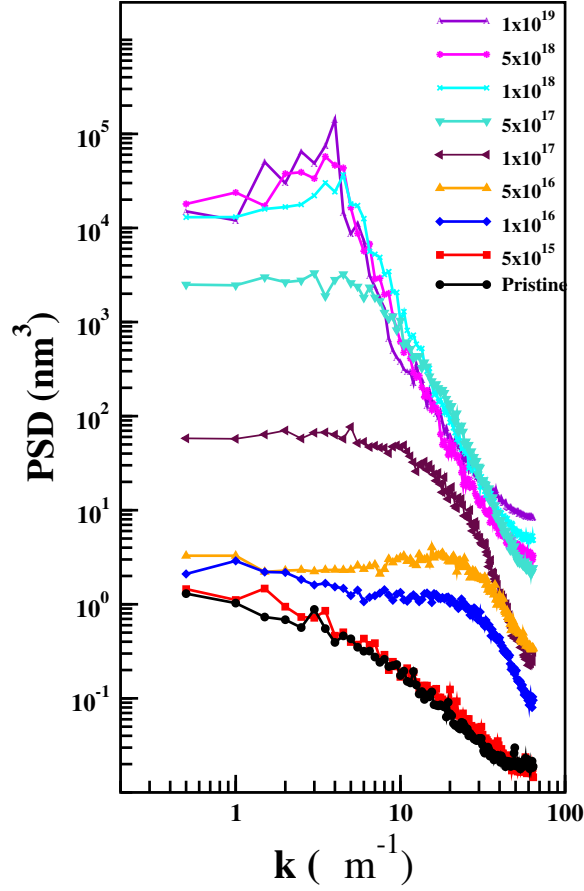


Figure 6.5: PSD as a function of spatial frequency k for pristine TiO_2 as well as after irradiation.

rection alone. Power Spectral Density (PSD), however, is the fourier transform of the surface and is useful for achieving full information from the vertical and spatial directions as well as correlations. For understanding spatial properties as well as any underlying periodicity of nanostructured self affine surfaces, analysis in reciprocal space becomes very important. For local surface height $h(r)$ at position $r=(x,y)$ and spatial frequency k , PSD can be defined as [26]

$$PSD = \frac{1}{Area} \left| \int \int \frac{d^2r}{2\pi} e^{-ik \cdot r} \langle h(r) \rangle_t \right|^2, \quad r = (x, y), \quad (6.7)$$

1-dimensional PSD has been analyzed for the pristine as well as ion irradiated surfaces and is shown in fig. 6.5. These curves reflect two prominent behaviors. In the low k region, the constant PSD indicates the random uncorrelated white noise. The high k region on the other hand indicates correlations on the surface. Presence of any

prominent peaks will indicate some specific periodicities on the surface. No prominent peaks are observed in fig. 6.5 at low fluences. However, at higher fluences ($\geq 1 \times 10^{18}$ ions/cm²) a weak peak can be noticed near k of $2.5 \mu m^{-1}$. This indicates the presence of periodic ripples on these surfaces (see also fig. 6.1). At high k , PSD shows the following scaling form for γ [26]:

$$PSD \sim k^{-\gamma} \quad (6.8)$$

The high k region of PSD has been fitted with this power law behavior, and γ was estimated for all the fluences. Fig. 6.6 plots γ as a function of irradiation time and fluence.

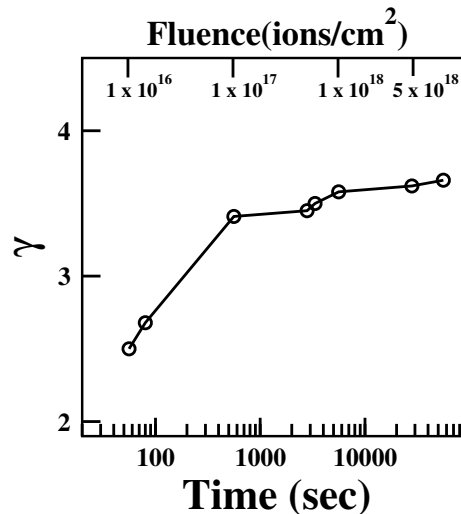


Figure 6.6: Exponent γ as a function of irradiation time (t) and fluence.

γ is observed to be 2.5-2.7 for low fluences. For higher fluences $>5 \times 10^{16}$ ions/cm², γ increases and nearly saturates at ~ 3.5 . Earlier studies show that for $\gamma \sim 2$ knock off phenomenon are important, at $\gamma \sim 3$ bulk diffusion becomes most significant, and at $\gamma \sim 3.5$ surface erosion is dominant [27,28]. Thus at low fluences (with γ between 2 and 3) surface seems to be driven by knock off processes and bulk diffusion. At higher fluences, with $\gamma \sim 3.5$, surface dynamics is governed by sputter induced erosion.

6.4 Conclusion

The present chapter utilizes the scaling formalism to explore the surface dynamics of Ar^+ ion irradiated single crystal rutile TiO_2 surfaces. The crystalline surfaces initially become rougher with ion irradiation. However, they become locally smoother at high fluences. Scaling results also display that though at low fluences knock on processes, conjugated with bulk diffusion, predominantly influence the surface morphology, sputter induced erosion controls the surface dynamics at high fluences.

Bibliography

- [1] A Fujishima, K Honda, *Nature.*, 238, 37 (1972).
- [2] S Majumder, D Paramanik, V Solanki, B P Bag, S Varma, *Appl. Phys. Lett.*, 98, 053105 (2011).
- [3] Y. Cui, Q. Wei, H. K. Park and C. M. Lieber, *Science*, 293, 1289 (2001)
- [4] F Frost, A Schindler, F Bigl, *Phys. Rev. Lett.*, 85, 4116 (2000).
- [5] V Solanki, S Majumder, I Mishra, P Dash, C Singh, D Kanjilal, S Varma, *J. Appl. Phys.*, 115, 124306 (2014)
- [6] Udai B. Singh, Compesh Pannu, Dinesh C. Agarwal, Sunil Ojha, Saif A. Khan, Santanu Ghosh, and Devesh K. Avasthi, *J. Appl. Phys.*, 121, 095308 (2017)
- [7] R Bradley, J. M. Harper, *J. Vac. Sci. Technol. A*, 6, 2390 (1988).
- [8] S. Facsko, T Dekorsy, C Koerdtt, C Trappe, H Kurz, A Vogt, H. L Hartnagel, *Science*, 285, 1551 (1999).
- [9] X Chen, S.S Mao, *Chem. Rev.*, 107, 2891 (2007).
- [10] D. K. Avasthi, Y. K. Mishra, D. Kabiraj, N. P. Lalla, J. C Pivin, *Nanotechnology*, 18, 125604 (2007).
- [11] S. R. Joshi, T. Bagarti, S. Varma, *Surf. Sci.*, 641, 170 (2015).
- [12] P. J. Sigmund, *P. J. Mat. Sci.*, 8, 1545 (1973).
- [13] M. A. Makeev, R. Cuerno, A.L. Barabasi, *Nucl. Instr. Meth. Phys. Res. B.*, 197, 185 (2002).

- [14] E. Chason, W.L. Chan, J.Phys. Condens. Matter, 21, 224016 (2009).
- [15] R. Cuerno, H.A. Makse, S.Tomassone, S.T Harrington and H.E. Stanley, Phys. Rev. Lett., 75, 4464 (1995).
- [16] F. Family, T. Vicsek, Dynamics of fractal surface, World Scientific: Singapore, 1991
- [17] A. L. Barabasi, H.E Stanley, Fractal Concepts in Surface Growth, Cambridge University Press: Cambridge,1995
- [18] V. Solanki, S.R Joshi, I. Mishra, D. Kanjilal, S. Varma, Metall. and Mat. Trans. A, 49, 3117 (2018)
- [19] V. Solanki, S. Majumder, I. Mishra, S.RJoshi, D. Kanjilal, S.Varma, Rad. Eff. Def. Solids., 168, 518 (2013).
- [20] J.F. Ziegler, M.D Ziegler, J.P Biersack, Nucl. Instr. Meth. Phys. Res. B., 268, 1818 (2010).
- [21] F. Hayot, C Jayaprakash, C. Josserand, Phys. Rev. E, 47, 911 (1993).
- [22] I Gupta, B.C Mohanty, Sci. Rep., 6, 33136 (2016)
- [23] P Sana, L Vazquez, R, Cuerno, S Sarkar, J.Phys. D: Appl. Phys., 50, 435306 (2017)
- [24] J.H Hua, H Guo, Phys. Rev. E, 47, 1007 (1993)
- [25] M.A. Makeev, A.L. Barabasi, Appl. Phys. Lett., 71, 2800 (1997).
- [26] D. Paramanik, S. Varma, Nucl. Instr. Meth. Phys. Res. B., 244, 81 (2006).
- [27] M.W. Tong, R.S. Williams, Annu. Rev. Phys. Chem., 45, 401 (1994)
- [28] S.R. Joshi, A. Chanda, D. Kanjilal, S. Varma, Thin Solid Films., 639, 145 (2017).

Chapter 7

Resistive Switching Properties and Photoabsorption Behavior of Ti ion implanted ZnO thin films

7.1 Introduction

Nanodimensional ZnO has received enormous interest as it presents a multitude of impressive and fascinating properties such as a large exciton binding energy (60 meV), excellent biocompatibility, high thermal, chemical stability etc. [1–3]. These properties propose numerous promising applications in a variety of interdisciplinary fields like optoelectronic devices, sensors, solar cells, paints, medicine, glucose sensors, resistive switching devices etc. [4–12]. Regulation and development of ZnO based devices for visible light applications face challenges and limitations due to its wide band gap (3.37 eV) which, on the other hand, facilitates UV range implementations. Consequently, it encounters low efficiency in absorbing most of the solar range spectrum. Doping ZnO thin films and nanomaterials with metals (e.g. Ni, Mn, Co) and non-metals (e.g. C, N, S) are considered some of the routes for enhancing their visible light absorption [13–18]. A check on electron-hole recombination, which is detrimental for device response, is also essential for achieving the desired characteristics [19] .

A variety of methods have been applied for doping ZnO thin films and nanostructures [20–22]. Among these, ion implantation is a technologically single step method that can introduce dopants in the host lattice at appropriately estimated ranges. This procedure can sometimes also produce many non-equilibrium and far- from- equilib-

rium conditions leading to many metastable structures [23]. Consequently, often many unique properties, not seen in the usual doping procedures, become possible. During implantation, incoming ions interact with target atoms, as well as electrons, and undergo numerous losses before they get implanted at the range, determined by the parameters of the incident ion and the host. An ion can lose energy basically through two primary phenomenon: nuclear and electronic energy loss. Elastic scattering with the target atoms causes nuclear energy loss (S_n) whereas electronic energy loss (S_e) is produced due to inelastic interactions with electrons. At low (keV) energies, former is more important and at higher (MeV) energies, later becomes relatively more predominant [24]. Implantation and preferential sputtering can sometimes also lead to the development of defects, such as vacancies and adatoms, in the material [25]. For the case of metal oxides like ZnO and TiO₂, creation of oxygen vacancies is an immensely important and necessary aspect for the emergence of many exceptional functional properties like superparamagnetism, bio-compatibility, wetting nature, higher photoabsorption etc. [26–32].

Recently, resistive random access memory (RRAM) has attracted much attention as a potential candidate for the next-generation memory device owing to its advantages for non volatility, high speed, high density, and low power consumption [33]. Many oxides such as perovskites, ferroelectric and binary transition metal oxides exhibit resistive switching (RS) characteristics [34–36]. In these systems, oxygen vacancy (O_V) states play a major role in facilitating and directing the switching mechanism through the formation, and rupturing, of conducting filaments (CF) upon the application of the suitable bias [23,37,38]. Two associated conditions, high resistance state (HRS) and low resistance state (LRS), in the I- V profile are induced by appropriate voltages. There are very few studies investigating RRAM behavior in ZnO based systems [39,40]. Although, ion beams are influential candidate for introducing controlled vacancies, their role in ZnO thin films for RRAM related investigations have not been explored.

In chapters 3 and 4 we had presented a detailed investigation on 50 keV Ti ion implantation in thin TiO₂ films. The as-deposited as well as ion implanted films are of mixed type, containing both rutile and anatase forms of TiO₂. However, these

films undergo a structural phase transformation from anatase to rutile, at a critical fluence. Presence of oxygen vacancy states, that increase with fluence, appears to assist in this transformation. The presented results also illustrate an important role of these vacancies in enhancing the photoabsorption (PA) behavior and initiating RS mechanism in TiO₂ films.

The present chapter explores the 50 keV Ti ion implantation in thin ZnO films. Existence of some similarities in mechanisms and basic features, with implanted TiO₂ thin films, can be expected due to the same energy of impinging ions and their similar energy loss values (S_n is 1.159 and 1.250 keV/nm whereas S_e is 0.199 and 0.172 keV/nm in TiO₂ and ZnO, respectively) [41]. They both also share a predominance of S_n related processes during implantation. Techniques like grazing incidence X-ray diffraction (GIXRD), Raman spectroscopy with UV laser, photoluminescence (PL), X-ray photoelectron spectroscopy (XPS), UV-Visible spectroscopy and conducting atomic force microscopy (c-AFM) techniques have been utilized. A rise in oxygen vacancies, with fluence, as well as their role in PA response and RS mechanism in the implanted ZnO films has been explored here in detail. The films show a systematic elevation of photoabsorption and a bandgap tailoring with fluence. Interestingly, the switching mechanism is demonstrated only for the positive bias conditions whereas a rectifying behavior occurs for the negative voltages.

7.2 Experimental

7.2.1 Sample preparation

ZnO thin films of 80 ± 5 nm thickness were deposited on Au/Ni/SiO₂/Si substrate using radio frequency magnetron sputtering technique. Commercially available 99.99% pure ZnO target was used for this purpose. Other parameters are the same as those used, for TiO₂ deposition, in chapters 3 and 4. The substrates were prepared in the following manner. First, 12 nm thin Ni layer was grown on p-SiO₂/Si(100) substrate. A gold layer of thickness 50 nm was then deposited on Ni/SiO₂/Si. Both Ni and Au layers were grown by e-beam technique, details of which are discussed in chapter 3.

ZnO thin films were implanted with 50 keV Ti ions at normal incidence. Different

fluences of 1×10^{12} , 1×10^{13} , 1×10^{14} , and 1×10^{15} ions/cm² were used for implantation. Two fluxes were used viz. 3×10^9 (for first two fluences) and 1.7×10^{11} ions/cm².sec (for last three fluences). A high vacuum (5×10^{-6} Torr) condition was maintained during implantation. The projected range and the longitudinal straggling of Ti ions in ZnO, calculated using SRIM code are found to be 28 and 11 nm, respectively [41]. Ti ions are thus fully confined within ZnO film.

7.2.2 Experimental details

The structural investigations of the ion implanted ZnO thin films were undertaken using high resolution GIXRD technique (Bruker-D8 Discover). The spectra were recorded at grazing incidence configuration with incident angle of 0.5° and 2θ range of 20° - 60° . Micro UV-Raman measurements were carried out using UV (325 nm) Laser on a T64000 triple monochromator Horiba Jobin Yvon system with a liquid nitrogen cooled CCD detector. XPS spectra of ZnO thin films were acquired on a PHI5000 Versa Probe II (ULVAC PHI, Inc.) system, equipped with a micro-focused (100 μ m, 25 W, 15 kV) monochromatic Al-K $_{\alpha}$ source (1486.6 eV). The optical absorption spectra of ZnO films were recorded in the wavelength range of 200-900 nm. The UV-Vis measurements were performed using Cary 5000 spectrophotometer with an integrating sphere using BaSO₄ as a standard. The photoluminescence (PL) spectra were recorded at room temperature in the range of 330-750 nm using same T64000 triple monochromator Horiba Jobin Yvon system. A UV (325 nm) He-Cd laser was used as excitation source. Conducting AFM (c-AFM) measurements were carried out in Park XE-7 system. During c-AFM measurement, voltage between the AFM tip and the bottom Au electrode is varied and corresponding current is recorded with compliance of 1 nA. The voltages have been swept between -10 to +10 V back and forth. c-AFM measurements were taken on different locations of the sample.

7.3 Result and discussion

Fig. 7.1(a) presents GIXRD results from the as-deposited as well as ion implanted ZnO films. The feature at 34.34° corresponds to the (002) planes, and indicates a

predominance of the hexagonal wurtzite structure in ZnO films [19]. Features at $\sim 38.25^\circ$ and 44.23° are related to (111) and (200) Au- planes from the gold film underneath ZnO [42]. The crystallite size (d) and the lattice parameter (c) in ZnO films have been estimated here using the following equations [43, 44]:

$$d = \frac{0.9\lambda}{\beta \cos \theta} \quad (7.1)$$

$$c = \frac{\lambda}{\sin \theta} \quad (7.2)$$

Here, λ is the X-ray wavelength, θ is the Bragg diffraction angle and β is the observed full width half maximum (FWHM). Table 7.1 lists the crystallite sizes and the lattice parameters for the as-deposited and ion implanted ZnO films.

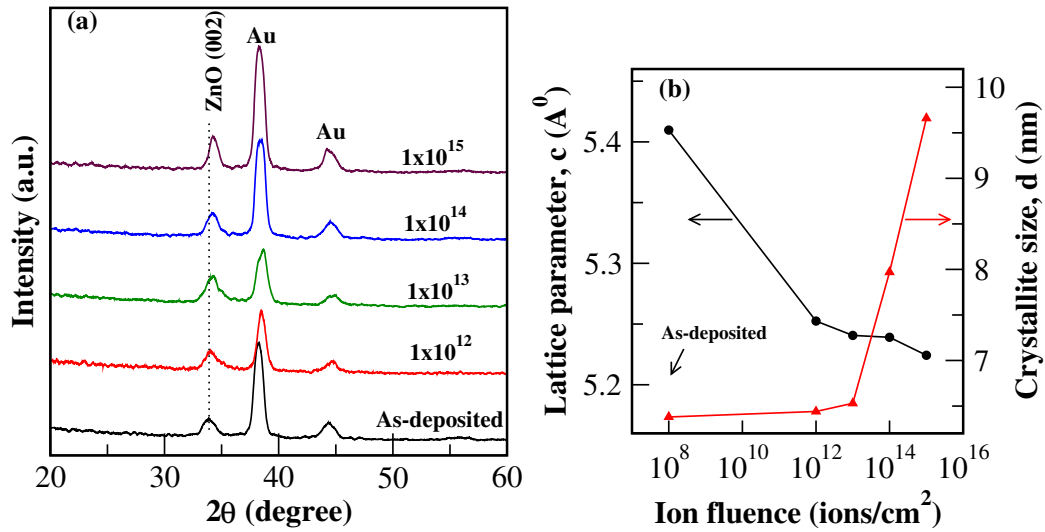


Figure 7.1: (a) GIXRD from as-deposited ZnO thin films and after ion implantation at various fluences (ions/cm^2), (b) Variation of lattice parameter, c , and crystallite size, d , with ion fluence.

Fig. 7.1(b) displays the variations in the crystallite size and lattice parameter as a function of ion fluence, for all the films. The crystallite size appears to be small (~ 6.5 nm) for the as-deposited films as well as after ion implantation at lower fluences (up to 1×10^{13} ions/cm²). However, development of larger sized (~ 11 nm) crystallites, at higher fluences, suggests an improved crystallinity of the films. A very mild shift of (002) feature, with fluence, may indicate towards the existence of some tensile strain

in the films [45]. This may also be associated with the weak reduction in the lattice parameter.

Table 7.1: Structural parameters of as-deposited and Ti ion implanted ZnO thin films

Sample	FWHM (β)(002)	2θ	d(nm)	c(\AA)
As-deposited	1.41	34.00	6.38	5.409
1×10^{12} ions/cm ²	1.35	34.12	6.44	5.253
1×10^{13} ions/cm ²	1.33	34.20	6.53	5.241
1×10^{14} ions/cm ²	1.09	34.21	7.97	5.239
1×10^{15} ions/cm ²	0.90	34.31	9.66	5.224

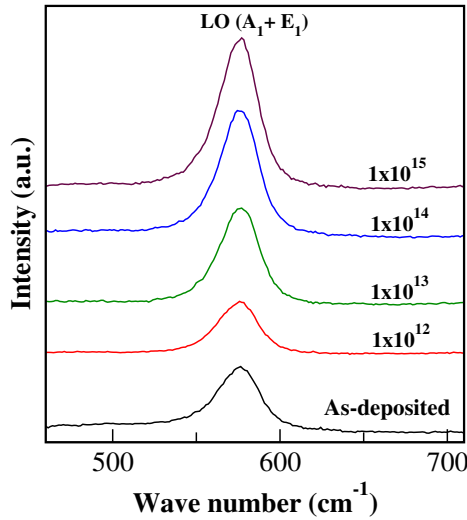


Figure 7.2: UV-Raman spectra from as-deposited ZnO thin films and after ion implantation with various fluences (ions/cm²).

Raman spectra from the as-deposited and ion implanted ZnO thin films are displayed in Fig. 7.2. With the excitation energy of the UV-laser similar to the bandgap of ZnO, resonant Raman scattering conditions can be achieved here [46]. All the spectra display a distinct feature near 578 cm⁻¹, corresponding to LO (A₁+E₁) mode of ZnO [19, 47]. The feature becomes sharper and more prominent with increasing fluence. This is indicative of an improvement in the crystallinity of the film, as also suggested by GIXRD measurements. This mode is also very sensitive to the lattice defects, particularly the oxygen vacancy sites (O_V) [19, 47]. As preferential sputtering during ion implantation can create oxygen vacancies, this mode will be effected by their presence as well. XPS studies, discussed later, have been utilized here to assess

the contribution of O_V states more distinctly.

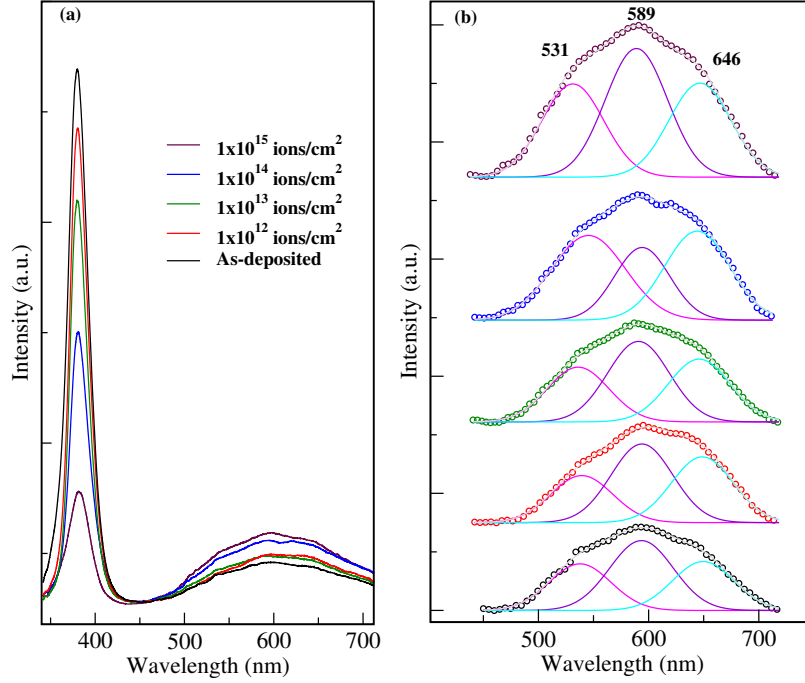


Figure 7.3: (a) Room temperature PL spectra of the as-deposited and ion implanted ZnO films (b) Corresponding magnified PL spectra in visible region.

Fig. 7.3 presents PL spectra of the as-deposited as well as ion implanted ZnO films. An ultraviolet emission peak at 378 nm (Fig. 7.3(a)) can be observed for all the films. Free exciton recombination, through an exciton-exciton collision process in ZnO, contributes to this band [48]. A dominant and broad emission band, centered around 600 nm, can also be noticed. This may be ascribed to the various defect states in ZnO, such as zinc interstitial (Zn_i), oxygen interstitial (O_i), zinc vacancy (V_{Zn}), oxygen vacancy (O_{vs}) or singly-ionized oxygen vacancy states [49, 50]. The deconvolution of this defect band yields three prominent components located around 531, 589 and 646 nm (Fig. 7.3(b)). These peaks are respectively attributed to a green emission (530-550 nm), yellow-orange emission (590-600 nm) and a red emission (650-670 nm) [51]. An overall increase in the intensity of the defect band, with ion fluence, can also be observed (Fig. 7.3(a)). Most prominent is the gradual enhancement of the green emission. This may be related to the increase of oxygen vacancy states with ion fluence, as also suggested by XPS results discussed below. The increase in defect states can also become responsible for the decreasing band edge emission

(Fig. 7.3(a)).

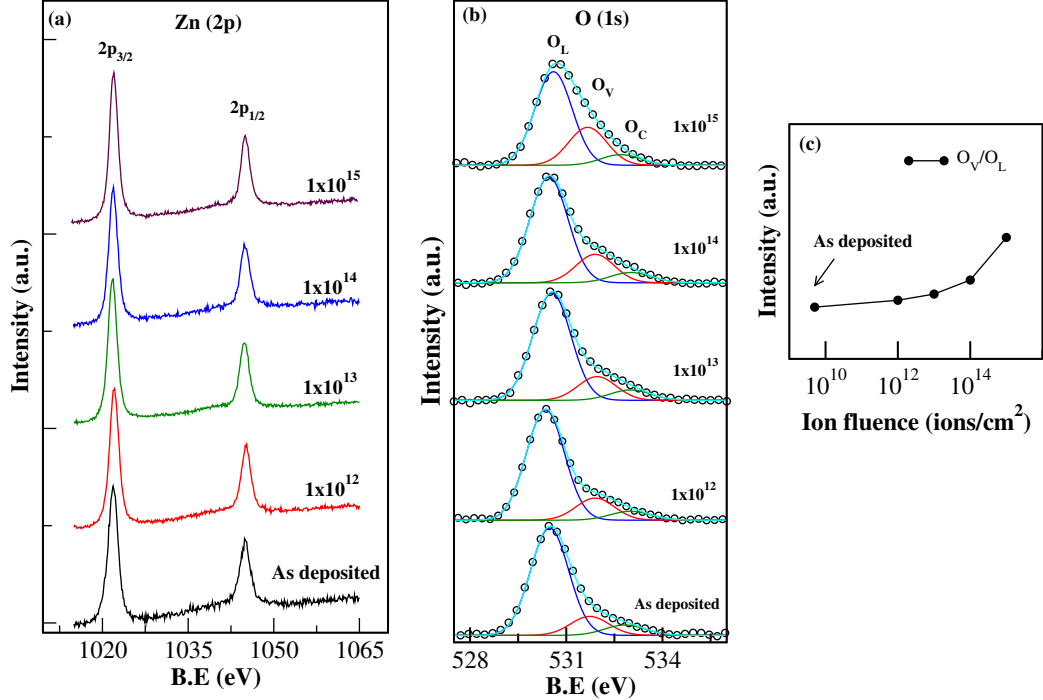


Figure 7.4: (a) Zn(2p) XPS spectra from as-deposited ZnO thin films and after ion implantation with various fluences (ions/cm²). (b) O(1s) XPS spectra at various fluences. Peaks have been fitted with three components related to bulk lattice oxygen (O_L), oxygen vacancies (O_V) and chemisorbed oxygen (O_C). (c) Ratio of the intensity of O_V w.r.t O_L , as a function of ion fluence.

XPS spectra from Zn(2p) region are presented for the as-deposited and ion implanted ZnO thin films in fig. 7.4(a). Two features corresponding to Zn $2p_{3/2}$ and Zn $2p_{1/2}$ states can be seen. For the as-deposited films, these features appear at the binding energies of 1021.9 eV and 1044.9 eV, respectively [52]. Fig. 7.4(b) shows the oxygen O(1s) spectra for all the films. These spectra have been deconvoluted with three components corresponding to the lattice oxygen (O_L), oxygen vacancy sites (O_V) and chemisorbed oxygen species on the surface (O_C) [53, 54]. For the as-deposited films these features are located at 530.1, 531.7, and 533.1 eV, respectively. The ratio of the intensity of O_V w.r.t O_L (Fig. 7.4(c)) enhances with fluence indicating an increase in the vacancy states, in concurrence with Raman and PL measurements presented here.

Fig. 7.5(a) shows the photoabsorbance spectra in the UV-Vis regime, for the as-

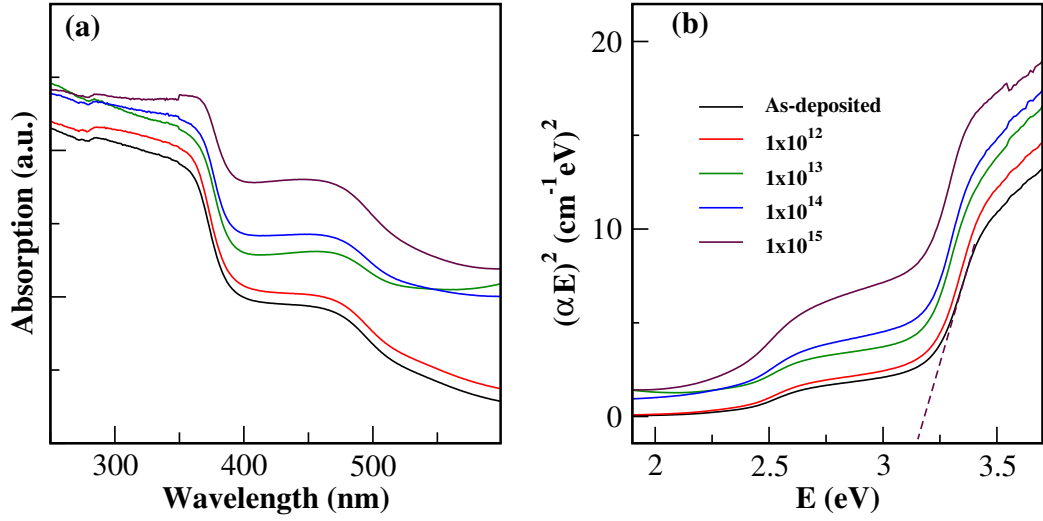


Figure 7.5: (a) Photoabsorbance response for as-deposited ZnO thin films and after ion implantation with various fluences (ions/cm²) (b) Tauc plots at various fluences (α is absorption coefficient and E is photon energy)

deposited and ion implanted ZnO thin films. The as-grown ZnO thin films show low absorbance in the visible region. However after ion implantation, a systematic increase in the photoabsorbance, both in UV as well as visible regions, is noticed. Moreover, the enhancement is relatively higher in the visible regime, becoming stronger with fluence. For the as-deposited ZnO films, the absorption edge appears nearly at 370 nm but delineates red shifting with increasing ion fluence. This clearly reflects initiation of a bandgap tailoring phenomenon controlled by ion implantation. Tauc plots (fig. 7.5(b)) display $(\alpha E)^2$ as a function of energy E for absorption coefficient α , and have been utilized to extract the bandgap energy, E_g , of the films. The as-deposited ZnO films exhibit a bandgap of 3.16 eV. Earlier studies have shown this bandgap to be influenced by the presence of oxygen vacancies [52]. For the implanted films, a systematic reduction in the bandgap with increasing fluence is observed. Creation of defect related localized states within the forbidden gap, during implantation, contribute to these modifications [55]. Consequently, fig. 7.5(b) exhibits a low (2.95 eV) bandgap for the films implanted at the highest fluence (1×10^{15} ions/cm²). This bandgap tailoring is promoting the enhanced photoabsorption response, seen especially in the visible regime in ZnO thin films.

The current-voltage (I-V) characteristics of ZnO thin films have been investigated

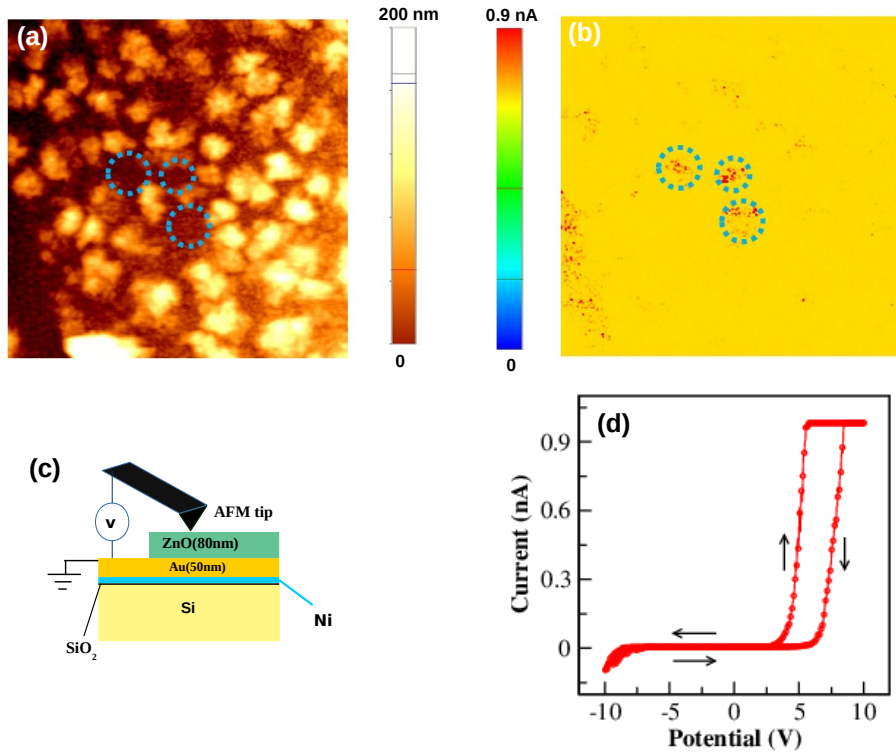


Figure 7.6: For ZnO thin films implanted with 1×10^{15} ions/cm² (a) AFM image (500×500 nm²) showing surface topography, (b) c-AFM image (500×500 nm²) showing a current map with +10V bias applied at Au back electrode, (c) schematic diagram of c-AFM experiments on ZnO/Au/Ni/SiO₂/Si with Pt/Ir tip acting as the movable top electrode for c-AFM, (d) local I-V characteristics acquired by sweeping the applied potential across the AFM tip and Au back electrode from -10 V to +10 V and back to -10 V, compliance current (I_c) was 1 nA.

here. No detectable current response was observed for the as-deposited films as well as for films implanted at low fluences. However, films implanted with the fluence of 1×10^{15} ions/cm² exhibit a voltage dependent current response. The surface morphology and the corresponding c-AFM images are displayed in Fig. 7.6(a) and (b), respectively. The circled regions in fig. 7.6(b) refer to the location of the pronounced surface current density. Schematic diagram of c-AFM experiments on ZnO/Au/Ni/SiO₂/Si is illustrated in fig. 7.6(c).

Local I-V characteristics of ZnO thin film, implanted at the highest fluence is shown in fig 7.6(d). A sweeping voltages of magnitude ± 10 were applied in the se-

quence of $0.0\text{ V} \rightarrow 10.0\text{ V} \rightarrow 0.0\text{ V} \rightarrow -10.0\text{ V} \rightarrow 0.0\text{ V}$. When a positive bias is applied to the top electrode, the current rises steadily and resistance undergoes a transition (fig. 7.6(d)) from a high resistance state (HRS) to a low resistance state (LRS). The smooth profile is indicative of the absence of any extra processes, such as electroforming. This insulating-to-conducting transition is attributed to the formation of conducting filamentary path by the oxygen vacancies in the film during transition which allows the charge carriers to flow. In the present study, ZnO thin films implanted at the highest fluence (1×10^{15} ions/cm²), having highest oxygen vacancies, only demonstrate switching behavior.

During the negative voltage sweep, the current is extremely low, reflecting a conversion from LRS to HRS. Thus, I-V characteristics here are significantly asymmetric, possibly indicating towards the formation of a Schottky-like barrier in the metal/oxide interface. ZnO is a well-known n-type semiconductor with the work function around 4.71 eV [58]. The work function of Pt and Au are 5.65 eV and 5.15 eV [56,57], respectively. Therefore, the Schottky barrier at Pt/ZnO interface is larger than at Au/ZnO interface. When a negative voltage is applied to Pt electrode, the barrier height is too high for electrons to pass easily, creating a rectifying behavior at Pt/ZnO interface. Won et al. have reported similar behavior at Pt/WO_x interface for Pt/WO_x /Au device [57]. In the present study, for ZnO thin films an asymmetric I-V response is observed. Specifically, a HRS to LRS transition is noticed under the positive bias conditions. For the negative voltage regime, development of a Schottky barrier leads to a rectification behavior.

7.4 Conclusion

The present study investigates Ti ion implantation in ZnO thin films. GIXRD and Raman spectroscopy results indicate that the crystallinity of the films improve with ion fluence. For the as-deposited films the crystallites are nearly 6.5 nm in size but are found to be nearly 11 nm at the highest fluence. An enhancement in the oxygen vacancy states, with fluence, is also delineated. The ion implanted films present a higher PA response in the UV-Visible regime, significantly more in the visible range.

This is accompanied by a band edge tailoring, where a systematic reduction in the bandgap energy with fluence occurs. An asymmetric RS phenomenon is demonstrated by the films implanted at the highest fluence (1×10^{15} ions/cm²). Although in positive bias conditions a switching behavior, from HRS to LRS, is expressed in the I-V profile, rectifying nature is seen under negative voltages. Oxygen vacancies play a crucial role in the modulation of PA response as well as in RS mechanism.

Bibliography

- [1] B. Liu and H. C. Zeng, *J. Am. Chem. Soc.*, 125, 4430 (2003)
- [2] L. Guo, Y. L. Ji and H. Xu, *J. Am. Chem. Soc.*, 124, 14864 (2002).
- [3] Z. Y. Jiang, T. Xu, Z. X. Xie, Z. W. Lin, X. Zhou, X. Xu, R. B. Huang and L. S. Zheng, *J. Phys. Chem. B*, 109, 23269 (2005).
- [4] W. J. E. Beek, M. M. Wienk, M. Kemerink, X. Yang and R. A. J. Janssen, *J. Phys. Chem., B*, 109, 9505 (2005).
- [5] S. Ju, K. Lee, D. B. Janes, M. H. Yoon, A. Facchetti and T. J. Marks, *Nano Lett.*, 5, 2281 (2005).
- [6] H. Kind, H. Yan, B. Messer, M. Law and P. Yang, *Adv. Mater.*, 14, 158 (2002).
- [7] R. Konenkamp, R. C. Word and M. Godinez, *Nano Lett.*, 5, 2005 (2005).
- [8] O. Harnack, C. Pacholsk, H. Weller, Akio Yasuda and Jurina M. Wessels, *Nano Lett.*, 3, 1097 (2003).
- [9] M. Huang, S. Mao, H. Feick, H. Yan, Y. Wu, H. Kind, E. Weber, R. Russo and P. Yang, *Science*, 292, 1897 (2001)
- [10] X. Wen, Y. Fang, Q. Pang, C. Yang, J. Wang, W. Ge, K. S. Wong and S. Yang, *J. Phys. Chem. B*, 109, 15303 (2005).
- [11] M. Peruzzi, J. D. Pedaring, D. B. Bauerle, W. Schwinger, F. Schaffler, *Appl. Phys. A*, 79, 187 (2014)
- [12] W Y Chang, Y C Lai, T B Wu, S F Wang, F Chen, *Appl Phys Lett*, 92, 022110 (2008)

- [13] R Ullah, J Dutta, J. Hazard. Mater., 156, 194 (2008).
- [14] C. A. K. Gouva, F. Wypych, S. G. Moraes, N. Durn, S. Peralta-Zamora, Chemosphere, 40, 427 (2000)
- [15] M Ahmad, E. Ahmed, Y. Zhang, N. R. Khalid, J. Xu, M Ullah, Z Hong, Curr. Appl. Phys., 13, 697 (2013).
- [16] S. Liu, C. Li, J. Yu, Q. Xiang, Cryst. Eng. Comm, 13, 2533 (2011).
- [17] F. Achouri, S. Corbel, L. Balan, K. Mozet, E. Giroto, G. Medjahdi, M. Ben Said, A. Ghrabi, R. Schneider, Mater. Des., 101, 309 (2016).
- [18] K.C Barick, S. Singh, M. Aslam, D Bahadur, Microporous Mesoporous Mater., 134, 195 (2010).
- [19] P. Dash , A. Manna, N.C. Mishra , Shikha Varma, Physica E: Low-dimensional Systems and Nanostructures, 107, 38 (2019)
- [20] U. Ozgur, Ya. I. Alivov, C. Liu, A. Teke, M. A. Reshchikov, S. Dogan, V. Avrutin, S.-J. Cho, and H. Morkoc, J. Appl. Phys., 98, 041301 (2005)
- [21] S. Z. Umbaidillah, N. A. M. Asib, A. N. Afaah, M. Rusop, and Z. Khusaimi, AIP Conference Proceedings, 2151, 020038 (2019)
- [22] N. A. Abdullah, Z. Khusaimi, and M. Rusop, Advanced Materials Research, 667, 329 (2013)
- [23] Ashis Manna, A. Barman, Shalik R. Joshi, B. Satpati, P. Dash, Ananya Chattaraj, S. K. Srivastava, P. K. Sahoo, A. Kanjilal, D. Kanjilal, and Shikha Varma, J. Appl. Phys., 124, 155303 (2018)
- [24] Ashis K. Manna, Vanaraj Solanki, D. Kanjilal, Shikha Varma, Radiation Effects and Defects in Solids, 174, 3 (2019)
- [25] P. M. R. Kumar, C. S. Kartha, K. P. Vijayakumar, T. Abe, Y. Kashiwaba, G. S. Okram, M. Kumar, S. Kumar, J. of Appl. Phys., 97, 13509 (2005)

- [26] Subrata Majumder, D. Paramanik, V. Solanki, B.P. Bag and ShikhaVarma, Appl. Phys. Lett. 98, 053105 (2011).
- [27] Subrata Majumder, I. Mishra, U Subudhi, Shikha Varma, Appl. Phys. Lett., 103, 063103 (2013).
- [28] Vanaraj Solanki, Subrata Majumder, Indrani Mishra, P. Dash, C. Singh, D. Kanjilal and Shikha Varma, Jour. Appl. Phys., 115, 124306 (2014).
- [29] V. Solanki, I. Mishra, S.R. Joshi, P. Mishra, P. Dash, N.C. Mishra, D. Kanjilal and Shikha Varma, Nucl. Instr. Res. Meth. B, 365, 82 (2015).
- [30] Vanaraj Solanki, Shalik R. Joshi, Indrani Mishra, D. Kabiraj, N.C. Mishra, D.K. Avasthi, and Shikha Varma, Jour. Applied Physics, 120, 054303 (2016).
- [31] Shalik Ram Joshi, B. Padmanabhan, Anupama Chanda, V. K. Malik, N. C. Mishra, D. Kanjilal and Shikha Varma, Applied Physics A, 122, 713 (2016)
- [32] Shalik Ram Joshi, B. Padmanabhan, Anupama Chanda, N. Shukla, V.K. Malik, D. Kanjilal, Shikha Varma, Jour. of Magnetism and Magnetic Materials, 465, 122 (2018).
- [33] G I Meijer, Science, 319, 1625 (2008); K Shiguya, R Dittmann, S B Mi, R Waser, Adv Mater, 22, 411 (2010)
- [34] A Sawa, Mater Today, 11, 28 (2008)
- [35] S L Li, J Li, Y Zhang, K Tsukagoshi, Appl Phys A Mater Sci Process, 103, 21 (2011)
- [36] Shen W, Dittmann R, Waser R, J Appl Phys, 107, 094506 (2010)
- [37] A. Barman, C. P. Saini, P. Sarkar, B. Satpati, S. R. Bhattacharyya, D. Kabiraj, D. Kanjilal, S. Dhar, and A. Kanjilal, J. Appl. Phys., 118, 224903 (2015)
- [38] A. Barman, C. P. Saini, P. K. Sarkar, A. Roy, B. Satpati, D. Kanjilal, S. K. Ghosh, S. Dhar, and A. Kanjilal, Appl. Phys. Lett., 108, 244104 (2016)

- [39] Sunghun Lee, Jung-Bong Park, Myoung-Jae Lee, and John J. Boland, AIP ADVANCES, 6, 125010 (2016)
- [40] Fatih Gul, Hasan Efeoglu, Superlattices and Microstructures, 101, 172 (2017)
- [41] J. F. Ziegler, J. P. Biersack and M. D. Ziegler, SRIM - The Stopping and Range of Ions in Matter (SRIM Co., Chester, MD,USA, 2008).
- [42] Guangwei Geng, Penglei Chen, Nannan Wang, Minghua Liu, Bo Guan, Yu Liu, Changchun Yang, RSC Adv., 7, 51838, (2017)
- [43] B.D. Cullity, S. R. Stock, Elements of x-ray Diffraction, Prentice Hall, 2001
- [44] O. Lupan, T. Pauporte, L. Chow, B. Viana, F. Pelle, L. K. Ono, B. Roldan Cuenya, H. Heinrich, Appl.Surf.Sci., 256, 1895 (2010)
- [45] R. Taziwa, E. Meyer, D. Katwire and L. Ntozakhe, Journal of Nanomaterials, 9095301 (2017)
- [46] L. Bergman, X.-B. Chen, J. Huso, J. L. Morrison, H. Hoeck, J. Appl. Phys., 98, 093507 (2005)
- [47] V. Russo, M. Ghidelli, P. Gondoni, C. S. Casari and A. Li Bassi, J. Appl. Phys., 115, 073508 (2014)
- [48] K. Samanta, P. Bhattacharya, R. S. Katiyar, Appl. Phys.Lett., 87,101903 (2005)
- [49] Y.Wang, J.Piao, Y.Lu, S.Li and J.Yi, Materials Research Bulletin, 83, 408 (2016)
- [50] M. R. Alenezi, S. J. Henley, N. G. Emerson, S. R. P. Silva, Nanoscale, 6, 235 (2014)
- [51] A. Shetty, K. K. Nanda, Appl. Phys. Lett., 100, 242108 (2012); A. Escobedo-Morales, U. Pal, Appl. Phys. Lett., 93, 193120 (2008)
- [52] Vanaraj Solanki, Shalik R. Joshi, Indrani Mishra, D. Kabiraj, N. C. Mishra, D. K. Avasthi, and Shikha Varma, J. Appl. Phys., 120, 054303 (2016)

- [53] M.Chen, X. Wang, Y. H. Yu, Z. L. Pei, X. D. Bai, C. Sun, R. F. Huang, L.S. Wen, *Appl. Surf. Sci.*, 158, 134 (2000)
- [54] Z. G. Wang, X.T. Zu, S. Zhu, L. M. Wang, *Phys. E*, 35, 199 (2006)
- [55] G A Amin, S M El-Sayed, H M Saad, F M Hafez and M Abd-El-Rahman, *Radiat. Meas.*, 42, 400 (2007)
- [56] H B.Michaelson, *J Appl. Phys.*, 48, 4729 (1977)
- [57] Seokjae Won, Sang Yeon Lee, Jucheol Park, Hyungtak Seo, *Scientific reports*, 7, 10186 (2017)
- [58] Min WEI, Chun-Fu LI, Xue-Ran DENG, Hong DENG, *Energy Procedia*, 16, 76 (2012)

Chapter 8

Cu₂O-ZnO nanostructured films grown by Co-electrodeposition: Photo-absorption behavior & Non-Enzymatic Glucose Sensing via Cyclic Voltammetry

8.1 Introduction

Electrochemical sensors have attracted enormous interest in many fields, like clinical diagnostics, biotechnology and food industry, for their reliable and fast detection of glucose [1–3]. Several glucose sensors have been developed on the principles of amperometric enzyme electrodes, with glucose oxidase, which demonstrate good selectivity and sensitivity [4, 5]. They however can suffer with poor stability caused by the enzyme glucose oxidase which is known to get severely effected by factors like pH, humidity, temperature, ionic detergents, many types of interferences and high cost [6]. This has motivated the explorations of non-enzymetic glucose sensors for improving the electrocatalytic activity and selectivity towards the oxidation of glucose. Nanostructured electrodes of noble metals (Ag, Au, Pt, Pd) and their alloys as well as transition metals (Ni, Cu) and their oxides present many attractive characteristics with functional templates for such sensors [7–13]. Copper and its oxides demonstrate many excellent characteristics for amperometric sensing [14–17]. Combined hybrid nano-structures also show improved glucose sensing primarily due to efficient electron

transfer rates and morphological properties. Fabrication of high performance enzyme-less glucose sensors however is a challenge as the composition and morphology of the sensor can drastically modulate the sensing properties. Such sensors demand investigations of appropriate hybrid structures for improving the sensing characteristics [11]. Hybrid nano-structured films present superior moiety for enzyme-less glucose sensing due to the large associated surface area which can induce enhanced diffusion and mass transport. This can effectively improve glucose detection with high sensitivity.

With exciting properties like biocompatibility, non-toxicity and chemical stability, ZnO is an excellent functional material for bio-sensing applications [18, 19]. Crystalline ZnO nanostructures are considered to be efficient glucose sensor due to fast electron transfer rates between the active sites and the electrode. Cu₂O exhibits excellent properties for catalysis, electrochemical water splitting and gas sensing. These characteristics along with its non-toxic nature, low cost, appropriate redox potential, high electrocatalytic activity, excellent stability makes it a promising candidate for non-enzymatic electrochemical sensors [20]. However, the conductivity of Cu₂O is poor which is not favorable for fast electron transfer. In this direction, for increasing its electrochemical sensing properties, several morphologies have been investigated by growing nano-composites or thin films of Cu₂O on variety of conducting templates, like graphene [21], NiO/graphene oxide(GO) [22], Carbon nano-tubes (CNT) [23] etc..

In chapter 3-6, we have discussed the ion irradiation of TiO₂. The phase transformation of TiO₂ after Ti ion implantation as well as several functional properties like resistive switching and photo-absorbance have been investigated. The evolution of TiO₂ nanostructured film via scaling functions have also been discussed. In chapter 7, Ti ion implantation of ZnO thin films has been explored. These films demonstrate a resistive switching behaviour for implantation undertaken at the highest fluence. Modification in photo-absorbance response and band gap tailoring have also been investigated.

The present chapter explores the glucose sensing nature of ZnO as well as after introducing Cu²⁺ ions via electrodeposition methods. This synthesis route displays formation of Cu₂O-ZnO hybrid nanostructured (HN) films. Good transfer rates of ZnO combined with the suitable band alignment of Cu₂O will be expected to provide

interesting sensing as well as optical properties. Preparation methods for such systems usually require multiple complex steps which can contribute to many uncertainties. Conjugated hybrid nanostructures of Cu₂O-ZnO prepared in single step, on the other hand, can provide a simpler, attractive and fast response systems with larger control on the morphology as well as characteristic properties. Additionally, the nano- hybrid Cu₂O-ZnO morphology can produce larger diffusion leading to enhanced enzyme-less biosensing.

ZnO is a wide band gap (3.2 eV) material which absorbs only a small part(5%) of the solar spectrum. Cu₂O on the other hand is a narrow band gap material. Hybrid structure of Cu₂O and ZnO will be expected to display good matching with solar visible spectrum. In literature, several routes have been suggested for conjugating them with other metal, oxides, graphene etc. in order to achieve enhanced PA response and band gap modification [24, 25].

Here, first we have developed nano- hybrid Cu₂O-ZnO nanostructure network by the techniques of single step co-electrodeposition (CED) and carefully investigated their enzymeless glucose sensing via cyclic voltammetry. We have compared these results with the pure ZnO nanostructures grown by the electro- deposition method. The technique of CED, used here for growing conjugated Cu₂O-ZnO hybrid HN film, is remarkably a simple single step process. This technique induces electro-deposition of multiple ions simultaneously and promotes development of nanostructured surface morphologies. Such CED processes have not been applied earlier for the development of Cu₂O-ZnO based biosensors. Here, low concentrations of Cu²⁺ ions (1% and 10%) for CED of Cu₂O-ZnO nanostructures have been investigated. Results presented here show that the nanostructured material integrates the electron transfer efficiency of ZnO with electrochemical activity of Cu₂O. These hybrid nanostructures exhibit non-enzymetic amperometric detection of glucose. Remarkable improvement in the overall detection is observed for Cu₂O-ZnO HN film compared to ZnO nanostructures alone.

The prepared Cu₂O-ZnO hybrid nanostructures have been characterized for their Photo-absorbance(PA) properties also. Here the Cu₂O-ZnO hybrid structures show higher PA as well as band gap tailoring effects.

8.2 Experimental

8.2.1 Chemical and Reagents

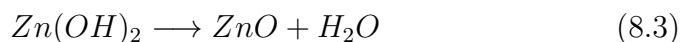
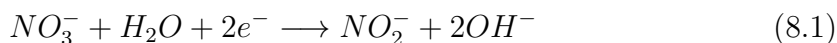
All reagents and materials used here like zinc nitrate ($\text{Zn}(\text{NO}_3)_2 \cdot 6\text{H}_2\text{O}$), hexamethylenetetramine ($(\text{CH}_2)_6\text{N}_4$ (HMT), Glucose, NaOH, $\text{CuCl}_2 \cdot 2\text{H}_2\text{O}$, Asorbic Acid (AA), Uric acid (UA) and Dopamine acid (DA) were of analytical grade and were used as received without further purification. High quality deionized water ($18.25 \text{ m}\Omega \text{ cm}$) was used in all the experiments.

8.2.2 Preparation of ZnO-nanostructures using Electrodeposition Method

Prior to the experiments, indium tin oxide (ITO) substrates (from MTI corp.) underwent standard cleaning process where the samples were sequentially cleaned for 5 min each in acetone and ethanol. Subsequently samples were rinsed in deionized water for multiple times and dried in air at room temperature. ZnO-nanostructures were produced via electrodeposition on the ITO substrate. For this purpose, a three-electrode electrochemical configuration was used with ITO substrate as the cathode, Pt sheet as the counter electrode (anode) and Ag/AgCl as the reference electrode [24]. An aqueous solution containing 10 mM zinc nitrate and HMT was used as the electrolyte. HMT acts as a surfactant in the preferential growth of ZnO structures. It is also a source of OH^- ions in solution, necessary for growth of ZnO [28]. The electrodeposition was carried out for 10 min at a fixed cathodic voltage of -0.8 V with solution rotated at 100 rpm by a magnetic stirrer. These depositions were carried out at 70°C under normal atmospheric conditions. The ZnO/ITO samples were taken out immediately after the completion of the electrodeposition and were rinsed in deionized water.

8.2.3 Preparation of Hybrid Cu₂O-ZnO nanostructures using single step coelectrodeposition (CED) Method

The electrochemical cell was prepared in similar fashion as discussed above. Only difference was in the aqueous solution which contains 10 mM zinc nitrate, HMT as well as a small concentration of CuCl₂.2H₂O. The experiments were conducted for two concentrations 0.1 mM (1%) and 1 mM (10%) of CuCl₂.2H₂O in the solution. The deposition was carried out on ITO for 10 min at a fixed cathodic voltage of -0.8 V with solution rotated at 100 rpm by a magnetic stirrer. These depositions were carried out at 70° C under normal atmospheric conditions. All the solutions were prepared with deionized Milli-Q purified water. This results in the formation of nano- hybrid conjugated Cu₂O-ZnO nanostructures on the ITO surface. Simultaneous formation of hybrid ZnO [26, 27] (steps 1-3) and Cu₂O [24] (step 4) nanostructures occur via following reactions :



The formation of hybrid Cu₂O-ZnO nanostructures occurs via a single step CED process on ITO. Fig. 8.1 schematically illustrates the formation process of the CED grown hybrid Cu₂O-ZnO nanostructures.

Two types of Cu₂O-ZnO samples were grown here by the CED method described above. During growth, the concentration of Zn²⁺ was always kept fixed (10 mM), but two concentrations of Cu²⁺ were used. The sample prepared with 0.1 mM of Cu²⁺ and 10 mM Zn²⁺ will be referred to as C₁ in this manuscript. The sample with 1 mM of Cu²⁺ and 10 mM Zn²⁺ is referred as C₁₀.

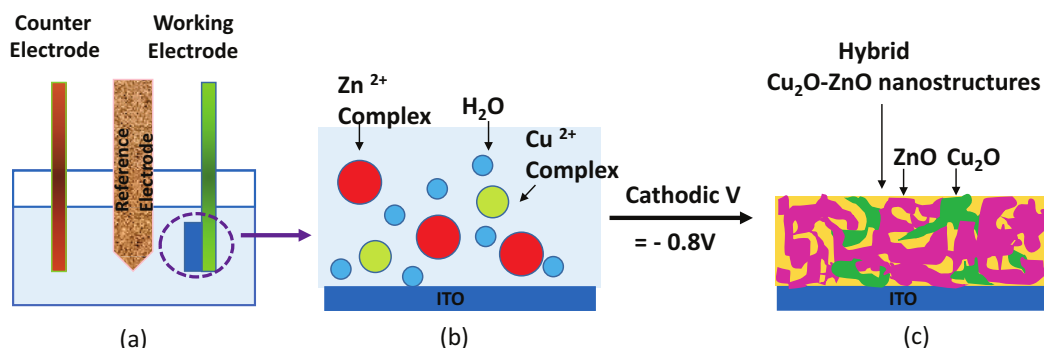


Figure 8.1: Schematic illustration of the CED process and growth of $\text{Cu}_2\text{O-ZnO}$: (a) Growth cell (b) simultaneous presence of both Cu^{2+} and Zn^{2+} ions in the solution (c) CED growth of hybrid $\text{Cu}_2\text{O-ZnO}$ nanostructures upon application of cathodic voltage.

8.2.4 Glucose Sensing Experiments via cyclic voltammetry

Experiments were carried out at room temperature, in a conventional three-electrode system. All the potentials are mentioned against an Ag/AgCl reference electrode. Cyclic voltammetry (CV) measurements of the electrodeposited ZnO nanostructures and CED-grown $\text{Cu}_2\text{O-ZnO}$ nanostructures were undertaken in 20 ml, 0.1 M NaOH electrolyte under ambient conditions, in the presence or absence of glucose. The potential was varied from -0.3 to 0.8 V at the scan rate of 10 mV/s. The chronoamperometric (CA) studies were also performed. CA curves have been obtained after adding a known amount of glucose.

8.2.5 Characterization techniques

Field-emission scanning electron microscope (FESEM) from Carl Zeiss, Germany (20 keV electrons) was used for investigating the morphology and the nanostructure- size on the as-prepared samples. Energy-dispersive X-ray spectroscopy (EDX) detector attached with FESEM system was utilized for the chemical and compositional analysis. X-ray diffraction (XRD) measurements were performed using a $\text{Cu-K}\alpha$ (0.154 nm) radiation (Bruker D8 Advance, Germany). High resolution transmission elec-

tron microscope (HRTEM) with 200 keV electrons (JEOL JEM-2010) was utilized for the imaging of morphology as well as structural analysis. Detailed structural analysis was performed using HRTEM along with selected area electron diffraction (SAED) pattern capabilities. Micro-Raman measurements were performed with the help of a 488 nm Ar⁺ laser in backscattering geometry on a T64000 triple monochromator (Horiba Jobin Yvon) having a Liquid nitrogen-cooled CCD detector. X-ray photoelectron spectroscopy (XPS) was performed using the PHI 5000 Versa Probe II (ULVAC-PHI) system with Al-K α source (1486.6 eV). The optical absorptions spectra of the samples were recorded in the wavelength range of 200-900 nm using Cary 5000 UV-Visible spectrophotometer. Electrochemical measurements, cyclic Voltammetry (CV) and chrono-amperometry (CA) were performed on Autolab PGSTAT 302N. All the experiments were repeated at least five times to verify the reproducibility.

8.3 Results and Discussion

8.3.1 Structure and Morphology

SEM image of the ZnO nanostructures, fabricated by electrodeposition method, is shown in Fig. 8.2(a). The nanostructures display an average diameter of about 250 nm. SEM images after single step co-electrodeposition (CED) of C₁ and C₁₀ show surface with nanostructured morphologies in fig. 8.2(b) and fig. 8.2(c), respectively. The energy dispersive X-ray (EDX) results display presence of Cu, Zn and O. They also show concentration of Cu to be \sim 1% and 10% respectively on C₁ and C₁₀ samples, as expected. EDX mappings from C₁₀ sample are also shown in fig. 8.2 for Zn, O and Cu elements. The distribution of Cu element is similar to that from O. The distribution of Zn element appears homogeneous and uniform. These results suggest that the as-prepared CED surfaces have conjugated nano-hybrid structures.

To analyse the phase structures of the samples, XRD patterns were investigated. The as-fabricated ZnO sample displays a polycrystalline matrix with a preferential growth along the (002) direction (fig. 8.3). Characteristic peaks at 31.8 $^\circ$, 34.5 $^\circ$, 36.3 $^\circ$, 47.6 $^\circ$, 56.6 $^\circ$, 62.9 $^\circ$ and 68.0 $^\circ$ correspond to (100), (002), (101), (102), (110), (103) and (112) lattice planes of ZnO [28,29]. The XRD from hybrid Cu₂O-ZnO nanostructures

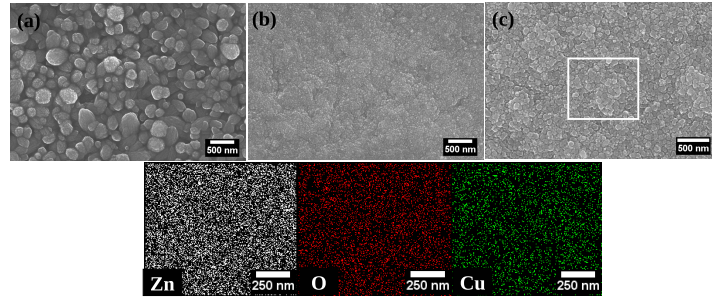


Figure 8.2: (a) SEM image of electrodeposited ZnO nanostructures. SEM images from Hybrid Cu₂O-ZnO nanostructures (b) C₁ and (c) C₁₀. EDX elemental mapping images of Zn, O, and Cu in the C₁₀ sample, taken from the box of (c).

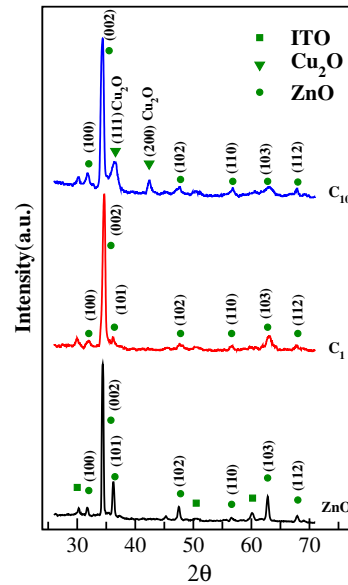


Figure 8.3: XRD of ZnO nanostructures as well as of Cu₂O-ZnO nanostructures C₁ and C₁₀.

is also presented for C₁ and C₁₀ samples. Prominent features for Cu₂O at 36.6° and 42.4°, corresponding to (111) and (200) lattice planes, are seen for the C₁₀ samples [30, 33]. C₁, however does not show Cu₂O related peaks probably due to small Cu content. Raman measurements, discussed later, show presence of Cu₂O in C₁.

Fig. 8.4 shows the TEM observations of CED-grown C₁₀ sample. The low magnification TEM image is presented in fig. 8.4(a). Fig. 8.4(b) displays high resolution TEM (HRTEM) micrograph. Fig. 8.4(c,d,e) are high resolution (filtered) images of selected areas from fig. 8.4(b). Inter-planar spacing of the fringes are found to be 0.286 nm and 0.260 nm corresponding to d(100) and d(002) of ZnO. The d-spacing

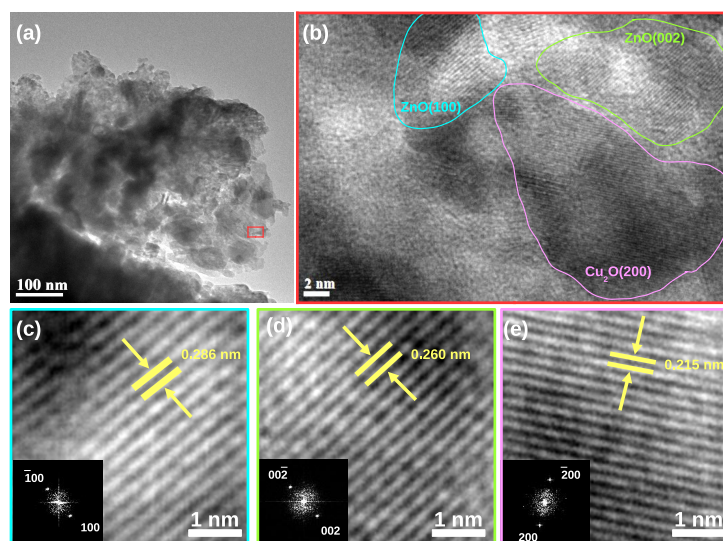


Figure 8.4: (a) Low magnification TEM micrograph of $\text{Cu}_2\text{O-ZnO C}_{10}$ sample (b) high resolution TEM image of marked region in (a); (c), (d) and (e) high resolution (filtered) images from blue, green and magenta regions respectively and inset shows their corresponding FFT patterns.

of 0.215 nm is attributed to $d(200)$ of Cu_2O . Insets of fig. 8.4(c,d,) show their corresponding Fast Fourier transform (FFT) patterns, which can readily be indexed with $\text{ZnO}(100)$ and $\text{ZnO}(002)$, respectively. FFT from $\text{Cu}_2\text{O}(111)$ is shown in the inset of fig. 8.4(e). The lattice planes for ZnO and Cu_2O , as observed here by TEM, correspond well with the XRD results shown in fig. 8.3. These TEM images indicate the presence of conjugated $\text{ZnO-Cu}_2\text{O}$ hybrid nanostructures on the surface.

Fig. 8.5(a) shows Raman spectrum from the electro-deposited ZnO nanostructures. Features at 99, 334, 439 and 579 cm^{-1} respectively correspond to $E_2(\text{low})$, $E_2(\text{high})-E_2(\text{low})$, $E_2(\text{high})$ and $E_1(\text{LO})$ of the wurtzite ZnO crystal [18]. Raman spectra from CED grown C_1 and C_{10} are also presented. In addition to the features from ZnO , Raman features of Cu_2O at 146, 214, and 628 cm^{-1} are also observed in these samples [30]. Both, C_1 as well as C_{10} , show ZnO and Cu_2O Raman features at similar positions indicating good reproducibility, repeatability and stability for the CED grown samples [18, 30–32].

High resolution XPS spectrum of $\text{Zn}(2p)$ from the electrodeposited ZnO nanostructures is shown in fig. 8.5(b). Two symmetric features, $2p_{3/2}$ and $2p_{1/2}$, are ob-

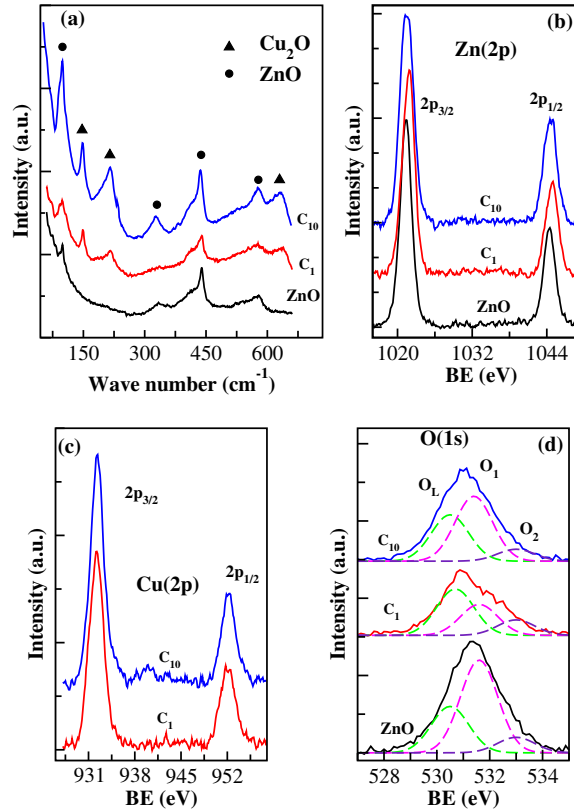


Figure 8.5: (a) Raman spectrum of ZnO nanostructures as well as of Cu₂O-ZnO nanostructures C₁ and C₁₀. (b) Zn(2p) core level XPS spectrum of ZnO nanostructures as well as of Cu₂O-ZnO nanostructures C₁ and C₁₀. (c) Cu(2p) core level XPS spectra from Cu₂O-ZnO nanostructures C₁ and C₁₀. (d) O(1s) XPS spectrum of ZnO nanostructures as well as of Cu₂O-ZnO nanostructures C₁ and C₁₀.

served at 1021.4 and 1044.4 eV, respectively. These features correspond to the Zn²⁺ sites [34]. Zn(2p) XPS from the CED grown C₁ and C₁₀ samples are also presented. High resolution XPS spectra of Cu(2p) from C₁ and C₁₀ samples are presented in fig. 8.5(c). The features at 932.2 and 952.1 eV, respectively, represent the Cu 2p_{3/2} and Cu 2p_{1/2} components of Cu₂O [35,36]. XPS results, thus, also show presence of Cu₂O and ZnO on CED grown surfaces. Based on the XPS integrated area and the Cu-2p/Zn-2p ratios, after appropriate normalization by the corresponding Atomic Sensitivity Factors (ASF), the atomic percentage of Cu in C₁ and C₁₀ samples was estimated to be ~1 at.% and 10 at.% respectively, as expected. Fig. 8.5(d) shows the oxygen (O1s) XPS spectra for the as-deposited ZnO as well as for the CED grown C₁ and C₁₀ samples. The O(1s) feature has been deconvoluted into three peaks [29,37].

The feature O_L at lowest binding energy (530.5 eV) may be ascribed to the lattice oxygen. The feature O_1 at 531.5 eV corresponds to the hydroxyl groups attached at the surface [29, 37]. The highest binding energy component O_2 at 533.1 eV can be assigned to the chemisorbed oxygen species on the surface.

8.3.2 Non-enzymatic Glucose sensing via cyclic voltammetry

(i) Cyclic Voltammetry and Amperometric response

The cyclic voltammetry (CV) profiles of the electrodeposited ZnO nanostructures as well as CED-grown Cu_2O -ZnO hybrid nanostructures, C_1 and C_{10} , have been investigated in the absence and presence of 1 mM glucose. No catalytic current was observed on the electrodeposited ZnO nanostructures without (fig. 8.6(a)) or with glucose (fig. 8.6(b)). Thus, ZnO-nanostructures alone do not show any response to glucose in the enzymeless detection process. For Cu_2O -ZnO hybrid C_1 sample, no reduction peak is noticed in the absence of glucose (fig. 8.6(a)). A reduction peak around 0.65 V vs. Ag/AgCl is observed for Cu_2O -ZnO hybrid C_{10} sample, in the absence of glucose (fig. 8.6(a)). This peak is associated with Cu(II)/Cu(III) redox couple [14].

No oxidation peak is observed in fig. 8.6(a) for C_1 and C_{10} samples in the absence of glucose. However, addition of 1 mM glucose induces large catalytic currents in both C_1 and C_{10} samples which respectively show peak currents of 0.43 and 1.31 mA/cm² (fig. 8.6(b)). This enhancement in the oxidation peak currents, observed respectively at 0.58 and 0.41 V for CED grown Cu_2O -ZnO C_1 and C_{10} samples, correspond to the irreversible glucose oxidation due to the conversion of Cu(II) to Cu(III) [38]. Several reaction steps are involved in the electrocatalytic oxidation of glucose at the hybrid Cu_2O -ZnO nanostructures in NaOH medium. The possible reaction steps are [20, 33, 39–41]:

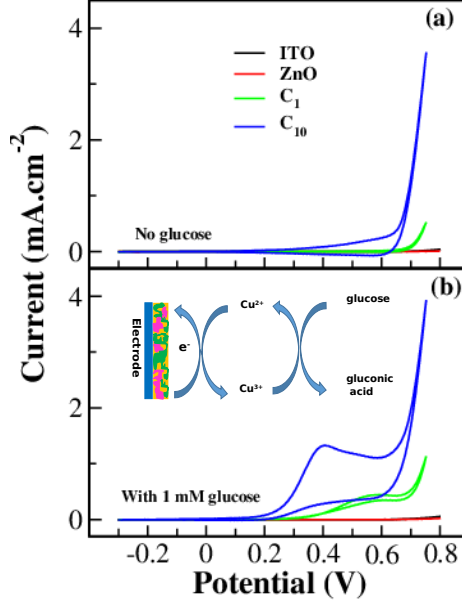
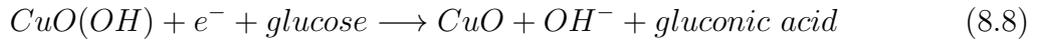
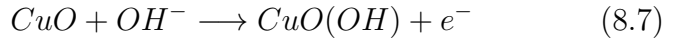
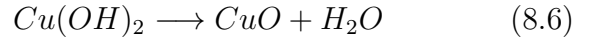
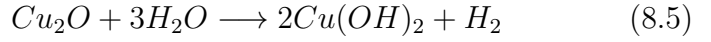


Figure 8.6: (a) Blank CV curves for ITO, ZnO nanostructures and for Cu₂O-ZnO nanostructures C₁ and C₁₀. (b) CV curves with 1 mM glucose for ITO, ZnO nanostructures and for Cu₂O-ZnO nanostructures C₁ and C₁₀. The scan rate is 10 mV/sec. Inset shows the schematic illustration of the Electron transfer process for enzymeless Glucose electro-oxidation on hybrid Cu₂O-ZnO nanostructure electrode.



In the beginning, Cu(I) gets electrochemically oxidized to Cu(II) with the formation of Cu(OH)₂. Then, formation of Cu(III) on the hybrid Cu₂O-ZnO surfaces with fast electron transfer rates takes place. Fig 8.6(b) (inset) schematically illustrates the electron transfer processes taking place on the a CED grown Cu₂O-ZnO surface during the non-enzymetic detection of Glucose. Conversion of glucose to gluconic acid leads to the increase in the oxidation peak current in CED grown Cu₂O-ZnO samples, C₁ and C₁₀ (seen in fig. 8.6(b)). The Cu(III) species are crucial for mediating fast

electron- transfer as well as are responsible for high catalytic activity.

Thus, C_1 and C_{10} samples with hybrid Cu_2O -ZnO nanostructures are able to produce high electrocatalytic activity promoting the oxidation of glucose. This efficiency can be ascribed to several factors e.g. the conjugated hybrid nature of the nanostructures, the kinetic effects due to increased electroactive nanostructured surface, and the fast electron transfer rate from the glucose to the hybrid nanostructures. Systematic increase in the peak current for C_{10} compared to C_1 indicates a controlled role of the hybrid nanostructures in the oxidation of glucose. Note that electrodeposited ZnO nanostructures alone do not show any response to non enzymatic glucose sensing (in fig. 8.6(b)).

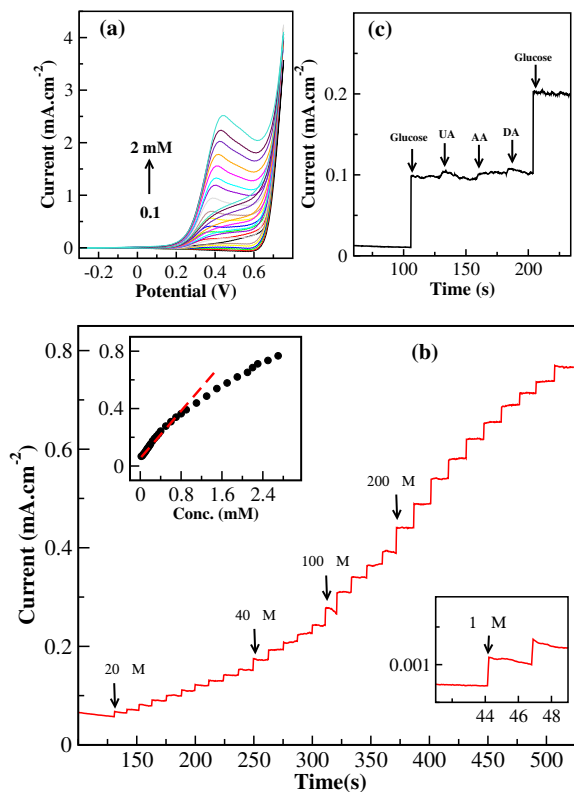


Figure 8.7: (a) CV curves of Cu_2O -ZnO sample C_{10} upon addition of different concentrations of Glucose (b) Amperometric response of Cu_2O -ZnO sample C_{10} upon successive addition of Glucose with marked concentrations to 0.1 M NaOH solution at an applied potential of 0.4 V. Inset (top) shows the corresponding calibration curve of the current vs. concentration of glucose. Inset (bottom) shows a partial magnification of the current response towards a low concentration of glucose solution. (c) Amperometric response of Cu_2O -ZnO sample C_{10} to 0.2 mM glucose and successive injection of interfering species (0.02 mM UA, 0.02 mM AA, and 0.02 mM DA) in 0.1 M NaOH with stirring.

With the systematic increase of glucose concentration, a gradual increase in the catalytic peak current intensity in the CED-grown Cu₂O-ZnO nanostructures is observed. This is shown for the C₁₀ sample at a scan rate of 10 mV/sec in fig. 8.7(a). C₁ samples also exhibit similar glucose sensing behaviour. These results show that Cu₂O-ZnO nanostructures support fast electron transport via hybrid nanostructures. CV measurements have also been performed on CED-grown Cu₂O-ZnO nanostructures at different scan rates. The peak currents display a linear behavior as a function of scan rates.

The CA (I-t) curve obtained after the addition of different concentrations of glucose on C₁₀ sample at +0.4 V (vs. Ag/AgCl) is shown in fig. 8.7(b). The results show a systematic and fast response to glucose by the CED grown Cu₂O-ZnO hybrid nanostructures. The calibration curve is shown in the inset (top) and displays a sensitivity of 441.2 $\mu\text{A mM}^{-1} \text{ cm}^{-2}$, correlation coefficient of 0.9998, linear range of 0.02 - 1 mM and low detection limit (LOD) of 0.13 μM under a signal/noise ratio of 3. Responding to 200 μM of glucose, the oxidation current achieved steady state within < 3 s indicating fast transfer rates for electrons in hybrid Cu₂O-ZnO nanostructures.

We have compared the performance of our Cu₂O-ZnO nanostructured electrode with other non-enzymatic nano-composite glucose sensors based on Cu₂O/graphene, Cu₂O/RGO, Cu₂O/metals and Cu₂O/CNT and Cu₂O only (table 8.1). All the electrodes mentioned in table 8.1, except ours and [20], have been fabricated by multi-step growth procedures. Ours, however is the only electrode that has been prepared by a simple single step CED technique. Moreover, our CED grown Cu₂O-ZnO electrode does not use Glassy Carbon electrode (GCE), rather it uses ITO. Also, here we do not use Nafion as a protective layer. All the electrodes of other studies in the table 8.1, except [20] have been prepared using GCE and all of them (except [20, 22, 49]) use Nafion layer.

Importantly, although refs. [50, 51] and [23, 46, 48] demonstrate higher sensitivity and lower LOD, respectively, than our Cu₂O-ZnO based electrode, still unlike our case all of them are fabricated on GCE and use Nafion layer. Comparing with Cu₂O/metal, Cu₂O/graphene and Cu₂O/RGO based electrodes, our electrode show many favorable analytical properties when considered that these have been prepared

Table 8.1: Comparison of the non-enzymetic glucose sensing properties of the hybrid Cu₂O-ZnO sample C₁₀ with some other glucose sensors based on Cu₂O.

Materials	Sensitivity	Linear Range (mM)(μ M)	LOD (μ M)	Ref.
Cu ₂ O/GO	0.285 mA mM ⁻¹ cm ⁻²	0.3-3.3	3.3	[44]
Cu ₂ O/CRG		0.1-1.1	1.2	[45]
Cu ₂ O/RGO	185 μ A mM ⁻¹	0.01-6.0	0.05	[46]
Cu ₂ O hollow nanocube	52.5 μ A mM ⁻¹	0.001-1.7	0.87	[47]
Cu-Cu ₂ O nanoporous NPs	123.8 μ A mM ⁻¹ cm ⁻²	0.01-5.5	0.05	[48]
Cu ₂ O nanocubes	121.7 μ A mM ⁻¹ cm ⁻²	0-0.5	38.0	[33]
Cu ₂ O-Cu	62.29 μ A mM ⁻¹ cm ⁻²	0.05-6.75	37	[20]
Cu@Cu ₂ O/RGO	145.2 μ A mM ⁻¹ cm ⁻²	0.005-7.0	0.5	[21]
Cu ₂ O/NiO _x /GO	285.0 μ A mM ⁻¹ cm ⁻²	0.002-0.87	0.4	[22]
Cu ₂ O-Au nanocomposites	185.0 μ A mM ⁻¹ cm ⁻²	0.002-0.1	0.5	[49]
Au@Cu ₂ O core-shell	715.0 μ A mM ⁻¹ cm ⁻²	0.05-2.0	18	[50]
Cu ₂ O/MWCNT	2143 μ A mM ⁻¹ cm ⁻²	0.0005-2.5	2	[51]
Cu ₂ O/MWCNTs nanocomposites		0.00005-0.01	0.05	[23]
Hybrid Cu ₂ O-ZnO (C ₁₀)	441.2 μ A mM ⁻¹ cm ⁻²	0.02 -1	0.13	This work

in a single step process and no protective Nafion layer is used. Moreover, flatter electrodes based on ITO can be easily integrated in circuits, compared to GCE. Glucose sensing with Cu₂O-ZnO nanostructures, as in present study, with no Nafion layer indicates that these electrodes are very robust. Moreover, the sensitivity, linear range, LOD and the fast response of the present Cu₂O-ZnO nanostructured electrodes is observed to be very good.

(ii) Interference, Reproducibility and stability of hybrid Cu₂O-ZnO electrode

Non-interference is an important property for any sensor. The electrochemical response of the interfering species, like Asorbic Acid(AA), Uric Acid (UA) and dopamine (DA), was investigated on the nano-hybrid Cu₂O-ZnO sample C₁₀ and the results are shown in fig. 8.7(c). Although the glucose concentration in human blood is about 30-50 times larger than these interfering species [42], still a very large concentration of the interfering species (glucose:interfering species being 10:1) was used to estimate the sensitivity. For these investigations 0.2 mM glucose injection was followed with successive injection of the 0.02 mM of the interfering species in 0.1 M

NaOH solution. As observed from fig. 8.7(c), the electrochemical current response from glucose is much more pronounced than the interfering species.

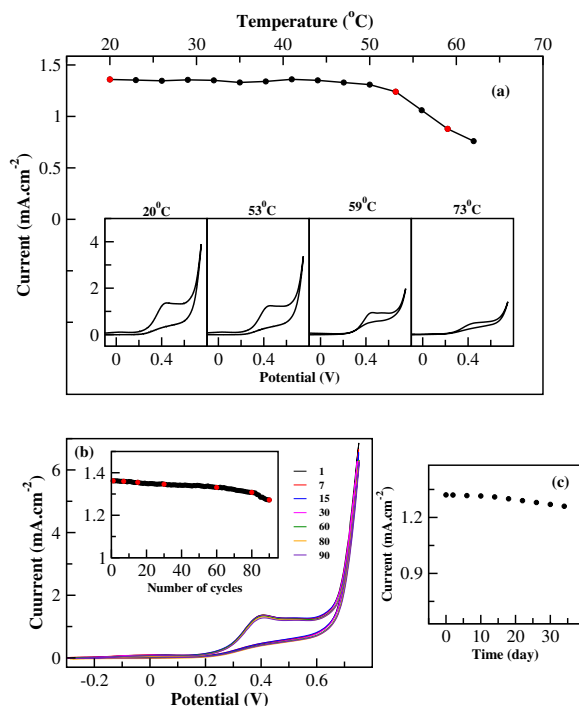


Figure 8.8: (a) The stability of the Cu₂O-ZnO sample C₁₀ in 0.1 M NaOH solution containing 1 mM glucose at different temperatures from 20° - 62° C. Inset shows CV of Cu₂O-ZnO C₁₀ sample at different temperatures. (b) CV of the Cu₂O-ZnO C₁₀ sample in 0.1 M NaOH solution at a scan rate 10 mV/s containing 1 mM Glucose at different cycles. Inset shows the variation of the maximum response current density for the Cu₂O-ZnO C₁₀ sample in 0.1 M NaOH containing 1 mM glucose up to 90 cycles. (c) Stability of the Cu₂O-ZnO C₁₀ sample over 34 day period using 0.1 M NaOH with 1 mM glucose at +0.4 V.

The temperature of the solution is an important factor that affects the electrocatalytic oxidation of glucose [43, 52]. The effect of temperature on the electrochemical response of glucose for the conjugated Cu₂O-ZnO C₁₀ electrode has been investigated. Fig. 8.8(a) shows the maximum oxidation current density response of the conjugated Cu₂O-ZnO electrode in 0.1 M NaOH solution at various temperatures. The current density is nearly constant up to 50° C indicative of good thermal stability of the electrodes towards temperature. Inset shows the modification of CV profile as a function of temperature. Long-term stability and reproducibility of sensors are also of critical importance for practical applications [52, 53]. The stability of hybrid Cu₂O-ZnO

nanostructured glucose sensors was evaluated by periodical measurements for a number of cycles using 0.1 M NaOH with 1 mM glucose at +0.4 V. As shown in fig 8.8(b) the maximum oxidation current density is stable up to 80 cycle, maintaining a response of 4.4%. This again suggests a good electrode stability. The stability of the maximum current density is about 4.8% of its initial response after 34 days (see Fig. 8.8(c)). Several electrodes were prepared under same conditions and their current response to 1.0 mM glucose provides a relative standard deviation of 3.1%. The reason for good temperature and long-term stability can be attributed to the nano-hybrid structure of Cu₂O-ZnO electrode indicating that these nanostructures remain stable during the electrochemical oxidation of glucose.

These electrodes have some distinct advantages. First they have been produced by a simple single step co-electrodeposition route on a planar ITO. Hybrid conjugated nanostructures provide numerous transport channels, thus enhancing the direct electron transfer between the active sites and the electrode. These reasons contribute to the high sensitivity, high affinity, good reproducibility and high stability of the conjugated hybrid Cu₂O-ZnO nanostructured biosensors fabricated here. Being deposited by electrochemical method, it is possible to achieve this hybrid nanostructured geometry on any planar substrate. Moreover, with planar geometry these can be more easily incorporated in circuits and chips. Thus, the as prepared hybrid conjugated Cu₂O-ZnO nanostructures provide an excellent template for enzymeless glucose detection.

8.3.3 Photo-absorption response and band gap modification of Cu₂O-ZnO hybrid nanostructures

Fig. 8.9 shows a UV-Vis absorbance spectrum from electrodeposited ZnO nanostructures. An absorption edge is observed at 372 nm which corresponds to the direct band-gap of ZnO at 3.32 eV (see Tauc plot in inset). No significant absorbance is observed in the visible range. This is as expected due to the large bandgap of ZnO [34]. UV-Vis spectra from C₁ and C₁₀ samples indicate band gap tailoring as well as higher photo-absorption response in the UV and visible (400-800 nm) regions. The band gap for C₁ is at 3.21 eV. For C₁₀ sample, a much reduced band-gap of 2.75 eV is

observed (inset fig. 8.9). This represents a band-gap of a composite structure like $\text{Cu}_2\text{O-ZnO}$. Band gaps in the range of 2 to 2.5 eV have been reported for N doped Cu_2O [54]. Band gap of 2.75 eV is in visible range and consequently C_{10} displays a pronounced absorbance in the visible regions. Interestingly, the absorbance in the visible range and in the UV region has got enhanced. The band gap tailoring as well as the enhanced UV and visible region photo-absorption from CED-grown C_{10} samples, here, indicate an effective and synergistic photo-response of the $\text{Cu}_2\text{O-ZnO}$ hybrid nanostructures.

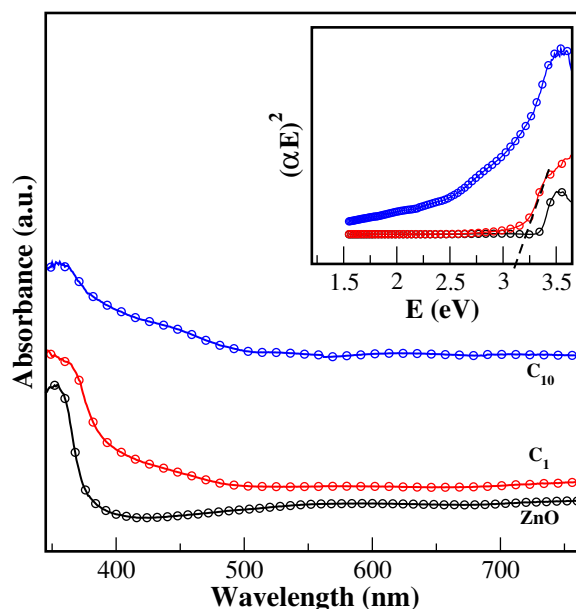


Figure 8.9: Photo response UV-Vis spectra of ZnO nanostructures and from C_1 and C_{10} . Inset shows the Tauc plots and the associated bandgaps (α is absorption coefficient and E is photon energy).

In conjugated hybrid nanostructures like $\text{Cu}_2\text{O-ZnO}$, some p/n hetero-junctions between narrow band gap p-type Cu_2O semiconductor and wide band gap n-type ZnO semiconductor may be getting created. Upon photo-absorption, excitons of e-h pairs get formed. Since the conduction band of ZnO is lower than that of Cu_2O [30], the excited electrons can transfer from Cu_2O to ZnO with the holes transferring in the opposite direction. With 3-dimensional nanostructured surface morphology, electron-hole charge separation may increase causing a reduction in the recombination rate promoting the photo-absorbance response

8.4 Conclusion

The present study investigates the hybrid nanostructures of Cu₂O-ZnO that have been fabricated via CED technique. Here, the conjugated nanostructures were produced in a single step process making the technique very repeatable and reproducible. Two concentrations of Cu²⁺ have been used here, leading to the fabrication of C₁ and C₁₀ nanostructures of conjugated Cu₂O-ZnO. In both the cases surfaces display excellent response for non-enzymatic glucose sensing via cyclic voltammetry. The Cu₂O-ZnO sample C₁₀ shows a sensitivity of 441.2 $\mu\text{A mM}^{-1} \text{cm}^{-2}$, linear range of 0.02 - 1 mM, LOD of 0.13 μM and a fast electron transfer rates of < 3 s for glucose detection. Investigations have also been done on pure-ZnO nanostructures, grown by electrodeposition technique. These ZnO nanostructures, however, do not show any non-enzymatic glucose sensing nature. Good non-enzymatic glucose sensing nature of Cu₂O-ZnO electrode occurs through a combined synergetic response of hybrid conjugated nanostructures. Together they all facilitate large number of active sites as well as free channels for fast glucose detection. The Cu₂O-ZnO electrodes exhibit good temperature and long-term stability indicating them to be promising non-enzymatic glucose sensors. CED grown conjugated hybrid nanostructures of Cu₂O-ZnO also display an enhanced UV-Vis photo absorption response as well as band gap tailoring inducing higher photo-absorbance response in the UV-Vis region.

Bibliography

- [1] D.Y. Zhai, B. Liu, Y. Shi, L. Pan, Y. Wang, W. Li, R. Zhang and G. Yu, ACS Nano, **4**, 3540 (2013)
- [2] A. Kros, S.W.F.M. van Hovell, N.A.J.M. Sommerdijk, and R.J.M. Nolte, Adv. Mater., **13**, 1555 (2001)
- [3] X.H. Niu, Y. Li, J. Tang, Y.Hu, H. Zhao, M. Lan, Biosens. Bioelectron., **51**, 22 (2014)
- [4] S. H. Lim, J. Wei, J. Lin, Q. Li, J. KuaYou, Biosens. Bioelectron., **20**, 2341 (2005)
- [5] A. Rodrigues, M.V. Castegnaro, J. Arguello, M.C.M. Alves, J. Morais, Appl. Surf. Sci. **402**, 136 (2017)
- [6] A.L. Sun, J.B. Zheng, and Q.L. Sheng, Electrochim. Acta, **65**, 64 (2012)
- [7] T.Dayakar, K. Venkateswara Rao, M. Vinodkumar, K. Bikshalu, B. Chakradhar, K. Ramachandra Rao, Appl. Surf. Sci., **435**, 216 (2018).
- [8] Y.Lee, D. Park, J.Park, and Y. Kim, Sensors **8**, 6154 (2008)
- [9] J. Wang, D. F. Thomas, and A. Chen, Anal. Chem. **80**, 997 (2008)
- [10] S. Liu, B. Yu, T. Zhang, Electrochim. Acta, **102**, 104 (2013)
- [11] K. Tian, M.Prestgard, A.Tiwari, Mater. Sci. Eng. C, **41**, 100 (2014)
- [12] Wei Huang, Yang Cao, Yong Chen, Juan Pengb, Xiaoyong Lai, Jinchun Tu, Appl. Surf. Sci., **396**, 804 (2017).

- [13] Magdalena Jarosz, Robert P. Socha, Pawe J zwick, Grzegorz D. Sulka, *Appl. Surf. Sci.*, **408**, 96 (2017).
- [14] C. Zhou, L. Xu, J. Song, R. Xing, S. Xu, D. Liu & H. Song, *Sci. Rep.*, **4**, 7382 (2014)
- [15] S.A. Kumar, H. Cheng, S. Chen, S. Wang, *Mater. Sci. Eng. C*, **30**, 86 (2010)
- [16] J. Zhang, X. Xiao, Q. He, L. Huang, S. Li, and F. Wang, *Anal. Lett.*, **47**, 1147 (2014)
- [17] J.Wu and F. Yin, *Integr. Ferroelectr.*, **147**, 47 (2013)
- [18] L. Chow, O. Lupan , G. Chai , H. Khallaf , L.K. Ono , B. Roldan Cuenya , I.M. Tiginyanu , V.V. Ursaki, V. Sontea, A. Schulte, *Sensors and Actuators A*, **189**, 399 (2013)
- [19] M. Li, G. Meng, Q. Huang, and S. Zhang, *Sci. Rep.*,**4**, 4284 (2014)
- [20] L. Wang, J. Fu. H. Hou, Y. Song, *Int.J. Electrochem. Sci.*, **7**, 12587 (2012)
- [21] H. Huo, C. Guo, G.Li, X. Han and C. Xu, *RSC Adv.*, **4**, 20459 (2014)
- [22] B. Yuan, C. Xu, L. Liu, Q. Zhang, S. Ji, L. Pi, D. Zhang, Q. Huo, *Electrochim. Acta*, **104**, 78 (2013)
- [23] Xiaojun Zhang, Guangfeng Wang, Wei Zhang, Yan Wei, Bin Fang, *Biosens. Bioelectron.*,**24**, 3395 (2009)
- [24] O. Lupan, T. Pauporté, B. Viana, P. Aschehoug, *Electrochim. Acta*, **56**, 10543 (2011)
- [25] Z. Gao, J. Liu, F. Xu, D. Wu, Z. Wu, and K. Jiang, *Solid State Sci.*, **14**, 276 (2012)
- [26] Yasemin Caglar , Anda Arslan , Saliha Ilican , Evrim Hr , Seval Aksoy , Mujdat Caglar, *J. Alloys and Compd.*, 574, 104 (2013)

- [27] G. Yao, M. Zhang, J. Lv, Kai Xu, S. Shi, Z. Gong, J. Tao, X. Jiang, L. Yang, Y. Cheng, G. He, X. Chen, and Z. Sun, *J. Electrochem. Soc.*, **162**, D300 (2015)
- [28] S N Sarangi, *J. Phys. D: Appl. Phys.*, **49**, 355103 (2016)
- [29] Chao Wang, Huiqing Fan, Xiaohu Ren, and Jiawen Fang, *Appl. Phys. A Mat. Sci & proces.*, **124**, 99 (2018).
- [30] Y. Liu, F. Ren, S. Shen, Y. Fu, C. Chen, C. Liu, Z. Xing, D. Liu, X. Xiao, W. Wu, X. Zheng, Y. Liu, and C. Jiang, *Appl. Phys. Lett.*, **106**, 123901 (2015)
- [31] P. Soundarrajan , K. Sankarasubramanian , M. Sampath , T. Logu , K. Sethuraman, K. Ramamurthi, *Physica E*, **71**, 56 (2015)
- [32] P. K. Sharma , Ranu K. Dutta, Avinash C. Pandey, *J. Magn. Magn. Mater.*, **321**, 4001 (2009)
- [33] S. Felix, P. Kollu, B.P.C. Raghupathy, S.K. Jeong, A.N. grace, *J. Chem. Sci.*, **126**, 25 (2014)
- [34] Vanaraj Solanki, Shalik R. Joshi, Indrani Mishra, D. Kabiraj, N. C. Mishra, D. K. Avasthi, and Shikha Varma, *J. Appl. Phys.*, **120**, 054303 (2016)
- [35] T. Robert, M. Bartel, and G. Offergeld, *Surf. Sci.*, **33**, 123 (1972)
- [36] J. Ghijsen, L. H. Tjeng, J. van Elp, H. Eskes, J. Westerink, G. A. Sawatzky, and M. T. Czyzyk, *Electronic structure of Cu₂O and CuO*, *Phys. Rev. B.*, **38**, 11322 (1988)
- [37] Anita Hastir, Nipin Kohli, Ravi Chand Singh, *Journal of Physics and Chemistry of Solids*, **105**, 23 (2017).
- [38] H.X. Wu, W.M. Cao, Y. Li, G. Liu, Y. Wen, H.F. yang, S.P. Yang, *Electrochim. Acta*, **55**, 3734 (2010)
- [39] A.J. Wang, J.J. Feng, Z.H. Li, Q.C. Liao, Z.Z. Wang and J.R. Chen, *Cryst. Eng. Comm.* **14**, 1289 (2012)

- [40] L. Zhang, Y.Ni and H. Li, *Microchim. Acta.*, **171**, 103 (2010)
- [41] R. Khan, R. Ahmad, P. Rai, L.W. Jang, J.H. Yun, Y.T. Yu, Y.B. Hahn, I.H. Lee, *Sensors and Actuators B*, **203**, 471 (2014)
- [42] Yan Zhong, Tielin Shi, Zhiyong Liu, Siyi Cheng, Yuanyuan Huang, Xiangxu Tao, Guanglan Liao, Zirong Tang, *Sensors and Actuators B*, **236**, 326 (2016)
- [43] Yuwei Zhao, Huiqing Fan , Ke Fu, Longtao Ma, Mengmeng Li, Jiawen Fang, *Int. J. Hydrogen Energy*, **41**, 16913 (2016)
- [44] Minmin Liu, Ru Liu, Wei Chen, Graphene wrapped Cu₂O nanocubes: *Biosens. Bioelectron.*, **45**, 206 (2013)
- [45] Y. Qian, F. Ye, J. Xu and Z.G. Le, *Int. J. Electrochem. Sci.*, **7**, 10063 (2012)
- [46] D. L. Zhou, J. J. Feng, L. Y. Cai, Q. X. Fang, J. R. Chen and A. J. Wang, *Electrochim. Acta*, **115**, 103 (2014)
- [47] Z. Gao, J. Liu, J. Chang, D. Wu, J. He, K. Wang, F. Xu and K. Jiang, *Cryst. Eng. Comm*, **14**, 6639 (2012)
- [48] Y. Zhao, Y. Li, Z. He and Z. Yan, *RSC Adv.*, **3**, 2178 (2013)
- [49] Qiyan Hu, Fenyun Wang, Zhen Fang, Xiaowang Liu, *Colloids Surf. B Biointerfaces*, **95**, 279 (2012)
- [50] Ya Su, Hua Guo, Zuoshang Wang, Yumei Long, Weifeng Li, Yifeng Tu, *Sensors and Actuators B*, **255**, 2510 (2018)
- [51] Xuemei Zhou, Huagui Nie, Zhen Yao, Youqing Dong, Zhi Yang, Shaoming Huang, *Sensors and Actuators B*, **168**, 1 (2012)
- [52] Hailin Tian, Huiqing Fan, Jiangwei Ma, Longtao Ma, Guangzhi Dong, *Electrochim. Acta*, **247**, 787 (2017)
- [53] Hailin Tian, Huiqing Fan, Mengmeng Li, Longtao Ma, *Acs. Sens.*, **1**, 243 (2016)
- [54] Y. Nakano, S. Saeki, and T. Morikawa, *Appl. Phys. Lett*, **94**, 022111 (2009)

Chapter 9

$\text{Cu}_x\text{O-ZnO}$ ($x=1,2$) and CuO-TiO_2 nanostructures: Photo-absorption behavior and Non-Enzymatic Glucose Sensing via Cyclic Voltametry

9.1 Introduction

Quest for an efficacious glucose sensor, with high sensitivity, has received extraordinary attention due to its enormous beneficial role in human health, and is instrumental for exceptional research in clinical diagnosis, biotechnology, food industry etc. [1–3]. These sensors are primarily based on frameworks that operate via enzymatic or non-enzymatic detection. The traditional enzyme based glucose sensors are widely applied as they present good sensitivity and selectivity [4, 5]. These, however, face several challenges and drawbacks due to the enzyme based reactions. The thermal and chemical instability of the enzymes degrades the sensors and often minor variations in the environmental conditions, like humidity, pH, temperature, presence of ionic detergents, interference species etc. can severely influence their performance [6]. Such complexities have contributed to focused research towards the non-enzyme based glucose detection. In this direction, several metals (Ag, Au, Pt, Pd, Ni, Cu), metal oxides, alloys etc. have been investigated recently [7–13]. The performance of sensors crucially depend on their morphology and the associated electron transport channels.

Nanostructured composite systems present an exceptional platform that can simultaneously enhance the reaction zone as well as improve the electron transfer rates. Such properties are also desirable in many advanced technologies including energy devices, optoelectronic devices and environmental remediation [14, 15].

Nanostructured ZnO and TiO₂ demonstrate many promising applications for solar cell, photocatalysis, bio-sensing, gas sensing etc. [16–24]. Being biocompatible and non-toxic, these are important candidates for medical and biotechnology related applications also [25–29]. As a semiconductor, nanodimensional copper oxide (Cu₂O and CuO) displays several fascinating properties for photocatalysis, biosensors, solar cells, photo-electrochemical water splitting, gas sensors and field transistors [30–34]. Attributed by many exceptional characteristics like, non-toxic nature, low cost, outstanding redox behavior, environmental stability and low over-potential for electron-transfer reactions [35–37], these oxides are considered significant candidates for glucose detection. However, their poor conductivity poses a challenge. Consequently, their integration with graphene [38], NiO/graphene oxide [39] and graphene/carbon nanofiber [40] etc. have been explored for improving electron transfer characteristics. Conjugation of copper oxides with metal oxides like ZnO presents a unique framework where coupled system may display synergistic effect to enhance transport behavior and stability. Such nano-composite templates will be expected to induce enhanced reaction zones, assisted by larger surface area, improved diffusion and mass transport leading to better detection performance. A few studies have discussed the glucose sensing phenomenon after the growth of CuO on ZnO nanostructures [41, 42].

The present chapter explores the co-electrodeposition (CED) route to form Cu_xO-ZnO (x=1,2) nanostructured composites and discusses their glucose sensing via cyclic voltammetry. Photo-absorption behavior of these nanostructures have also been explored. In chapter 8, two low concentrations of Cu²⁺, 1% (sample C₁) and 10% (sample C₁₀), were introduced for preparing nanostructures. XRD, XPS and TEM results delineated the presence of Cu₂O-ZnO hybrid nanostructures and Cyclic Voltammetry results demonstrate enhanced non-enzymatic glucose detection. C₁₀ expresses a higher sensitivity, than C₁, towards glucose detection. Here, many other promising characteristics like good stability, low detection limit, long linearity range etc.

were also noticed. Though both, C₁ and C₁₀, exhibit band gap tailoring effects, C₁₀ demonstrates higher UV-Vis photo response. These results have been discussed in chapter 8. In order to further explore the effect of varying Cu²⁺ concentration on the glucose sensing and photoabsorption behavior, in the present chapter nanostructures have been prepared with a high (50%) Cu content (sample C₅₀) using CED. Techniques of XPS, Raman and XRD indicate that the nanostructures are of mixed Cu_xO-ZnO form (x=1,2). CED grown samples with 2% Cu content (sample C₂), however, demonstrate only Cu₂O-ZnO type nanostructures. Investigations on these C₂ composites have also been presented here for comparison. Although Cu_xO-ZnO with 50% Cu content demonstrates better non-enzymatic glucose sensing behavior compared to C₂, the best results are shown by C₁₀ discussed in the previous chapter. Photo- absorption behavior of these nano-composite materials, in UV-Vis regime, has also been discussed here. The response in the visible region shows enhancement with increasing Cu content. Band gap tailoring appears to be responsible for these effects.

In this chapter, glucose sensing behavior of CuO-TiO₂ nanostructures (sample T₁₀) prepared with 10% Cu²⁺ was also investigated by cyclic voltammetry. Grown by chemical method, nanostructures show presence of CuO-TiO₂ via XRD and Raman techniques. The sensitivity (of T₁₀) is, however, low compared to ZnO based hybrid nanostructures. Photoabsorption properties of T₁₀ are also presented.

9.2 Experimental

9.2.1 Chemical and Reagents

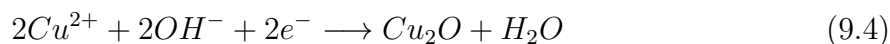
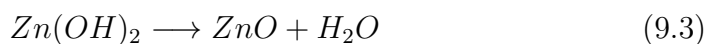
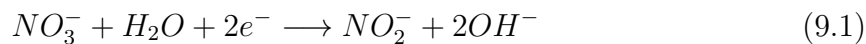
Zinc nitrate (Zn(NO₃)₂.6H₂O), hexamethylenetetramine ((CH₂)₆N₄), Titanium tetraisopropoxide (TTIP), Cu(NO₃)₂, CuCl₂.2H₂O, Glucose, NaOH, KOH, Asorbic Acid (AA), Uric acid (UA) and Dopamine acid (DA) were purchased from Sigma Aldrich. All the chemicals were of analytical grade and used as-received without further purification. Indium tin oxide-coated glass electrode (ITO) was purchased from MTI corporation. Ultra-pure deionized water (18.25 mΩ cm) was used for all the experiments.

9.2.2 Preparation of ZnO and Cu_xO-ZnO nanostructures using Electrodeposition Method

Nanostructures of ZnO were electrodeposited in an electrochemical workstation using standard three-electrode system with ITO as the working electrode (cathode), Pt sheet as the counter electrode (anode) and Ag/AgCl as the reference electrode. Before the experiment, ITO glasses were cleaned successively in acetone (5 min) and ethanol (5 min) in an ultrasonic bath. They were then rinsed several times using deionized water and dried in air. The electrochemical cell was prepared with an aqueous solution of 10 mM zinc nitrate and hexamethylenetetramine (HMT). HMT plays a vital role as surfactant which controls the preferential growth of ZnO nanostructures [43]. The electrodeposition was performed at a fixed cathodic voltage of -0.8 V and at a constant temperature of 70°C.

The technique of co-electrodeposition (CED), as discussed in chapter 8, was utilized here also to grow Cu_xO-ZnO (x=1,2) nanostructures. Samples were synthesized using two concentrations of CuCl₂.2H₂O (0.2 mM and 5 mM) as Cu²⁺ precursor in the solution. An aqueous solution, containing zinc nitrate, HMT and CuCl₂.2H₂O was used as the electrolyte. The concentrations of zinc nitrate and HMT were kept fixed (10 mM) during electrodeposition. The samples prepared with 0.2 mM of Cu²⁺ and 10 mM of Zn²⁺ have been labeled here as C₂, whereas the samples prepared with 5 mM of Cu²⁺ and 10 mM of Zn²⁺ have been referred to as C₅₀. All the other parameters associated with the electrodeposition have been kept same as discussed in chapter 8. After depositing for 10 minutes, samples were rinsed with distilled water and dried in air.

The possible mechanism for the formation of ZnO and Cu_xO-ZnO nanostructures can be illustrated as follows [43–46]:



9.2.3 Glucose Sensing via Cyclic Voltammetry Experiments using ZnO and Cu_xO-ZnO electrodes

All the glucose sensing experiments were carried out in a conventional three electrode system within 20 ml of 0.1 M NaOH electrolyte solution. Cyclic voltammetry (CV) measurements of the electrodeposited ZnO and Cu_xO-ZnO nanostructured samples were investigated in the presence and absence of glucose. The potential was varied from -0.3 to 0.8 V vs. Ag/AgCl at the scan rate of 10 mV/s. The chronoamperometric (CA) studies were performed by successive addition of known amount of glucose into a 20 ml of 0.1 M NaOH solution.

9.2.4 Preparation of TiO₂ and CuO-TiO₂ nanostructures

TiO₂ and CuO-TiO₂ nanostructures have been synthesized via chemical route. TiO₂ precursor solution was prepared by mixing 5 ml of 0.4 M Titanium tetraisopropoxide (TTIP) and 20 ml of ethanol. A 50 mM KOH solution was then added, drop by drop, until the solution precipitated. Finally, the precipitate was extracted by filtering the solution. This precipitate was rinsed several times with distilled water and was dried overnight at 80°C.

For the preparation of CuO-TiO₂ nanostructures, first a Cu²⁺ precursor solution was prepared with 25 ml of 8 mM Cu(NO₃)₂. It was added into the TTIP solution and stirred for 30 minutes at room temperature. The concentration of Cu²⁺ in the final solution is 10% of TTIP. The remaining procedure is similar to that used for the preparation of TiO₂ nanostructure, i.e. 50 mM KOH was slowly added and the precipitate was extracted which was then rinsed and dried at 80°C. These samples

have been labeled as T₁₀.

9.2.5 Glucose Sensing via Cyclic Voltammetry Experiments using TiO₂ and CuO-TiO₂ modified GCE electrodes

All the glucose sensing experiments have been carried out in a three electrode system with a Ag/AgCl reference electrode, a Pt sheet as counter electrode and CuO-TiO₂ or TiO₂ modified glassy carbon electrode (GCE) as a working electrode. To prepare the working electrode, GCE was first polished with 0.3 and 0.05 μm alumina slurry, followed by rinsing with deionized Millipore water. It was then sonicated successively with 1:1 nitric acid, acetone, deionized water and dried at room temperature. The as-prepared TiO₂ powder was suspended in ethanol at a concentration of 5 mg/mL and stored for multiple use. TiO₂ modified GCE (T/GCE) was prepared by dropping an appropriate volume of this suspension on to GCE and then dried at room temperature. CuO-TiO₂ modified GCE (CT/GCE) were prepared in the similar fashion. Cyclic voltammetry (CV) measurements were carried out in 20 ml of 0.1 M NaOH electrolyte under ambient conditions, in the presence or absence of glucose. The potential was varied from 0 to 0.8 V at the scan rate of 30 mV/s.

9.2.6 Characterization techniques

The structural and phase identification of the Cu_xO-ZnO and CuO-TiO₂ nanostructures were investigated by high resolution X-ray diffraction (Bruker, D8-Discover) technique using Cu-K α radiation (0.154 nm). Micro-Raman measurements were carried out in the back scattering geometry with a 488 nm Ar⁺ laser on a T64000 triple monochromator (Horiba Jobin Yvon). All the electrochemical experiments were conducted on AutoLab PGSTAT 302N electrochemical work station. The measurements have been repeated several times to check for the reproducibility. Cary 5000 spectrometer system, equipped with an integrating sphere assembly, was used for acquiring UV-visible diffuse reflectance spectra. The FEI-ESEM (Environmental Scanning Electron Microscope) Quanta 200 system was used to investigate the morphology of the CuO-TiO₂ nanostructures. Surface morphology of Cu_xO-ZnO nanostructures has been studied by Atomic Force Microscopy (AFM) using Multimode V (Bruker Instru-

ments) in tapping mode. PHI 5000 Versa Probe II (ULVAC-PHI) system, with Al-K α source (1486.6 eV), has been utilized for X-ray photoelectron spectroscopy (XPS) studies. Field-emission scanning electron microscope (FESEM) from Carl Zeiss, Germany, (using 20 keV electrons) was utilized for the morphological and compositional studies. The system is equipped with Energy-dispersive X-ray spectroscopy (EDX) detector.

9.3 Result and discussion

9.3.1 Investigations on ZnO & Cu_xO-ZnO nanostructures

(i) Structure and Morphology of ZnO and Cu_xO-ZnO nanostructures

Fig. 9.1(a) shows micro-Raman spectra of ZnO and the electrodeposited Cu_xO-ZnO recorded at room temperature in the wave number range of 70-660 cm^{-1} . Raman spectra of electrodeposited ZnO nanostructures exhibit features at 99, 334, 439 and 579 cm^{-1} , which respectively correspond to E₂(low), E₂(high)-E₂(low), E₂(high) and E₁(LO) modes of wurtzite ZnO [28]. Raman spectra of C₂ and C₅₀ nanocomposites are also presented here. In addition to ZnO related features, prominent features are seen at 146, 214 and 638 cm^{-1} for C₂ which indicate the formation of Cu₂O phase [47]. Consequently, C₂ sample appears to consist of ZnO-Cu₂O. For C₅₀ samples, both ZnO and Cu₂O related Raman features appear to have become weaker. On the other hand, new modes at 300 and 621 cm^{-1} reflect the development of CuO [48]. Thus, C₅₀ appears to contain both, CuO as well as Cu₂O, in conjunction with ZnO. This suggests that C₅₀ has a mixed Cu_xO-ZnO (x=1,2) type framework. Additionally, the reduced Raman intensity of E₂(high) mode of ZnO also suggests some degradation in wurtzite lattice [49, 50]. Consequently, C₂ and C₅₀ display a slightly different character, with former being predominantly of Cu₂O-ZnO type whereas later having a Cu_xO-ZnO (x=1,2) nature. In chapter 8, C₁ and C₁₀ samples, respectively with 1% and 10% of Cu precursor, also exhibited a Cu₂O-ZnO formation. These results reflect a scenario where CED of Cu²⁺ with ZnO contributes to Cu₂O-ZnO at lower concentrations but Cu_xO-ZnO at a high (50%) concentration.

XPS investigations have been undertaken to understand the surface chemical com-

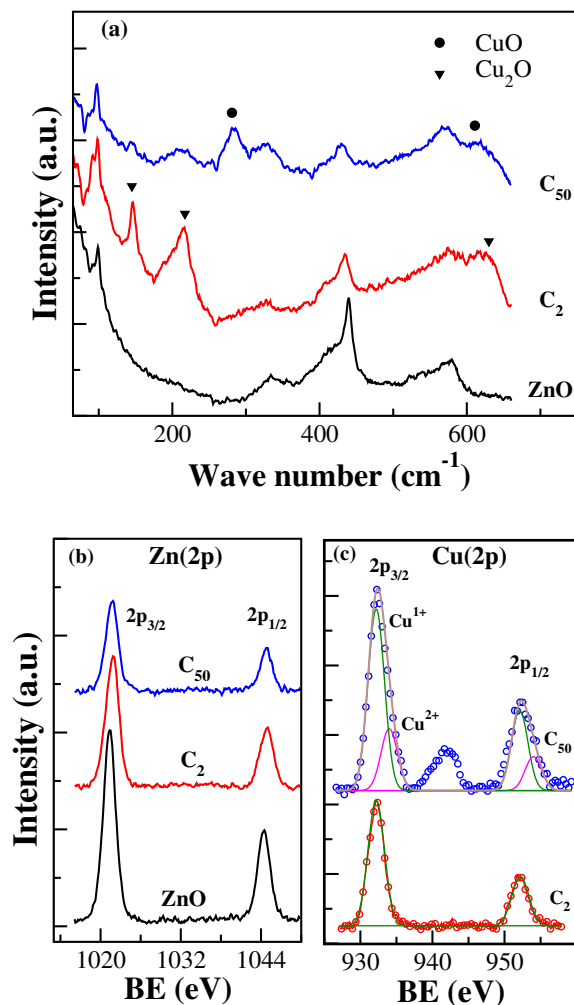


Figure 9.1: (a) Raman spectra of CED grown ZnO, C₂ and C₅₀. (b) XPS of Zn(2p) and (c) XPS of Cu(2p)

position of the electrodeposited samples. Fig. 9.1(b) displays XPS of Zn(2p) for the as-deposited ZnO, C₂ and C₅₀ samples. For ZnO, two main features at 1021.4 and 1044.4 eV correspond to Zn 2p_{3/2} and Zn 2p_{1/2}, respectively [16]. The intensity of these features get somewhat reduced for C₂ and C₅₀. This may be related to the the formation of the composite structures. XPS spectrum of Cu(2p) for the CED grown C₂ (Fig. 9.19(c)) displays two symmetric peaks related to Cu 2p_{3/2} and Cu 2p_{1/2} at 932.2 and 952.1 eV, respectively, indicating the presence of Cu₂O state [51, 52]. XPS from C₅₀, on the other hand, shows a distinct shake- up satellite feature at 942 eV indicating the existence of CuO phase [54, 55]. Higher Cu(2p) signal here corresponds to the increased Cu content. The deconvolution of Cu 2p_{3/2} demon-

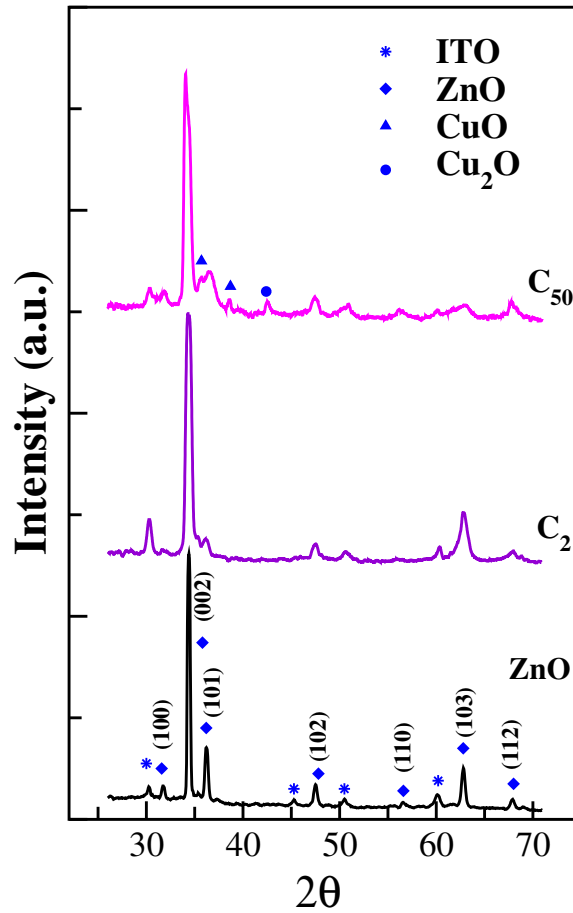


Figure 9.2: XRD of ZnO, C₂ and C₅₀.

strates two features at 932.2 and 934.1 eV which can be assigned to Cu⁺ and Cu²⁺ states, respectively [53,54]. These results concur with Raman spectroscopy measurements presented here that show formation of Cu₂O-ZnO for C₂, but mixed Cu_xO-ZnO (x=1,2) for C₅₀.

Fig. 9.2 shows XRD for the electrodeposited ZnO, C₂ and C₅₀ samples. ZnO sample displays features at 31.82^o, 34.32^o, 36.45^o, 47.61^o, 56.59^o, 62.86^o and 67.99^o due to (100), (002), (101), (102), (110), (103) and (112) lattice planes, respectively, suggesting the sample to be of polycrystalline nature [43]. The preferential growth along (002) direction expresses a predominance of wurzite ZnO structure. XRD of both, C₂ and C₅₀, show ZnO related lattice planes. However due to the small Cu content, C₂ does not exhibit any Cu₂O related features as expressed by Raman and XPS. C₅₀, on the other hand, displays presence of both CuO and Cu₂O phases. The

features at 35.57° and 38.64° respectively indicate $(\bar{1}11)$ and (111) planes of CuO whereas the peak at 42.42° is related to $\text{Cu}_2\text{O}(200)$ planes [56]. These results are in agreement to XPS and Raman measurements.

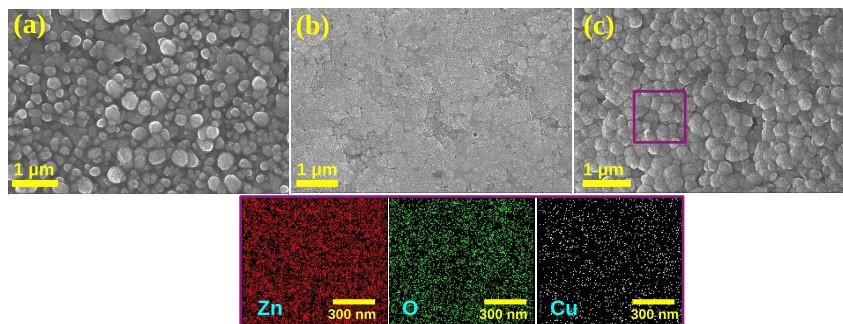


Figure 9.3: FESEM image of (a) electrodeposited ZnO, (b) C_2 and (c) C_{50} . EDX (in bottom) is shown for C_{50} with elemental mapping images of Zn, O, and Cu taken from the box of (c).

The surface morphology of the as-deposited ZnO, C_2 and C_{50} has been investigated by FESEM (Fig. 9.3). ZnO surfaces show bigger and distinctly distinguishable nanostructures with an average diameter of ~ 350 nm (Fig. 9.3(a)). Several prominent changes occur after the incorporation of Cu precursor as shown for C_2 and C_{50} . Although C_2 presents a smoother profile, formation of well formed nanostructures, with an average diameter of ~ 200 nm can be seen on C_{50} . Energy dispersive X-ray (EDX) technique has been utilized here to investigate the compositional distribution. EDX mapping of C_{50} shows the presence of copper (Cu), zinc (Zn) and oxygen (O) elements and their nearly homogeneous distribution on the surface.

AFM has also been utilized to study the surface topography. 2D and 3D images from the as-deposited ZnO, C_2 and C_{50} are shown in Fig. 9.4. As suggested by FESEM, as-grown ZnO displays well formed larger nanostructures with an average diameter of ~ 400 nm, whereas on C_{50} , the nanostructures are smaller with an average diameter of ~ 180 nm. The surface roughness of the as-deposited ZnO and C_{50} has been measure to be 70 and 45 nm, respectively. Both these surfaces display nearly hemispherically shaped nanostructures. On the other hand, C_2 , presents a disordered rougher surface. Though the overall surface roughness is 37 nm, no distinct nanostructures can be observed. The Cu incorporated surfaces are seen to be smoother than as-deposited ZnO. The difference in the surface morphology may be driven by

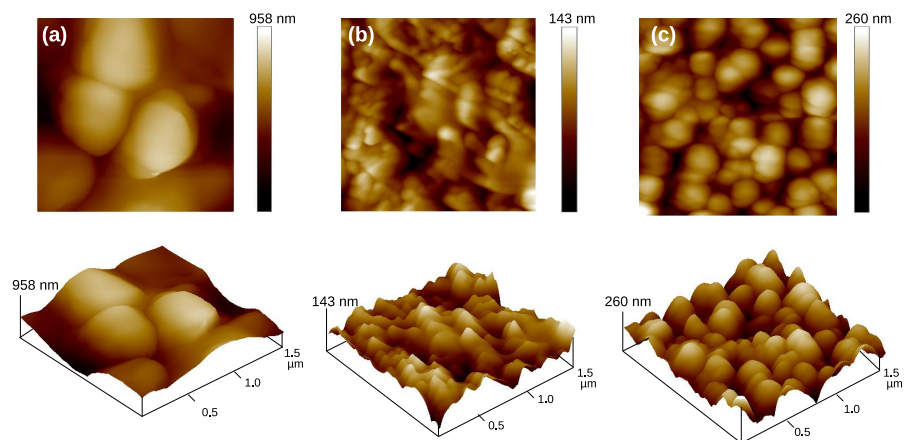


Figure 9.4: Top: Two-dimensional ($1.5\mu\text{m} \times 1.5\mu\text{m}$) AFM images of (a) electrodeposited ZnO, (b) C_2 and (c) C_{50} . Bottom shows the corresponding three-dimensional AFM images.

Cu content and its oxidation states.

(ii) Non-enzymatic Glucose Sensing via cyclic voltammetry experiments for $\text{Cu}_2\text{O-ZnO}$ and $\text{Cu}_x\text{O-ZnO}$ nanostructures

The glucose sensing properties of the electrodeposited ZnO as well as CED-grown C_2 and C_{50} samples have been studied using CV technique. Fig. 9.5 illustrates CV response in the absence and presence of 0.6 mM glucose. For ZnO nanostructures, no current can be observed without (fig. 9.5(a)) or with glucose (fig. 9.5(b)). In the absence of glucose, although C_2 shows no current response, C_{50} demonstrates a weak reduction peak at 0.6 V, caused by Cu(II)/Cu(III) redox couple [57]. Upon addition of 0.6 mM glucose, both C_2 and C_{50} display a catalytic current. This current response indicates that the glucose is getting irreversibly oxidised due to the conversion of Cu(II) to Cu(III) [58].

The possible mechanism for glucose oxidation on C_2 and C_{50} electrodes, in alkaline medium can be expressed as [59–64]:

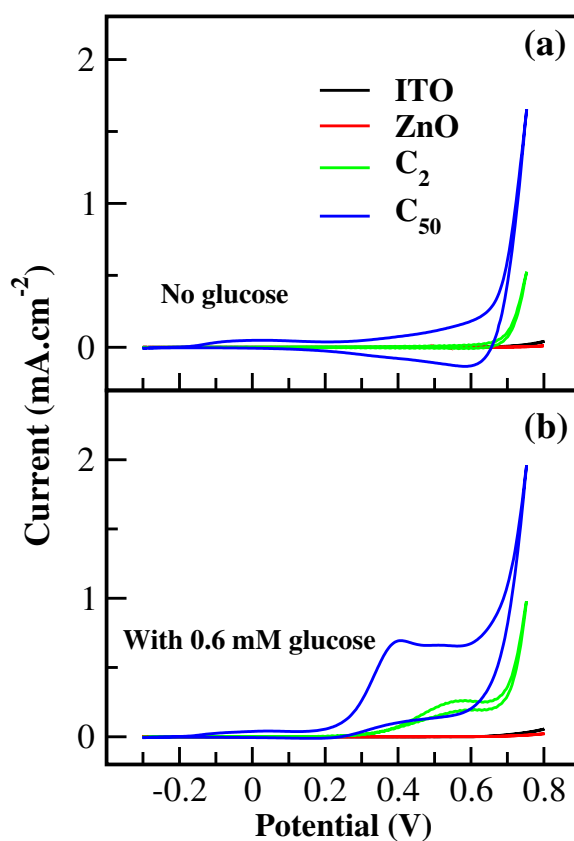
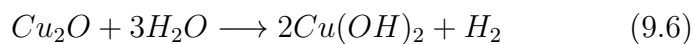


Figure 9.5: CV curves for ITO, ZnO, C₂ and C₅₀ electrodes in (a) absence of glucose and (b) presence of 0.6 mM glucose. The scan rate is 10 mV/sec.

The reaction begins with the oxidation of Cu(I) to Cu(III) via Cu(II) where the released electrons form the oxidation peak current. Glucose is electrochemically oxidized to gluconic acid with the help of Cu(III), which is again reduced back to Cu(II). Cu(III) species act as fast electron-transfer mediators and induce high catalytic activity towards glucose oxidation. C₅₀ electrodes display a larger catalytic current

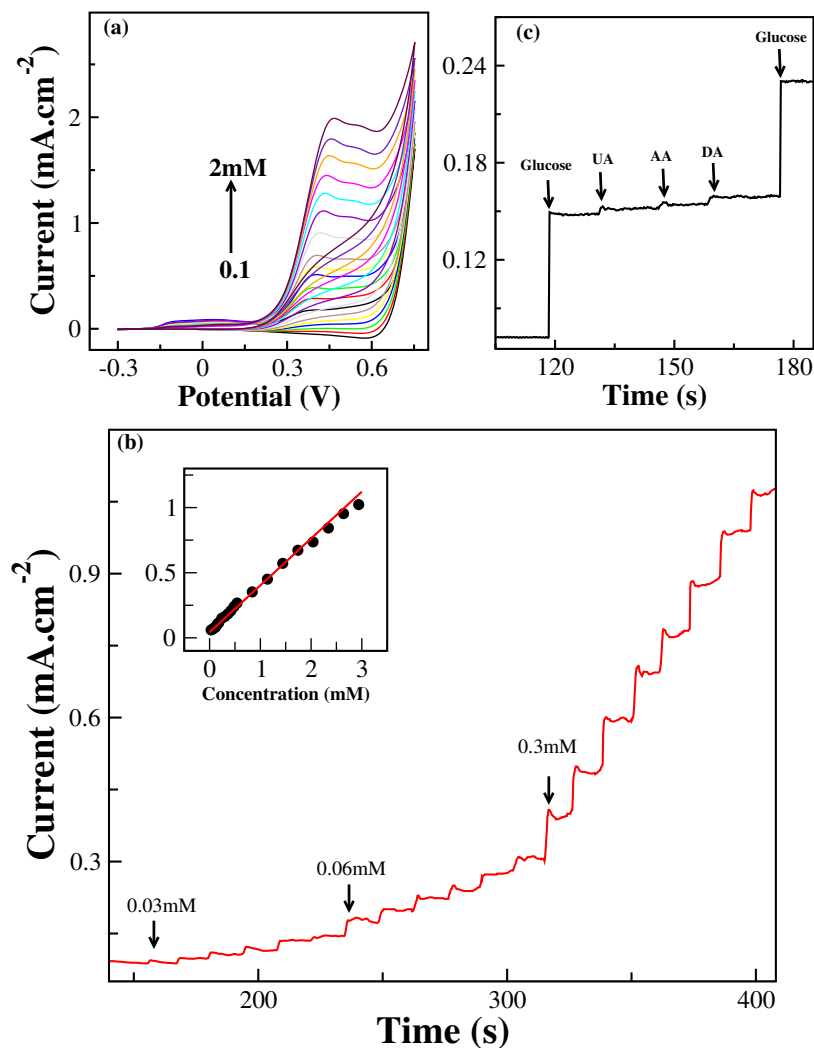


Figure 9.6: (a) CV curves of C₅₀ upon addition of different concentrations of Glucose. (b) Amperometric response of C₅₀ upon successive addition of glucose with marked concentrations to 0.1 M NaOH solution at an applied potential of 0.4 V. Inset (top) shows corresponding calibration curve. (c) Amperometric response of C₅₀ to 0.2 mM glucose and successive injection of interfering species (0.02 mM UA, 0.02 mM AA, and 0.02 mM DA) in 0.1 M NaOH with stirring.

(0.57 mA.cm⁻²) compared to C₂. This better current response may be related to the existence of Cu_xO-ZnO nanostructures with well- formed boundaries in C₅₀ and the associated surface morphology. Exhibiting good glucose sensing behavior, C₅₀ samples have been further investigated for their CV and amperometric response. Fig. 9.6(a) shows CV response while different concentrations of glucose were added successively in 0.1 M NaOH solution. Though the current response is very weak initially, it increases steadily at the higher concentrations of glucose. Systematic increase in the

catalytic peak current for C_{50} indicates a controlled role of these nanostructures in the oxidation of glucose.

Fig. 9.6(b) displays the steady state amperometric response of C_{50} electrode in 0.1 M NaOH solution with successive addition of glucose with marked concentrations, at an applied potential of 0.42 V. With the addition of glucose, C_{50} electrode demonstrates a fast current response. The calibration curve (inset of Fig. 9.6(b)) presents current as a function of glucose concentration. The results show a wide linear range of 0.03-3 mM and a sensitivity of $384.6 \mu\text{A mM}^{-1} \text{ cm}^{-2}$. The low detection limit (LOD) has been estimated to be $0.7 \mu\text{M}$ at signal/noise ratio of 3.

(iii) Non-interference, Reproducibility and stability of $\text{Cu}_x\text{O-ZnO}$ electrode

With many bio-entities like uric acid (UA), ascorbic acid (AA) and dopamine (DA) usually co-existing with glucose in a human body fluid, the non-interference test is very essential to evaluate the selectivity of the glucose sensors. Although the concentration of these interfering agents in human blood is very small ($<1/30$) in comparison to glucose [65], still large concentrations of these species have been used here. The non-interference test has been performed on C_{50} electrode with 0.2 mM glucose injection followed by a step wise addition of 0.02 mM of the interfering species in 0.1 M NaOH solution. A large current response was recorded from glucose as shown in Fig. 9.6(c). Thus, C_{50} electrode exhibits a good selectivity towards glucose detection, even in the presence of interfering species.

Long-term stability and reproducibility are other important parameters determining the quality of a glucose sensor. The long-term stability of the C_{50} electrode has been evaluated by storing them in ambient conditions and intermittently measuring their current response. The electrode is observed to retain 95% of its initial current response (fig. 9.7) even after 30 days of storage time, suggesting excellent electrode stability. The reproducibility of these electrodes have also been investigated carefully. Several electrodes were fabricated under same experimental conditions and their current response to 0.6 mM glucose provided an R.S.D of 4.2%, confirming that the fabrication method is highly reproducible. The long-term stability and repro-

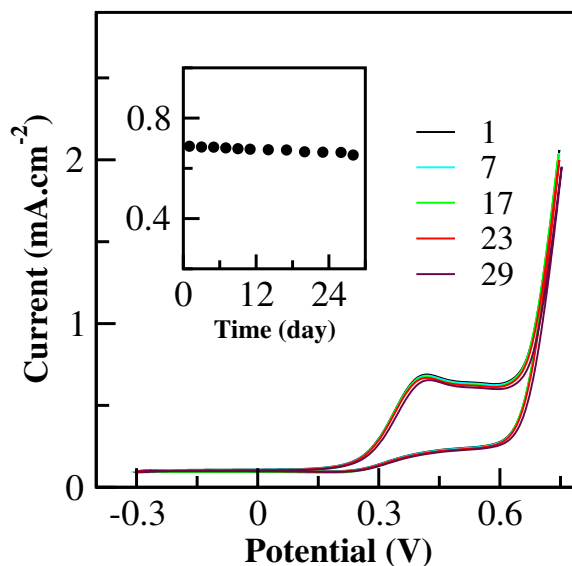


Figure 9.7: CV profile of the C₅₀ electrode in 0.1 M NaOH containing 0.6 mM glucose at different days. Inset shows corresponding stability curve of peak oxidation current as a function of days.

ducibility of C₅₀ electrode can be attributed to the chemical stability of Cu_xO-ZnO nanostructure.

There are several advantages for the electrodes prepared by CED technique. Being of planar geometry, the electrode can be fitted effortlessly in circuits and chips. Moreover the nanostructures can be fabricated, by the simple single step CED method, on any conducting substrate. Researchers often use Nafion as a binder layer to protect the catalyst. Our work on the other hand, presents a distinct route to grow Cu_xO-ZnO nanostructures directly on ITO substrate. This does not require any GCE electrode or the protective Nafion layer.

9.3.2 Photo-absorption response and band gap tailoring in Cu₂O-ZnO and Cu_xO-ZnO nanostructures

UV-Visible diffuse reflectance spectra of the electrodeposited ZnO, C₂ and C₅₀ are displayed in fig. 9.8. The photoabsorbance (PA) response of the as-deposited ZnO nanostructures is reasonably poor in the visible region. Many alterations can be observed after the incorporation of Cu. For C₂, although the response in 500- 800 nm

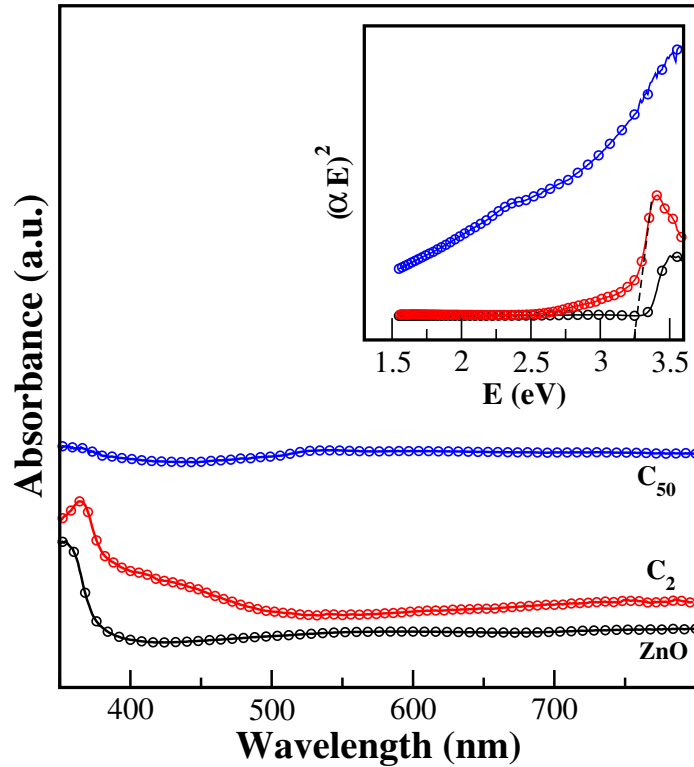


Figure 9.8: UV-Vis Photo response of ZnO, C₂ and C₅₀. Inset shows Tauc plots and the associated band gap (α is absorption coefficient and E is photon energy).

region is similar to that for ZnO, it improves for UV regime and within 400- 500 nm. Moreover, the absorbance edge displays a shift towards higher wavelengths reflecting a lowering of effective band gap. This can be caused through the coupling of bands of the two metal oxides, ZnO and Cu_xO. Tauc plot (inset) has been used to estimate the band gaps which are found to be 3.32 eV for ZnO and 3.16 eV for C₂. Significantly higher Photo-response, in the visible as well as UV regimes, is noticed for C₅₀ sample. Here, a much smaller bandgap of 2.3 eV may be predominantly responsible for this behavior, reflecting a synergistic effect of Cu_xO-ZnO type nanostructures.

9.3.3 Investigation of CuO-TiO₂ composite structure

(i) Structure and Morphology of TiO₂ and CuO-TiO₂ composite

SEM of the as-deposited TiO₂ and T₁₀ samples are displayed in fig. 9.9. The micrograph of TiO₂ exhibits the presence of many non-uniform sized particles. A large number of them have diameters in the range of 100-400 nm. Variation in sizes

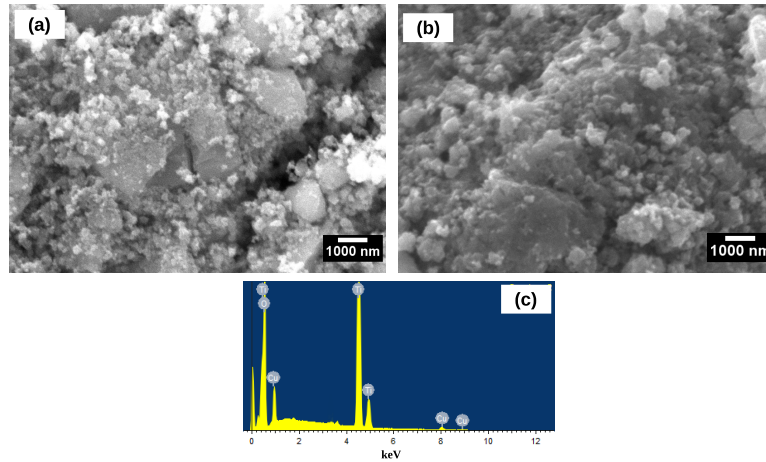


Figure 9.9: SEM image of (a) as-deposited TiO₂ and (b) T₁₀ composites. (c) EDX of T₁₀.

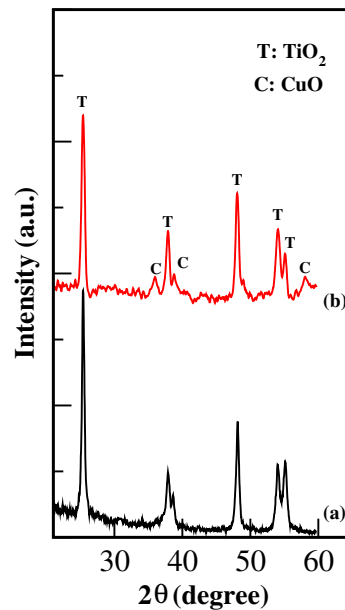


Figure 9.10: XRD patterns of (a) as-deposited TiO₂ and (b) T₁₀ composites.

may be arising due to the agglomeration of nano-particles. Similar morphology is also observed for T₁₀ samples where 10% Cu has been incorporated. EDX results (fig. 9.9(c)) also indicate the presence of Cu in this composites.

XRD from the as-deposited TiO₂ and T₁₀ samples are displayed in fig. 9.10. The diffraction peaks at 25.4°, 37.9°, 38.7°, 48.3°, 54.1° and 55.2°, for the as-deposited TiO₂ samples, correspond to (101), (004), (112), (200), (105) and (211) lattice planes

of anatase form (JCPDS 89-4921). For T_{10} , in addition to anatase TiO_2 related features, diffraction peaks ascribed to CuO phase (JCPDS 89-2531) can be observed. No other crystalline phases corresponding to Cu_2O , Cu or mixed copper-titanium oxide ($CuTiO_3$) were observed. These measurements indicate existence of CuO- TiO_2 in T_{10} .

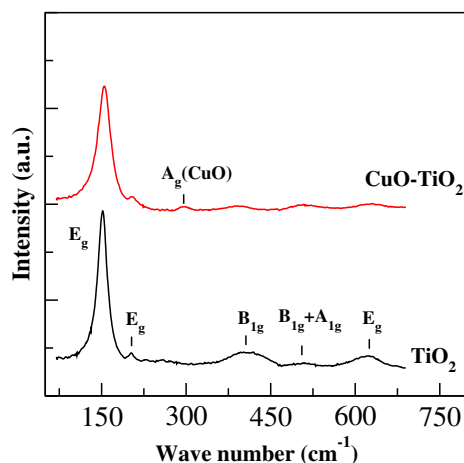


Figure 9.11: Raman spectrum of as-deposited TiO_2 and CuO- TiO_2 (T_{10}) composites.

Fig. 9.11 illustrates Raman spectra of the as-prepared TiO_2 and T_{10} sample. As-deposited TiO_2 displays several Raman features at 153, 200, 400, 509 and 630 cm^{-1} . These respectively correspond to E_g , E_g , B_{1g} , ($A_{1g}+B_{1g}$) and E_g modes of anatase TiO_2 [66]. In addition to the strong E_g mode from anatase TiO_2 , Raman spectrum of T_{10} exhibits a weak feature at 295 cm^{-1} which is attributed to A_g mode of CuO [67]. As reflected by XRD measurements, here Raman results also suggest T_{10} composites to be of CuO- TiO_2 type.

(ii) Non-enzymatic Glucose sensing via cyclic voltammetry experiments of CuO- TiO_2 composites

CV measurements of modified TiO_2 /Glassy Carbon Electrode (T/GCE) and T_{10} /Glassy Carbon Electrode (CT/GCE) have been carried out in 20 mL of 0.10 M NaOH solution in the presence and absence of 4 mM glucose (Fig. 9.12(a)). No peak was observed for T/GCE in the presence of glucose (Fig. 9.12a(i)), implying that these electrodes are inactive for enzymeless glucose detection. CT/GCE also does not exhibit much

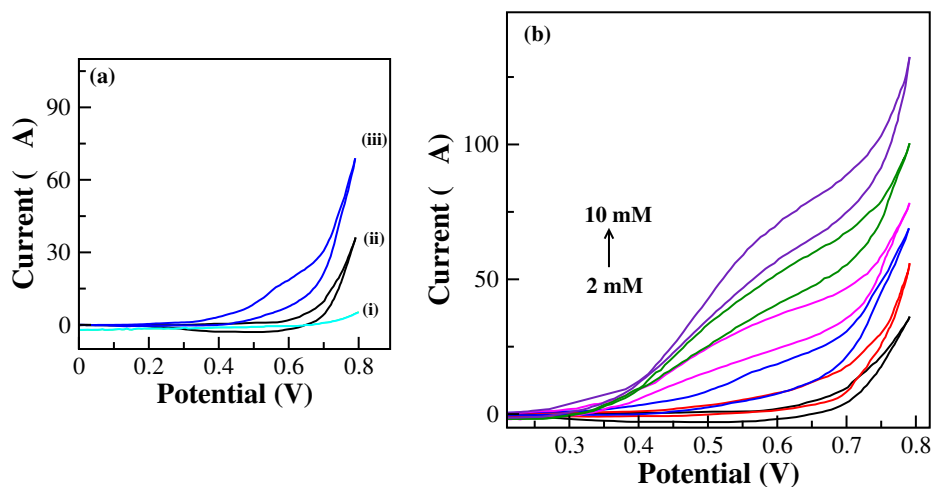


Figure 9.12: (a) CV curves of T/GCE (i) and CT/GCE (iii) in the presence of 4.0 mM glucose. CV of CT/GCE in absence of glucose (ii). (b) CV curves of CT/GCE upon addition of different concentrations of glucose in 0.10 M NaOH solution. Glucose concentrations ranged from 2 to 10 mM. Scan rate was $30 \text{ mV}\cdot\text{s}^{-1}$

appreciable current response in the absence of glucose (Fig. 9.12a(ii)). Here, a broad reduction peak is observed at around +0.60 V which corresponds to the conversion of Cu(III) to Cu(II) [68,69]. Interestingly, a significant oxidation peak is noticed for CT/GCE in the presence of 4 mM glucose (Fig. 9.12a(iii)). This is attributed to the irreversible glucose oxidation due to the conversion of Cu(II) to Cu(III) [69]. The current response appears to become prominent at ~ 0.4 V and increases up to 0.7 V, with the peak at 0.57 V. The effect of sequential glucose addition and its detection via CT/GCE is presented in Fig. 9.12(b) where CV curves of CT/GCE upon successive addition of glucose in 0.10 M NaOH solution are shown. The gradual increase in the peak current with glucose concentration indicates a high stability of the modified CT/GCE. The sensitivity for this electrode, as calculated from CV profiles, is found to be $10 \mu\text{A mM}^{-1}$.

9.3.4 Photo-absorption response and band gap modification of CuO-TiO₂ composite structure

The UV Vis diffuse reflection spectra of TiO₂ and T₁₀ composites are displayed in fig. 9.13. Compared with TiO₂, T₁₀ shows an enhanced photo absorbance in the visible

region. Although a sharp absorption edge is observed for the as-deposited TiO_2 , it gets shifted towards longer wavelengths for T_{10} . Tauc plot (inset) has been utilized to measure the optical band gaps. The as-deposited TiO_2 sample exhibit an indirect band gap of ~ 3.05 eV whereas for T_{10} a band gap of ~ 2.45 eV is observed. Good visible range photo-absorption behavior can be attributed to the smaller bandgap in T_{10} .

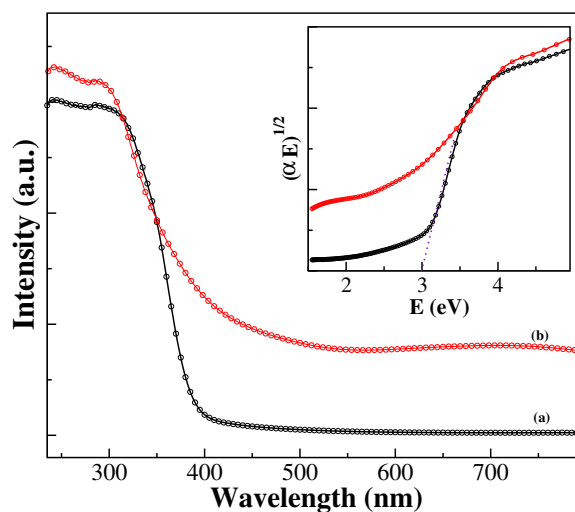


Figure 9.13: UV-visible absorption spectra of (a) as-deposited TiO_2 and (b) T_{10} composites. Inset shows Tauc plot and the associated band gaps (α is the absorption coefficient and E is the energy).

9.4 Conclusion

In summary, we have synthesized and investigated $\text{Cu}_x\text{O-ZnO}$ type nanostructures via a simple, fast, and effective CED method. This is a very low-cost and robust technique which presents good repeatability and reproducibility for the formation of nanostructures. In this chapter, two concentrations of Cu precursor, namely 2% (C_2) and 50% (C_{50}), have been utilized. While C_2 sample reflects a $\text{Cu}_2\text{O-ZnO}$ character, C_{50} samples are of mixed $\text{Cu}_x\text{O-ZnO}$ type ($x=1,2$). ZnO , C_2 and C_{50} samples have been investigated for their glucose sensing behavior via cyclic voltammetry. Although as-deposited ZnO does not show any catalytic response toward glucose, C_{50} displays higher electrocatalytic activity than C_2 . The characteristic parameters for C_{50} towards glucose detection have been measured. They show a sensitivity of

384.6 $\mu\text{A mM}^{-1} \text{cm}^{-2}$, a linear range of 0.03 - 3 mM and a low detection limit (LOD) of 0.7 μM . This electrode exhibits a good long-term stability and reproducibility. Through band gap tailoring effects, C₅₀ also demonstrates a significantly improved photo response, in UV and visible regimes, compared to C₂.

These observations are consistent with the results presented in chapter 8 where we had investigated similar nanostructures after Cu²⁺ incorporation of 1% (C₁) and 10% (C₁₀). Both the samples, C₁ and C₁₀, demonstrated presence of Cu₂O-ZnO type nanostructures. So, the overall results presented here show that at lower Cu concentrations (e.g 1%, 2% and 10%), CED promotes formation of Cu₂O-ZnO whereas at higher (50%) Cu concentration, mixed Cu_xO-ZnO (x=1,2) develops. Among all the samples discussed here for glucose detection, C₁₀ (with 10% of Cu²⁺ content) demonstrated best sensitivity, 441.2 $\mu\text{A mM}^{-1} \text{cm}^{-2}$, for non-enzymatic sensing of glucose via cyclic voltammetry. Existence of Cu₂O-ZnO type nanostructures conjugated with higher Cu²⁺ content, among the samples with similar compositional nature, may assist in establishing this. The sensitivity towards the non-enzymatic glucose sensing for all the samples, discussed here and in chapter 8, have been listed in Table 9.1.

Table 9.1: Comparison of Non-enzymatic Glucose sensitivity via cyclic voltammetry. Photo-absorption Band gaps as measured by UV-Vis spectroscopy are also mentioned.

Samples	Cu ²⁺ content	Sensitivity ($\mu\text{A mM}^{-1}\text{cm}^{-2}$)	Band gap (eV)	Ref.
C ₁	1%	72.3	3.21	Chapter 8
C ₂	2%	128.5	3.16	Chapter 9
C ₁₀	10%	441.2	2.75	Chapter 8
C ₅₀	50%	384.6	2.30	Chapter 9

Investigations of photoabsorbance property was undertaken for all the samples and an enhanced response, in UV as well as visible regions, is observed with increasing Cu²⁺ content (fig. 9.14). The respective band gaps for C₁, C₂, C₁₀ and C₅₀ have been determined here and are found to be 3.21, 3.16, 2.75 and 2.3 eV (see Table 9.1).

The present chapter also discusses the synthesis of CuO-TiO₂ composite structures. These have been synthesized via a simple and low-cost chemical method. Incorporated with 10% Cu²⁺ content, these CuO-TiO₂ (T₁₀) composites show a sensitivity of 6.6 $\mu\text{A mM}^{-1}\text{cm}^{-2}$ towards non-enzymatic glucose detection. Cu₂O-ZnO

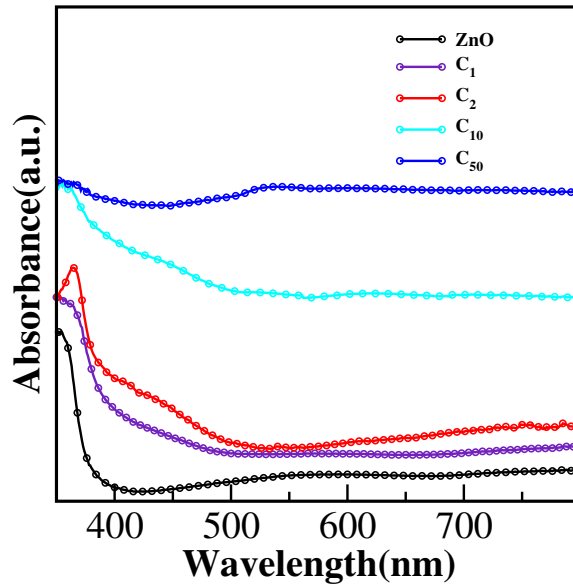


Figure 9.14: UV-Vis Photo response of ZnO, C₁, C₂, C₁₀ and C₅₀.

nanostructures prepared with same Cu (10%) content, on the other hand, show much superior sensitivity (Table 9.1) as measured by cyclic voltammetry.

CuO-TiO₂ composite (T₁₀) structures have also been studied for their photo absorption properties. They display an enhanced photo response and a band gap tailoring compared to the as-deposited TiO₂.

Bibliography

- [1] D.Y. Zhai, B. Liu, Y. Shi, L. Pan, Y. Wang, W. Li, R. Zhang and G. Yu, *ACS Nano*, 4, 3540 (2013)
- [2] A.Kros,S.W.F.M.van Hovell, N.A.J.M. Sommerdijk, and R.J.M. Nolte, *Adv. Mater.*, 13, 1555 (2001)
- [3] X.H. Niu, Y. Li, J. Tang, Y.Hu, H. Zhao, M. Lan, *Biosens. Bioelectron.*, 51, 22 (2014)
- [4] S. H. Lim, J. Wei, J. Lin, Q. Li, J. KuaYou, *Biosens.Bioelectron.*, 20, 2341 (2005)
- [5] A. Rodrigues, M.V. Castegnaro, J. Arguello, M.C.M. Alves, J. Morais, *Appl. Surf. Sci.*, 402, 136141 (2017)
- [6] A.L. Sun, J.B. Zheng, and Q.L. Sheng, *Electrochim. Acta*, 65, 64 (2012)
- [7] T.Dayakar, K. Venkateswara Rao, M. Vinodkumar, K. Bikshalu, B. Chakradhar, K. Ramachandra Rao, *Appl. Surf. Sci.*, 435, 216 (2018).
- [8] Y.Lee, D. Park, J.Park, and Y. Kim, *Sensors*, 8, 6154 (2008)
- [9] J. Wang, D. F. Thomas, and A. Chen, *Anal. Chem.*, 80, 997 (2008)
- [10] S. Liu, B. Yu, T. Zhang, *Electrochim. Acta*, 102, 104 (2013)
- [11] K. Tian, M. Prestgard, A.Tiwari, *Mater. Sci. Eng. C*, 41, 100 (2014)
- [12] Wei Huang, Yang Cao, Yong Chen, Juan Pengb, Xiaoyong Lai, Jinchun Tu, *Appl. Surf. Sci.*, 396, 804811 (2017).

- [13] Magdalena Jarosz, Robert P. Socha, Pawe J zwik, Grzegorz D. Sulka, *Appl. Surf. Sci.*, 408, 96102 (2017)
- [14] Y. Yin, Robert M. Rioux, Can K. Erdonmez, Steven Hughes, Gabor A. Somorjai, A. Paul Alivisatos, *Science*, 304, 711 (2004)
- [15] Clemens Burda, Xiaobo Chen, Radha Narayanan, and Mostafa A. El-Sayed, *Chem. Rev.*, 105, 1025 (2005)
- [16] Vanaraj Solanki, Shalik R. Joshi, Indrani Mishra, D. Kabiraj, N. C. Mishra, D. K. Avasthi, and Shikha Varma, *J. Appl. Phys.*, 120, 054303 (2016)
- [17] Hailin Tian, Huiqing Fan, Jiangwei Ma, Longtao Ma, Guangzhi Dong, *Electrochim. Acta*, 247, 787 (2017)
- [18] Chao Wang, Huiqing Fan, Xiaohu Ren, and Jiawen Fang, *Appl. Phys. A Mat. Sci & proces.*, 124, 99 (2018).
- [19] O.K. Varghese, G.K. Mor, C.A. Grimes, M. Paulose, N. Mukherjeeb, *J. Nanosci. Nanotechnol.*, 4, 733 (2004).
- [20] Z.-H. Zhang, Y. Yuan, G. Shi, Y.-J. Fang, L.-H. Liang, H.-C. Ding, L.-T. Jin, *Environ. Sci. Technol.*, 41, 6259 (2007).
- [21] G.K. Mor, K. Shankar, M. Paulose, O.k. Varghese, C.A. Grimes, *Nano Lett.*, 6, 215 (2006).
- [22] Hailin Tian, Huiqing Fan, Mengmeng Li, Longtao Ma, *Acs. Sens.*, 1, 243 (2016)
- [23] K. Zhu, N.R. Neale, A. Miedaner, A.J. Frank, *Nano Lett.*, 7, 69 (2007).
- [24] J.-X. Li, L.-X. Yang, S.-L. Luo, B.-B. Chen, H.-L. Lin, Q.-Y. Cai, S.-Z. Yao, *Anal. Chem.* 82 (2010) 2244.
- [25] A. L. Linsebigler, G. Q. Lu and J. T. Yates, *Chem. Rev.*, 95, 735 1995
- [26] A. Fujishima and K. Honda, *Nature*, 238, 37 (1972).
- [27] L. Yang, D. He and Q. Y. Cai, *J. Phys. Chem. C*, 111, 8214 (2007).

- [28] L. Chow, O. Lupan , G. Chai , H. Khallaf , L.K. Ono , B. Roldan Cuenya , I.M. Tiginyanu ,V.V. Ursaki, V. Sontea, A. Schulte, *Sensors and Actuators A*, 189, 399 (2013)
- [29] M. Li, G. Meng, Q. Huang, and S. Zhang, *Sci. Rep.*, 4, 4284 (2014)
- [30] N D Hoa, Quy N van, H Jung, D Kim, H Kim and S K Hong, *Sensors Actuators B*,146, 266 (2010)
- [31] P Raksa, A Gardchareon, T Chairuangstri, P Mangkorntong, N Mangkorntong and S Choopun, *Ceram. Int.*, 35, 649 (2009)
- [32] Li D, Hu J, Wu R and Lu J G., *Nanotechnology*, 21, 485 (2010)
- [33] Chen Z et. al., *J. Mater. Res.*, 25, 3 (2010)
- [34] Gubbala S, Thangala J and Sunkara M K,*Sol. Energy Mater. Sol. Cells.*, 91, 813 (2007)
- [35] Sumanta Kumar Mehera and G. Ranga Rao, *Nanoscale*, 5, 2089 (2013).
- [36] L. Wang, J. Fu. H. Hou, Y. Song, *Int., Int.J. Electrochem. Sci.*, 7, 12587 (2012)
- [37] K. Li, G. Fan, L. Yang, F. Li, *Sens. Actuators B Chem.*, 199, 175 (2014).
- [38] H. Huo, C. Guo, G.Li, X. Han and C. Xu, *RSC Adv.*, 4, 20459 (2014)
- [39] B. Yuan, C. Xu, L. Liu, Q. Zhang, S. Ji, L. Pi, D. Zhang, Q. Huo, *Electrochim. Acta*, 104, 78 (2013)
- [40] Daixin Ye, Guohai Liang, Huixiang Li, Juan Luo, Song Zhang, Hui Chen, Jilie Kong, *Talanta*, 116, 223 (2013)
- [41] Tetsuro Soejima, Kohei Takadaa, Seishiro Ito, *Applied Surface Science*, 277, 192 (2013)
- [42] Bin Cai, Yu Zhou, Minggang Zhao, Hui Cai, Zhizhen Ye, Lei Wang, Jingyun Huang, *Applied Physics*,118, 989 (2015)

- [43] S N Sarangi, *J. Phys. D: Appl. Phys.*, **49**, 355103 (2016)
- [44] G. Yao, M. Zhang, J. Lv, Kai Xu, S. Shi, Z. Gong, J. Tao, X. Jiang, L. Yang, Y. Cheng, G. He, X. Chen, and Z. Sun, *J. Electrochem. Soc.*, **162**, 300 (2015)
- [45] Yasemin Caglar, Anda Arslan, Saliha Ilican, Evrim Hr, Seval Aksoy, Mujdat Caglar, *J. Alloys and Compd.*, **574**, 104 (2013)
- [46] O. Lupan, T. Pauporté, B. Viana, P. Aschehoug, *Electrochim. Acta*, **56**, 10543 (2011)
- [47] Y. Liu, F. Ren, S. Shen, Y. Fu, C. Chen, C. Liu, Z. Xing, D. Liu, X. Xiao, W. Wu, X. Zheng, Y. Liu, and C. Jiang, *Appl. Phys. Lett.*, **106**, 123901 (2015)
- [48] M. Rashad,¹ M. Rsing, G. Berth, K. Lischka, and A. Pawlis, *Journal of Nanomaterials.*, 714853, (2013)
- [49] P. Soundarrajan , K. Sankarasubramanian , M. Sampath , T. Logu , K. Sethuraman, K. Ramamurthi, *Physica E*, **71**, 5663 (2015)
- [50] K. Sharma, Ranu K. Dutta, Avinash C. Pandey, *Journal of Magnetism and Magnetic Materials*, **321**, 4001 (2009).
- [51] J. Ghijsen, L. H. Tjeng, J. van Elp, H. Eskes, J. Westerink, G. A. Sawatzky, and M. T. Czyzyk ,*Phys. Rev. B.*, **38**, 11322 (1988)
- [52] T. Robert, M. Bartel, and G. Offergeld, *Surf. Sci.*, **33**, 123 (1972)
- [53] Daqiang Gao, Jing Zhang, Jingyi Zhu, Jing Qi, Zhaohui Zhang, Wenbo Sui, Huigang Shi, *Desheng Xue, Nanoscale Res. Lett.*, **5**, 769 (2010)
- [54] Amare Aregahegn Dubale, Chun-Jern Pan, Andebet Gedamu Tamirat, Hung-Ming Chen, Wei-Nien Su, Ching-Hsiang Chen, John Rick, Delele Worku Ayele, Belete Asefa Aragaw, Jyh-Fu Lee, Yaw-Wen Yang and Bing-Joe Hwang, *J. Mater. Chem. A*, **3**, 12482 (2015)
- [55] M. Tariq Qamar, M. Aslam, Iqbal M. I. Ismail, Numan Salah, and A. Hameed, *ACS Appl. Mater. Interfaces*, **7**, 8757 2015

- [56] Ulugbek Shaislamov, Karthikeyan Krishnamoorthy, Sang Jae Kim, Wongee Chun and Heon-Ju Lee, *RSC Adv.*, **6**, 103049 (2016)
- [57] C.Zhou, L. Xu, J. Song, R. Xing, S. Xu, D. Liu H. Song, *Sci. Rep.*, **4**, 7382 (2014)
- [58] H.X. Wu, W.M. Cao, Y. Li, G. Liu, Y. Wen, H.F. yang, S.P. Yang, *Electrochim. Acta*, **55**, 3734 (2010)
- [59] L. Wang, J. Fu. H. Hou, Y. Song, *Int., Int.J. Electrochem. Sci.*, **7**, 12587 (2012)
- [60] A.J. Wang, J.J. Feng, Z.H. Li, Q.C. Liao, Z.Z. Wang and J.R. Chen, *Cryst. Eng. Comm.* **14**, 1289 (2012)
- [61] L. Zhang, Y.Ni and H. Li, *Microchim. Acta.*, **171**, 103 (2010)
- [62] S. Felix,P. Kollu, B.P.C. Raghupathy, S.K.Jeong, A.N. grace, *J. Chem. Sci.*, **126**, 25 (2014)
- [63] R. Khan, R. Ahmad, P. Rai, L.W. Jang, J.H. Yun, Y.T. Yu, Y.B. Hahn, I.H. Lee, *Sensors and Actuators B*, **203**, 471 (2014)
- [64] Song Li, Yajie Zheng, Gaowu W. Qin , Yuping Ren, Wenli Pei, Liang Zuo, *Talanta*, **85**, 1260 (2011)
- [65] Yan Zhong, Tielin Shi, Zhiyong Liu, Siyi Cheng, Yuanyuan Huang, Xiangxu Tao, Guanglan Liao, irong Tang, *Sensors and Actuators B*, **236**, 326 (2016)
- [66] Chen, C.A. Chen, Y.M. Huang, Y.S. Tsai, D.S. Tiong, K.K. Liao, *Cryst Eng Comm*, **11**, 2313 (2009)
- [67] Vaseem, M. Hong, A.R. Kim, R.T. Hahn, *J. Mater. Chem. C*, **1**, 2112 (2013)
- [68] Q. Xu, Y. Zhao, J.Z. Xu, J.J. Zhu, *Sens. Actuators B: Chem.*, **114**, 379 (2006)
- [69] S.T. Farrell, C.B. Breslin, *Electrochim. Acta*, **49**, 4497 (2004)

Chapter 10

ZnO nanorods fabricated via Hydrothermal method: Photo-absorbance behavior and Photocatalytic properties

Nanostructures of zinc oxide (ZnO) demonstrate many interesting and novel properties, including wide band gap (3.32 eV) and large exciton binding energy (60 meV) [1–5]. These properties suggest numerous applications in the field of solar cells, sensors, optoelectronic devices, photo-catalysis etc. [6–14]. The nanostructured dimension and morphology, however can modulate the properties and thus can affect the device performance [15]. Recently, one dimensional (1-D) structure (e.g. nanorod, nanowire etc.) have received immense attention in sensors, photocatalysis, optoelectronic devices etc. [11–14]. They have large surface to volume ratio and offer direct carrier conduction path [16]. These are two important factors that provide an edge over other forms of nanostructures.

ZnO is known to be a good photocatalyst material [17–19]. This is primarily due to the presence of native defect states (e.g. oxygen vacancy). In addition, it has high reaction and mineralization rates that can produce hydroxyl ions more efficiently in aqueous solution [20, 21]. Surface area and surface defects play a crucial role in the photocatalysis process. Nano-dimensional structures such as nanorods offer large effective surface area, leading to higher photo-absorption and photocatalytic activity [22]. Presence of large amount of surface defects also enhance the photocatalytic efficiency by increasing carrier trapping. This consequently reduces the

electron-hole recombination rates [23]. The high surface to volume ratio as well as the presence of surface defects in the nanorods of ZnO, therefore, are expected to display excellent photo-catalytic response.

To synthesize ZnO NRs, various growth methods have been proposed, such as aqueous hydrothermal growth [24,25], physical vapour deposition [26], metal organic chemical vapour deposition [27], chemical vapour deposition [28] and thermal evaporation [29–31]. Among them, hydrothermal method is found to be an easy and cost-effective technique for the growth of these NRs. The structure and properties of NRs, however are sensitive to the parameters such as pH of the solution, reaction temperature, molarity etc. A variety of NRs can be synthesized by changing these parameters. In earlier studies, structures like nanowires (NWs) [32,33], nanoflakes [34], nanorods [35], nanobelts [36], and nanotubes [37] have been obtained. Particularly, growth of well-aligned ZnO NR arrays, prepared by hydrothermal technique with well controlled size and height can be interesting for photocatalysis.

Recently, highly ordered ZnO NR arrays have shown many promising applications. However, the utilization of ZnO NR arrays in dye waste-water treatment, under visible light, has not received much attention. Baruah et al. synthesized microwave hydrolysed ZnO nanorods with quasi stable surface states that demonstrate a better degradation efficiency of 97% in comparison to the conventionally prepared rods, showing efficiency of 90% [23]. Creation of oxygen deficient states, due to the fast crystallization process, promotes the higher photocatalytic activity. Xiaon Cai et al. have reported that ZnO NRs on Zn substrates, guided by nanostructure morphology, lead to some exposed polar surfaces of ZnO nanocrystals [38]. This gives rise to a relatively higher catalytic activity under ambient conditions for azo dyes [38]. Bora et al. have prepared ZnO NRs by hydrothermal method and studied their photocatalytic activities under visible light by controlling surface defects through different annealing conditions [39]. Degradation efficiency of nearly 90% and 55%, in 180 min, was observed after annealing at 250°C and 450°C, respectively [39].

In chapters 8 and 9, we have studied $\text{Cu}_x\text{O-ZnO}$ nanostructures prepared by co-electrodeposition technique. These nanostructures demonstrate non enzymatic glucose sensing characteristics via cyclic voltammetry. These nanostructure also exhibit

Cu content dependent Photo-absorption and bandgap modifications. The photo-absorption behaviour and resistive switching properties have also been investigated, in chapter 7, after Ti ion irradiation of ZnO thin films. Here, the enhancing ion fluence reduces the band gap and improves the visible regime absorption. The present chapter discusses the hydrothermal growth of ZnO nano-rods. Results show development of aligned ZnO NR arrays with preferential alignment. Photo-absorption behavior and photocatalytic nature of these arrays have been investigated here.

In this chapter, vertically aligned ZnO NRs were synthesized on seed layers using a simple and cost-effective hydrothermal method. FESEM and XRD techniques were employed to investigate the surface morphology and crystal structures of the ZnO NRs. In addition, the photocatalytic activity of these ZnO NRs has been evaluated using methylene blue (MB) as a model dye. Our focus in the present study is to investigate the morphology and photocatalytic activity of 1-D aligned nanostructures as they will be expected to have advantage in providing direct carrier conduction path. Here we are proposing simple method to obtain 1-D vertically aligned nanostructures. The role of surface defect states in sub-band formation and in visible light photoabsorption has been investigated.

10.1 Experimental Details

Homogenous and uniform ZnO seed layers were prepared by sol-gel spin coating technique. Zinc acetate dihydrate [$\text{Zn}(\text{CH}_3\text{COO})_2 \cdot 2\text{H}_2\text{O}$], 2-methoxyethanol (2-ME) and monoethanolamine (MEA) were used as precursor, solvent and stabilizer respectively. For second type of seed layer, aluminium doped zinc oxide (AZO) films were prepared by DC sputtering method using ZnO : Al_2O_3 (2wt.%) target. All the seed layers, prepared by both sol-gel spin coating method and DC sputtering, were annealed at 500°C for 2 hours. In this experiment, Si(100) wafers and indium tin oxide (ITO) coated glasses have been used as substrates. Prior to the seed layer deposition process, the substrates were ultrasonically cleaned with acetone and isopropanol.

Prior to the growth of the NRs, seed layers of ZnO have been grown on different substrates. ZnO NRs were then synthesized on the seed layer via hydrothermal

method. For this purpose, an aqueous solution of 35 mM zinc nitrate hexahydrate ($\text{Zn}(\text{NO}_3)_2 \cdot 6\text{H}_2\text{O}$) and 35 mM of hexamethylene tetramine (HMT) were prepared. To synthesize the NRs, the substrates were immersed inside the solution with seed layer facing downwards. The temperature of the bath was maintained at 70°C for 3h, during growth process. After the growth was over, the samples were taken out and rinsed several times with deionized water. Finally, these ZnO NRs on different substrates were annealed at 500°C for 2h.

The structural investigation of the samples were performed by grazing incidence X-ray diffraction (GIXRD) using Bruker D8 Discover diffractometer with CuK_α ($\lambda=1.54059 \text{ \AA}$) incident radiation in the range of $20\text{-}80^\circ$. Micro-Raman measurement were carried out using T64000, HORIBA Scientific Raman System with 514 nm laser excitation. Raman spectra were recorded in the range of 80 to 700 cm^{-1} . The morphology and elemental composition of the samples were investigated by scanning electron microscopy (SEM) and energy dispersive X-ray spectroscopy (EDS) analysis using a field emission scanning electron microscope (FE-SEM) Zeiss Ultra 55 microscope operated at 20 kV. The optical absorption spectra of the ZnO NRs were acquired in the wavelength range of 200-900 nm using Shimadzu UV-Visible spectrophotometer (UV-2450) with integrating sphere using BaSO_4 as a standard. The photoluminescence spectra (PL) were recorded in a spectral range of 330-750 nm using T64000 HORIBA system with 325 nm line of He-Cd laser excitation source.

The photocatalytic activity of the prepared ZnO NRs was studied by using Methylene blue (MB) as a model dye. For this experiment, the ZnO NRs arrays were dipped into the $10 \mu\text{M}$ aqueous solution of MB. Before exposing to light, the above solution with NR arrays was magnetically stirred for 20 min to establish absorption-desorption equilibrium. The whole set up was kept under a 100 W bulb (with a luminous irradiance of $10 \text{ mW}/\text{cm}^2$) with the nanorod surfaces facing the light source. The UV-Visible measurements were performed at fixed time intervals, to follow the degradation of MB.

10.2 Results and discussion

Fig. 10.1 shows the schematic layer structure of four sets of samples used in the present study. Sample A was ZnO seed layer, grown by sol-gel spin coating method on Si(100) substrate. For sample B, ZnO seed layer was grown on ITO and then ZnO NRs were deposited by hydrothermal method. Same procedure was followed to prepare ZnO NRs on Si(100) substrate and the sample is named as C. For sample D, the seed layer of aluminium doped ZnO (AZO) was deposited by DC sputtering method on Si (100) and then ZnO NRs were deposited hydrothermally on the seed layer.

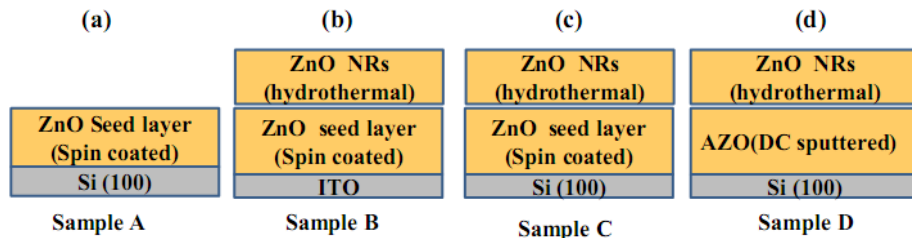


Figure 10.1: Schematic of the layer structures of samples A to D ((a) to (d) respectively) used in this work.

The SEM image and GIXRD pattern of ZnO seed layer (Sample A) are shown in fig. 10.2(a) and (b), respectively. From fig. 10.2(a) it is observed that the seed layer is uniform and densely packed with an average grain size of about 25 nm. The GIXRD pattern (fig. 10.2(b)) indicates that seed layers are of wurtzite structure and is oriented along (002) plane.

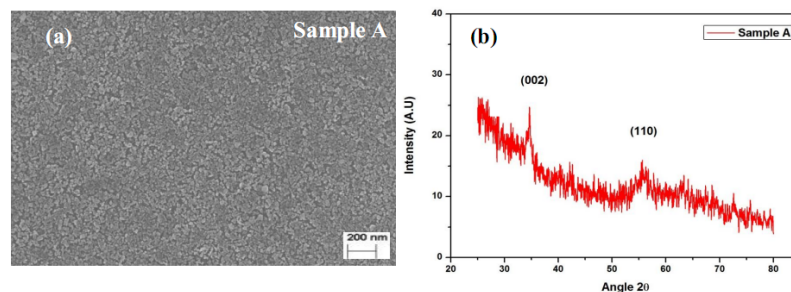


Figure 10.2: (a) SEM images of ZnO seed layer (sample A) and its (b) GIXRD spectrum.

The SEM images (top and side view) of ZnO NRs (Sample B) are shown in

fig. 10.3(a) and (b), respectively. These NRs show hexagonal faceting and diameter of about 100 nm. Fig. 10.3(b) shows the side view of NRs demonstrating that these NRs were vertically aligned with identical length size $\sim 3\mu\text{m}$. Further, these NRs have well defined hexagonal facets along the length (inset fig. 10.3(b)) indicating that they have wurtzite structure of ZnO. The chemical composition of these ZnO NRs was studied by an EDS analysis (fig. 10.3(c)). Four peaks identified as Zinc and Oxygen in the spectrum indicate that NRs are composed of zinc and oxygen only without any other impurities. Fig. 10.3(d) shows the GIXRD pattern of ZnO NRs having four diffraction peaks; (100), (002), (102) and (103) at $2\theta = 30.38, 34.41, 47.8$ and 62.86° , respectively. These peaks match well with the JCPDS data (card No. 36-1451) and correspond to the lattice constants 3.249 \AA and 5.206 \AA .

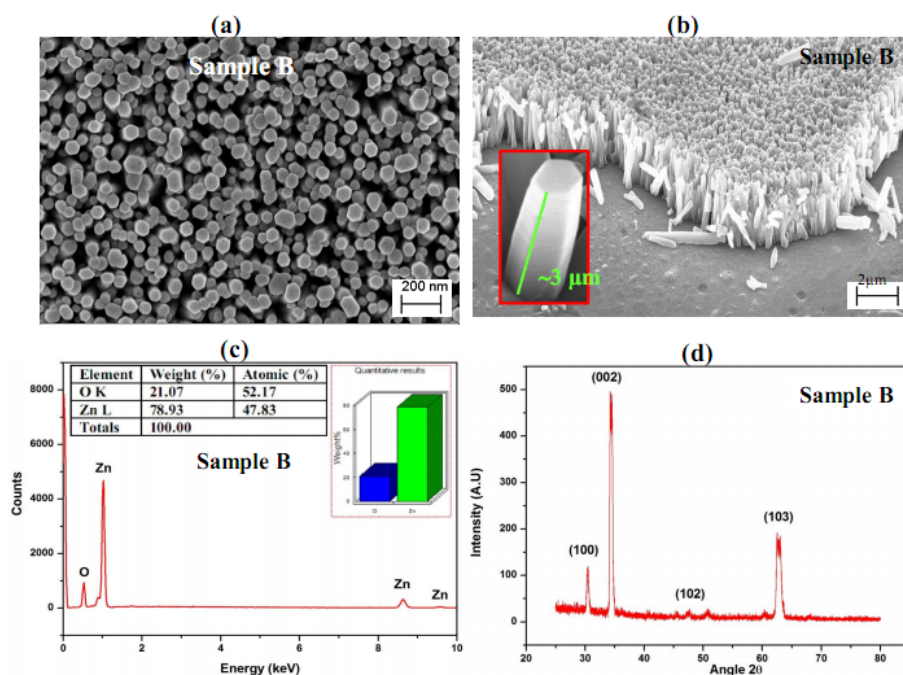


Figure 10.3: For sample B, top view (a) and side view (b) SEM images. (c) EDS spectrum and (d) GIXRD Spectrum.

The top view SEM images (fig. 10.4(a) and 10.4(b)) of sample C and D show that they are of nearly same ($\sim 100 \text{ nm}$) diameter. The GIXRD pattern of ZnO NRs (samples C and D) (fig. 10.4 (c, d)) indicate five reflection peaks of hexagonal wurtzite structure, (002), (101), (102), (110) and (103) at $2\theta = 34.41, 36.27, 47.8, 56.34$ and 62.86 degree, respectively. These peaks match well with the standard JCPDS data.

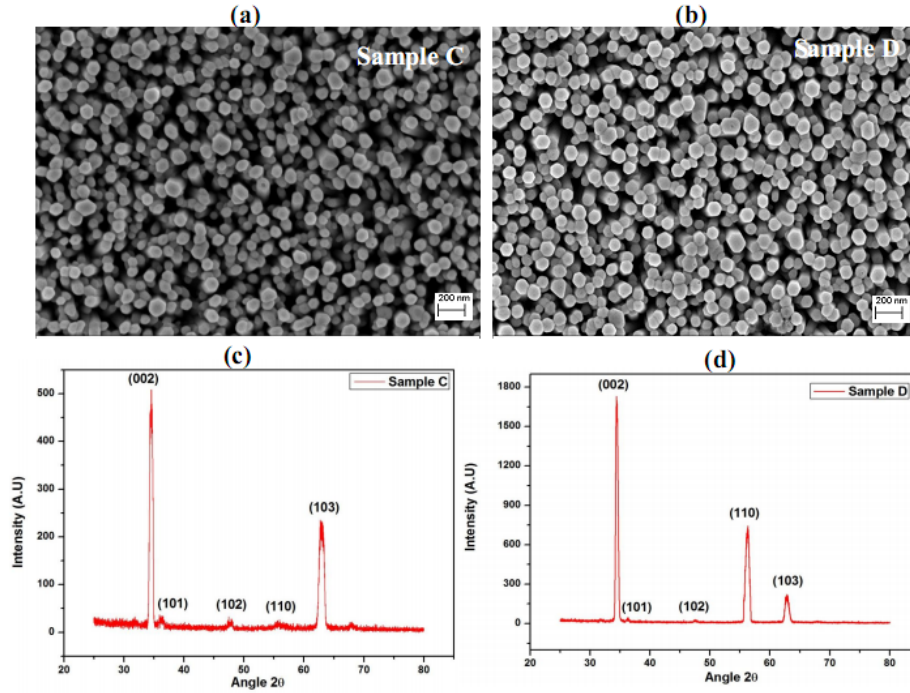


Figure 10.4: Top view SEM images of ZnO nanorods (a) Sample C and (b) Sample D, GIXRD Spectra of (c) Sample C and (d) Sample D.

Intensity variation of some of the peaks, e.g (110) and (103), may be due to the presence of different seed layers. The sharp peak (002) reflects that these NRs have grown along the c axis and its high intensity suggests that NRs are perpendicular to the substrate surface. The lattice constants, ‘ a ’ and ‘ c ’ for the Wurtzite structure can be estimated as [40];

$$a = \sqrt{\frac{1}{3}} \frac{\lambda}{\sin \theta} \quad (10.1)$$

$$c = \frac{\lambda}{\sin \theta} \quad (10.2)$$

The (002) plane has been considered for the calculation and we obtained lattice constants $a = 3.005\text{\AA}$ and $c = 5.213\text{\AA}$, similar to JCPDS data. The narrow width of (002) peak indicates an excellent crystalline structure of ZnO NRs, with their growth along the [002] orientation of ZnO seed layer. The crystallite size of these NRs was calculated using Scherrer formula [41]:

$$d = \frac{0.9\lambda}{\beta \cos \theta} \quad (10.3)$$

where d is the crystallite size, λ is the wavelength of the X-ray and β is the broadening of the diffraction line measured at the half of its maximum intensity (FWHM) in radians for (002) peak. θ is the corresponding angle of diffraction.

Table 10.1: Structural parameters of ZnO NRs.

Sample	FWHM $\beta(002)$	2θ	d (nm)	$\frac{a}{c}$
B	0.56	34.54	14.87	0.5777
C	0.50	34.41	16.65	0.5771
D	0.44	34.44	18.92	0.5770

Table 10.1 gives the structural parameters of ZnO NRs deposited on different substrates. It was observed that the crystallite size lies within the range of 10 to 20 nm. The larger d and smaller FWHM values indicate better crystallization. Hence, sample D shows better crystallinity than sample B or C. Interestingly, the well aligned ZnO NRs in samples B, C, D are only observed when the deposition takes place on the seed layers. In the absence of any seed layer, the growth of ZnO NRs does not produce well aligned structures rather produces flower like structures. Fig. 10.5 shows the growth of ZnO flowers with nano rods of ~ 200 nm diameter and $3 \mu\text{m}$ length on Si(100) without any seed layer.

Fig. 10.6 displays the Raman spectra of ZnO single crystal as well as ZnO NRs prepared by hydrothermal method on different substrates. The Wurtzite-type lattice structure of ZnO belongs to C_{6v}^4 space group with two formula units per primitive cell [42]. Group theory of wurtzite ZnO structure predicts, $A_1(z) + 2B_1 + E_1(x, y) + 2E_2$ optical phonon modes at the Γ point of the Brillouin zone [43]. Both A_1 and E_1 modes are infrared and Raman active but A_1 is polarized along z direction and E_1 is polarized along xy plane. Fig. 10.6 shows that ZnO single crystal has two dominant

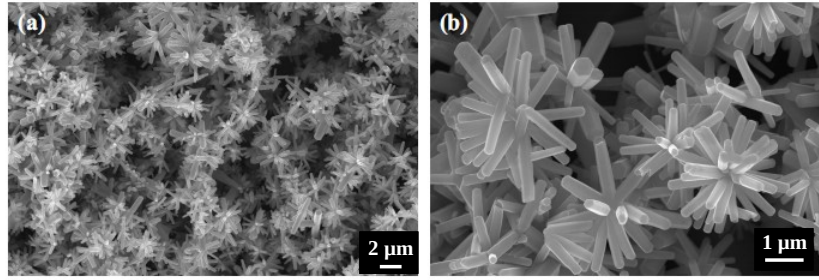


Figure 10.5: (a) top view (b) magnified view SEM images of ZnO NRs grown without seed layer.

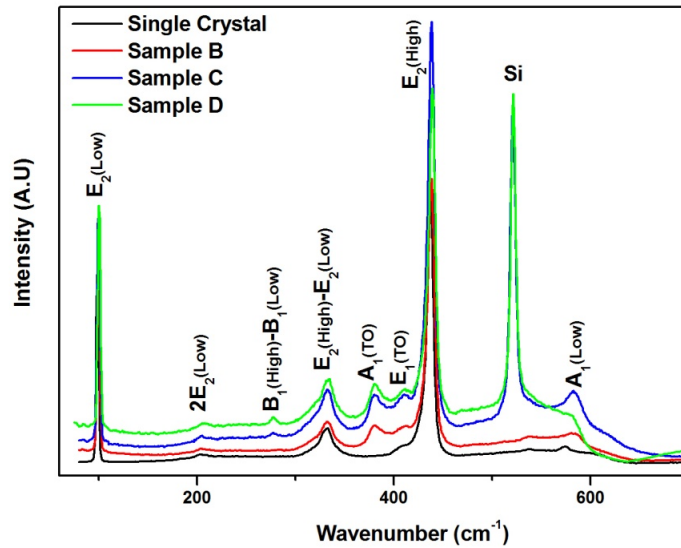


Figure 10.6: Raman spectra of ZnO single crystal and ZnO NRs.

peaks at 98.46 cm^{-1} and 437.83 cm^{-1} , which are assigned to the E_2 (low) and E_2 (high) mode of non polar optical phonons and are associated with the motion of Zn sub lattice and oxygen, respectively [43]. Strong E_2 (high) mode is a characteristic of the wurtzite lattice and good crystallinity. The weaker peak at 332.48 cm^{-1} has been attributed to the second order Raman scattering arising from the zone boundary phonons E_2 (High)- E_2 (Low) of multiphonon process. The weak peaks at 201.8 cm^{-1} and 574.28 cm^{-1} are assigned to $2E_1$ (Low) and A_1 (Low) modes. Furthermore, A_1 (low) is directly associated with oxygen vacancies. This indicates that the prepared nanorods have some oxygen vacancy which may also be promoting photocatalytic

activity.

Table 10.2: Wave number and symmetries of the modes found in Raman spectrum of ZnO single crystal, nanorods and their assignments.

Mode of symmetry	Peak position(cm^{-1})			
	ZnO single crystal	Sample B	Sample C	Sample D
$E_2(\text{low})$	98.46	99.17	99.87	100.51
$2E_2(\text{low})$	204.51	204.51	205.22	205.23
$B_1(\text{high})-B_1(\text{low})$		284.4	280.16	276.69
$E_2(\text{high})-E_2(\text{low})$	332.48	332.48	332.48	331.87
$A_1(\text{TO})$		381.26	380.56	379.98
$E_1(\text{TO})$	405.3	412.37	410.25	411.82
$E_2(\text{high})$	437.83	438	438.54	439.42
$A_1(\text{LO})$	574.28	583.48	582.06	581.63

Raman peaks of NRs have been compared with those from the single crystal (Table-10.2). The Raman active modes of NRs are nearly same as those from the single crystal, with few exceptions. $A_1(\text{TO})$ mode, seen in NRs, is not present in single crystal. Another peak at 412 cm^{-1} assigned to be $E_1(\text{TO})$ mode is not prominent in case of single crystal. Both $A_1(\text{TO})$ and $E_1(\text{TO})$ modes reflect the strength of the polar lattice bonds [44] that are prominent in case of NRs. Although B_1 mode is Raman inactive, a weak peak at 284 cm^{-1} was observed which has been assigned to the B_1 (High) - B_1 (Low) second order mode [45]. The appearance of this mode is attributed to disorder-activated Raman scattering. The defects or impurities can break the translational symmetry of the lattice which will induce these type of scattering [46]. In addition, in case of NRs, the $E_2(\text{low})$ and $E_2(\text{high})$ modes are observed to be shifted towards higher wave numbers compared to the single crystal.

Fig. 10.7 shows high resolution of $E_2(\text{low})$ and $E_2(\text{high})$ modes. For $E_2(\text{high})$ peak, the position (FWHM) is found to be $437.83 \text{ cm}^{-1}(7.09 \text{ cm}^{-1})$ for the single crystal ZnO whereas for samples B, C, D these are $438 \text{ cm}^{-1} (8.07 \text{ cm}^{-1})$, $438.54 \text{ cm}^{-1} (8.04 \text{ cm}^{-1})$ and $439.42 \text{ cm}^{-1} (7.3 \text{ cm}^{-1})$, respectively. This indicates that sample D has better crystalline quality than other samples. E_2 mode is very sensitive to stress and the nature of the stress (compressive or tensile) can be identified from the peak shift [47]. ZnO single crystal can be assumed to be stress-free and devoid of any hydrostatic stress, originated from point defects. The E_2 (high) peak position exhibits

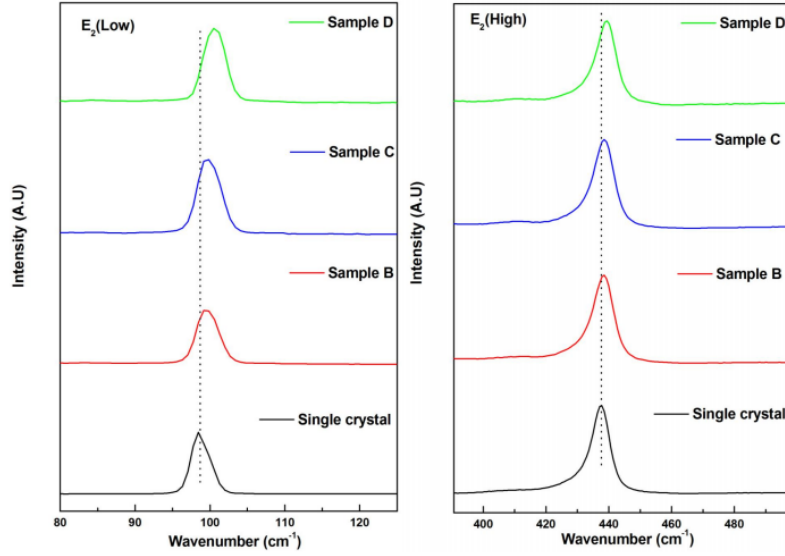


Figure 10.7: Magnified Raman spectra of ZnO single crystal and ZnO NRs.

a blue shift of nearly $1\text{-}2\text{ cm}^{-1}$ for ZnO NRs compared to the single crystal. This indicates ZnO NRs are under compressive stress. In this study, we have observed a new Raman mode $A_1(\text{TO})$ for NRs. Broadening and frequency shifts in other Raman modes of NRs, compared to the single crystal, are also noticed. Similar Raman peak shifts, towards higher wave number, for ZnO NRs have also been reported in the literature [48].

The optical absorbance spectra of ZnO NRs (Samples B, C, D) in the UV-visible wavelength range are presented in fig. 10.8 and the inset shows the photo-absorbance from the single crystal. When a photon of energy greater than the band gap of the semiconductor is absorbed, electrons get excited from valence band to conduction band and an abrupt increase in the absorbance is observed. Fig. 10.8 shows the absorption spectra of ZnO NRs. Two band edges \tilde{E}_1 and \tilde{E}_2 were observed which correspond to the direct band-gap and vacancy related band, respectively [49–51]. The absorption band edge \tilde{E}_1 of NRs is comparable to that of pure single crystal ZnO (390 nm) [52]. An enhanced photo absorption in the visible region was observed for NRs of samples C and D. This may be due to the presence of surface defect states in ZnO NRs which improve the absorption by allowing sub-bandgap transitions and consequently produce electron-hole pair under visible light illumination [23, 39].

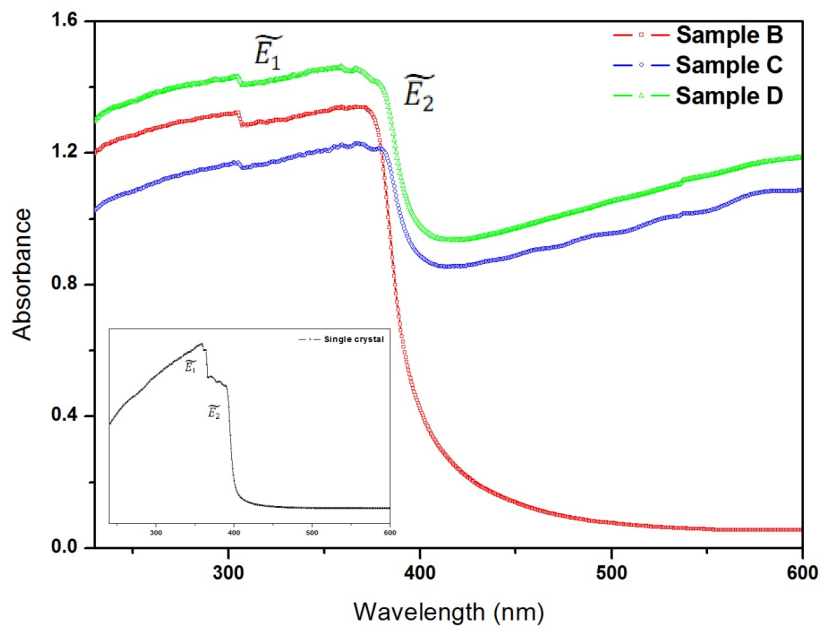


Figure 10.8: UV-visible absorbance spectra of ZnO NRs and single crystal (inset).

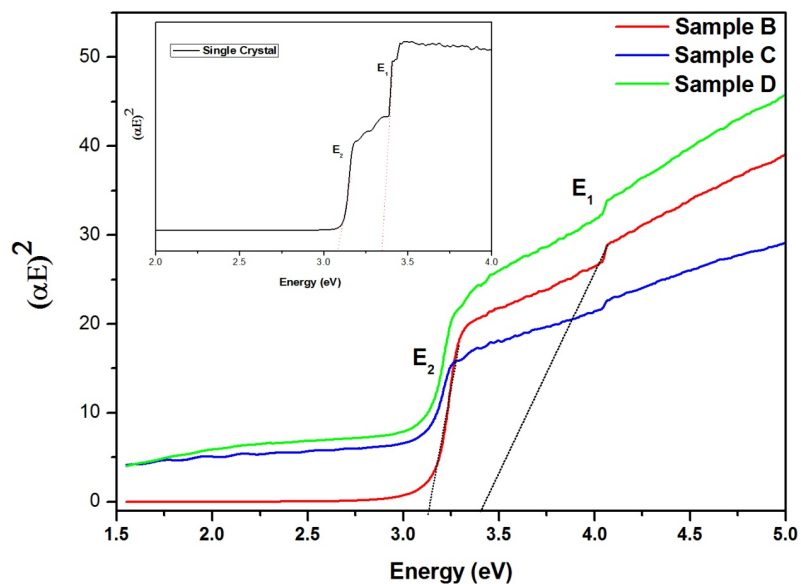


Figure 10.9: Tauc plots (α is absorption coefficient and E is energy of photons) of ZnO NRs. Inset shows Tauc plot of single crystal.

Fig. 10.9 shows the optical band gap of these NRs and single crystal (inset), as calculated from Tauc plots. For samples B, C, D the ZnO-band gap energy (E_1) was observed at 3.39, 3.3 and 3.25 eV, respectively. The vacancy related band (E_2) was observed at 3.12, 2.92 and 2.88 eV, respectively. The ZnO band gap observed here is comparable to that of wurtzite bulk ZnO [50].

The room temperature photoluminescence (PL) spectra of ZnO seed layer and NRs are shown in fig. 10.10. The PL spectra are useful in evaluating the recombination rate of the charge carriers [53]. The ultraviolet emission peak for all samples are observed at 378 nm which is due to the exciton recombination and corresponds to the near-band edge excitonic emission for ZnO [54]. The broad visible emission is due to single and double ionized oxygen vacancies [55]. Magnified PL spectra (fig. 10.10 insets) show that all these samples have a broad emission band in the range of 450-750 nm centred near 600 nm, which is due to the presence of point defects in ZnO [55]. For sample A, this broad peak is de-convoluted into three components, centred at 534, 591 and 649 nm. The peak at 534 nm is attributed to the green emission (530-550 nm) which is due to the transition from conduction band to the oxygen vacancy state. Features at 591 nm and 649 nm are due to the yellow-orange emission (590-600nm) and red emission (650-670 nm), respectively. The yellow-orange emission is due to the transition from conduction band to the oxygen interstitial state whereas the red emission is attributed to the transition from Zn to the oxygen interstitial state [57]. The Gaussian components centered at 534 and 591 nm are due to the surface defects. Both the singly (V_o^+) and doubly (V_o^{++}) charged oxygen vacancies states contribute to the green emission in ZnO [58]. It was observed that relative concentration of oxygen vacancy sites are more in case of nanorods than in the seed layer (sample A). It was also found that the excitonic PL intensities of NRs (sample B, C, D) were less than that from the seed layer (sample A) suggesting that the separation rate of photo-induced electrons and holes is more in case of NRs (specially in case of sample D). Rates of recombination of electrons and holes thus seem to have become least in the NR sample-D [59]. Therefore, surface oxygen vacancies as well as excellent charge carrier separation in sample D, among other NRs, will contribute to the better photocatalytic activity.

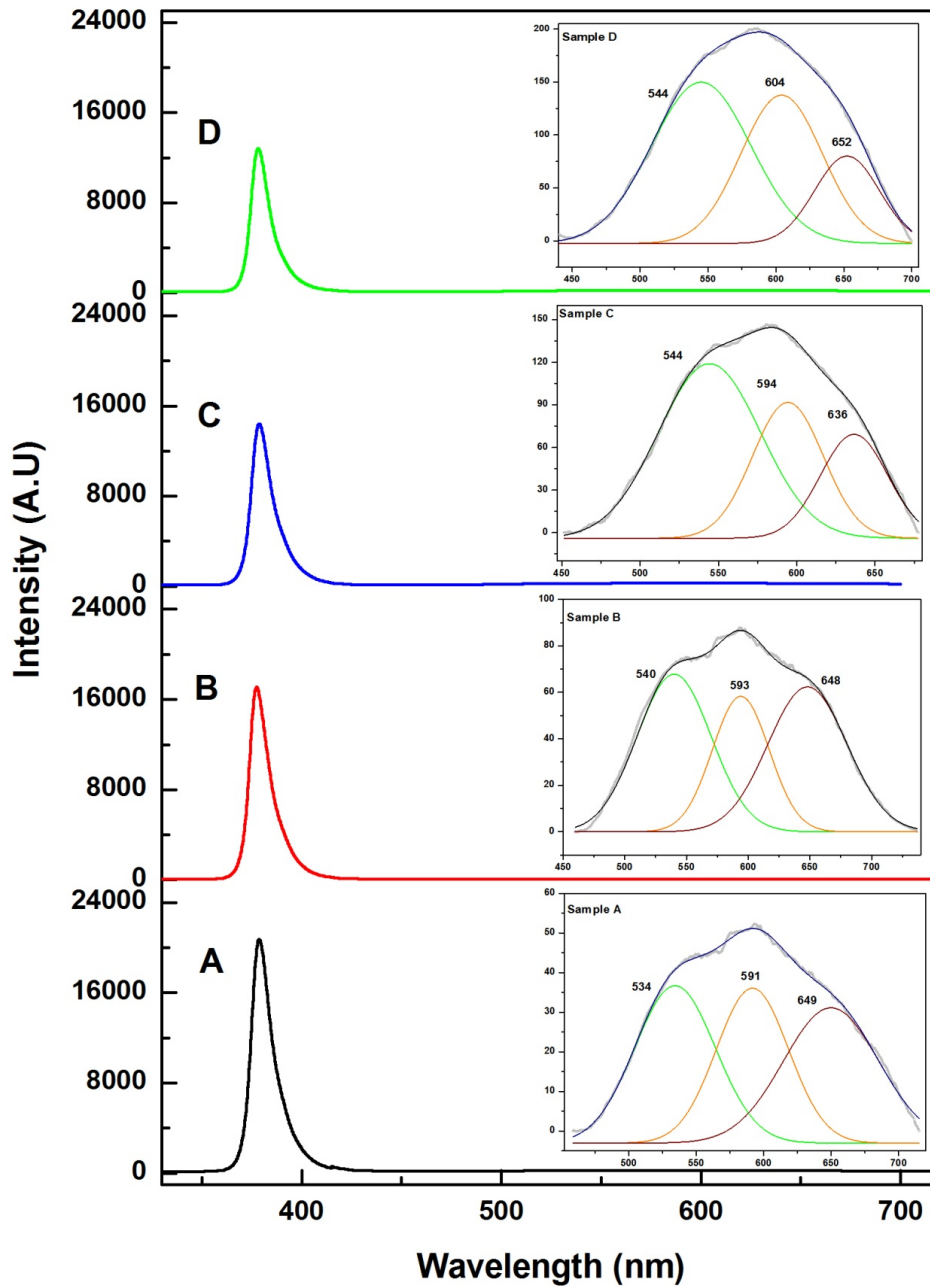


Figure 10.10: Room temperature PL spectra of ZnO seed layer (Sample A) and nanorods (Sample B, C, D).

We have studied degradation of Methylene blue (MB) dye for investigating photocatalytic activity of all the samples. Fig. 10.11 displays the time-dependent absorption

spectra of MB dye under visible light irradiation for all samples. Photocatalytic activity of MB solution alone was used as a control (data not shown). The peak at ~ 660 nm was selected for monitoring the degradation of MB.

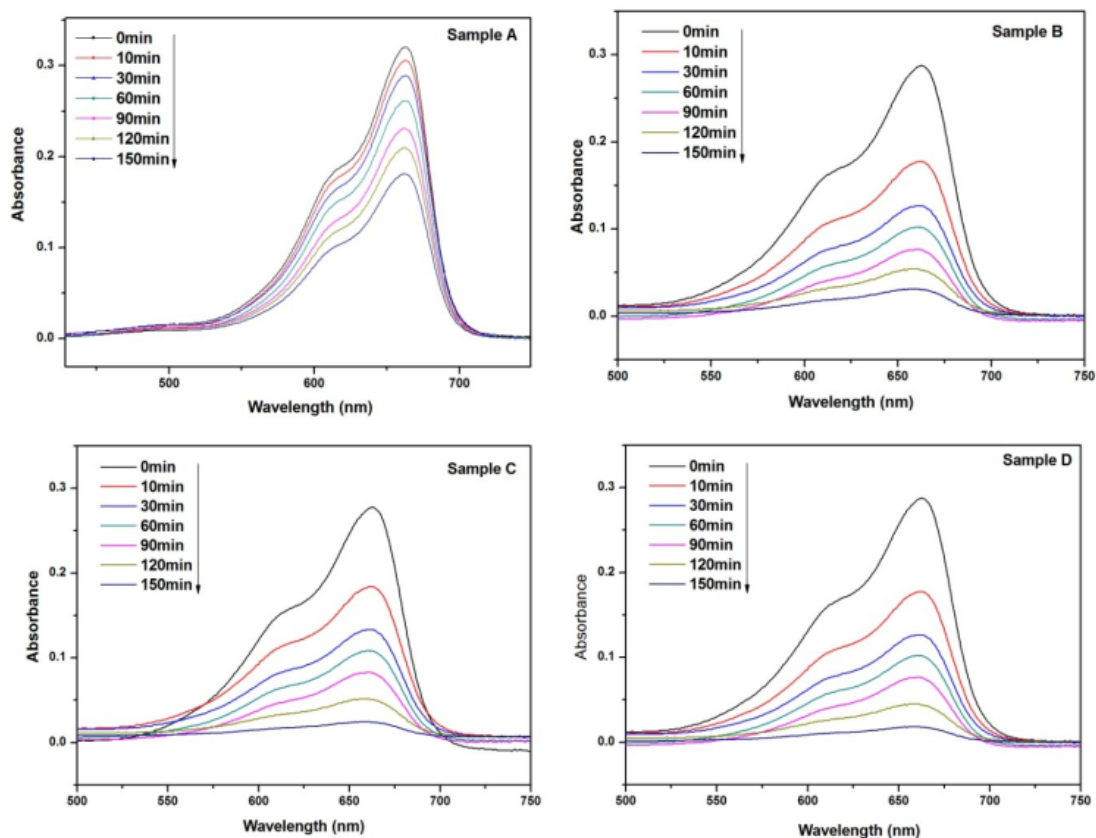


Figure 10.11: Time-dependent UV-Vis absorbance spectra of the MB solution using ZnO seed layer and NRs as photocatalysts.

The nanoparticle film (seed layer) of sample-A, when placed in MB solution, showed poor MB degradation after 150 min. On the other hand, for ZnO NR arrays, the MB solution has been observed to degrade completely in 150 minutes. Thus, a good MB degradation was observed for all NR arrays. However, the degradation rate is more for sample D than B or C. This finding is in accordance to absorbance and emission results. Hence, ZnO nanorod arrays demonstrate excellent MB degradation. In the absence of any photocatalyst (i.e. when no sample was placed) in MB solution, almost no reduction in the absorbance peak was observed, under irradiation, indicating no loss for MB.

Time-dependent degradation of MB is shown in fig. 10.12. The relative con-

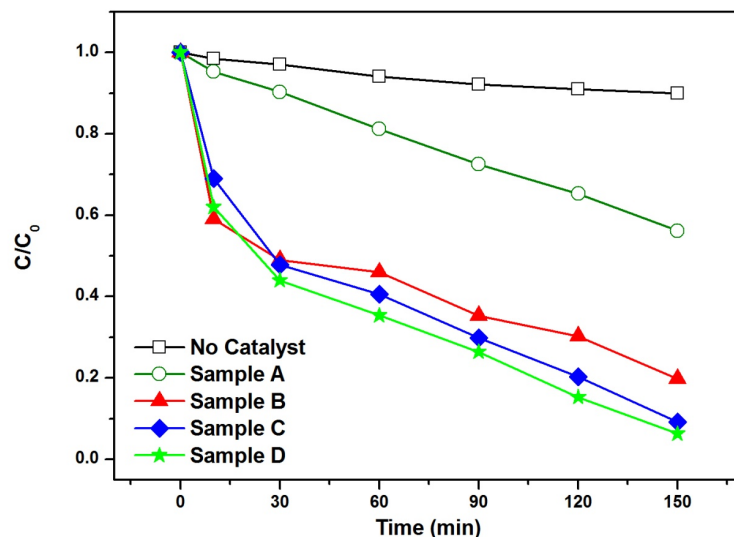


Figure 10.12: Variation of degradation rate of the MB dye with irradiation time for ZnO seed layer (sample A) and NRs (samples B,C,D)

centration (C/C_0) of MB is plotted as a function of time. Here, C_0 is the initial concentration of MB before irradiation and C is the concentration at the irradiation time, t . In the absence of any photocatalyst (i.e when no sample was placed) in MB solution, the MB degradation was poor even after 150 min. For the nanoparticle film (seed layer) sample-A, some degradation of MB has been noticed. However, far superior MB degradation was achieved for NR arrays (samples B,C,D), with sample-D displaying the maximum degradation capability. Percentage of degradation after visible light irradiation for 150 minutes, were found to be $\sim 93\%$ for sample D, $\sim 90\%$ in the case of sample C and $\sim 80\%$ in the case of sample B, respectively. These results indicate the excellent photocatalytic response of ZnO NRs in degradation of organic dyes upon visible light irradiation. The excellent photocatalytic response ($\sim 70\%$) was observed within 60 minutes of photo irradiation for ZnO NR arrays. Among all the NR samples, sample D shows highest photocatalytic activity of 93% in 150 min. Photocatalytic properties of hydrothermally grown ZnO NRs using MB degradation in visible light has been studied by Bora et al. who observed an efficiency of nearly 90% and 55%, in 180 min, after annealing at 250°C and 450°C, respectively [39].

Baruah et.al. also reported an efficiency of 90% in 180 min, for hydrothermally produced ZnO NRs [23]. For microwave hydrolysed ZnO NRs, with quasi stable surface states, they observed 97% efficiency in 180 min.

Several factors such as phase structures, carrier recombination, composition, crystallinity, particles size, surface defects, surface hydroxyl groups etc. strongly influence the photocatalytic activity of metal oxides [60]. Earlier studies have shown that surface morphology play a pivotal role in controlling the photocatalytic activity of ZnO nanostructures [61–64]. In our case, the enhanced catalytic performance of ZnO NRs can be explained by synergic effect of two factors; the morphology (1-D nanostructures) of the samples and the sub-band formation due to the oxygen vacancy states. The space charge region preferentially develops along the longitudinal direction in 1-D aligned ZnO nanocrystallites [56]. This promotes photo generated electrons to flow along the length in the crystallite causing their delocalization. A drastic decrease in electron-hole recombination probability is thus expected [56]. Consequently, presence of large number of electrons-hole pairs on the active sites of the nanocrystal surface results higher photo-catalytic activity in comparison to nanoparticle (seed layer) thin films. This is confirmed from the PL results.

The enhanced photocatalytic activity of NRs in visible light, as observed in this study, can also be attributed to the surface defect states on ZnO NRs. Presence of defect states lead to sub-bandgap transitions under visible light irradiation. Active electron-hole pairs thus created will be effectively transferred to the adsorbed MB molecules to participate in the redox reaction, thus improving the MB degradations. Better photocatalytic activity as well as improved transfer rates are thus achieved [39, 65]. Wang et.al. have reported that impurity states become less localised and begin to overlap with the valence band edge as the number of oxygen vacancies increase, causing a rise in the valence band position [66]. Thus, the NRs become more efficient for absorption of visible light. This is confirmed from the absorbance results. The findings from this work can be important for future investigations on controlling the defect states of ZnO NRs, by various growth conditions, which can further enhance the photocatalytic activities.

10.3 Conclusions:

This chapter discusses the photocatalytic activity of ZnO NR arrays which were synthesized on Si and ITO substrates via a simple hydrothermal method. From structural and morphological characterizations, it was observed that the as-grown nanorods are crystalline having wurtzite hexagonal phase along the c-axis. Vertically aligned ZnO NR arrays show enhanced photocatalytic activity as compared to ZnO nanoparticle (seed layer) thin films. Surface defect states in ZnO NRs enhance the visible light absorption by allowing sub-band gap transitions and producing active electron-hole pairs for redox reactions. For 1-D nanostructures, photo generated electrons can flow along the crystal length leading to an increased delocalization of electrons. Thus, 1-D nano-structured crystals exhibit a remarkable decrease in electron-hole recombination rate. These two factors lead to enhancement of photocatalytic activity of NRs. The developed methodology presents a convenient environment friendly route for achieving improved photocatalytic activity under visible light.

Bibliography

- [1] B. Liu and H. C. Zeng, *J. Am. Chem. Soc.*, 125, 4430 (2003).
- [2] L. Guo, Y. L. Ji and H. Xu, *J. Am. Chem. Soc.*, 124, 14864 (2002).
- [3] Z. Y. Jiang, T. Xu, Z. X. Xie, Z. W. Lin, X. Zhou, X. Xu, R. B. Huang and L. S. Zheng, *J. Phys. Chem. B*, 109, 23269 (2005).
- [4] H. Huang, S. Yang, J. Gong, H. Liu, J. Duan, X. Zhao and R. Zhang, *J. Phys. Chem. B*, 109, 20746 (2005).
- [5] X. H. Zhang, S. Y. Xie, Z. Y. Jiang, X. Zhang, Z. Q. Tian, Z. X. Xie, R. B. Huang and L. S. Zheng, *J. Phys. Chem. B*, 107, 10114 (2003).
- [6] M. Law, L. Greenel, J. C. Johnson, R. Saykally and P. Yang, *Nat. Mater.*, 4, 455 (2005).
- [7] P. Ravirajan, A. M. Peiro, M. K. Nazeeruddin, M. Graetzel, D. D. C. Bradley, J. R. Durrant and J. Nelson, *J. Phys. Chem. B*, 110, 7635 (2006).
- [8] W. J. E. Beek, M. M. Wienk, M. Kemerink, X. Yang and R. A. J. Janssen, *J. Phys. Chem. B*, 109, 9505 (2005).
- [9] S. Ju, K. Lee, D. B. Janes, M. H. Yoon, A. Facchetti and T. J. Marks, *Nano Lett.*, 5, 2281 (2005).
- [10] H. Kind, H. Yan, B. Messer, M. Law and P. Yang, *Adv. Mater.*, 14, 158 (2002).
- [11] R. Konenkamp, R. C. Word and M. Godinez, *Nano Lett.*, 5, 2005 (2005).
- [12] O. Harnack, C. Pacholsk, H. Weller, Akio Yasuda and Jurina M. Wessels, *Nano Lett.*, 3, 1097 (2003).

- [13] M. Huang, S. Mao, H. Feick, H. Yan, Y. Wu, H. Kind, E. Weber, R. Russo and P. Yang, *Science*, 292, 1897 (2001)
- [14] X. Wen, Y. Fang, Q. Pang, C. Yang, J. Wang, W. Ge, K. S. Wong and S. Yang, *J. Phys. Chem. B*, 109, 15303 (2005)
- [15] Y. Cui, Q. Wei, H. K. Park and C. M. Lieber, *Science*, 293, 1289 (2001).
- [16] S. Dhara and P. K. Giri, *Reviews in Nanoscience and Nanotechnology*, 2, 1 (2013).
- [17] A. M. Ali, E. A. C. Emanuelsson, D. A. Patterson, *Appl. Catal., B*, 97, 168 (2010).
- [18] S. K. Pardeshi, A. B. Patil, *J. Mol. Catal. A: Chem.*, 308, 32 (2009).
- [19] M. Qamar, M. Muneer, *Desalination*, 249, 535 (2009).
- [20] I. Poullos, D. Makri, X. Prohaska, *Global NEST Journal*, 1, 55 (1999).
- [21] E. R. Carraway, A. J. Hoffman, M. R. Hoffmann, *Environ. Sci. Technol.*, 28, 786 (1994).
- [22] G. L. Hornyak, J. Dutta, H. F. Tibbals, A. Rao, *Introduction to nanoscience (CRC Press: Boca Raton)*, 2008.
- [23] S. Baruah, M. A. Mahmood, M. T. Z. Myint, T. Bora and J. Dutta, *Beilstein J. Nanotechnol.*, 1, 14 (2010) .
- [24] Q. Ahsanulhaq, K. Jin-Hwan, and H. Yoon-Bong, *Nanotechnology*, 18, 485307 (2007).
- [25] Y. J. Lee, T. L. Sounart, D. A. Scrymgeour, J. A. Voigt and W. P. J. Hsu, *J. Cryst. Growth*, 304, 80 (2007).
- [26] S. C. Lyu, Zhang Y. Zhang, C. J. Lee, H. Ruh and H. J. Lee, *Chem. Mater.*, 15, 3294 (2003).
- [27] J. J. Wu and S. C. Liu, *J. Phys. Chem. B*, 106, 9546 (2002).

- [28] A. Umar, S. Lee, Y. H. Im and Y. B. Hahn, *Nanotechnology*, 16, 2462 (2005).
- [29] A. Umar and Y. B. Hahn, *Appl. Phys. Lett.*, 88, 173120 (2006).
- [30] A. Umar, H. W. Ra, J. P. Jeong, E. K. Suh and Y. B. Hahn, *Korean J. Chem. Eng.*, 23, 499 (2006).
- [31] A. Umar, B. Karunagaran, E. K. Suh and Y. B. Hahn, *Nanotechnology*, 17, 4072 (2006).
- [32] Syed M. Usman Ali, O. Nur, M. Willander, B. Danielsson, *Sensor Actuat B Chem*, 145, 869 (2010).
- [33] M. Kashif, U. Hashim, M. E. Ali, K. L. Foo, Syed M. Usman Ali, *J Nano Mat*, 7 (2013).
- [34] M. Kashif, Syed M. Usman Ali, M. E. Ali, H. I. Abdulgafour, U. Hashim, M. Willander, Z. Hassan, *Phys Status Solid A*, 209, 143 (2012).
- [35] M. Kashif, U. Hashim, Syed M. Usman Ali, A. S. Alaeddin, M. Willander, M. E. Ali, *Microelectron Int*, 29, 1 (2012)
- [36] Y. B. Li, Y. Bando, T. Sato, K. Kurashima, *Appl Phys Lett*, 81, 144 (2002).
- [37] Syed M. Usman Ali, M. Kashif, Z. H. Ibupoto, M. Fakhar-e-Alam, U. Hashim, M. Willander, *Micro & Nano Lett* , 6, 609 (2011).
- [38] X. Cai, B. Han, S. Deng, Y. Wang, C. Dong, Y. Wang and I. Djerdj, *Cryst Eng Comm*, 16, 7761 (2014).
- [39] T. Bora, P. Sathe, K. Laxman, S. Dobretsov, J. Dutta, *Today*, 284, 11 (2017).
- [40] O. Lupan, T. Pauporte, L. Chow, B. Viana, F. Pelle, L. K. Ono, B. Roldan Cuenya and H. Heinrich, *Appl. Surf. Sci.*, 256, 1895 (2010).
- [41] B. D. Cullity, S.R. Stock, *Elements of X-Ray Diffraction*, (Prentice Hall),2001.
- [42] C. Bundesmann, N. Ashkenov, M. Schubert, D. Spemann, T. Butz, E. M. Kaidashev, M. Lorenz, M. Grundmann, *Appl. Phys. Lett.*, 83, 1974 (2003).

- [43] C. A. Arguello, D. L. Rqusseau, S. P. S. Porto, *Phy Rev*, 181, 1351 (1969).
- [44] T. C. Damen, S. P. S. Porto, *B. Tell, Phys. Rev.*, 142, 570 (1966).
- [45] F. J. Manj, *J. Appl. Phys.*, 97, 053516 (2005).
- [46] M. Tzolov, *Thin Solid Films*, 379, 28 (2000); D. Das and P. Mondal, *RSC Advances*, 4, 35735 (2014).
- [47] Y. Huang, M. Liu, Z. Li, Y. Zeng, S. Liu, *Materials Science and Engineering B*, 97, 111 (2003).
- [48] Aurangzeb Khan, *J. Pak. Mater Soc.*, 4, 5 (2010).
- [49] B. C. Mohanty, Y. H. Jo, D. H. Yeon, I. J. Choi, and Y. S. Cho, *Appl. Phys. Lett.*, 95, 062103 (2009).
- [50] V. Srikant and D. R. Clarke, *J. Appl. Phys.*, 83, 5447 (1998).
- [51] V. Solanki, S. R. Joshi, I. Mishra, D. Kabiraj, N. C. Mishra, D. K. Avasthi, and Shikha Varma, *Journal of Applied Physics*, 120, 054303 (2016).
- [52] Y. C. Zhang, X. Wu, X. Y. Hu, and R. Guo, *J. Cryst. Growth*, 280, 250 (2005).
- [53] M. M. Khan, S. A. Ansari, J. Lee and M. H. Cho, *Nanoscale*, 5, 4427 (2013).
- [54] K. Samanta, P. Bhattacharya and R. S. Katiyar, *Appl. Phys. Lett.*, 87, 101903 (2005).
- [55] M. R. Alenezi, S. J. Henley, N. G. Emerson and S. R. P. Silva, *Nanoscale*, 6, 235 (2014).
- [56] X. Zhang, J. Qin, Y. Xue, P. Yu, B. Zhang, L. Wang and R. Liu, *Sci. Rep.*, 4, 4596 (2014).
- [57] A. Shetty and K. K. Nanda, *Appl. Phys. Lett.*, 100, 242108 (2012); A. Escobedo-Morales and U. Pal, *Appl. Phys. Lett.*, 93, 193120 (2008).
- [58] K. Vanheusden, W. L. Warren, C. H. Seager, D. R. Tallant, J. A. Voigt, B. E. Gnade, *J. Appl. Phys.*, 79, 7983 (1996).

- [59] J. Liqiang, Q. Yichun, W. Baiqi, L. Shudan, J. Baojiang, Y. Libin, F. Wei, F. Honggang and S. Jiazhong, *Sol. Energy Mater. Sol. Cells*, 90, 1773 (2006).
- [60] S. Liu, C. Li, J. Yu & Q. Xiang, *Cryst Eng Comm.*, 13, 2533 (2011).
- [61] L. Xu, Y. Hu, C. Pelligra, C. Chen, L. Jin, L. Huang, S. Sithambaram, M. Aindow, R. Joesten, S. L. Suib, *Chem. Mater.*, 21, 2875 (2009).
- [62] Z. Liu, Q. Zhang, Y. Li, H. Wang, *J. Phys. Chem. Solids*, 73, 651 (2012).
- [63] X. Wang, Q. Zhang, Q. Wan, G. Dai, C. Zhou, B. Zou, *J. Phys. Chem. C*, 115, 2769 (2011).
- [64] F. Lu, W. Cai, Y. Zhang, *Adv. Funct. Mater.*, 18, 1047 (2008).
- [65] R. M. Sheetz, I. Ponomareva, E. Richter, A. N. Andriotis, M. Menon, *Phys. Rev. B*, 80, 195314 (2009).
- [66] J.P. Wang, Z.Y. Wang, B.B. Huang, Y.D. Ma, Y. Y. Liu, X. Y. Qin, X. Y. Zhang, Y. Dai, *ACS Appl. Mater. Interfaces*, 4, 4024 (2012).

Chapter 11

Conclusion

The present thesis discusses the fabrication of TiO_2 and ZnO nanostructured films by several routes, like sputter deposition, electrodeposition and hydrothermal. These films present many advanced functional properties like resistive switching (RS), photo absorbance (PA) response and non-enzymatic glucose sensing. RS and PA characteristics are also expressed by thin TiO_2 and ZnO nanostructured films after they have been ion irradiated by Ti ions. Such ion irradiated TiO_2 films delineate a structural transformation with anatase content rising, compared to rutile form, beyond a critical fluence. Non-enzymatic glucose sensing behavior has been investigated, using the cyclic voltammetry, for $\text{Cu}_x\text{O-ZnO}$ ($x=1,2$) and CuO-TiO_2 based nanostructured films. These films have been respectively prepared by co-electrodeposition method and chemical route. ZnO nano-rod (NR) arrays, prepared by hydrothermal route, have been investigated for their PA response and photocatalytic activity.

In chapter 1, we discuss the fundamental concepts of the formation of nanostructures, basics of ion-matter interactions and the theoretical framework of the pattern formation via ion irradiation. The significance of the scaling theory for understanding the nano-patterning of surfaces, structural phase transitions, photo-absorbance behavior and resistive switching properties have been introduced here. The salient features of glucose sensing characteristics via cyclic voltammetry have also been presented. Chapter 2 discusses the basic synthesis routes, utilized in this thesis, along with the methodology and experimental setups. Various techniques that have been applied here for the characterization of the nanostructured films as well as for measuring associated functional properties are presented. Structures, crystalline forms

as well as the advanced properties of the materials, investigated here, have also been introduced.

TiO₂ nanostructured films have been investigated in the next four chapters (3 to 6). Some important properties of these films, such as photo-absorbance (PA) characteristics and resistive switching (RS) behavior, have been studied here. Thin films of TiO₂ (80 nm) have been sputter deposited on Au/Ni/SiO₂/Si substrate and subsequently ion implanted at several fluences ranging from 1×10^{10} to 1×10^{15} ions/cm². In chapter 3, we have discussed the structural phase transformation and the electrical resistive switching properties of these films after they were implanted with 50 keV Ti ions. Resonance Raman measurements with UV laser, grazing incidence X-ray diffraction (GIXRD), high resolution transmission electron microscopy (HRTEM), x-ray photoelectron spectroscopy (XPS), and atomic force microscopy (AFM) techniques have been utilized to investigate the modifications in thin films. The as-deposited as well as ion implanted films delineate the existence of mixed phases, rutile (R) and anatase (A). Interestingly at a critical fluence, a structural phase transformation, from A to R is observed. This transformation increases with influence and its initiation appears to be depth dependent. Raman and HRTEM studies reveal that rutile regions grow in size at the expense of anatase zones. The role of anatase crystalline-dimension on the transformation have also been explored. GIXRD results and phonon-confinement model (PCM) applied to Raman spectra show that the as-deposited films contain bigger anatase- nanocrystallites in comparison to the ion implanted films. All the films show presence of oxygen vacancies. These vacancies grow in number with ion fluence, and appear to play a pivotal role in A-R transition. Formation of the conducting filaments, through the migration of oxygen vacancies under the influence of the appropriate bias, appears to become responsible for the development of bipolar resistive switching in TiO₂ nanostructured films, implanted at the highest fluence.

Chapter 4 discusses the A-R structural transformation in Ti ion implanted TiO₂ thin films by utilizing visible Raman spectroscopy technique. Resonance Raman spectroscopy with UV laser is a more surface sensitive technique, compared to the visible laser induced Raman spectroscopy. Both visible- Raman and GIXRD measurements reveal that the transformation occurs at a critical fluence of 1×10^{13} ions/cm². Reso-

nance Raman (chapter 3) suggested this fluence to be slightly higher at the surface, indicating a depth dependence for the initiation of the transformation. PA properties and band gap modifications, of the ion implanted TiO₂ thin films, have also been studied. Photo-absorption measurement in UV-Visible (UV-Vis) regime show shifts in the band edge, as a function of ion fluence. The band gaps (E_g), estimated here using Tauc plots, display a systematic decrease for fluences higher than 1×10^{13} ions/cm². This also supports enhancement of R content in the TiO₂ films after A- R transformation.

In chapter 5, scaling formalism has been applied to understand the dynamical evolution of the as-deposited and ion implanted TiO₂ thin films. The implantation of TiO₂ thin films was undertaken with 50 keV Ti ions. Morphological investigations have been performed by utilizing AFM technique. The as-deposited surfaces show presence of nanostructures. A reduction in the sizes of these nanostructures is observed after implantation. Additionally, the rms surface roughness also decreases. These results reflect a surface smoothening upon implantation. Dynamics of the surface evolution has also been investigated through height-height correlation function (HHCF) and power spectral density (PSD) analysis. The scaling parameters like, roughness exponent (α), growth exponent (β) and correlation length (ξ) have been extracted. The results reveal that diffusion dominated smoothening processes are significant in controlling the dynamics of the ion irradiated TiO₂ thin films.

In chapter 6, surface dynamics of Ar⁺ ion irradiated single crystal rutile TiO₂(110) has been investigated by utilizing the scaling formalism. Surface rms roughness, HHCF and PSD have been utilized to extract various scaling parameters, including α , β and ξ . Although at low fluence conditions ($\leq 5 \times 10^{16}$ ions/cm²), the scaling dynamic analysis and HHC provide $\alpha \sim 0.72 - 0.74$, $\beta \sim 0.3$ and $\gamma \sim 0.25 - 0.27$, at higher fluences (between 5×10^{16} and 5×10^{17} ions/cm²), $\alpha \sim 0.85$ and $\beta \sim 1$ are observed. A saturation in roughness is observed for fluences $> 5 \times 10^{17}$ ions/cm². Scaling results demonstrate that although at low fluences the dynamics and evolution of single crystal rutile TiO₂ surface is dominantly controlled by the knock- on and bulk diffusive processes, sputter induced erosion is important at high fluences.

In the next four chapters (7 to 10), we have discussed the synthesis of ZnO nanos-

structured films by a few different methods, e.g. sputter deposition, co-electrodeposition and hydrothermal. Some important functional properties of ZnO films like, photo-absorption behavior, resistive switching and non-enzymatic glucose detection via cyclic voltammetry, have been studied here. In chapter 7, we discussed the RS and PA properties of the ZnO thin films which have been sputter deposited and subsequently ion implanted with 50 keV Ti ions. The ion fluence was varied from 1×10^{12} to 1×10^{15} ions/cm². Raman and GIXRD results reveal that the crystallinity of the films improve with ion fluence. XPS measurements confirm the presence of oxygen vacancies in the ion implanted films. The presented results show that oxygen vacancy states, created by ion implantation, play a pivotal role in modulating PA as well as electrical switching properties of the thin films. The formation of conducting filaments, upon the application of bias, assists in the RS mechanism via percolation of the current. RS phenomenon is, however, asymmetric. The switching from HRS to LRS (and back to HRS) is noticed for the positive voltages only, while a rectifying behavior occurs for the negative voltages. Enhancement in the photo-absorption response, with fluence, is associated with the bandgap tailoring in the ion implanted ZnO films.

Chapter 8 discusses the non-enzymatic glucose sensing behavior, via cyclic voltammetry, of the hybrid Cu₂O-ZnO nanostructures. These conjugated hybrid nanostructures have been prepared via the single step co-electrodeposition (CED) technique. Two low concentrations of Cu²⁺, 1% (sample C₁) and 10% (sample C₁₀), were used for fabricating hybrid nanostructures. Though ZnO nanostructures alone, grown by electrodeposition technique, do not exhibit any glucose sensing character, CED grown Cu₂O-ZnO hybrid nanostructures (C₁ and C₁₀) show non-enzymatic glucose sensing and amperometric behavior with cyclic voltammetry technique. Sample C₁₀ shows a good sensitivity of $441.2 \mu\text{A mM}^{-1} \text{cm}^{-2}$, linear range of 0.02 - 1 mM and low detection limit of $0.13 \mu\text{M}$ along with a fast response time (less than 3 sec). This sensor also exhibits a long-term stability and reproducibility. In this chapter, we have also explored the PA behavior of C₁ and C₁₀ nanostructures. Both of them display a higher PA response in the UV-Visible regime, compared to only ZnO nanostructures. Band gap tailoring is responsible for this enhancement.

Chapter 9 presents the non-enzymatic glucose sensing behavior, via cyclic voltam-

metry, of the $\text{Cu}_x\text{O-ZnO}$ ($x=1,2$) type composite nanostructures. They have been prepared using CED method with a high Cu concentration of 50% (sample C_{50}). Another sample with a low Cu concentration of 2% (sample C_2) shows $\text{Cu}_2\text{O-ZnO}$ type nanostructures. Both the samples display the non-enzymatic glucose sensing behavior, via cyclic voltammetry. Sample C_{50} shows a sensitivity of $384.6 \mu\text{A mM}^{-1} \text{cm}^{-2}$, linear range of 0.03 - 3 mM and a low detection limit of 0.7 μM . Results have also been compared with the findings of chapter 8. Overall, it is noticed that the films C_1 , C_2 and C_{10} , prepared with lower Cu content (1%, 2% and 10%, respectively), display $\text{Cu}_2\text{O-ZnO}$ type nanostructures. On the other hand C_{50} , prepared with high (50%) Cu content have nanostructures of $\text{Cu}_x\text{O-ZnO}$ ($x=1,2$) form. Among these, C_{10} demonstrates highest sensitivity for the non-enzymatic sensing of glucose.

Photo-absorption response of nanostructured films, C_1 , C_2 , C_{10} and C_{50} has been explored, in chapters 8 and 9, for UV-Visible range. A significant band gap tailoring is observed such that E_g reduces, with increasing Cu content. C_{50} with lowest bandgap exhibits highest photo-absorption in the visible range.

Chapter 9 also discusses non-enzymatic glucose sensing behavior, via cyclic voltammetry, of the CuO-TiO_2 type composites (sample T_{10}) that were prepared via chemical route. These composites, however, illustrate poor sensitivity, compared to $\text{Cu}_2\text{O-ZnO}$ or $\text{Cu}_x\text{O-ZnO}$ based nanostructures studied here, for glucose. An improved photo-absorption response in the visible range for T_{10} , compared to TiO_2 has been observed.

Chapter 10 presents morphological, structural and photo-absorbance properties of the aligned ZnO nanorods (NRs) synthesized by a simple hydrothermal method. Field emission scanning electron microscopy (FESEM), GIXRD, Raman, UV-Visible and Photoluminescence (PL) spectroscopic techniques have been employed to characterize NR arrays. Results show that crystallinity and alignment of ZnO NRs lead to good photocatalytic activity in the presence of visible light. PL spectra revealed a decrease in the UV emission, suggesting a reduced recombination of the photo generated carriers. The visible region emission is due to the surface oxygen vacancies. Increase of charge separation rate observed from emission spectra and the vacancy related sub-bands in the absorbance spectra are together responsible for the enhanced visible light photocatalytic activity of ZnO NRs. Vertically aligned, 1-dimensional morphol-

ogy of ZnO NRs and the presence of oxygen vacancy states assist in the visible light photocatalytic degradation of Methylene Blue dye.

In summary, the present thesis discussed the nanostructured films of TiO₂ and ZnO. Several methods like, sputter deposition, electrodeposition and hydrothermal technique have been utilized in the fabrication of these thin films. These nanostructured films exhibit immense potential as they present many advanced functional properties, like resistive switching, photo-absorption response and non-enzymatic glucose sensing via cyclic voltammetry. Nanostructured thin films of TiO₂ and ZnO, prepared by sputter deposition show resistive switching behavior in films that have been irradiated with Ti ions at a fluence 1×10^{15} ions/cm². Oxygen vacancies play a significant role in RS and PA response investigated here. Photo-absorbance response in both, TiO₂ and ZnO films, exhibits a bandgap modulation. In TiO₂ films, a structural phase transformation from anatase to rutile is also observed at a critical fluence. This has been investigated in detail using Raman spectroscopy. Dynamical evolution of these films, investigated using the scaling formalism, shows diffusion dominated smoothening process. Cu_xO-ZnO (x=1,2) and CuO-TiO₂ composite nanostructures, prepared respectively by CED and chemical routes, display non-enzymatic glucose sensing behavior with cyclic voltammetry. ZnO nanorod arrays, prepared by hydrothermal methods, show photo-catalytic response conjugated with good photo-absorbance behavior in the visible region.